Ignition Modelling for Turbulent Non-Premixed Flows

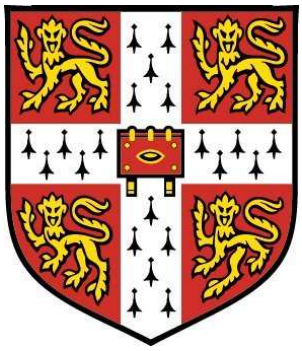

University of Cambridge
Department of Engineering

———

This dissertation is submitted for the degree of
Doctor of Philosophy

by:

Edward S. Richardson – Downing College

Wednesday, 16th of May, 2007

Declaration

This dissertation is the result of my own work and includes nothing which is the outcome of work done in collaboration except where specifically indicated in the text. The dissertation contains approximately **43,900** words, **97** figures and four tables.

Hopkinson Laboratory, Cambridge
Wednesday, 16$\underline{\text{th}}$ of May, 2007

Edward Richardson

Acknowledgments

I am profoundly grateful to many people for their help in the preparation of this work. Most especially I thank my supervisor, Dr E. Mastorakos, for his tremendous support in many aspects of my study. In particular I thank him for his expert guidance combined with the freedom he has given me to explore this subject.

The implementation of the Conditional Moment Closure (CMC) developed in this work has benefited from contributions from E. Mastorakos, I.S. Kim, G. De Paola and A. Triantafyllidis (Cambridge), and Y.M. Wright (E.T.H. Zurich). Without this valuable collaboration it would not have been possible to attempt the calculations in this thesis. I am extremely grateful to my exact contemporary, G. De Paola, for his patience, intelligence and enthusiasm during the many hours we have spent together trying to understand and implement the CMC.

I have learned an enormous amount from working with Nilanjan Chakraborty, who produced the DNS data studied in chapter 4. Furthermore I acknowledge his cheerful help in the painful task of deriving the conditional turbulent flux equation. I thank S. Cant for permission to use his DNS code.

All experimental results used in this thesis were obtained by other members of Dr Mastorakos' research team at Cambridge, therefore I am indebted to S.F. Ahmed, T. Marchione, R. Balachandran and J. Dawson for the high quality of their work in the laboratory, and for the access and insight they have given me to their results.

For their technical input I thank P. Benie (Cambridge), R. Eggels and C.D. Goddard (Rolls-Royce plc.), A. Sánchez (Universidad Carlos III de Madrid), H. Ernst (CoSiLab support), L. Vervisch (I.N.S.A Rouen). Financial support has been received from the UK Engineering and Physical Sciences Research Council and Rolls-Royce plc.

Finally I would like to express my gratitude for the patience, support and strength I have received from my friends, family, colleagues and crew mates during this work. Above all I acknowledge the influence from there being 'too many strong women in my life', and I dedicate this thesis to them.

Publications

Preliminary work for this thesis has been published in the following articles:

1. Numerical Investigation of Spark Ignition in a Laminar Methane-Air Counterflow [109].

2. Numerical Investigation of Forced Ignition in Laminar Counterflow Non-Premixed Methane-Air Flames [114].

3. Analysis of Direct Numerical Simulations of ignition fronts in turbulent non-premixed flames in the context of Conditional Moment Closure [113].

Other related works by the author include:

1. Modelling of Homogeneous Charge Compression Ignition Engines, E.S.Richardson, Cambridge University Engineering Department Masters Thesis (2003) [110].

2. Implementation of CHEMEQ2 for various turbulent combustion simulations, Hopkinson Laboratory report No.1 (2004) [111].

3. Application of the Fernández-Tarrazo et al. one-step chemistry model for partially premixed combustion to $n-$heptane, Hopkinson Laboratory report No. 2 (2006) [112].

4. Micromixing effects in a reacting plume by the Stochastic Fields method. A. Garmory, E.S. Richardson and E. Mastorakos, Atmospheric Environment (2006) [42].

Abstract

This thesis describes a numerical investigation of ignition modelling for turbulent non-premixed flows that is relevant to the simulation of ignition in aviation gas turbines.

The first part of this thesis describes a fundamental numerical investigation of ignition in non-premixed flows. Simulations of forced ignition in strained non-premixed laminar flows are presented. These show that fluid dynamic strain may preclude ignition of otherwise flammable mixtures and that the maximum ignitable strain rate may be lower than the critical strain rate for extinction of a steady, non-premixed flame.

Conditional Moment Closure (CMC) modelling is presented for forced ignition in gas and liquid fueled turbulent flows. The modelling was analysed using Direct Numerical Simulation (DNS) data for spark ignition kernels in turbulent non-premixed flow, with particular emphasis on the modelling of the conditional turbulent flux, and the conditional reaction rate. The analysis showed that counter-gradient conditional turbulent fluxes may arise due to an effect involving pressure fluctuations. A counter-gradient correction to the traditional eddy-diffusivity model is proposed.

The second part of this thesis describes the application of the CMC modelling to prediction of ignition in a range of experimental flows: a turbulent non-premixed jet, a non-premixed bluff body burner, and a spray-fueled bluff body burner. The main features of the experimental observations were captured, however the rate of flame propagation is over-predicted in each case. This has been attributed to the limitations of the first order reaction rate closure for these problems and the limitations of the Reynolds averaged Navier-Stokes modelling used for the turbulent flow.

The properties of the proposed correction to the conditional turbulent flux modelling are demonstrated in the context a lifted turbulent jet flame. New terms arising in the two phase CMC equations are discussed and are seen to play a significant role in spray-fueled combustion in a bluff body stabilised burner.

Finally a predictive tool for preliminary combustor design studies is developed with reference to a variety of experimental and industrial ignition data.

The present work provides a practical and theoretical basis for the extension of the CMC ignition modelling to the Large Eddy Simulation framework and to the predictive simulation of aviation gas turbine ignition.

Table of Contents

Table of Contents i

List of Figures iv

List of Tables xiii

1 Introduction 1
- 1.1 Combustion challenges . . . 1
- 1.2 Gas turbine ignition . . . 2
  - 1.2.1 Design challenges . . . 2
  - 1.2.2 Design methods . . . 3
- 1.3 Turbulent combustion simulation . . . 4
  - 1.3.1 Direct numerical simulation . . . 4
  - 1.3.2 Reynolds averaged Navier-Stokes modelling . . . 5
  - 1.3.3 Large eddy simulation . . . 5
  - 1.3.4 Turbulent reacting flow modelling . . . 6
- 1.4 Objectives of this study . . . 8

2 Conditional moment closure and its numerical solution 9
- 2.1 CMC modelling for ignition problems . . . 9
  - 2.1.1 Primary closure hypotheses . . . 11
  - 2.1.2 CMC sub-models . . . 13
- 2.2 Implementation of the CMC . . . 16
  - 2.2.1 The coupling of the CFD and CMC codes . . . 16
  - 2.2.2 Chemical reaction . . . 19
  - 2.2.3 Spark ignition . . . 23
  - 2.2.4 CMC and two phase combustion . . . 24
  - 2.2.5 Numerical implementation . . . 28
- 2.3 Summary . . . 29

3 Analysis of ignition in laminar strained non-premixed flow 31
- 3.1 Background . . . 31
- 3.2 Formulation . . . 33

3.2.1 Configuration and computational code . . . 33
3.2.2 Spark representation . . . 34
3.3 Results and discussion . . . 35
3.3.1 Ignition limits . . . 35
3.3.2 Ignition evolution . . . 40
3.3.3 Implications for ignition in turbulent flow . . . 48
3.4 Conclusions . . . 49

4 Analysis of ignition in turbulent non-premixed flow 51
4.1 Background . . . 51
4.2 Formulation . . . 52
4.2.1 Simulations . . . 52
4.2.2 Conditional moment equations . . . 54
4.3 Results and discussion . . . 60
4.3.1 Flow patterns . . . 60
4.3.2 CMC equation analysis . . . 61
4.3.3 Reaction rate closure . . . 68
4.3.4 Conditional fluxes . . . 70
4.4 Conclusions . . . 75

5 Modelling for ignition of a lifted methane jet flame 80
5.1 Background . . . 81
5.1.1 The turbulent jet . . . 81
5.1.2 Ignition of partially premixed flow . . . 81
5.1.3 Propagation and stabilisation of jet flames . . . 82
5.2 CMC simulation . . . 85
5.2.1 Flow configuration . . . 85
5.2.2 Turbulent flow field . . . 87
5.2.3 Application of the CMC model . . . 94
5.2.4 Numerical sensitivity of the CMC solution . . . 96
5.2.5 Target problems . . . 99
5.3 Results and discussion . . . 100
5.3.1 Spark ignition . . . 100
5.3.2 Edge flame propagation . . . 103
5.3.3 The steady lifted flame . . . 110
5.3.4 Conditional turbulent flux modelling . . . 115
5.4 Conclusions . . . 118

6 Modelling for ignition of bluff body stabilised flames 121
6.1 Background . . . 121
6.2 CMC simulation . . . 124
6.2.1 Flow configuration . . . 124
6.2.2 Turbulent flow field . . . 125

6.2.3 Application of the CMC model . . . 134
6.2.4 Numerical sensitivity of the CMC solution . . . 135
6.2.5 Target simulations . . . 135
6.3 Results and discussion: Methane flame . . . 136
6.4 Results and discussion: Spray fueled flow . . . 140
6.5 Analysis of the CMC evaporation terms . . . 149
6.6 Conclusions . . . 151

7 Analysis of combustor ignitability 153
7.1 Background . . . 153
7.2 Model development . . . 155
7.2.1 Modelling . . . 155
7.2.2 Implementation . . . 163
7.3 Application to a lifted methane jet flame . . . 165
7.4 Other applications . . . 170
7.4.1 Methane bluff body flame . . . 170
7.4.2 Heptane spray flame . . . 172
7.4.3 Gas turbine ignition . . . 176
7.4.4 Time scale analysis . . . 183
7.5 Conclusions . . . 187

8 Conclusions 188
8.1 Spark ignition of turbulent non-premixed flow . . . 188
8.2 Flame propagation in turbulent non-premixed flow . . . 190
8.3 Ignition of spray fueled flow . . . 191
8.4 Ignition simulation for design . . . 192
8.5 Areas for further research . . . 193

Bibliography 211

A Appendix 212
A.1 Derivation of the CMC energy equations in two phase flow . . . 212
A.1.1 The CMC enthalpy equation with fuel evaporation . . . 212
A.1.2 The CMC temperature equation with fuel evaporation . . . 215
A.2 Second order reaction rate closure . . . 216
A.3 Derivation of the conditional turbulent flux transport equation . . . 217
A.3.1 Overview . . . 217
A.3.2 Instantaneous balance equations . . . 218
A.3.3 The conditional species mass fraction equation . . . 219
A.3.4 The conditional velocity equation . . . 221
A.3.5 Final steps . . . 223
A.4 An estimate for the mixture fraction variance during spray evaporation 226

List of Figures

2.1 The modelled flame $n-$heptane laminar flame speed versus equivalence ratio at 1bar and 300K, compared to experimental measurements by Huang et al (crosses) [53], and by Davis and Law (circles) [30]. 22

2.2 The maximum conditional temperature observed in steady zero dimensional CMC calculations found using the one step model for $n-$heptane, Eq. 2.14-2.18 versus N_0, the peak value of the conditional scalar dissipation rate given by the AMC closure, Eq. 2.10. 22

2.3 Mixture fraction space profiles of reactant mass fraction and temperature conditional expectations from use of the one step $n-$heptane mechanism, Eq. 2.14-2.18 (solid lines) and the Held et al. detailed mechanism [52] (dashed lines). 23

3.1 Transient temperature profiles in physical space during a successful ignition event. Spark B from table 3.1. 36

3.2 The loci of the ignitability limits for $3000K$ sparks (x) and $4000K$ sparks (o) for the $X = 0$ flame. The stoichiometric mixture fraction and the static rich and lean flammability limits are indicated. 37

3.3 The locus of the ignitability limits for $3000K$ sparks in a flame with $X = 0.8$. The stoichiometric mixture fraction and the static rich and lean flammability limits are indicated. 37

3.4 Transient temperature profiles in mixture fraction space for sparks A, B and C. 41

3.5 Transient mass fraction profiles in mixture fraction space for methane and oxygen for sparks A, B and C. 42

3.6 Transient heat release profiles in mixture fraction space for sparks A, B and C. The inset graph is an enlargement showing the stabilised heat release profile for case B. 44

3.7 Transient OH mass fraction profiles in mixture fraction space for sparks A, B and C. 45

3.8 Transient temperature profiles in mixture fraction space for sparks D, E and F. 46

3.9 Transient heat release profiles in mixture fraction space for sparks D, E and F. 47
3.10 Transient OH mass fraction profiles in mixture fraction space for sparks D, E and F. 48

4.1 Schematic drawing of the mixture fraction profile and the cylindrical ignition source for the turbulent mixing layer configuration. 53
4.2 The stoichiometric iso-surface (blue) and the iso-surface of $T = 0.5$ (red) for $u'/S_L = 4$. 61
4.3 Contours of unconditional flux in the y-direction and of the usual gradient model at $t = 2.1t_{sp}$ and for $u'/S_L = 4$. 62
4.4 Distributions in the y-direction of the cross stream averaged conditional pressure and temperature at $\eta = \xi_{st}$ and the indicated times. . 62
4.5 The spatial distribution of the various source terms in the CMC equation at $\eta = \xi_{st}$. (a): Run L1, $t = 1.05t_{sp}$; (b): Run L1, $t = 3.15t_{sp}$; (c): Run M1, $t = 1.05t_{sp}$; (d): Run M1, $t = 3.15t_{sp}$; (e): Run H1, $t = 1.05t_{sp}$; (f) Run H1, $t = 3.15t_{sp}$. 65
4.6 The budget for the CMC equation across mixture fraction. (a): Run L1, $t = 3.15t_{sp}$, at $\langle T|\eta_{st}\rangle = 0.85$; (b): Run M1, $t = 3.15t_{sp}$, $\langle T|\eta_{st}\rangle = 0.85$; (c): Run H1, $t = 3.15t_{sp}$, $\langle T|\eta_{st}\rangle = 0.5$. 66
4.7 The CMC equation terms normal to the flame surface, Eq 4.6 at $\eta = \xi_{st}$. (a): Run L1, $t = 1.05t_{sp}$; (b): Run L1, $t = 3.15t_{sp}$; (c): Run M1, $t = 1.05t_{sp}$; (d): Run M1, $t = 3.15t_{sp}$; (e): Run H1, $t = 1.05t_{sp}$; (f) Run H1, $t = 3.15t_{sp}$. 67
4.8 Conditional chemical source term for temperature as measured from the DNS (solid), from the first order closure (dots), and from the second order closure (dashed). (a): Run L1, $t = 3.15t_{sp}$; (b): Run H1, $t = 3.15t_{sp}$. 68
4.9 Temperature scatter plots for the samples used for cross stream averaging where $\langle T|\eta_{st}\rangle = T_{sample}$ and for flame front averaging where $\langle T\rangle = T_{sample}$. (a): Run L1, $t = 3.15t_{sp}$, $T_{sample} = 0.85$; (b): Run L1, $t = 3.15t_{sp}$, $T_{sample} = 0.5$; (c): Run H1, $t = 3.15t_{sp}$, $T_{sample} = 0.5$. . . . 69
4.10 The spatial dependence of the stoichiometric conditional turbulent temperature flux (solid), the gradient diffusion model (dotted) and the counter gradient flux estimate from section 4.2.2 (dashed), using cross stream averages. (a): Run L1, $t = 1.05t_{sp}$; (b): Run L1, $t = 3.15t_{sp}$; (c): Run M1, $t = 1.05t_{sp}$; (d): Run M1, $t = 315t_{sp}$; (e): Run H1, $t = 1.05t_{sp}$; (f) Run H1, $t = 3.15t_{sp}$. 72
4.11 The cross stream averaged conditional turbulent temperature flux plotted versus mixture fraction at $\langle T|\eta_{st}\rangle = T_{sample}$. (a): Run L1, $t = 3.15t_{sp}$, $T_{sample} = 0.85$; (b): Run M1, $t = 3.15t_{sp}$, $T_{sample} = 0.85$; (c): Run H1, $t = 3.15t_{sp}$, $T_{sample} = 0.5$. Key as in Fig. 4.10. 73

4.12 The turbulent temperature flux normal to the mean flame surface conditioned on stoichiometry and averaged over iso-surfaces of $\langle T \rangle$. (a): Run L1, $t = 3.15t_{sp}$; (b): Run M1, $t = 3.15t_{sp}$; (c): Run H1, $t = 3.15t_{sp}$. Key as in Fig. 4.10. 74
4.13 The terms of the conditional turbulent flux Eq. 4.12 for Run L1 at $t = 3.15t_{sp}$ using cross stream averages. Spatial plots are conditioned on stoichiometry, mixture fraction plots are stationed at $\langle T|\eta \rangle = 0.85$. (a) and (b): The main source/sink terms; (c) and (d): The main transport terms conditioned on stoichiometry; (e) and (f): The minor terms. 76
4.14 The terms of the conditional turbulent flux Eq. 4.12 for Run M1 at $t = 3.15t_{sp}$ using cross stream averages. Spatial plots are conditioned on stoichiometry, mixture fraction plots are stationed at $\langle T|\eta \rangle = 0.85$. (a) and (b): The main source/sink terms; (c) and (d): The main transport terms conditioned on stoichiometry; (e) and (f): The minor terms. 77
4.15 The terms of the conditional turbulent flux Eq. 4.12 for Run H1 at $t = 3.15t_{sp}$ using cross stream averages. Spatial plots are conditioned on stoichiometry, mixture fraction plots are stationed at $\langle T|\eta \rangle = 0.50$. (a) and (b): The main source/sink terms; (c) and (d): The main transport terms conditioned on stoichiometry; (e) and (f): The minor terms. 78

5.1 Sketch showing the form of the triple flame in a laminar lifted diffusion flame, [44]. 84
5.2 Schematic diagram of the turbulent jet burner with the spark electrodes, reproduced from Ahmed and Mastorakos [2]. 86
5.3 High speed camera images of ignition at $r/d_j = 0$, $z/d_j = 40$ followed by flame propagation upstream, $W_j = 25.5ms^{-1}$. The time after the spark is given under each image,[2]. 87
5.4 Mean axial velocity along the centre line of the jet for $W_j = 12.5ms^{-1}$ and $W_j = 25.5ms^{-1}$ from the CFD solution and from equation 5.1. . 89
5.5 Mean axial velocity versus radius at z=10, 20, 40 and $60D_j$ for the $W_j = 12.5ms^{-1}$ case. Black lines are from the CFD solution, red lines from equation 5.1. 90
5.6 Mean axial velocity versus radius at z=10, 20, 40 and $60D_j$ for the $W_j = 25.5ms^{-1}$ case. Black lines are from the CFD solution, red lines from equation 5.1. 90
5.7 Axial turbulent kinetic energy along the centre line of the jet for $W_j = 12.5ms^{-1}$ and $W_j = 25.5ms^{-1}$. 91

5.8 Axial turbulence intensity versus radius at z=10, 20, 40 and $60D_j$. Black lines are from the $W_j = 12.5ms^{-1}$ CFD solution, red lines for the $W_j = 25.5ms^{-1}$ CFD solution, symbols are measured values for the experiment with an air jet and $W_j = 21ms^{-1}$, [2]. 91
5.9 Mean mixture fraction along the centre line of the jet for $W_j = 12.5ms^{-1}$ and $W_j = 25.5ms^{-1}$ from the CFD solution. The mixture fraction profile predicted by equation 5.2 is shown in green. 92
5.10 Mean mixture fraction versus radius at z=10,20,40 and $60D_j$. Black lines are from the $W_j = 12.5ms^{-1}$ CFD solution, red lines from the $W_j = 25.5ms^{-1}$ CFD solution, and symbols are from equation 5.2. . . 93
5.11 Mixture fraction r.m.s versus radius at z=10,20,40 and $60D_j$. Black lines are from the $W_j = 12.5ms^{-1}$ CFD solution, red lines are from the $W_j = 25.5ms^{-1}$ CFD solution, and symbols are from equation 5.3. 93
5.12 Propagation of a partially premixed flame front in mixture fraction space for $n_\eta = 81$ and 101, and $\Delta T = 10^{-5}s$ and $\Delta T = 10^{-6}s$, $N_0 = 5s^{-1}$ 97
5.13 Conditional temperature profiles after the $500ms$ spark time, resulting from zero-dimensional CMC calculations corresponding to spark energies of $3.5mJ$, $4mJ$ and $5mJ$. Three levels of scalar dissipation are shown, $\chi/\chi_{ext} = 0.01$ (solid), $\chi/\chi_{ext} = 0.01$ (dotted) and $\chi/\chi_{ext} = 0.19$ (dashed). 101
5.14 Simulated unconditional temperature evolution, in Kelvin, for Simulation 1: $W_j = 12.5ms^{-1}$ with a $5mJ$, $0.5ms$ spark at $z = 40D_j$, with CFD-CMC coupling. Time after spark initiation is given at the top of each image. Iso-lines of mean mixture fraction are shown in black for the lean flammability limit $\tilde{\xi} = 0.0502$ (inner), stoichiometry, $\tilde{\xi} = 0.0976$ (middle) and the rich flammability limit, $\tilde{\xi} = 0.158$ (outer). The plot for $20ms$ contains a white contour of $\langle T|\eta_{st}\rangle = 0.8(T_{ad} - T_0) + T_0$. 104
5.15 CMC temperature equation source terms, Eq: 5.5 and the total rate of change for conditional temperature, at (a): $t = 1ms$; (b): $t = 3ms$. The simulations conditions are the same as in Fig. 5.14. 105
5.16 Positions of the upstream flame front versus time, for $W_j = 12.5ms^{-1}$ (black) and $W_j = 25.5ms^{-1}$ (red); averaged from 10 fast camera images, [2] (solid), simulated with 1D uncoupled CMC (dashed), simulated with 1D coupled CMC (dotted), and simulated with 2D axisymmetric coupled CMC (dash-dotted). 106
5.17 Mixture fraction space contours along the mean stoichiometric contour for conditional temperature, K, and conditional heat release, Ks^{-1}. The lean flammability limit ($\xi = 0.0503$), stoichiometry ($\xi = 0.0976$) and the rich flammability limit ($\xi = 0.1582$) are drawn with dotted white lines. Simulation 1. 108

5.18 Conditional temperature and the balance of terms in the CMC temperature equation for $W_j = 12ms^{-1}$ simulation at $20ms$. (a): Spatial profiles along the mean stoichiometric contour, conditioned on stoichiometry; (b) Mixture fraction profiles at $\langle T|\eta\rangle = 0.8(T_{ad} - T_0) + T_0$ on the mean stoichiometric contour; (c) Mixture fraction profiles at $z = 0.108m$ on the mean stoichiometric contour; (d) Mixture fraction profiles at $\langle T|\eta\rangle = 0.8(T_{ad} - T_0) + T_0$ on the centre line. Simulation 1. 111
5.19 Contours of conditional temperature, heat release rate, Y_{O_2} and Y_{CH_4} for the stabilised lifted flame. $W_j = 12.5ms^{-1}$, solved with 1D CMC and the 1-step chemistry model. The lower (blue) and upper (red) bounds of the colour scale for each quantity were; $293 - 2200K$, $0 - 10^6 Ks^{-1}$, $0 - 0.233$ and $0 - 0.35$ respectively. Dashed lines are shown at selected mixture fractions as in Fig. 5.17. 113
5.20 Contours of conditional temperature, heat release rate, Y_{O_2} and Y_{CH_4} for the stabilised lifted flame. $W_j = 12.5ms^{-1}$, solved with 1D CMC and the Smooke reaction mechanism. The colour scales and mixture fraction lines are the same as Fig. 5.19. 114
5.21 Contours of the conditional mass fractions, Y_{CO}, Y_{H2}, Y_{OH} and Y_O for the stabilised lifted flame. $W_j = 12.5ms^{-1}$, solved with 1D CMC and the Smooke reaction mechanism. The the lower (blue) and upper (red) bounds of the colour scale for each quantity were; $0 - 0.045$, $0 - 0.002$, $0 - 0.0045$ and $0 - 0.002$ respectively. Dashed lines are shown at selected mixture fractions as in Fig. 5.17. 114
5.22 The stoichiometric conditional axial velocity for the skeletal and 1-step reaction schemes plotted along the axial direction, for the stabilised lifted flame with $W_j = 12.5ms^{-1}$. 115
5.23 The balance of the CMC temperature equation terms, for 1D coupled simulations of the stabilised $W_j = 12.5ms^{-1}$ lifted flame; (a): with the standard eddy diffusivity model; (b): with the conditional counter gradient diffusion term. 118

6.1 A schematic diagram of the bluff body configuration. The expected flow pattern is indicated with solid arrows. The central recirculation zone (CRZ) and side recirculation zones (SRZ) are labeled. 122
6.2 Burner geometries: premixed, non-premixed and spray fueled from left to right. 125
6.3 A comparison of the Reynolds-stress CFD solution with PDA measured velocity moments for case 0, [31]. (a): mean axial velocity; (b): mean radial velocity; (c): axial Reynolds stress, $\widetilde{ww}$; (d): radial Reynolds stress, $\widetilde{uu}$. 127

6.4 Mean (black) and root mean square (red) axial velocity profiles across the inlet annulus. Measurements from positions 180^o apart are shown by crosses and circles, the Reynolds stress prediction is the solid line. Hot wire velocity measurements by S.F. Ahmed. 128
6.5 (a) Mean and (b) R.M.S. mixture fraction measurements for case B_{PLIF} [3]. 129
6.6 Radial ($z = 0.1m$) and axial ($r = 0$) profiles of the mean mixture fraction for un-reacting flow in case B. F.I.D. measurements by S.F. Ahmed. 129
6.7 Mean and R.M.S mixture fraction contours for case B using the Reynolds stress model. 130
6.8 Mean and R.M.S mixture fraction contours for case B using the RNG $k - \epsilon$ model. 131
6.9 (a): Mean azimuthal velocity, V (ms^{-1}); (b): Mean axial velocity, W (ms^{-1}). Case Y prior to ignition. 132
6.10 (a): Mean and (b): variance contours for mixture fraction, case Y prior to ignition. 133
6.11 (a): Instantaneous cross sectional Mie scattering image of the non-burning fuel spray, case Z. The bluff body is central, image dimensions: $70mm$ wide and $80mm$ high, a reflection from the glass enclosure shows along the right hand side; (b): A predicted droplet parcel distribution prior to ignition for case Y. The image is the right hand half of a transect across the injector, which is at the bottom left corner, image dimensions: $35mm$ wide and $80mm$ high. 133
6.12 Average OH-PLIF images at different times from the spark. Case B. Ignition at $z = 25mm, r = 0mm$. The images cover a region of 70x50mm [1]. 136
6.13 Simulated unconditional temperature evolution for case B, (K). The dashed white lines are iso-lines of mean mixture fraction, the innermost representing the rich flammability limit ($\xi = 0.089$), the next line is stoichiometric ($\xi = 0.055$) and the outer line represents the lean flammability limit, ($\xi = 0.0289$). 137
6.14 Simulated unconditional heat release rate evolution for case B, (Ks^{-1}). Iso-lines of mean mixture fraction are shown as in Fig. 6.13. 138
6.15 Simulated unconditional mean axial velocities for case B at (a): $5ms$ and (c): $100ms$, and the corresponding mean mixture fraction contours (b) and (d). The iso-lines of mean mixture fraction are shown in (a) and (c) as in Fig. 6.13. In the colour scale, red corresponds to $15ms^{-1}$ and $w = \xi = 0.5$, and blue corresponds to $w = 0ms^{-1}$ and $\xi = 0.0$. 139
6.16 Profiles of (a) the mixture fraction PDF, and (b) the conditional temperature at points A, B and C at $t = 100ms$. 140

6.17 Conditional temperature and the balance of terms in the CMC temperature equation for case B, $100ms$ after ignition. (a): Spatial profiles along an axial transect through point C, conditioned on stoichiometry; (b) Spatial profiles along a radial transect through point C, conditioned on stoichiometry; (c) Mixture fraction space profiles at point C. 141
6.18 2200Hz fast camera images of the flame evolution at the times indicated for a successful spark at $r = 0$, $z = 23mm$ in case Y. The image contrast has been reduced in order to make the kernel visible, particularly from $t = 3ms$ to $15ms$. The images show the entire cross section of the enclosure ($70mm$ diameter, $80mm$ height). Measurements by Marchione and Mastorakos [83]. 142
6.19 Simulated unconditional temperature evolution for case Y, (K). The dashed white lines are iso-lines of mean mixture fraction, the innermost representing the rich flammability limit ($\xi = 0.199$), the next line is stoichiometric ($\xi = 0.062$) and the outer line represents the lean flammability limit, ($\xi = 0.035$). 145
6.20 Simulated unconditional heat release rate evolution for case Y, (Ks^{-1}). Iso-lines of mean mixture fraction are shown as in Fig. 6.19. 146
6.21 Predicted droplet parcel distributions at (a) $3ms$ and (b) $45ms$ after ignition. Image dimensions: $35mm$ wide and $80mm$ high. 147
6.22 Profiles of (a) the mixture fraction PDF, and (b) the conditional temperature at points A, B and C. $t = 45ms$ 147
6.23 The conditional temperature and the balance of terms in the CMC temperature equation for case Y, $45ms$ after ignition. (a): Spatial profiles along an axial transect through point C; (b) Spatial profiles along a radial transect through point C; (c) Mixture fraction space profiles at point C. 148
6.24 The balance of CMC terms at point A (neglecting the spray source terms) in (a) the conditional temperature equation, and (b) the conditional fuel mass fraction equation for case Y at $45ms$ after ignition. The spray source terms of Eq. 6.1 and in the conditional temperature equation (see chapter 2) have been post-processed and are also shown. 150

7.1 (a): Flammability factor contours (filled coloured contours) using a presumed $\beta-$function pdf and rich flammability limit, stoichiometric and lean flammability limit mean mixture fraction isolines (black) based on the RANS flow field solution from chapter 5; (b): Contours of edge flame index (filled coloured contours) and isoline of mean flow speed equal to $\sqrt{\rho_u/\rho_b}S_L$ (white). Jet with $U_j = 12.5ms^{-1}$ and X_{air}=30%, $D_j = 5mm$. 158

7.2 Contours of velocity parallel to the mean mixture fraction iso-surfaces equal to $\sqrt{\rho_u/\rho_b}S_L$ (black) and contours of $\xi = \xi_{st}$ (red), for the inert CFD solution (solid) and the coupled 1D CMC solutions (dots), (chapter 5). (a): $U_j = 12.5ms^{-1}$; (b): $U_j = 25.5ms^{-1}$. 159
7.3 Induced velocity from volumetric line sources given by equation 7.5. . 161
7.4 (a):Contours of modelled propagation speed (coloured) and stabilisation surface (green), $U_j = 12.5ms^{-1}$; (b): Contours of modelled propagation speed (coloured) and stabilisation surface (green), $U_j = 25.5ms^{-1}$; (c): Contours of premixed turbulent flame speed (coloured) as a function of local mean mixture fraction from Eq:7.3 and isoline of mean flow speed equal to $\sqrt{\rho_u/\rho_b}S_L$ (black); (d): Premixed turbulent flame speed, S_T (coloured) and the iso-line of flow speed equal to $\sqrt{\rho_u/\rho_b}S_L$ (black), $U_j = 25.5ms^{-1}$. 166
7.5 (a): Measured ignition probability (coloured contours) and estimated mean contours of lean flammability limit, stoichiometric and rich flammability limit mixture fraction (black), $U_j = 12.5ms^{-1}$. ; (b): Spark effectiveness (coloured) and mean stoichiometric mixture fraction contour (black) from the CFD, $U_j = 12.5ms^{-1}$. 167
7.6 (a): Measured ignition probability (coloured contours) and mean contours of lean extinction limit, stoichiometric and rich extinction limit mixture fraction (black), $U_j = 25.5ms^{-1}$. ; (b): Spark effectiveness (coloured contours) and mean stoichiometric mixture fraction contour (black), $U_j = 25.5ms^{-1}$. 168
7.7 (a): Mean mixture fraction contours (coloured); (b): Flammability factor contours (coloured). Rich ($\xi = 0.089$), stoichiometric and lean ($\xi = 0.029$) mean mixture fraction iso-lines (white), Case B. 171
7.8 (a): Edge flame index; (b): Predicted propagation speed in ms^{-1}. Case B. 171
7.9 (a): Measured ignition probability for area corresponding to the green rectangle, Ref. [3]; (b): Spark effectiveness contours (coloured), stabilisation surfaces are shown with a white contour. Case B. 172
7.10 Mean axial velocity, case Z. 173
7.11 (a): Mean gaseous mixture fraction contours from the steady unreacting flow prediction (coloured), and the mean lean flammability limit contour $\xi = 0.0353$ (black) ; (b): Conservative flammability factor contours, case Z. 174
7.12 (a): Measured ignition probability for area corresponding to the green rectangle.; (b): Spark effectiveness contours (coloured) and stabilisation surfaces (black), case Z. 175
7.13 Mean axial velocity prediction for combustor inside the ignition loop (case 1). The dimensions and exact combustor shape are not given for reasons of confidentiality. 178

7.14 (a): Conservative mixture fraction for combustor, case 1; (b): Conservative mixture fraction based flammability factor, case 1. 178
7.15 Contours of the stoichiometric laminar flame speed for $n-$heptane mixed with air following isentropic compression at a variety of altitudes, based on the standard atmosphere and the Held et al. [52] $n-$heptane mechanism. 179
7.16 3D flame particle trajectories viewed in the azimuthal direction with stabilisation and flammable regions indicated, (a): case 1; (b): case 2 with $\dot{m}_2 = 1.57\dot{m}_1$. 181
7.17 Spark effectiveness versus axial spark location and various ignition kernel penetrations for case 1 (black) and case 2 (red). 182
7.18 Effects of model parameters on spark effectiveness prediction. The curve for stabilisation zone radius $= 2R_{swirl}$ peaks off the graphs at 0.65 182
7.19 (a): Contours of $\nabla\tilde{\xi} \times \bar{\mathbf{U}}$ (coloured) and $|\nabla \times \bar{\mathbf{U}}| = 2000$ (black); (b): Contours of the turbulent mixing frequency $\tilde{\epsilon}/\tilde{k}$ (s^{-1}) (coloured) and flammability factor $= 0.5$ (white). 185
7.20 (a): Contours of mean mixing layer residence time; (b):Contours of the mean number of turbulent mixing time scales flame particles are resident in the mixing layer. The mixing layer surface $|\nabla\xi \times \bar{\mathbf{U}}| = 150$ is shown in black. 186

List of Tables

3.1 Details for sparks A-F. 38

5.1 $k - \epsilon$ parameters for the round turbulent jet. 88
5.2 1D uncoupled grid sensitivity run details, simulation duration $t = 40ms$. 98

6.1 Classification of bluff body flows, giving the volume flow rates of the fuel and air streams, $\dot{Q}_1$ and $\dot{Q}_2$ respectively. 125

Chapter 1

Introduction

1.1 Combustion challenges

Combustion has been the dominant energy source since the inception of human industry. Current and future pressures from anthropogenic pollutant emission and limited fossil fuel availability demand technical, economic and socio-political innovation in energy utilisation. However combustion has a role to play in a variety of potential energy technologies across the spectrum of sustainability. Therefore, there remains a great need to train combustion engineers and to extend humankind's ability to harness combustion through applied research.

Turbulent combustion encapsulates a fascinating combination of physical phenomena, which continues to be unraveled by a host of international academics applying increasingly capable experimental and computational resources. In many cases, including this thesis, the objective is to produce a mathematical description of combustion processes for practical use by engineers.

1.2 Gas turbine ignition

1.2.1 Design challenges

The complete simulation of aviation gas turbine ignition is currently beyond the capabilities of engine designers. The processes involved include many challenging phenomena such as highly turbulent flow, multicomponent liquid fuel spray, atomisation, evaporation and combustion, and forced ignition. None of these may normally be treated independently. Simulation of gas turbine ignition therefore requires combustion engineering to progress at a fundamental level making it a worthy subject for a doctoral thesis.

Since the jet engine combustor may be extinguished, perhaps due to pilot error or excessive ingestion of water, the ability to ignite an aviation gas turbine during flight is a significant design and operational requirement. American and European civil air safety authorities presently require submission and validation of an altitude-airspeed envelope illustrating restart capability, these envelopes generally incorporate a maximum restart altitude ranging from 20,000 to 30,000 feet.

Ignition of an annular combustor, of the kind used in civil turbo-fan engines, requires that ignition is instigated by electric discharge igniters, usually located at two positions around the annulus. This must be followed by flame spread around the entire annulus of the combustor ('light-around'). Stabilisation of a flame is not necessarily sufficient to ensure the engine accelerates to idle ('pull-away') as required for full recovery, since low levels of combustion efficiency may provide insufficient power.

The surface-discharge igniter is used on nearly all aircraft. Its operation and some alternative igniters are summarised by Lefebvre [76]. The circular discharge face is usually set into the outer combustor liner and results in a high energy plasma kernel whose expansion drives itself outwards from the surface.

Large turbo-fan engines have historically employed rich primary zone annular combustors. Pollutant emission considerations are causing manufacturers to consider increasing the proportion of combustor air flow passing through the burner, thus making the combustion leaner. The dominant concept is staged combustion where a small pilot and a larger lean atomiser are incorporated into the burner, possibly concentrically. This shift in combustor design requires corresponding progress in the design methods used to ensure ignitability.

1.2.2 Design methods

Predictive computational fluid dynamic (CFD) capability in this area is extremely limited. The application of appropriately advanced combustion models is still receiving development and validation [12]. Only when a combustor is scaled from an existing geometry can relight performance be reliably predicted [76].

New combustor designs are subjected to ground-based testing of altitude relight prior to flight testing. The combustor (sector) is loaded into a wind tunnel where air temperature, pressure and flow rate may be varied independently. Thus the air-fuel ratios giving successful ignition are identified throughout the flight envelope. If necessary, modifications may be made to the design. However, doing so at the stage of an engine's development where testing has begun is likely to be extremely costly. Experimental study of the ignition process is highly challenging due to the combustor geometry and the large amounts of unevaporated fuel, such that should a particular design exhibit inadequate ignitability there may be few clues available to rectify the problem [105].

Simulation of the ignition process using CFD, with appropriate turbulent combustion modelling has the potential to provide engine designers with detailed information about the combustor ignitability. This may be extremely valuable as either a predictive design tool for assessing combustor ignitability, or as a diagnostic tool

when attempting to modify the ignitability of combustor designs. The present thesis attempts to provide some information in this direction.

1.3 Turbulent combustion simulation

1.3.1 Direct numerical simulation

Direct numerical simulation (DNS) attempts to integrate the equations describing a turbulent flame without employing averaging or modelling. A Newtonian fluid is fully described by the Navier-Stokes equations in conjunction with appropriate transport equations for enthalpy and the chemical species present. For turbulent combustion these equations may employ Fick's laws of diffusion, the Fourier law of heat conduction, the ideal gas law, and neglect Soret and Dufour effects with little error. Additionally the rate of chemical reaction between the various species must be provided as a function of the available quantities (temperature, pressure, concentrations). Using appropriate boundary conditions, integration of the resulting equation system would result in an essentially exact simulation of a turbulent flame.

In reality, several difficulties arise. Firstly, it has not been possible to obtain sufficiently accurate measurements to generate a complete mathematical description of hydrocarbon combustion chemistry. Secondly, all scales of turbulence must be resolved in space and time such that CPU time scales approximately as the Reynolds number cubed [101], which severely limits the flows which may be simulated.

Employing high accuracy numerical discretisation, highly efficient solution algorithms and intelligently chosen test problems, DNS has been used successfully to explore turbulent combustion phenomena that are not currently resolvable through experimental measurement. It provides a great deal of flexibility in the post-processing of data making it a valuable research tool for turbulence and for modelling. In chapter 4 of this thesis, DNS of ignition in turbulent non-premixed flow

is used for analysis of the turbulent combustion modelling of these flows.

1.3.2 Reynolds averaged Navier-Stokes modelling

The Reynolds averaged Navier-Stokes (RANS) approach is widely known and used [101], and involves solving Favre, ensemble averaged transport equations for mass, momentum and species. A number of closure models exist for the Reynolds stresses $\widetilde{\mathbf{v}''\mathbf{v}''}$, where $\mathbf{v}''$ denotes the Favre fluctuation vector for velocity. The $k-\epsilon$ closure used in chapter 5 involves solution of modelled transport equations for the turbulent kinetic energy and for its dissipation. The Reynolds stress model used in chapter 6 involves solution for the six components of the Reynolds-stress tensor and one additional equation for a turbulent mixing time scale.

The mean reaction rate also requires modelling since in turbulent combusting flows it can not be accurately closed using the averaged species concentrations and temperature [101]. Turbulent combustion models are discussed in section 1.3.4.

The spatial and temporal resolution necessary to resolve the RANS equations is vastly less than for DNS, which has allowed widespread use of RANS in industry. The accuracy of RANS CFD is determined by the validity of the modelling employed, which can depend on the details of the flow.

1.3.3 Large eddy simulation

Large eddy simulation (LES) involves solution of spatially filtered Navier-Stokes equations, where the filter dimension is within the inertial subrange of the turbulent spectrum [78]. The sub-filter scale turbulent processes, which include micro-scale mixing and reaction, must again be modelled. However since the unsteady large scale motions of the flow are solved directly, the true physics of the flow can be preserved. This feature may be highly desirable in flame ignition and

propagation problems where flow intermittency [4] and large scale motions [59; 128] can play a dominant role. The numerical resolution necessary to conduct a LES calculation, and hence the computational expense, usually falls in between RANS and DNS simulations, since the filter size can generally be much larger than the Kolmogorov length scale. Large eddy simulation is very attractive for the modelling of the turbulent ignition process, and development work is underway in this regard, for example Ref. [12] and [135].

1.3.4 Turbulent reacting flow modelling

The ratio of turbulent mixing time scales to the time scales of combustion reactions, referred to as a Damköhler number, is such that the two processes may not be treated independently in many combustion problems of practical interest. Thus treating the Reynolds averaged, or the filtered reaction rate as a function of the local mean temperature and composition leads to large errors, and a sophisticated turbulent combustion model can be necessary.

A large number of combustion models are suited to either non-premixed or fully premixed combustion. The ignition of the fuel spray in an aviation gas turbine combustor is expected to involve combustion across the full spectrum of fuel-air mixedness, and requires a correspondingly comprehensive, or adaptable combustion model.

The flamelet model [97] is applicable to either premixed or non-premixed combustion, using a description of the combustion chemistry of any degree of complexity, however it is a local combustion model. Attempts to apply the model to problems with elliptic spatial dependence, for example where mixture at different locations interacts through turbulent transport as expected in relight, require less rigorous adaptations to the model [98]. The conditional moment closure [69] takes an alternative theoretical approach and produces a spatially elliptic model. In common

with the flamelet model it involves a local balance between scalar dissipation processes and reaction. The CMC may be applied to either premixed or non-premixed problems with an appropriate choice of conditioning variables, however the choice of a reactive conditioning variable poses modelling difficulties which are an area of active research. Application of either the flamelet model or the CMC to a partially premixed problem can require the use of two local solution space coordinates in order to describe both fuel-oxidiser mixing and product-reactant mixing, bringing further modelling complexity.

The transported probability density function (PDF) model [101] is a rigorously derived mixing model in which the reaction rate appears in closed form. Thus the model can be applied to problems with any degree of fuel-oxidiser pre-mixing without any adaptation. However the need to model the micromixing processes remains. The PDF equation is usually solved by means of stochastic (Monte Carlo) methods, whether Lagrangian, Eulerian, or employing the more recent 'Stochastic Fields' approach [89; 138]. The turbulent combustion simulations can require a very large number of stochastic realisations making this approach more computationally intensive than the previous models.

LES calculations employing relatively simple turbulent combustion closures, for example the dynamically thickened flame model [77], have shown considerable promise for computation of non-premixed flame ignition and propagation [12].

The conditional moment closure framework is adopted in this work since it balances moderate computational expense with a rigorous description of the turbulent mixing processes believed to be necessary for predictive design simulations.

1.4 Objectives of this study

This work hopes to make progress toward industrially accessible modelling for aviation gas turbine ignition. This is attempted by investigation of fundamental combustion physics and modelling for ignition problems, chapters 3 and 4, and by implementation of an advanced turbulent reacting flow model, and its development for a range of experimental ignition problems, chapters 5 and 6. Finally, the current understanding of the processes at work during ignition of the experimental test cases is synthesised to produce an analytical approach for considering the ignitability of potential designs based on a very limited amount of CFD data, chapter 7.

The simulations presented in this work are confined to RANS modelling. While the current modelling and implementation may be extended into a LES model [135], there remain sufficient modelling challenges to be overcome while working with the better established RANS approach. Detailed literature reviews on various aspects of ignition of laminar and turbulent non-premixed flames, on simulation methods, and on modelling are given in the appropriate chapters.

Chapter 2

Conditional moment closure and its numerical solution

2.1 CMC modelling for ignition problems

The conditional moment approach seeks to model accurately the processes of turbulence-chemistry interaction through the solution of transport equations for conditionally averaged species and energy equations, [69]. An ensemble averaged quantity in a turbulent flow may be evaluated by conducting a statistically large number of experiments and averaging the desired quantity at a particular location in time and space. A conditional expectation represents the result of ensemble averaging subject to a particular condition, such as the value of a scalar quantity coinciding with the level of a 'sample space variable'. In non-premixed systems the mixture fraction, representing the mass fraction of gas originating from the fuel stream, provides a very convenient conditioning variable. This is due to it being a conserved scalar (spray combustion being an exception) and due to its physical significance in non-premixed combustion. The mixture fraction conditioned average of the mass fraction of species α is written $\langle Y_\alpha | \xi = \eta \rangle$. The angled brackets are used to denote the ensemble averaging, and the stated condition is that the mixture fraction ξ should equal the sample space variable η. The nomenclature for a conditionally averaged mass fraction may be shortened to $\langle Y_\alpha | \eta \rangle$ or just Q_α.

Q_T refers to the conditional expectation of temperature. Conditional fluctuations are denoted by a double prime so that the instantaneous value $Y_\alpha = Q_\alpha + Y''_\alpha$. A discussion of the nature of conditional averaging and the related mathematics is provided by Klimenko and Bilger [69].

Equations for conditionally averaged mixture fractions have been derived from the transport equation for the joint scalar Probability Density Function (PDF) [68], and alternatively by decomposing the relevant variables into conditional mean and fluctuating parts [9]. Both methods result in the same closed CMC equation for reactive species mass fractions:

$$\frac{\partial Q}{\partial t} + \langle \mathbf{v}|\eta\rangle \cdot \nabla Q = \langle N|\eta\rangle \frac{\partial^2 Q}{\partial \eta^2} + \langle W|\eta\rangle - \frac{div(\rho_\eta \langle \mathbf{v}'' Y''|\eta\rangle P(\eta))}{P(\eta)\rho_\eta} \tag{2.1}$$

where the scalar dissipation rate $N = D(\nabla\xi)^2$. In order, the terms represent accumulation and convection of the conditional mass fractions. The right hand side has transport in mixture fraction space due to the conditional scalar dissipation $\langle N|\eta\rangle$ and the conditional expectation of the chemical source term. The final term involves conditional turbulent fluxes of the reactive scalar. These are often considered diffusive in nature making Eq. 2.1 elliptic in space. Therefore the conditional turbulent flux term is partly responsible for stabilisation of turbulent flames [61] and is expected to be important in the ignition of a gas turbine combustor. Some combusting flows exhibit very little spatial variation of conditional moments, in which case the conditional velocity and turbulent flux terms may be neglected. Absence of the spatial transport terms in Eq. 2.1 results in the 'zero dimensional' CMC equation.

The attraction of the conditionally averaged approach is that the variance of a mixture fraction conditioned sample may be relatively small, meaning that the conditional reaction rate may be closed accurately using the conditionally averaged composition, known as 'first order closure'. This approach is adopted and tested in this thesis.

2.1.1 Primary closure hypotheses

The derivation of the basic CMC closure is now widely known [9; 68; 69] and hence not reproduced here. The modelling of the spatial transport term involving $\rho_\eta \langle \mathbf{v}'' Y'' | \eta \rangle$ is of particular interest throughout this work, therefore its origins and relationship to the primary closure hypotheses will be discussed.

The PDF derivation method by Klimenko, resulting in Eq. 2.2, requires closure for the diffusive flux J_Y, of the conditionally averaged species mass fractions Q in conserved scalar space. A high Reynolds number assumption has been made and conditional density fluctuations have been neglected.

$$\begin{aligned} \frac{\partial \rho_\eta Q P(\eta)}{\partial t} + div(\rho_\eta \langle \mathbf{v} Y | \eta \rangle P(\eta)) = \rho_\eta \langle W | \eta \rangle P(\eta) \quad &+ \quad \frac{\partial J_Y}{\partial \eta} \\ J_Y \equiv 2\rho_\eta \langle D(\nabla Y \cdot \nabla \xi) | \eta \rangle P(\eta) \quad &- \quad \frac{\partial \rho_\eta \langle NY | \eta \rangle P(\eta)}{\partial \eta}. \end{aligned} \tag{2.2}$$

This is achieved by applying a diffusion approximation of the form, Eq. 2.3.

$$J_Y = AQ + B\frac{\partial Q}{\partial \eta} \tag{2.3}$$

A and B should be independent of Q in order to preserve the linear properties of turbulent scalar transport. A and B are fully determined by the necessary constraint that in unreacting flow (without evaporative sources) the quantity Q takes a linear profile in mixture fraction space determined by the initial and boundary conditions. The closure for J_Y then takes the form of Eq. 2.4.

$$J_Y = -\frac{\partial \rho_\eta \langle N | \eta \rangle P(\eta)}{\partial \eta} Q + \rho_\eta \langle N | \eta \rangle P(\eta) \frac{\partial Q}{\partial \eta} \tag{2.4}$$

This results in the basic closed equation, Eq. 2.5, which may be manipulated to

give equation 2.1 using the transport equation for the mixture fraction PDF.

$$\frac{\partial \rho_\eta Q P(\eta)}{\partial t} + div(\rho_\eta \langle \mathbf{v} Y | \eta \rangle P(\eta)) = \rho_\eta \langle W | \eta \rangle P(\eta) \quad - \quad \frac{\partial^2 \rho_\eta \langle N | \eta \rangle P(\eta)}{\partial \eta^2} Q \quad + \quad \rho_\eta \langle N | \eta \rangle P(\eta) \frac{\partial^2 Q}{\partial \eta^2} \tag{2.5}$$

The decomposition derivation method of Bilger [9] results in the unclosed equation, Eq. 2.6.

$$\begin{aligned} \rho_\eta \frac{\partial Q}{\partial t} \quad + \quad & \rho_\eta \langle \mathbf{v} | \eta \rangle \cdot \nabla Q = \rho_\eta \langle N | \eta \rangle \frac{\partial^2 Q}{\partial \eta^2} + \rho_\eta \langle W | \eta \rangle - e_Q - e_y \\ e_Q \quad \equiv \quad & \langle div(\rho D \nabla Q) + \rho D \nabla \xi \cdot \nabla \frac{\partial Q}{\partial \eta} | \xi(\mathbf{x}, t) = \eta \rangle \\ e_Y \quad \equiv \quad & -\langle \rho \frac{\partial Y''}{\partial t} + \rho \mathbf{v} \cdot \nabla Y'' - div(D \rho \nabla Y'') | \xi(\mathbf{x}, t) = \eta \rangle \end{aligned} \tag{2.6}$$

Terms e_Q and e_Y require closure. The molecular diffusion processes contained in e_Q are expected to become negligible at high Reynolds number, therefore this term is usually neglected. e_Y is closed by using the hypothesis stated in Eq. 2.7.

$$e_Y P(\eta) d\eta = -div(\rho_\eta \langle \mathbf{v}'' Y'' | \eta \rangle P(\eta)) d\eta \tag{2.7}$$

This hypothesis has the necessary property that the unconditional average value of e_Y is recovered by integrating Eq. 2.7 over the full range of mixture fraction, however it is not necessarily unique in this regard. Application of this closure hypothesis also results in the basic, closed CMC equation, Eq. 2.1.

Klimenko and Bilger [69] note that while the unclosed equations, Eqs. 2.2 and Eqs. 2.6, and their respective closure hypotheses appear different, the resulting closed equation is the same. Indeed, they show that the unclosed equations are also equivalent and thus deduce that the closure hypotheses must be the same. The

necessary and sufficient conditions for the closure hypothesis to be valid are a matter of on going research.

In the decomposition derivation the conditional turbulent flux term arises during the closure of e_Y. In the PDF derivation method its occurrence appears unrelated to the closure employed. Thus the form of the term is only indirectly linked to the closure hypothesis employed.

2.1.2 CMC sub-models

Reaction rate closure

The use of mixture fraction as the conditioning variable can result in low conditional fluctuations of the reactive scalars. The first-order closure involves expressing the conditional expectation of the chemical source term as a function of the conditional mean mass fractions, temperature and pressure, disregarding the conditional fluctuations:

$$\begin{aligned} \langle w_\alpha|\eta\rangle &= \dot{\omega}_\alpha(Q_\alpha, Q_T, P) \\ \langle w_H|\eta\rangle &= -\sum_{\alpha=1}^{N} h_\alpha \langle w_\alpha|\eta\rangle \end{aligned} \tag{2.8}$$

h_α is the specific enthalpy for species α. The expression for the reaction rate may involve any level of complexity using the available input variables as described in section 2.2.2.

Alternative closures such as the second order [69; 84], or double conditioned closures [19; 69; 72], may be appropriate in flows which involve large conditional fluctuations. Such flows include auto-igniting mixtures, where the variation of scalar dissipation histories results in differing chemical evolutions [84; 95], flows with local extinction and re-ignition processes [72; 73], and flows with partially premixed flame

propagation, chapter 4.

The complete modelling and solution of the conditional moment closure with detailed chemistry to the second order remains both theoretically and practically challenging. Therefore several researchers in the field have developed schemes requiring the solution of a reduced set of second order quantities [73; 95].

Conditional scalar dissipation models

The amplitude mapping closure has been used to model the conditional scalar dissipation rate throughout this work, [91]. The conditional scalar dissipation profile is given by a Gaussian shape:

$$\begin{aligned} \langle N|\eta\rangle &= N_0 G(\eta) \\ G(\eta) &= \exp\left(-2\left[erf^{-1}(2\eta-1)\right]^2\right) \\ N_0 &= \frac{\tilde{\chi}}{2\int_0^1 G(\eta)\tilde{P}(\eta)d\eta} \end{aligned} \tag{2.9}$$

Alternative models by Girimaji [45], and more recently by Devaud et al. [35] confer an advantage in certain flows. The treatment of the conditional scalar dissipation in spray fueled flames is an open area of research, with no established model available incorporating evaporative effects into the scalar dissipation model.

Conditional velocities

The linear approximation for the conditional expectation of velocity is given by Eq. 2.10 [69]. The unconditional covariance $\widetilde{\mathbf{v}''\xi''}$ is available from the gradient

modelling for the mean mixture fraction equation, Eq. 2.11.

$$\langle \mathbf{v}|\eta\rangle = \tilde{\mathbf{v}} + \frac{\widetilde{\mathbf{v}''\xi''}}{\widetilde{(\xi'')^2}}(\eta - \tilde{\xi}) \tag{2.10}$$

$$\widetilde{\mathbf{v}''\xi''} = -D_t \nabla\tilde{\xi} \tag{2.11}$$

The modelling of Eq. 2.10 is supported by some experimental data [74] and the DNS data of Swaminathan and Bilger [129], who present an additional 'gradient' model.

Conditional turbulent flux

Closure for $\langle \mathbf{v}''Y_\alpha''|\eta\rangle$ is conventionally formulated by analogy with the diffusion approximation frequently used for the unconditional scalar flux:

$$\langle \mathbf{v}''Y_\alpha''|\eta\rangle = -D_t \nabla Q_\alpha \tag{2.12}$$

Given the widespread use of the diffusion approximation in modelling of unreacting turbulent flow, Eq. 2.12 appears physically reasonable and returns the unconditional gradient diffusion model when integrated with the mixture fraction PDF. Equation 2.12 has never directly been validated for combusting flow. The diffusion approximation may give serious errors in predictions for fully premixed turbulent combustion. Diffusivities can become negative, which is referred to as counter gradient transport [14; 15; 79; 143].

Phenomenologically, counter gradient transport results from the pressure gradient set up by the dilatation within the flame, which causes the lower density products to accelerate away from the flame. In a turbulent flame with sufficiently high heat release, this tendency for products to accelerate toward the region of high product concentration effectively makes the correlation between $\mathbf{v}''$ and Y'' more

positive.

A detailed discussion of Eq. 2.12 is given in chapter 4, where its validity is investigated in the context of non-premixed edge flame propagation.

2.2 Implementation of the CMC

The ignition and flame propagation processes modelled in this work necessitate transient calculation and involve significant modification of the flow field due to the mean heat release from combustion. This requires the possibility of a coupling between the solution of the flow field (ie. momentum, mass and mixture fraction PDF conservation equations) and the solution of the CMC turbulent combustion model (ie. conditional species and energy transport equations). The few attempts to use the CMC in this way have included transient Diesel engine combustion simulation [95; 147], where the CMC has been coupled with a well established flow field solver using RANS. This allows attention to be focused on the accurate solution and modelling of the CMC equations. The same approach has been pursued in this work. The implementation presented is for gas fueled flows, however an extension to spray fueled flows is given in section 2.2.4.

2.2.1 The coupling of the CFD and CMC codes

The low Mach number flow field equations have been solved using a commercially available finite volume method, RANS solver [20]. The CMC is solved on an independently defined finite-difference grid. A fractional step solution approach is applied, firstly advancing the flow field by one global time step and reporting the Favre averaged velocity $\widetilde{\mathbf{v}}$, turbulent kinetic energy $\widetilde{k}$, turbulent energy dissipation $\widetilde{\epsilon}$, mixture fraction $\widetilde{\xi}$, mixture fraction variance $\widetilde{\xi''^2}$, pressure P, and the rate of pressure change $\partial P/\partial t$ for every cell on the CFD mesh. Using this information the

CMC code then advances the combustion model equations by the global timestep before returning the Favre averaged temperature $\widetilde{T}$ and molecular weight $\widetilde{W_{mol}}$ into each cell of the CFD mesh, completing the two way coupling. This implementation is a development of that being employed by Mastorakos, Kim, Wright and De Paola [61; 95; 147] in other applications.

The CFD mesh must resolve the gradients of variables actively solved on it, in addition to the unconditional density gradients which result from the mean temperature and molecular weights returned from the CMC code. The CMC grid is required to resolve the gradients of the conditionally averaged quantities solved on it. These gradients are expected to be very low except within the propagating turbulent flame fronts in ignition problems. Within the turbulent flame brush, conditional gradients may greatly exceed those of the unconditional gradients (eg. of density) being resolved on the CFD mesh [33]. For numerical expedience it has been necessary to use variable spacings in both the CFD and CMC grids resulting in regions where one CMC grid node corresponds to many CFD cells and vice-versa. In the former case, the CFD quantities are Favre averaged over all CFD cells belonging to a CMC node. In the latter case linear interpolation is applied to obtain the necessary quantities at the position of the CMC node. The values of $\langle N|\eta\rangle$, $\langle \mathbf{v}|\eta\rangle$ and $\rho_\eta P(\eta) D_t$ which are used in the CMC sub-models are evaluated at the resolution of the CFD mesh before being PDF averaged for use on the CMC grid. This procedure is set out in Eq. 2.13 for the evaluation of the conditional scalar dissipation model.

$$\langle N|\eta\rangle_n = \frac{\sum\limits_m \widetilde{P}(\widetilde{\xi}_m, \widetilde{\xi''^2_m}, \eta)\langle N|\eta\rangle_m}{\sum\limits_m \widetilde{P}(\widetilde{\xi}_m, \widetilde{\xi''^2_m}, \eta)} \tag{2.13}$$

The subscript n refers to the CMC node and m refers to individual CFD cells belonging to the CMC node n. The mixture fraction PDF, $\widetilde{P}(\widetilde{\xi}_m, \widetilde{\xi''^2_m}, \eta)$ is presumed based on the solution for its mean and variance.

The presumed mixture fraction PDF

The transport of the mixture fraction PDF is modelled by the solution of the mean and variance equations for the mixture fraction, given in ref. [20]. These are used to presume the shape of the mixture fraction PDF. As in many previous works, eg. ref. [33], the presumed form $\beta-$function shape is used. Where the variance becomes very small ($< 10^{-8}$ in this work) a delta function ($P(\eta) = \int_0^1 \delta(\eta - \widetilde{\xi})d\eta$) is employed. A cut-off value for the PDF is set equal to 10^{-50} below which the probability is taken as zero.

CMC Boundary conditions

The spatial boundaries for conditional quantities are the Dirichlet (fixed value) type at the inlets to the domain. Flow outlets from the domain should be positioned such that the Von Neumann (fixed gradient) condition may be applied. In practice the boundary of the solution domain may in places be determined by surfaces in physical and conserved scalar space where the mixture fraction PDF falls below its cut off value. The region of conserved scalar space for which the PDF is finite is given by $\eta_{min} \leq \eta \leq \eta_{max}$. The CMC is undefined where the conserved scalar PDF becomes zero. The boundaries of conserved scalar space must satisfy the condition $P(\eta)\langle N|\eta\rangle \rightarrow 0$ as $\eta \rightarrow \eta_{min}, \eta_{max}$ [69]. The implication is that the chemical reaction and other source terms may be applicable at the conserved scalar boundary point, however the conditional scalar dissipation model should equal zero. The boundary conditions applied regarding spatial terms at boundaries where $P(\eta) \rightarrow 0$ are either Dirichlet or Von Neumann depending whether the local conditional velocity represents an inflow or outflow respectively.

Transient simulations present the possibility that the $P(\eta) \rightarrow 0$ boundary moves over time. The case where the region of finite $P(\eta)$ grows over time requires newly incorporated regions of the solution domain to be initialised. In this work a

practical approach has been adopted where the conditional values used for initialisation of the cell are found by a linear interpolation between the values at the previous boundary point, η_{min} or η_{max} and the unreacted composition corresponding to $\eta = 0$ or $\eta = 1$ respectively. This is justified by analogy to the composition which would arise due to an inert mixing process between two known compositions, and provided the progress of the $P(\eta) \to 0$ surface is well resolved, this modelling is expected to have limited influence on the solution.

2.2.2 Chemical reaction

Detailed combustion reaction mechanisms have been developed for many of the simple hydrocarbon fuels, for example the GRI mechanism for natural gas combustion [41] used in chapter 3. Such mechanisms are composed of a system of Arrhenius type reactions among the fuel, air and a potentially large numbers of intermediate and product species. The CMC model can handle chemical reaction schemes with any level of detail, however the CPU time and memory expended in the time integration of the chemical reaction mechanism tends to increase strongly with the number of reactions and species. An additional consideration is the numerical stiffness of the reaction set, which is a measure of the range of characteristic time scales present among the various chemical reactions. A high stiffness may require particularly time consuming integration techniques as discussed in section 2.2.5.

Depending on the objective of a modelling study, a compromise between the detailed description of the chemical reaction and the speed of solution may be appropriate. For example, Smooke's 16 species, 25 reaction skeletal mechanism for methane used in chapter 5 is intended to model the key reaction pathways necessary to satisfactorily predict the composition (and ultimately extinction) of strained methane diffusion flames [125]. As such, the low temperature reaction pathways needed for auto-ignition predictions, or reactions necessary to predict the formation

of oxides of nitrogen are not modelled.

Further simplification may be attempted, eventually resulting in the limit of a global one step model. Application of a one step global model tends to limit the range of phenomena and the range of conditions at which the model is applicable. The one step chemistry model proposed by Fernández-Tarrazo et al. [37] uses one step irreversible Arrhenius kinetics with unity reaction order and achieves encouraging results for partially premixed hydrocarbon combustion. By expressing the heat of reaction and the activation energy as a function of equivalence ratio the model is able to accurately reproduce the premixed flame speeds for the entire range of flammable mixtures.

The model parameters for methane - air combustion at ambient conditions used in chapter 5 are reported by Fernández-Tarrazo et al. [37]. A similar one step model for $n-$heptane - air combustion, Eq. 2.14-2.18, was developed during the course of this research [112], and used in Ch. 6.

The $n-$heptane oxidation model is given by,

$$C_7H_{16} + 11O_2 \rightarrow 7CO_2 + 8H_2O + q \tag{2.14}$$

with a global reaction rate of the form,

$$\omega = Be^{-T_a/T}C_{C_7H_{16}}C_{O_2} \tag{2.15}$$

and the heat release due to reaction of one mole of fuel,

$$q_0 = h_{C_7H_{16}} - 7h_{CO_2} - 8h_{H_2O} = 5401kJ.mol^{-1}. \tag{2.16}$$

The reduced heat release resulting from incomplete combustion at rich equivalence

ratios is modelled by,

$$\begin{cases} \phi \leq 1 & : \quad q/q_0 = 1 \\ \phi > 1 & : \quad q/q_0 = 1 - \alpha(\phi - 1). \end{cases} \tag{2.17}$$

The parameters selected for use in chapter 6 were $\alpha = 0.18$, $T_{a0} = 15000K$, $B = 2.4 \times 10^{14} cm^3.mol^{-1}s^{-1}$. T_a was expressed as,

$$\begin{cases} \phi \leq 0.74 & : \quad T_a/T_{a0} = 1 + 1.6948(\phi - 0.74)^2 \\ 1.13 \geq \phi > 0.74 & : \quad T_a/T_{a0} = 1 \\ \phi > 1.13 & : \quad T_a/T_{a0} = 1 + 0.0092(\phi - 1) + 0.9423(\phi - 1.13)^2. \end{cases} \tag{2.18}$$

This fit produces the variation of flame speed with equivalence ratio shown in figure 2.1.

Zero-dimensional CMC solutions for turbulent diffusion flames have been compared using the 1-step $n-$heptane scheme and a detailed mechanism by Held et al. [52]. The resulting critical strain rates for extinction N_{0ext} were $190s^{-1}$ and $285s^{-1}$ for the respective schemes. This level of difference is similar to that seen among more detailed mechanisms and also to the difference in critical strain rates seen between the one step methane scheme and experimental measurements [37]. The variation of peak temperature given by the zero-dimensional CMC calculation for $n-$heptane combustion versus scalar dissipation rate is given in Fig. 2.2.

Furthermore computations of diffusion flames accurately reproduce the critical strain rate for extinction of laminar methane - air flames [37], and the critical scalar dissipation rate of $n-$heptane - air flames in zero dimensional CMC calculations, see Fig. 2.2. The model also gives near extinction flames with oxygen leakage, as in Fig. 2.3, thereby overcoming known predictive limitations of one-step Arrhenius kinetics. Conversely the flame now leaks fuel which in the case of an $n-$heptane diffusion flame is unrealistic.

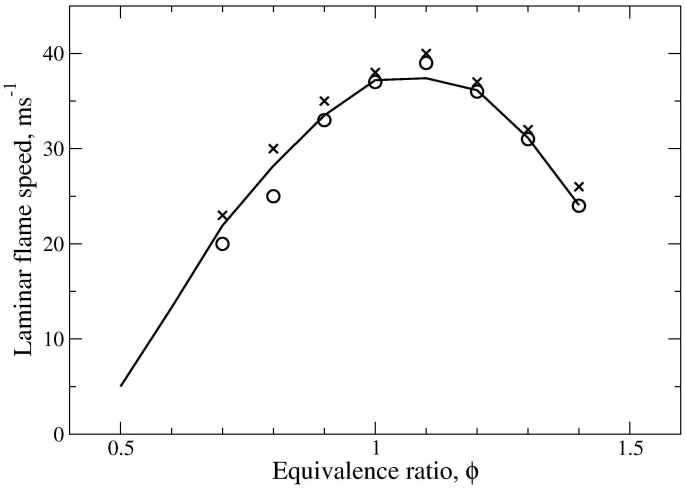

Figure 2.1: The modelled flame $n-$heptane laminar flame speed versus equivalence ratio at 1bar and 300K, compared to experimental measurements by Huang et al (crosses) [53], and by Davis and Law (circles) [30].

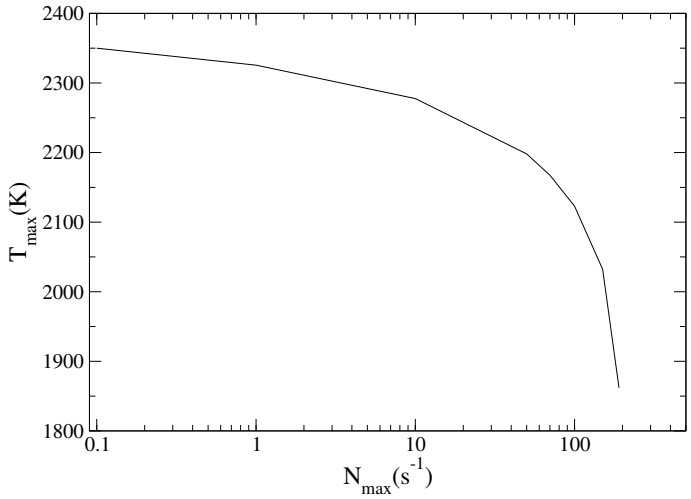

Figure 2.2: The maximum conditional temperature observed in steady zero dimensional CMC calculations found using the one step model for $n-$heptane, Eq. 2.14-2.18 versus N_0, the peak value of the conditional scalar dissipation rate given by the AMC closure, Eq. 2.10.

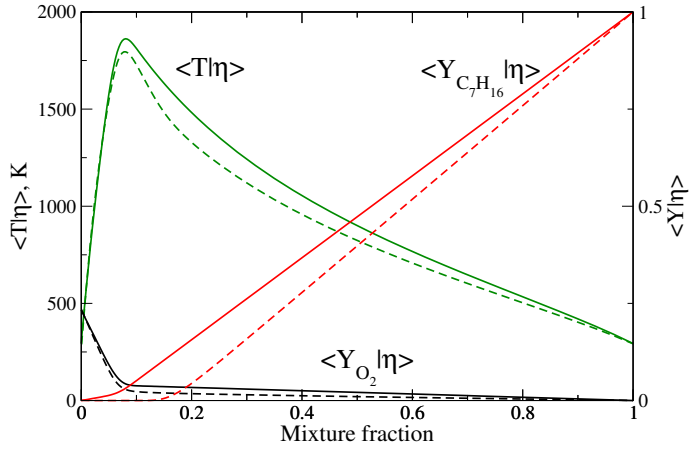

Figure 2.3: Mixture fraction space profiles of reactant mass fraction and temperature conditional expectations from use of the one step $n-$heptane mechanism, Eq. 2.14-2.18 (solid lines) and the Held et al. detailed mechanism [52] (dashed lines).

The use of a one step mechanism may be particularly appropriate in large turbulent flame propagation simulations, where the thermodynamic condition of the reactants is largely constant, and where the primary interest is in the interaction between the combustion heat release and the turbulent flow field. Where the mechanism has been derived for a particular operating condition it returns laminar flame speeds which can coincide exactly (depending on the complexity of the function for T_a/T_{a0}) with experimentally measured values. Those produced by detailed mechanisms, may be valid over a broader range but may give moderate errors at particular conditions. For example the GRI 3.0 detailed mechanism for natural gas underpredicts the propagation speed for laminar stoichiometric methane-air flames, $0.42ms^{-1}$, by around 7% at ambient conditions.

2.2.3 Spark ignition

Spark ignition has been approximated with two approaches in this work. The first approach involves inserting a burning zero-dimensional CMC solution at nodes representing a spark kernel, whose composition is then held constant for the spark

duration. The flame can spread from the kernel during the spark by convection and turbulent diffusion. After the spark time has elapsed it may extinguish or survive depending on the flow conditions. This approach does not alter the total enthalpy of the flow. The second approach involves the application of a conditional heat source in the temperature equation at the nodes in the ignition region. The conditional temperature source supplied is such that the conditional *unreacted* temperature remains constant across mixture fraction. This is motivated by the argument that since the gas temperature achieved inside the spark kernel is governed by the balance of electrical heat input, conduction and radiation, the temperature achieved is largely independent from the local mixture fraction. The user must specify $\dot{H}_{spark} = \partial \rho h / \partial t$ as a function of time and space to achieve a desired ignition energy. In this work its value is uniform in time and space in the spark region for the spark duration. The conditional temperature source is then given by Eq. 2.19:

$$\dot{T}_{spark}(\eta) = \frac{1}{c_p} \frac{\partial h}{\partial t} \left[\frac{(1-\eta)\langle c_p|\eta=0\rangle + \eta\langle c_p|\eta=1\rangle}{\langle c_p|\eta\rangle} \right] \tag{2.19}$$

2.2.4 CMC and two phase combustion

The CMC modelling discussed here only applies to the gas phase, with source terms resulting from interaction with the spray. The mixture fraction is defined as the mass of the gaseous material that originated from the liquid fuel stream. The inter-phase heat and mass transfer impacts the CMC model through the mixture fraction PDF, and also via source terms in the conditional species and energy equations. The value of the Favre averaged 'fractional' evaporation source for mass, S s^{-1}, and the heat transferred to the gas from the liquid phase, $\dot{h}_{evap}$ $J.kg^{-1}s^{-1}$, are obtained from the modelling used for the transport of the dispersed phase. In this work the spray has been solved using the Lagrangian spray solver available within the STAR-CD CFD code [20].

Ge and Gutheil noted that the usual $\beta-$function shape may fail to capture the correct form of the mixture fraction PDF during spray evaporation, based on full Monte Carlo solution of the mixture fraction PDF [43]. They go on to show that by defining the $\beta-$function between η_{min} and η_{max}, as proposed by Reveillon and Vervisch [107], a more satisfactory prediction of the PDF is achieved.

Where evaporation is taking place, the instantaneous fuel mass fraction is limited by the saturation value of the fuel at the local conditions. It is not obvious how this is best translated into a single upper bound for mixture fraction space at a particular location of a turbulent flow. Demoulin and Borghi discuss a transport equation for the mean saturation (ie. droplet surface) mixture fraction [32]. The solution of an equation for ξ_{sat} has not been attempted in this work. Also due to the Lagrangian spray solution method, the mean value of ξ_{sat} for the spray parcels in a particular CFD cell varies dramatically and is undefined in cells containing no droplet parcels. To avoid numerical difficulties the $\beta-$function PDF has been calculated between the boundaries $\eta = 0$ and $\eta = 1$.

Evaporation results in additional source terms in the transport equations for mean and variance of mixture fraction. The new source term for mixture fraction equals $\rho S\ kg.m^3 s^{-1}$, which is available directly from the spray solver. Reveillon and Vervisch group the evaporative terms of the variance equation into two terms, Eq. 2.21 [107].

$$\begin{aligned} \bar{\rho}\widetilde{\dot{\xi''^{2}_{evap}}^{+}} &= 2\bar{\rho}\widetilde{\xi''S}(1-\widetilde{\xi}) \\ \bar{\rho}\widetilde{\dot{\xi''^{2}_{evap}}^{-}} &= -\bar{\rho}\widetilde{\xi''^{2}S} \end{aligned} \tag{2.20}$$

In this work, the variance source term is either neglected, or treated with a development of the Reveillon and Vervisch 'single droplet model' [141], or the 'linear' model by Sreedhara and Huh [127]. Both models are based on presumed forms for the conditional evaporation rate, which are supported by DNS of sub-Kolmogorov

scale spray evaporation. The range of validity for the modelling is not clear.

The instantaneous species equations for $\frac{\partial \rho Y_\alpha}{\partial t}$ gain the evaporative source term $\rho S Y_{S\alpha}$, where $Y_{S\alpha}$ denotes the mass fraction of species α in the evaporating fuel mass. Rogerson [115] presents the derivation of the corresponding CMC equation for species mass fraction. Neglecting conditional fluctuations of the evaporation rate both Bilger's decomposition method and Klimenko's PDF equation method result in Eq. 2.21 [115; 116].

$$\begin{aligned} \frac{\partial Q_\alpha}{\partial t} + \langle \mathbf{v}|\eta\rangle \cdot \nabla Q_\alpha &= -\frac{div(\rho_\eta \langle \mathbf{v}'' Y_\alpha''|\eta\rangle P(\eta))}{P(\eta)\rho_\eta} + \langle W|\eta\rangle + \langle N|\eta\rangle \frac{\partial^2 Q_\alpha}{\partial \eta^2} \\ &\quad + S(\eta) Y_{S\alpha} - S(\eta) Q_\alpha - (1-\eta) S(\eta) \frac{\partial Q_\alpha}{\partial \eta} \end{aligned} \tag{2.21}$$

The final three terms arise due to the inter-phase mass transfer. In order, their meaning may be understood as a source term for the species which are evaporating (or condensing). The next term may be thought of as a dilution term resulting from the addition of new matter to the gas phase. The final term represents a convective flux in mixture fraction space due to the release and dilution of mixture fraction by evaporation. Where a spray (for example of water) does not contribute directly to the mixture fraction, the convective term is composed of only the diluting portion: $+\eta S(\eta) \frac{\partial Q_\alpha}{\partial \eta}$, [115].

Simulation of an igniting fuel spray also requires the CMC temperature equation. The instantaneous equation for enthalpy, $\frac{\partial \rho h}{\partial t}$ gains one term due to inter-phase mass transfer, $\rho S \sum_\alpha h_\alpha Y_{S\alpha}$, and another due to heat transfer from the liquid phase, $\rho \dot{h}_{evap}$. The two phase CMC temperature equation is derived in in appendix A.1. Assuming unity Lewis number for every species results in Eq. 2.22.

$$\begin{aligned}\frac{\partial Q_T}{\partial t} + \langle \mathbf{v}|\eta\rangle \cdot \nabla Q_T &= -\frac{div(\rho_\eta \langle \mathbf{v}'' T''|\eta\rangle P(\eta))}{P(\eta)\rho_\eta} + \sum_\alpha \frac{\langle W_\alpha|\eta\rangle h_\alpha}{\langle c_p|\eta\rangle} \\ &+\langle N|\eta\rangle \left\{ \frac{\partial^2 Q_T}{\partial \eta^2} + \frac{1}{\langle c_p|\eta\rangle}\left(\frac{\partial \langle c_p|\eta\rangle}{\partial \eta} + \sum_{\alpha=1}^{N} \frac{\partial Q_\alpha}{\partial \eta} c_{p\alpha} \right) \frac{\partial Q_T}{\partial \eta} \right\} \\ &-(1-\eta)S(\eta)\frac{\partial Q_T}{\partial \eta} + \frac{\langle \dot{h}_{evap}|\eta\rangle}{\langle c_p|\eta\rangle} \end{aligned} \tag{2.22}$$

Two new evaporative terms arise, the first is analogous to the convective term appearing in the species equation, and the final term is a conditional enthalpy source term analogous to the fourth term on the right hand side of equation 2.21.

Closure of the evaporative source terms in Eq: 2.21 and 2.22 requires a model for the conditional evaporation rate. The models of Vervisch and Domingo [141] and Sreedhara and Huh [127] are employed in chapter 6.

The CMC study of Diesel engine spray combustion by Wright et al. [147] took the approach of neglecting all source terms due to evaporation except in the equation for mean mixture fraction. The implicit assumption is that all evaporation takes place at $\eta = 1$. The analysis of Smith et al. [124], and Kim and Huh [63] produced a different set of evaporative source terms (which are a subset of those given in Eq. 2.21 and 2.22). It appears that the equations given here are a more complete description of the spray fueled CMC model. In chapter 6 the approach of Wright et al. has been employed, and the full solution of equations 2.21 and 2.22 is also attempted.

2.2.5 Numerical implementation

Discretisation

The CMC has been discretised on to orthogonal, finite difference grids in four dimensions (three in physical space and one in conserved scalar space). Second order central differences are used for second derivatives, and one-sided up-stream differences are used for first derivatives. The turbulent flux term has been evaluated by computing the inner first derivative, then multiplying by the density and mixture fraction PDF before taking the outer derivative. De Paola found this ordering less problematic numerically [95] than an alternative of applying the quotient rule to split the term in two as used by Devaud and Bray [33].

The discretisation used has potentially high numerical dissipation [60], thus care must be taken to provide sufficient resolution so that solutions become grid independent. Practical limitations on the number of CMC nodes used have required that the grids are clustered around regions with high first and second derivatives. In the case of the propagating jet flame, considered in chapter 5, the streamwise location of the refinement moves as the flame propagates. Where this occurs, the grid used is especially fine so that linear interpolation may be applied accurately to transfer information from the current grid to a new grid clustered at the current flame position.

Numerical integration

The solution of the set of ordinary differential equations giving the rate of change of the conditional quantities at every node in conserved scalar and physical space has been tackled using a fractional step approach. Each global time step, Δt_{global}, may be subdivided into CMC time steps of Δt_{CMC}. Firstly the spatial terms (conditional convection and conditional turbulent flux) are advanced by Δt_{CMC},

followed by the advancement of the potentially stiff conserved scalar space equation set. This allows different solvers, or solver settings to be used on the less stiff spatial transport equations. Both the global time step, which controls the fractional stepping between the CFD and the CMC, and the CMC time step, which controls the fractional stepping between the conserved scalar, and physical space terms of the CMC, must be small enough to avoid significant splitting errors.

The DVODPK solver has been used with non-stiff settings, to integrate the spatial terms throughout this work [17]. In stiff mode, the fully implicit, variable order, backwards differencing scheme used by DVODPK incurs a large starting over head each time it is applied to a different set of ODEs. The CHEMEQ2, asymptotically stable solver by Oran and Boris [86], has been implemented. Its predictor corrector implementation offers potentially large reductions in the start up overhead and consequently the CPU time expended [111]. The CHEMEQ2 solver requires more attention in order to ensure accurate and stable solutions are achieved. Ultimately the DVODPK solver was used for all CMC calculations presented in this thesis.

2.3 Summary

A practical and accurate implementation of the first order CMC has been developed for simulation of gaseous and spray fueled combustion. The importance of the conditional turbulent flux term in flame propagation situations is identified. New modelling of this term is discussed in chapter 4.

Contributions to CMC modelling in this chapter include a CMC model for forced ignition and the presentation of the CMC temperature equation for spray fueled combustion. Practical contributions include the application of a recent one step reaction scheme for partially premixed combustion [37] to $n-$heptane combustion and application of the implementation of the CHEMEQ2 solver [86] in the CMC

code. Further discussion and analysis of the CMC modelling presented above is provided in subsequent chapters based on *a priori* DNS solutions in chapter 4, and solution of the model for gas and spray fueled flows in chapters 5 and 6.

Chapter 3

Analysis of ignition in laminar strained non-premixed flow

A model for the forced ignition of turbulent non-premixed flow may need to incorporate local effects such as scalar dissipation and chemical reaction processes, as is attempted in the CMC. These processes have received limited attention in the context of turbulent ignition kernels, however strained laminar flows provide a convenient example in which to study the local effects present in particular turbulent reacting flows. This chapter uses simulations of ignition in strained laminar mixing layers to illustrate underlying processes and limits which can be encountered during ignition of turbulent flow.

3.1 Background

In laminar flows, the ignition success may have a probabilistic nature attributable to the randomness in the ignition system [71]. In turbulent non-premixed flows, above a certain spark energy the mixture fraction fluctuations introduce the main stochasticity in ignitability [4; 10], and the ignition probability in turbulent non-premixed jets has been successfully correlated with the probability of finding flammable mixture at the spark location. However, measurements of spark ignition

in a turbulent flow show a number of fluid dynamic influences in addition to the compositional effects. These include dependence on turbulence levels and on flow speed [2; 7]. Hence, a greater clarification of the effect of the flow on ignition of non-premixed flames is needed.

Rashkovsky [103] analysed numerically, and with simple chemistry, spark ignition of laminar non-premixed counterflow flames. He demonstrated that ignition, initiated by a hot gas kernel placed somewhere in the mixture, fails below a critical value of the Damköhler number. Direct Numerical Simulations of ignition in a turbulent fuel-air mixing layer [24], also with one-step chemistry, showed the development of a tribrachial structure, consistent with Ray et al. [104], and demonstrated that intense turbulence may not allow the spark to develop into a flame. Detailed chemistry simulations have not been performed yet for laminar non-premixed flame ignition and it is not fully clear what is the maximum strain rate for successful ignition. Such simulations are presented in this chapter.

The laminar counterflow configuration provides a well-defined flow field in which to examine the effect of strain on flame structure and it is used here for studying forced ignition processes. Forced ignition is instigated by a heat source (igniter), which can take a variety of forms, including heated surfaces, electrical sparks and laser pulses. Even igniters of the same type can have very different characteristics in terms of the spatial and temporal evolution of the energy input. An idealised thermal analysis of spark ignition [150][11] leads to the concept of a minimum ignition energy and to a minimum spark radius for ignition of the order of the premixed flame thickness [46]. Measurements of minimum ignition energy, around 0.30 mJ for stoichiometric methane-air mixtures [46], usually refer to the electrical energy provided to the spark electrodes. The energy retained by the flame kernel after conductive, acoustic and radiative losses is typically 2-16% [150] of this electrical energy. Alternative sparks include Laser Induced Spark Ignition that delivers a measurable quantity of energy to the fluid at the focus of the laser beam

over a relatively short period of time, 5-500 ns [99]. However, all types of sparks include complicated flow patterns, ionization, and shock waves [13; 71] and are hence not easy to represent numerically, although the discharge phase following breakdown has been successfully modelled [132].

In this chapter, simulations of ignition in a laminar methane-air counterflow mixing layer have been performed in order to display the variety of ignition behaviour possible for a range of strain rates. The spark is modelled as a region of hot inert gas with a finite thickness. Details of the flow and ignition formulation are given in the following section. The resulting ignitability limits are then discussed, and the transient flame structures are examined. Where topological effects such as flame curvature may be neglected, similar flame structures can be expected during the ignition of non-premixed turbulent flows.

3.2 Formulation

3.2.1 Configuration and computational code

The computational configuration is a non-premixed counterflow arrangement with planar geometry. RUN1DL is used to solve a low Mach number formulation of the flame equations in terms of a distance variable [118], including detailed molecular transport. Variable molecular properties and the GRI-Mech 3.0 detailed chemical scheme are employed for reactions between methane and air [41]. The 53 species GRI-Mech 3.0 has been optimised for combustion of natural gas using data in the range $1000 - 2500K$, and shows realistic extinction behaviour.

The system of equations is integrated on an adaptive grid with a modified Newton method [118], while ensuring grid independence of the solution. The fuel and air inlets are at $y = -6mm$ and $y = 6mm$ respectively, and the boundary temperature and pressures are $293K$ and $100kPa$. In the partially premixed flames

examined, the air volume fraction in the fuel stream, X, was 0.8, while the non-premixed case uses streams of pure methane (i.e. $X = 0$) and pure air. For $X = 0$, the stoichiometric mixture fraction is $\xi_{st} = 0.055$, while for $X = 0.8$, $\xi_{st} = 0.452$. The stagnation point is fixed at $y = 0\ mm$ and the inlet velocities are determined according to a specified strain rate S. The values of mixture fraction used to report data from the counterflow calculations are calculated using nitrogen atom conservation. The static lean and rich flammability limits of ignition of homogeneous methane-air mixtures are, respectively, fuel volume fractions of 5% and 15% [46], which translate to $\xi_{lean} = 0.0284$ and $\xi_{rich} = 0.089$ for $X = 0$ and $\xi_{lean} = 0.233$ and $\xi_{rich} = 0.732$ for $X = 0.8$. The strain rate at which the flame extinguishes is found by gradually incrementing the strain rate until extinction occurs to be $S_{ext} = 475 s^{-1}$ for the non-premixed case ($X = 0$) and $S_{ext} = 756 s^{-1}$ for $X = 0.8$, to within $1 s^{-1}$.

3.2.2 Spark representation

The spark is assumed to cause instantaneous heating of a slab with thickness $\Delta y_{sp} = 0.25 mm$ centred at y_{sp}. The peak temperatures T_{sp} used were 3000 K and 4000 K and a smooth but very thin interface between the spark and the surrounding inert fluid is used to avoid numerical problems initially. The spark temperatures used correspond to a constant pressure heat addition of $429 kJ m^{-3}$ and $558 kJ m^{-3}$ [140] based on the spark volume, hence the $4000 K$ spark contains about 30% more energy than the $3000 K$ spark. Repeating Glassman's [46] idealised spark analysis for this planar problem, one obtains that the critical spark half-width for successful ignition $r_f \geq \sqrt{\pi}\delta \approx 1.8\delta$, where $\delta = \alpha / S_L$. This contrasts with $r_f \geq 3.7\delta$ for the radius of a spherical spark [46]. Using the thermal diffusivity for air $\alpha = 2.15 \times 10^{-5} m^2 s^{-1}$ [140], and calculating methane's stoichiometric laminar flame speed as $S_L = 0.37 m s^{-1}$ from the code [118] with the same chemistry at $293 K$ and $1 bar$, the critical heat input width for the one-dimensional problem may be estimated as $0.2 mm$. Therefore the spark width considered in this work is slightly larger than

the critical spark width for successful premixed ignition. In addition, considering the fact that our spark temperature is higher than the adiabatic flame temperature of stoichiometric methane-air flames, we conclude that our spark representation ignites safely a homogeneous stagnant stoichiometric mixture. This has also been demonstrated by separate runs of RUN1DL.

The initial condition used is a converged inert flow with the spark's temperature profile subsequently imposed. The low Mach number formulation in RUN1DL does not capture pressure waves that may result from sudden temperature changes, nor is the chemical mechanism reliable at the high initial temperatures. Therefore the early evolution of the chemical composition and of the velocity field should not be given undue credence, however the total spark energy is still conserved. The temperature falls rapidly and subsequent predictions are more credible.

3.3 Results and discussion

3.3.1 Ignition limits

Figure 3.1 shows the evolution of the temperature profile during successful ignition of a non-premixed flame. The mixture at the centre of the spark is lean. The peak temperature has decreased from $4000K$ to $3848K$ within $2.0 \times 10^{-7}s$ due to diffusion of the spark and an initial predominance of endothermic reactions. As the heat release increases, the peak temperature rises to $3868K$ at $1.0 \times 10^{-6}s$. Heat from the flame diffuses through the mixing layer, while the spark energy is dissipated, and a steady diffusion flame has been established by $1.0 \times 10^{-2}s$. In the following, successful ignitions are deemed only the simulations that result in similar non-premixed flames after steady-state has been achieved.

A large number of ignition simulations were performed across a range of strain rates and spark positions. The resulting loci of mixing layer ignitability limits are

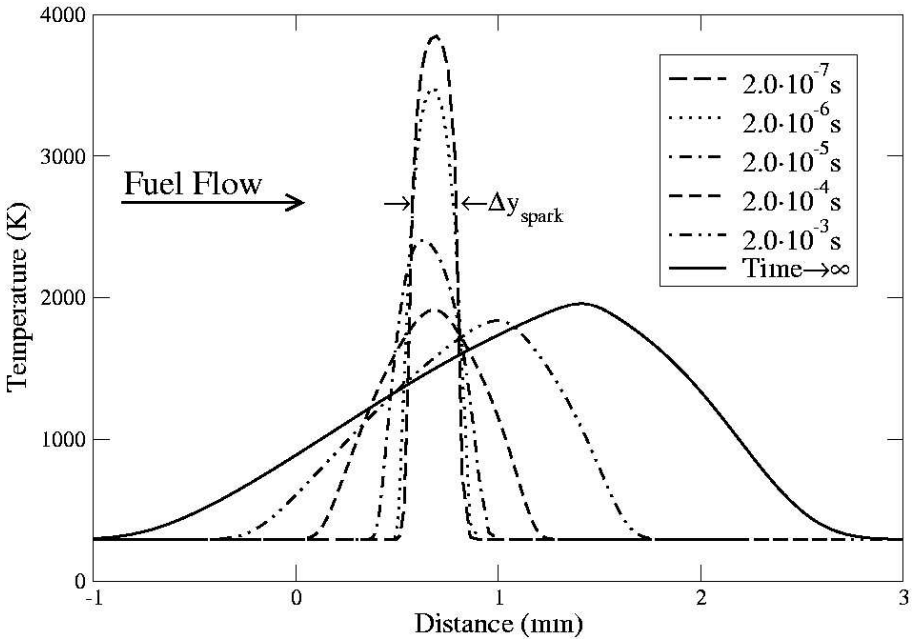

Figure 3.1: Transient temperature profiles in physical space during a successful ignition event. Spark B from table 3.1.

shown in Fig. 3.2 for the non-premixed case with $3000K$ and $4000K$ sparks. Figure 3.3 shows the ignitable region for $T_{sp} = 3000K$ sparks in the partially premixed case. In both figures, the position coordinate has been transformed using the factor $(S/S_{ext})^{1/2}$, which is proportional to the physical width of the inert mixing layer [100]. Through this transformation, contours of mixture fraction become vertical lines. The loci of stoichiometry and of the premixed static flammability limits [46] are shown for comparison. Figure 3.2 also shows the locations of three $4000K$ sparks labeled as A-C (Table 3.1), examined in greater detail later. Sparks A and C are outside the ignitable region, while B results in the steady diffusion flame seen in Fig. 3.1.

Sparks centred within the closed region in Figs. 3.2 and 3.3 result in successful ignition, while sparks outside this region do not lead to ignition. Ignition only occurs for sparks falling within a range of mixture fraction and below a certain strain rate. It can be possible to ignite the flow despite sparking at a non-flammable

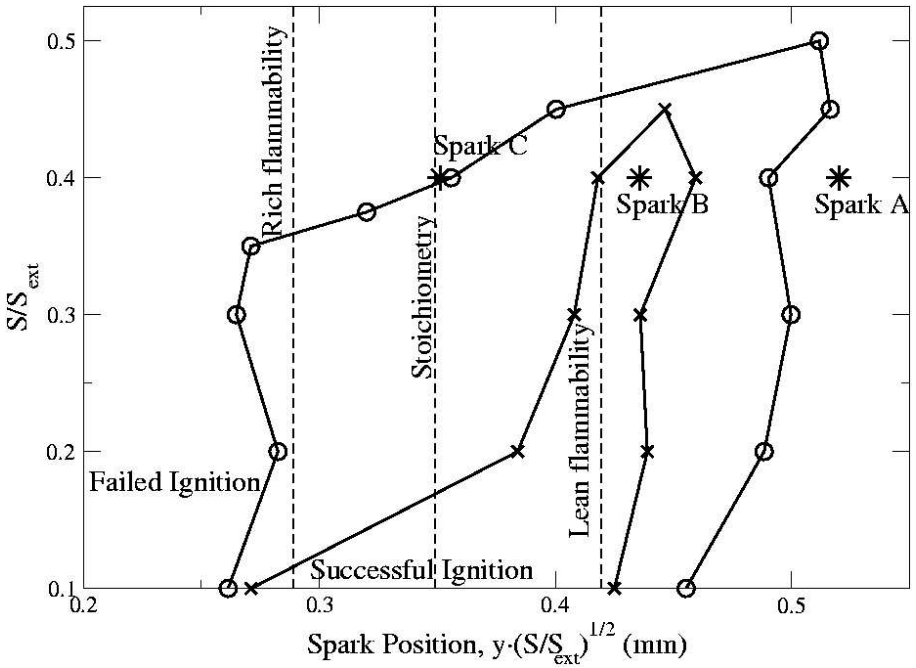

Figure 3.2: The loci of the ignitability limits for $3000K$ sparks (x) and $4000K$ sparks (o) for the $X = 0$ flame. The stoichiometric mixture fraction and the static rich and lean flammability limits are indicated.

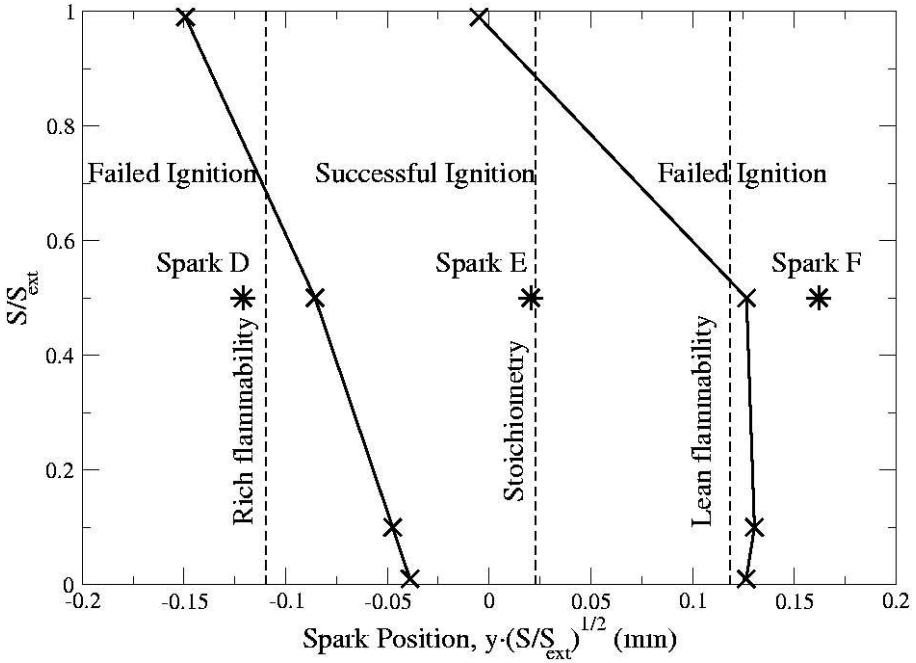

Figure 3.3: The locus of the ignitability limits for $3000K$ sparks in a flame with $X = 0.8$. The stoichiometric mixture fraction and the static rich and lean flammability limits are indicated.

Table 3.1: Details for sparks A-F.

	S (s^{-1})	y_{sp} (mm)	X	T_{sp} (K)	Success/Failure
Spark A	190.0	0.555	0	4000	F
Spark B	190.0	0.689	0	4000	S
Spark C	190.0	0.823	0	4000	F
Spark D	378.0	-0.169	0.8	3000	F
Spark E	378.0	0.029	0.8	3000	S
Spark F	378.0	0.229	0.8	3000	F

mixture fraction because sufficient heat and reactive species may still diffuse into the flammable region to lead to a sustainable flame. As the strain rate increases the mixing layer becomes narrower. At the extinction value of $S = 756s^{-1}$ (for the $X = 0.8$ flame), the width of the fluid slab between the static flammability limits is $0.225mm$, which is just less than the width of the spark. Thus, when the spark's centre lies outside the nominally flammable region there can still be a degree of overlap between the spark and the flammable region. Therefore, because in reality sparks have finite size, the presence of nominally flammable mixture at the spark centre is not necessarily a requirement for ignition. The fact that the ignitability limit is wider than the region bounded by the static flammability limits in Fig. 3.2 is consistent with the observed increased probability of igniting a non-premixed turbulent jet flame by increasing the spark size [2].

It is not possible to ignite a stable flame when the global strain rate is above the extinction strain rate S_{ext}. However, in the flame with $X = 0$, ignition did not occur above 45% of the extinction strain rate with the $3000K$ spark and not above 50% of S_{ext} for $T_{sp} = 4000K$. It may be expected that further increases in the spark energy will increase the maximum ignitable strain rate until it coincides with the extinction strain rate. The ignitable region for $T_{sp} = 3000K$ is completely within the ignitable area for $T_{sp} = 4000K$. Not only does increasing the spark energy make it possible to ignite at higher strain rates, it also increases the range of mixture fractions (e.g. the loci in Fig. 3.2 become wider with T_{sp}).

In the laminar counterflow configuration, both extinction and the quenching of an otherwise viable ignition kernel are largely controlled by the strain rate S. As a consequence, the critical strain rate of extinction and the critical strain rate of forced ignition could be expected to follow similar trends as the boundary conditions are changed, for example by increased premixing or inlet temperatures. In agreement with experiments (e.g. Mastorakos et al. [85]), the partially premixed flow has a higher extinction strain rate than the non-premixed flow (calculated as $756s^{-1}$ compared to $475s^{-1}$). Indeed, for the $3000K$ spark, a comparison between Figs. 3.2 and 3.3 shows that this spark is sufficient to ignite a partially-premixed flame up to the extinction strain rate, but it is sufficient to ignite the pure diffusion flame only for S up to 45% of S_{ext}.

In Figs. 3.2 and 3.3, the ignitability limits are not symmetrical about stoichiometry. In the non-premixed case, ignitability is favoured at lean mixture fractions as the strain rate is increased, while rich mixtures show greater ignitability in the partially premixed case. This is best understood through a consideration of the scalar dissipation profile in a counterflow. The scalar dissipation peaks close to the stagnation point (at $y = 0$ and a mixture fraction of $\xi = 0.5$) and so, for the $X = 0$ case, a spark in a lean region ($\xi < \xi_{lean}$) experiences a smaller scalar dissipation than a spark in the rich region ($\xi > \xi_{rich}$). This implies a greater resilience of the lean spark for the same strain rate. For the partially premixed flame, $\xi_{st} = 0.452$ and there is little difference in the scalar dissipation rate experienced by a lean and a rich spark. Hence the difference between the distances separating the ignitability limits from their respective flammability limits is less. However, Fig. 3.3 indicates that ignition of rich mixtures is more resilient to the effects of strain rate than ignition of lean mixtures for $X = 0.8$. The fact that the rich ignitability contour is sloping to the left may be attributed to the increasing overlap between the spark and the flammable region as the mixing layer gets thinner, off-setting the adverse effects of increased strain. The fact that the lean ignitability limit also slopes to the

left implies an additional chemical effect making the richer sparks more resilient to the dissipative effects of strain.

3.3.2 Ignition evolution

It has been seen that both strain and composition influence the survival of an ignition kernel. This section examines the detailed evolution of the kernel following the spark in the non-premixed flame. Figure 3.4 shows transient temperature profiles for sparks A, B and C in mixture fraction space. Spark A is located at a sufficiently lean mixture fraction that by the time appreciable spark energy arrives in the flammable region, the temperature has decreased too much for successful ignition. Spark B is successful. Spark C fails to ignite despite sparking the entire flammable region. While spark C seems more promising than the leaner spark B, it should be noted that the scalar dissipation rate gets higher closer to the stagnation point where $\xi = 0.5$ and this apparently leads to the quenching of spark C.

In case A, the consumption of oxygen and methane is very limited (Fig. 3.5). In case B, the reactants are initially consumed in the region of the spark and subsequently the premixed reactants from outside the spark region are consumed until a diffusion flame is achieved. The flame structure during this premixed phase is not clear from Fig. 3.5, however it involves flame fronts propagating across the mixing layer away from the spark. The flame front fades as it reaches very rich or very lean mixtures, but these transient reaction zones are evident in mixtures quite far from the static flammability limits. In case C, a large proportion of the reactants is consumed within the spark region, however there is greater fuel leakage than in case B. Consumption of the surrounding cold premixed reactants proceeds, but the flame is quenched before the stable diffusion flame condition is achieved.

The initial, strongly endothermic heat release seen in Fig. 3.6 is very short lived ($t < 10^{-6}s$) and is replaced by an exothermic heat release profile with two

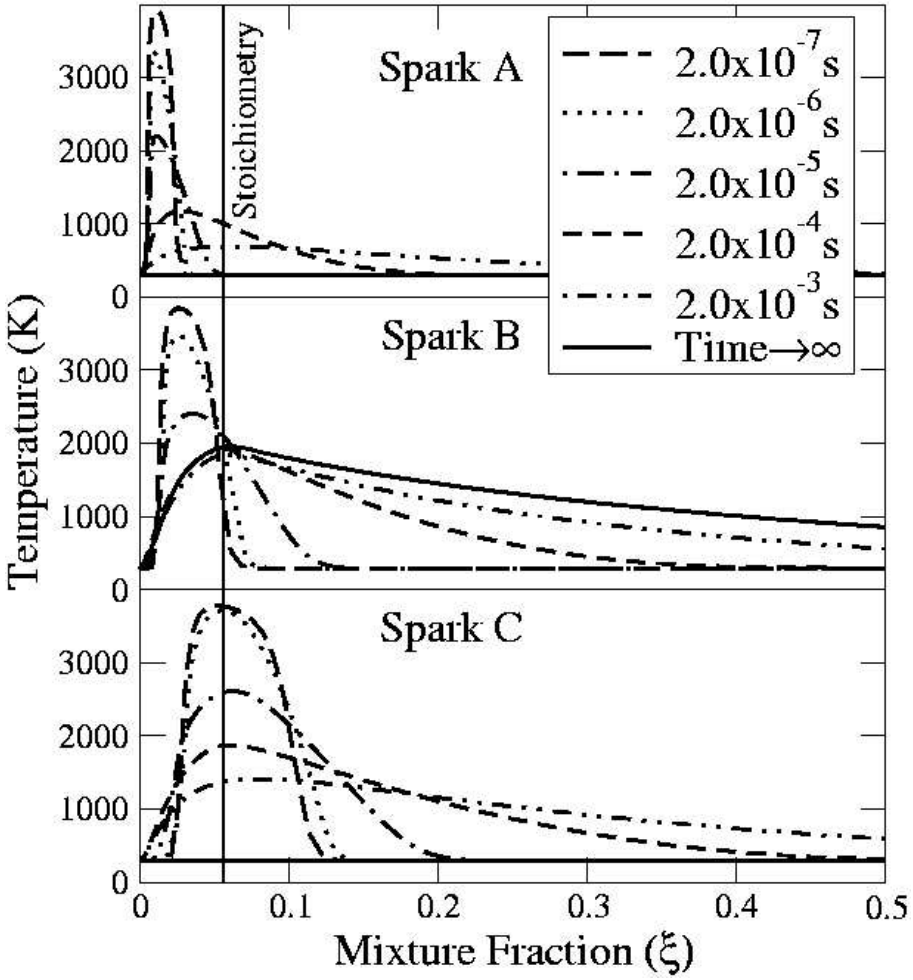

Figure 3.4: Transient temperature profiles in mixture fraction space for sparks A, B and C.

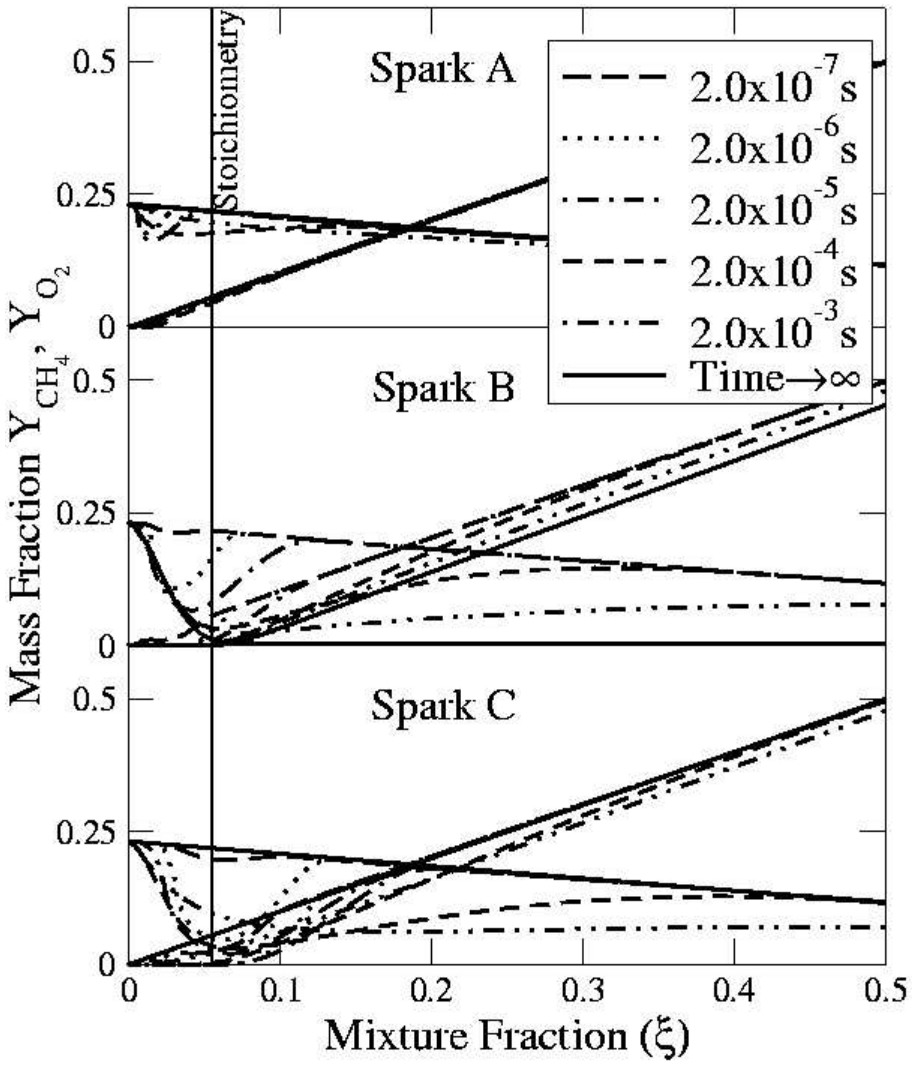

Figure 3.5: Transient mass fraction profiles in mixture fraction space for methane and oxygen for sparks A, B and C.

peaks close to the rich and lean edges of the spark. While the small physical size of the inflamed region may make it inappropriate to discuss individual flame fronts, the large heat release rates at the edges of the burning regions, rather than close to stoichiometry early on, indicate that premixed type reaction zones dominate for around $2.0 \times 10^{-4} s$. For successful ignition it is then necessary to stabilise a diffusion flame, as is seen in the case of spark B. The flame structure involving rich and lean fronts and an inner diffusion flame may be described as tribrachial [18]. The evolution of the OH concentration is reported in Fig. 3.7. In agreement with experimental observations [132], the predicted transient OH concentration peaks at around an order of magnitude higher than in the steady diffusion flame and then it decays while the temperature falls. The shape of the OH profile reflects that of the temperature, rather than the heat release.

The same qualitative behaviour can be observed for the differences between a successful and an unsuccessful spark for the partially-premixed case. Figure 3.8 shows that the initial heat from the spark diffuses into the un-burnt mixture and eventually a flame is established for Spark E, whilst the spark is quenched in the other two cases. Premixed flame fronts are not as distinct here as for $X = 0$ due to the large width of the diffusion-flame reaction zone in ξ-space for large air premixedness. However, the heat release profiles (Fig. 3.9) at early times show evidence of two peaks corresponding to the edges of spark. The heat release reaches high levels during the auto-ignition phase of the sparked region, but these quickly decay to zero in the case of failed sparks and to the much lower values (hardly visible with the scale of Fig. 3.9) associated with a non-premixed flame at ξ_{st} in the case of successful sparks.

The OH mass fraction profile in the flame with $X = 0.8$ (Fig. 3.10) shows that the OH has very small concentrations at $t = 2.0 \times 10^{-7} s$, but it then increases rapidly for all sparks and auto-ignition has occurred by $t = 2.0 \times 10^{-6} s$ (see also the switch between negative to positive heat release in Fig. 3.9). The OH then decays

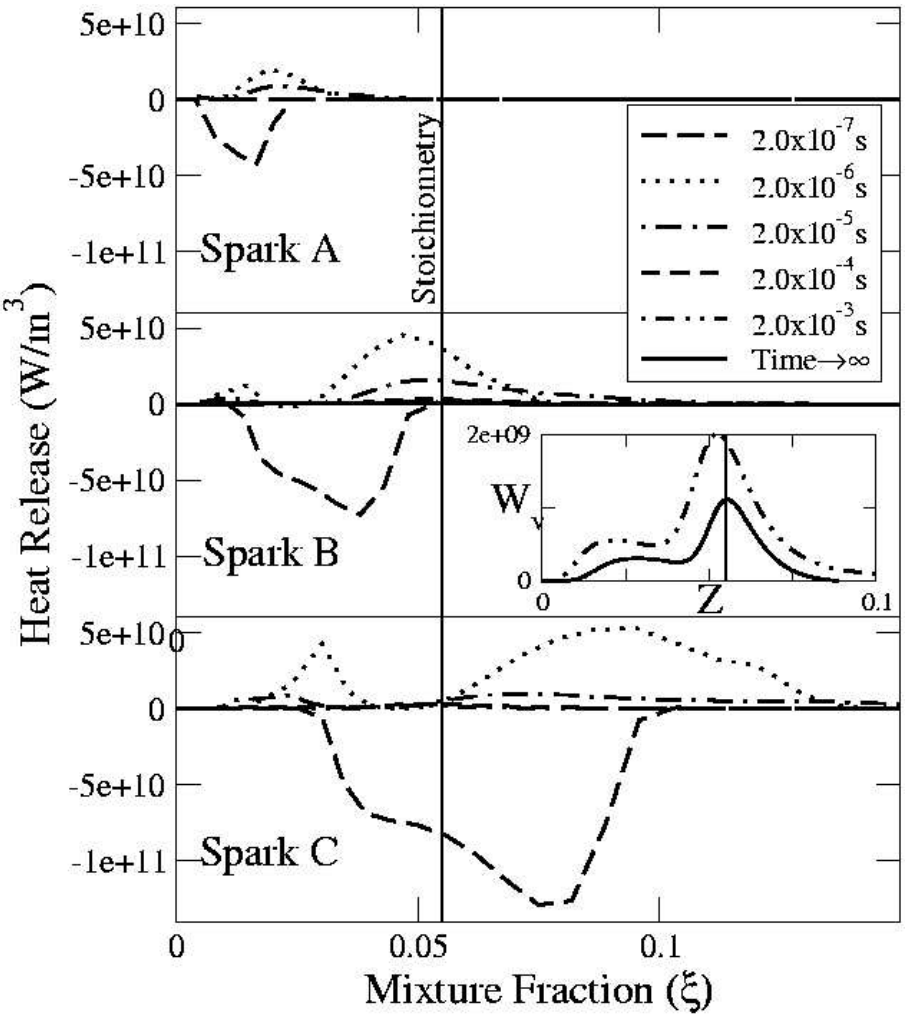

Figure 3.6: Transient heat release profiles in mixture fraction space for sparks A, B and C. The inset graph is an enlargement showing the stabilised heat release profile for case B.

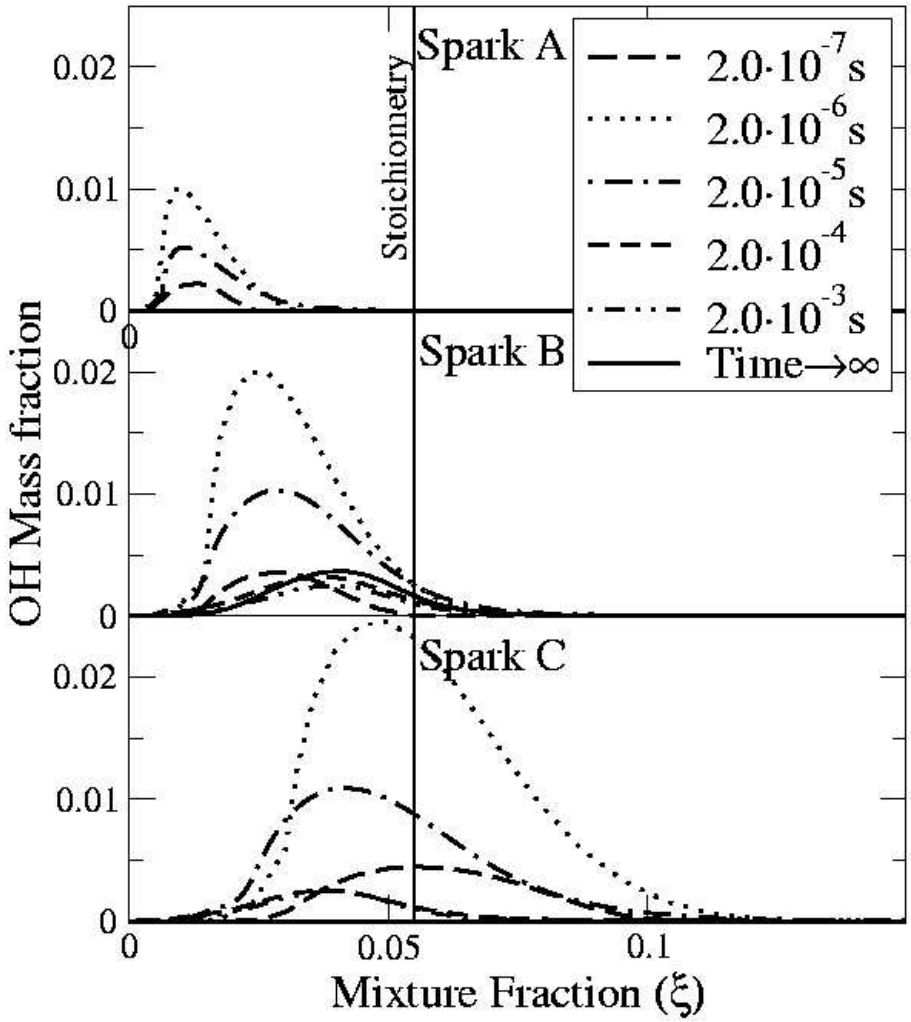

Figure 3.7: Transient OH mass fraction profiles in mixture fraction space for sparks A, B and C.

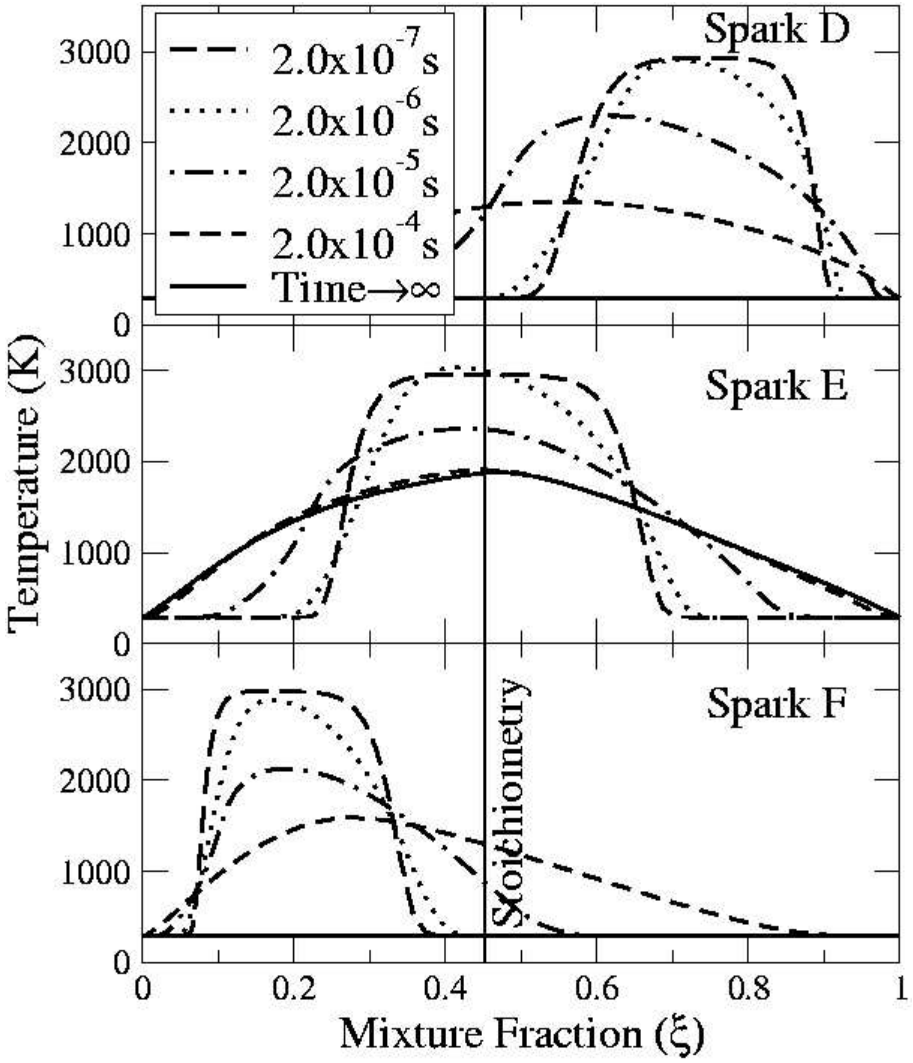

Figure 3.8: Transient temperature profiles in mixture fraction space for sparks D, E and F.

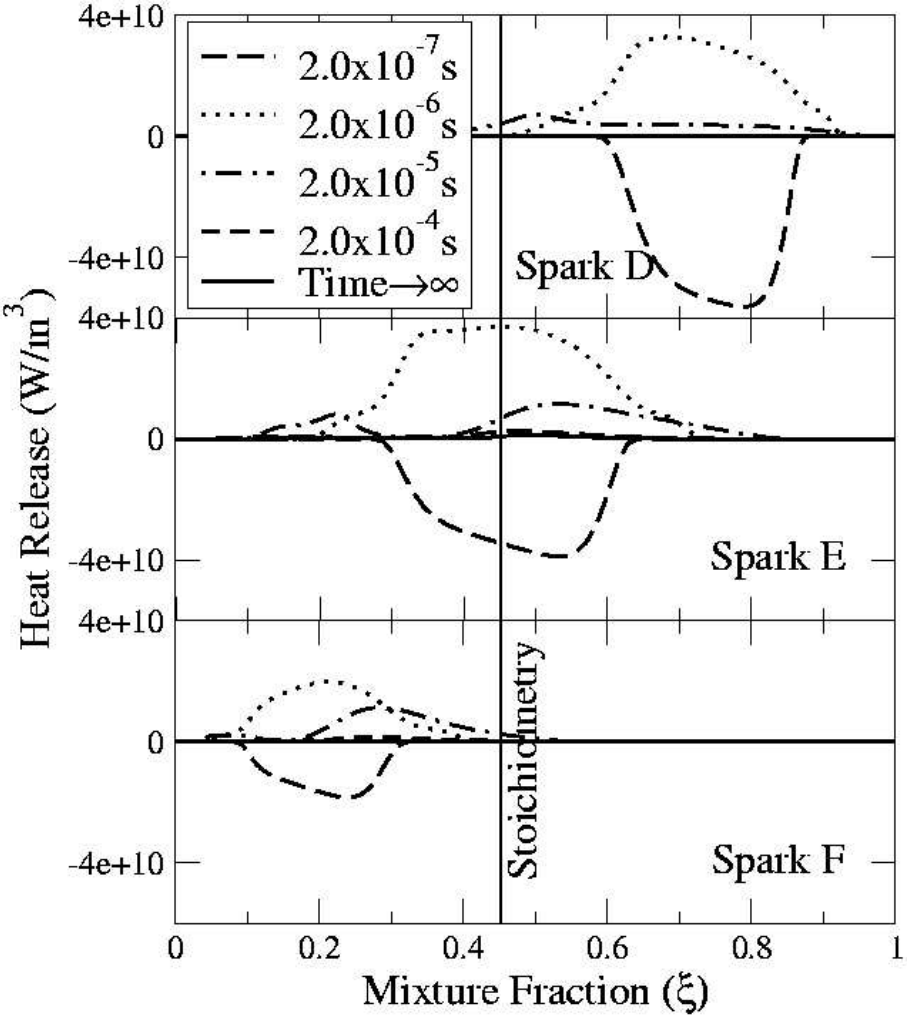

Figure 3.9: Transient heat release profiles in mixture fraction space for sparks D, E and F.

to virtually zero by $t = 2.0 \times 10^{-4} s$ for the failed sparks, with a flame stabilised by $t = 2.0 \times 10^{-3} s$ for the successful spark E. Again, super-equilibrium OH is observed initially due to the auto-ignition of the sparked mixture.

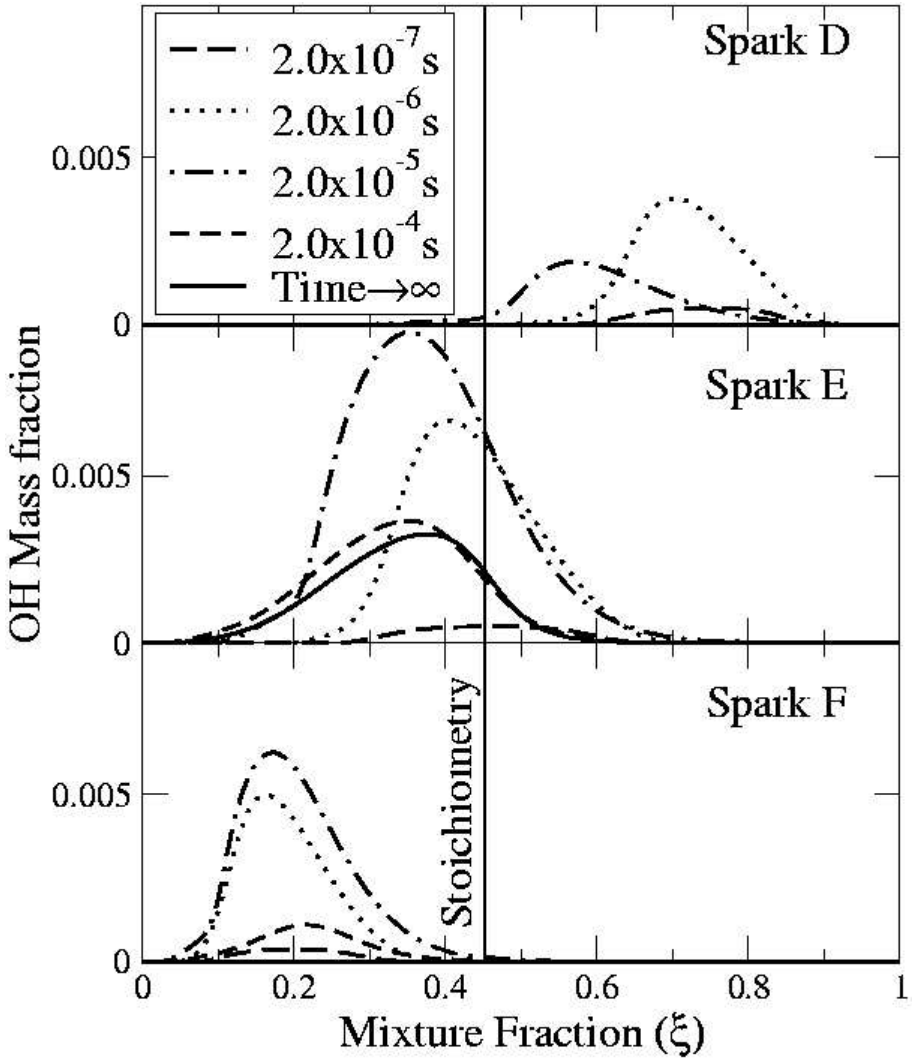

Figure 3.10: Transient OH mass fraction profiles in mixture fraction space for sparks D, E and F.

3.3.3 Implications for ignition in turbulent flow

Since practical sparks have a finite duration and in most engineering applications the spark kernel typically contains several mixing layers the scenario investi-

gated above and the related limits are rarely encountered in practice. However it is interesting to note that flames that occupy a narrow range in mixture fraction space, such as the ignition kernels discussed above, or the tip of a forward propagating edge or triple flame, are more sensitive to the level of strain than stable diffusion flames. The implication is that local effects such as scalar dissipation become significant and possibly limiting to edge flame propagation at strain rates below the strain rate which would extinguish a stable diffusion flame under the same conditions. The deleterious effect of strain on edge flame propagation is observed in both laminar [38; 55] and turbulent [24] edge flames. This highlights the need for the turbulent combustion model to correctly account for local mixing processes, in balance with reaction and macro-mixing processes. Chapter 4 examines this balance in the context of CMC modelling for turbulent ignition kernels.

3.4 Conclusions

Calculations of non-premixed and partially premixed laminar counterflow flames with detailed chemistry have been performed with a simulated spark to understand the factors affecting ignition success in non-premixed combustion. The results showed that there is a critical strain rate, which depends on the igniter, above which forced ignition is impossible for all spark positions. This critical value can be less than the extinction strain rate at which a steady flame becomes impossible, even for a spark thickness and energy that would ignite a stoichiometric homogeneous mixture. For a particular spark position relative to the stoichiometric mixture, failure to ignite is due to a combination of excessive dissipation and the local mixture flammability. Regions of very low scalar dissipation rate can have insufficient fuel to ignite, while otherwise flammable regions can fail to ignite due to the local dissipation rate being too high. The transient flame structure was analysed during successful and unsuccessful ignition. Once reactants have been consumed in the

ignition region, premixed flame fronts develop to consume the partially-premixed fluid. As the spark heat is diffused, the premixed fronts become less distinct and finally a non-premixed flame is stabilised.

Chapter 4

Analysis of ignition in turbulent non-premixed flow

This chapter describes analysis of direct numerical simulations of turbulent non-premixed ignition kernels. The analysis is used to investigate the CMC modelling necessary for ignition problems.

4.1 Background

The Conditional Moment Closure, equation 4.1, is to be applied in the modelling of igniting flows in chapters 5 and 6.

$$\frac{\partial Q_\alpha}{\partial t} = -\langle u_i|\eta\rangle \frac{\partial Q_\alpha}{\partial x_i} + \langle N|\eta\rangle \frac{\partial^2 Q_\alpha}{\partial \eta^2} + \rho_\eta \langle \dot{w}_\alpha|\eta\rangle - \frac{1}{\bar{\rho}\widetilde{P}(\eta)} \frac{\partial}{\partial x_i}\left(\langle u_i'' Y_\alpha''|\eta\rangle \bar{\rho}\widetilde{P}(\eta)\right) \quad (4.1)$$

During ignition and propagation of non-premixed turbulent flames it is common to encounter significant variations of conditionally averaged quantities, and this requires accurate modelling of the conditional mean velocity and turbulent flux. The latter term is usually modelled as [69]

$$\langle u_i'' Y''|\eta\rangle = -D_t \frac{\partial Q}{\partial x_i} \quad (4.2)$$

where D_t is an eddy diffusivity. Lifted flames [33; 61], autoignition of gas jets and sprays [64; 66; 147], bluff-body non-premixed flames [65], and fires [28] have been examined using the model of Eq. (4.2). In some of these, it has been found that the turbulent flux term is important for the overall success of the prediction. For example, a balance of terms in the CMC equation in the stabilisation region of a lifted flame [33; 61] shows that this term contributes significantly and hence it was concluded that it is important to examine its modelling. A similar conclusion was reached after exploring the results from two-dimensional solutions of Eq. 4.1 in an auto-igniting spray [147], which showed that CMC could possibly be used for all the phases of diesel engine combustion (autoignition, premixed, non-premixed), as long as the spatial transport terms are captured correctly.

Motivated by these trends and suggestions concerning the CMC sub-models, in this chapter, direct numerical simulations are examined for a non-premixed turbulent flame with a propagating edge. The simulations are designed to produce spatial gradients of the conditional averages and the results are analyzed in terms of Eq.4.1 and aim, in particular, to examine the validity of Eq. 4.2, and the closure employed for the conditional reaction rate. The transport equation for the conditional turbulent flux is also used to assist in the interpretation of the results. The DNS has been performed in collaboration with Dr N. Chakraborty and a fuller description of the numerical solutions is given in ref. [24].

4.2 Formulation

4.2.1 Simulations

The simulations were carried out using a three-dimensional fully compressible DNS code called SENGA [22; 23]. A single-step irreversible reaction is considered with an Arrhenius expression and the stoichiometry of methane ($\xi_{st} = 0.055$). The

conservation equations of mass, momentum, energy and mass fractions of fuel and oxidiser are solved in dimensionless form. The specific heats for all species are assumed equal and independent of temperature, Fick's law was used, and the Lewis numbers of all the species were unity. All first and second derivatives are evaluated using a 10^{th}-order central difference scheme, with the order of differentiation gradually dropping to second order one-sided finite difference near the non-periodic boundaries. Non-periodic boundaries are taken to be partially non-reflecting using the NSCBC technique [134]. Time advancement is carried out using a third order Runge-Kutta scheme.

An inert mixing layer between fuel and air which is allowed to interact with homogeneous isotropic turbulence at time $t = 0$, and then undergoes forced ignition as depicted in Fig. 4.1.

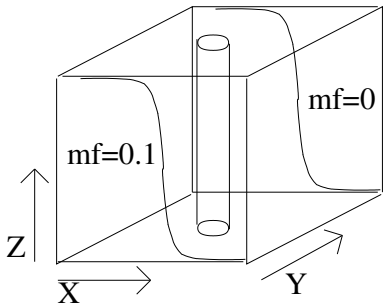

Figure 4.1: Schematic drawing of the mixture fraction profile and the cylindrical ignition source for the turbulent mixing layer configuration.

The initial turbulent velocity field is generated according to the Batchelor-Townsend spectrum and gives a characteristic velocity scale of u' and a length scale L_t. For all simulations, the grid spacing was smaller than the Kolmogorov length scale and about 10 grid points were placed within the thermal thickness of a stoichiometric unstrained laminar premixed flame $\delta = \alpha/S_L$, with α the thermal diffusivity and S_L the laminar burning velocity of a stoichiometric mixture.

The normalised temperature T is given by $(T_c - T_u)/(T_{ad} - T_u)$, where the adiabatic flame temperature of the stoichiometric mixture is T_{ad}, T_u is the cold gas

temperature, and T_c is the temperature calculated from the energy equation in the DNS. Details are given in [22; 23].

In contrast to ref. [24], the spark was modelled here as a thin cylinder spanning the domain in the z direction as shown in Fig. 4.1. This was done so that averages over z could be formed. A power source in the energy equation lasting t_{sp} was used, with $t_{sp} = 0.2\alpha/S_L^2$ to ensure ignition.

The source term followed a Gaussian distribution around the spark centre with an $1/e$ thickness of 1.5δ. For the spark duration, energy, and size used here, it was possible to have successful self-sustained combustion in quiescent homogeneous stoichiometric fuel-air mixture. The spark centre was at $y = 0.5$ and at an x position where $\xi = \xi_{st}$.

The mixing layer configuration had an initial mixture fraction profile which varies across the x-direction according to an error function. The partially non-reflecting boundary condition was applied in the x-direction and periodic boundaries were applied in the y and z directions, the coordinate system is shown in Fig. 4.1. To improve resolution across the flame zone, the maximum mixture fraction was 0.1. The domain was a cube with edges of length L. The cubes used had 128^3 points equally spaced along the coordinate directions, corresponding to $L/L_t \approx 6$. All lengths are non-dimensionalised by L and velocities by S_L.

Simulations were run for three turbulence levels $u'/S_L = 4$, 8 and 12 denoted by L1, M1 and H1 respectively. For all simulations $L_t/\delta = 3.4$.

4.2.2 Conditional moment equations

Conditional sampling procedures

The DNS configuration develops over time such that ensemble averages may be compiled, at a given point in time, from independent realisations of the same flow.

Multiple realisations for each case considered were not available. However, since the configuration is designed to be statistically uniform in the z direction, the ensemble average for a particular (x, y) location may also include the data at points along a line in the z direction. Here, the number of independent samples is estimated as the number of integral length scales across the z direction (around 6 for L1,M1,H1) multiplied by the number of independent realisations considered, which was one in all cases. In a turbulent flow, samples of these sizes can give an estimate for average quantities, however care must be exercised in the interpretation of data due to the high statistical uncertainty.

Conditional ensemble averages of a scalar ϕ may be estimated using the data where a z-line intersects with a mixture fraction iso-surface ($\eta = \xi$) giving, $\langle\phi|\eta\rangle_1(x, y)$, which is a function of x and y. Fifty levels were used for η between 0 and 0.1. Usually there is not enough data to populate all η space. Then alternatively, cross stream averaging and flame surface averaging have been employed. This ensures the stated conclusions are not functions of the averaging procedure. Since the estimated conditional averages are not necessarily smooth in either physical space or mixture fraction space, where possible, spatial derivatives are evaluated using the same discretisation as the original simulation prior to averaging. Where mixture fraction space derivatives are calculated, or for terms where it is not possible to take spatial derivatives prior to averaging (eg. term T_{pdf} in Eq. 4.4), the derivatives are based on a centred 7-point moving average of the quantity and evaluated using a scheme with second order accuracy.

A cross stream average is calculated by [69]

$$\langle\phi|\eta\rangle(y) = \frac{\int \langle\phi|\eta\rangle_1(x, y)\widetilde{P}(\eta, x, y)dx}{\int \widetilde{P}(\eta, x, y)dx} \tag{4.3}$$

The resulting cross-stream averaged CMC equation, for example the conditional

mass fraction, has a dependence in space only in the $y-$direction:

$$\frac{\partial Q}{\partial t} = \underbrace{-\langle v|\eta\rangle \frac{\partial Q}{\partial y}}_{T_{cv}} + \underbrace{\langle N|\eta\rangle \frac{\partial^2 Q}{\partial \eta^2}}_{T_m} + \underbrace{\rho_\eta \langle \dot{w}|\eta\rangle}_{T_c} - \underbrace{\frac{\partial}{\partial y}\langle v''Y''|\eta\rangle}_{T_{tf}} - \underbrace{\langle v''Y''|\eta\rangle \frac{\partial}{\partial y}\left[\ln \bar{\rho}\widetilde{P}(\eta)\right]}_{T_{pdf}} \tag{4.4}$$

A flame surface average consists of data along an iso-contour of unconditional mean temperature $\langle T\rangle(x,y)$. The averaging procedure for a $\langle T\rangle$ level denoted by τ is then

$$\langle \phi|\eta = \xi\rangle(\tau) = \frac{\int_x \int_y \langle \phi|\eta\rangle_1(x,y)\widetilde{P_F}(\eta,\tau,x,y).dy.dx}{\int_x \int_y \widetilde{P_F}(\eta,\tau,x,y).dy.dx} \tag{4.5}$$

where $\widetilde{P_F}(\eta,\tau,x,y)$ is the Favre probability density function for mixture fraction for the given value of τ, which is non-zero only where the condition $\langle T\rangle = \tau$ is realised.

For vector quantities, the component normal to the mean flame brush (ie. parallel to $\nabla\langle T\rangle$) has been evaluated. Taking averages at differing values of $\langle T\rangle$ permits the budget of CMC terms normal to the mean flame surface, as given for conditional species averages in Eq. 4.6, to be plotted through the turbulent flame brush. It should be noted that due to the spark energy the temperature exceeds the adiabatic flame temperature, therefore τ exceeds unity. Thirty levels were used for τ between 0 and 1.5.

$$\begin{aligned}\frac{\partial Q}{\partial t} = & - \underbrace{\langle u_n|\eta\rangle \frac{\partial Q}{\partial x_n}}_{T_{cv}} + \underbrace{\langle N|\eta\rangle \frac{\partial^2 Q}{\partial \eta^2}}_{T_m} \\ & + \underbrace{\rho_\eta \langle \dot{w}|\eta\rangle}_{T_c} - \underbrace{\frac{\partial}{\partial x_n}\langle u_n''Y''|\eta\rangle}_{T_{tf}} - \underbrace{\langle u_n''Y''|\eta\rangle \frac{\partial}{\partial x_n}\left[\ln \bar{\rho}\widetilde{P}(\eta)\right]}_{T_{pdf}}\end{aligned} \tag{4.6}$$

Second order closure

As noted in chapter 2, a second order closure, given by equation 4.7 may be appropriate in situations where the conditional mean reaction rate is not accurately modelled using the first order closure, in which 'F' is neglected. Both closures have been evaluated for the current DNS data. We use,

$$\langle \dot{w}|\eta\rangle = \dot{w}(\langle \mathbf{Y}|\eta\rangle, \langle T|\eta\rangle)\,[1+F] \tag{4.7}$$

where $\dot{w}(\langle \mathbf{Y}|\eta\rangle, \langle T|\eta\rangle)$ is the reaction rate evaluated using the conditionally averaged species mass fractions and the conditionally averaged temperature. For the present one step reaction model 'F' contains the covariances $\langle {Y_{Fu}}''{Y_{Ox}}''|\eta\rangle$, $\langle {Y_{Fu}}''T''|\eta\rangle$, $\langle {Y_{Ox}}''T''|\eta\rangle$, and $\langle {T''}^2|\eta\rangle$ which occur when the Taylor expansion, given in appendix A.2, for the mean reaction rate is truncated after the second order terms.

Conditional turbulent flux estimates

The conditional turbulent flux, measured from the DNS, may be compared with the conventional eddy diffusion model, Eq 4.2. There is currently no satisfactory model for the conditional turbulent flux which explicitly includes counter gradient transport effects. An estimate for this quantity is proposed here based on the reasoning of the Bray, Moss and Libby theory [14; 15; 79]. The estimate is evaluated from the DNS for comparison with the gradient diffusion model and the measured conditional turbulent flux.

The final expression, Eq. 4.10, is arrived at by considering a limiting case where fluid with differing mixture fractions do not interact. Additionally, the flame is considered to have negligible thickness such that the conditional joint progress variable-velocity PDF, $P(\mathbf{u}, c, \eta, \mathbf{x}, t)$ may be treated as bi-modal in progress variable space. Neither premise is expected to be accurate in the present non-premixed

simulations. The conditional Reynolds flux is then given by integrating the product of the conditional velocity and progress variable fluctuations, Eq. 4.8. Neglecting the conditional density fluctuations, and using ζ to refer to the sample space variable for the progress variable, results in Eq. 4.9. The conditional mean velocity jump across the flame is then modelled as the flame propagation velocity $S_E \underline{n_i}$ times $\tau(\eta) - 1$, where the heat release parameter $\tau(\eta) = \rho_u(\eta)/\rho_b(\eta)$.

$$\langle \rho u_i'' Y'' | \eta \rangle = \int_0^1 \int_{-\infty}^{\infty} \rho (u_i - \langle u_i | \eta \rangle)(c - \langle c | \eta \rangle) P(u_i, c, \eta, \mathbf{x}, t).du_i.dc \tag{4.8}$$

$$\rho_\eta \langle u_i'' Y'' | \eta \rangle = \rho_\eta \langle c | \eta \rangle (1 - \langle c | \eta \rangle)(\langle u_i | \eta = xi, \zeta = 1 \rangle - \langle u_i | \eta = xi, \zeta = 0 \rangle) \tag{4.9}$$

$$\langle u_i'' Y'' | \eta \rangle \approx -S_E \left[\frac{\rho_u(\eta)}{\rho_b(\eta)} - 1 \right] \langle c | \eta \rangle (1 - \langle c | \eta \rangle)(Y_b(\eta) - Y_u(\eta)).\underline{n_i}. \tag{4.10}$$

The edge flame speed, S_E, at which the flame front is expected to propagate relative to the flow is estimated as $\sqrt{\rho_u(\eta_{st})/\rho_b(\eta_{st})} S_L$ [24; 119]. The burned and unburned densities are taken as the lowest and highest realised values of conditional average density for each mixture fraction. $Y_b(\eta)$ and $Y_u(\eta)$ are found in the same way. $\underline{n_i}$ is a flame normal unit vector. The progress variable c is a function of mixture fraction, Eq. 4.11, so that it varies between zero and one at all values of η (except at $\eta = 0$ and $\eta = 1$ where it is undefined):

$$c = \frac{\xi Y_{F\infty} - Y_{Fu}}{\xi Y_{Fu\infty} - max[0, \frac{\xi - \xi_{st}}{1 - \xi_{st}}] Y_{Fu\infty}}. \tag{4.11}$$

Equation 4.10 constitutes a new model in the CMC method, adapted from the premixed flame literature. Its validity will be explored later in this chapter.

Conditional turbulent flux equation

In order to assist the interpretation of the results a transport equation for the conditional turbulent flux for a reacting scalar Y has been derived from the

decomposition method, appendix A.3, and the derivation confirmed from the PDF method [69]. Starting from the transport equations for u_i and Y, equations for $\rho_\eta\langle u_i|\eta\rangle$, $\rho_\eta\langle Y|\eta\rangle$, $\rho_\eta\langle u_i Y|\eta\rangle$, and $\rho_\eta\langle u_i|\eta\rangle\langle Y|\eta\rangle$ are derived. These are then used to give the transport equation for $\rho_\eta\langle u_i'' Y''|\eta\rangle$. The resulting equation becomes:

$$\begin{aligned}
&\frac{\partial}{\partial t}\left[\rho_\eta\langle u_i'' Y''|\eta\rangle\right] \underbrace{+\frac{\partial}{\partial x_j}\left[\rho_\eta\langle u_j|\eta\rangle\langle u_i'' Y''|\eta\rangle\right]}_{-T_A} = \underbrace{-\frac{\partial}{\partial x_j}\left[\rho_\eta\langle u_i'' u_j'' Y''|\eta\rangle\right]}_{T_T} \\
&\underbrace{-\rho_\eta\langle u_j'' Y''|\eta\rangle\frac{\partial\langle u_i|\eta\rangle}{\partial x_j}}_{T_U}\underbrace{-\rho_\eta\langle u_i'' u_j''|\eta\rangle\frac{\partial\langle Y|\eta\rangle}{\partial x_j}}_{T_\theta} \\
&\underbrace{-\langle Y''|\eta\rangle\frac{\partial\langle p|\eta\rangle}{\partial x_i}}_{T_\Pi}\underbrace{-\langle\frac{\partial p''}{\partial x_i}Y''|\eta\rangle}_{T_\pi}\underbrace{-\frac{\partial\langle p|\eta\rangle}{\partial\eta}\langle\frac{\partial\xi}{\partial x_i}Y''|\eta\rangle}_{T_P} \\
&\underbrace{+\langle Y''|\eta\rangle\langle\frac{\partial(\mu s_{ij}'')}{\partial x_j}|\eta\rangle}_{T_7}\underbrace{+\langle u_i''|\eta\rangle\langle\frac{\partial}{\partial x_j}(\rho D\frac{\partial Y''}{\partial x_j})|\eta\rangle}_{T_8}\underbrace{+\rho_\eta\langle\dot{w}'' u_i''|\eta\rangle}_{T_R} \\
&\underbrace{+\frac{\partial\langle u_i|\eta\rangle}{\partial\eta}\langle\frac{\partial}{\partial x_j}[(\mu-\rho D)\frac{\partial\xi}{\partial x_j}]Y''|\eta\rangle}_{T_{10}}\underbrace{+\langle\rho N Y''|\eta\rangle\frac{\partial^2\langle u_i|\eta\rangle}{\partial\eta^2}}_{T_{11}}\underbrace{+\langle\rho Sc N u_i''|\eta\rangle\frac{\partial^2\langle Y|\eta\rangle}{\partial\eta^2}}_{T_{12}}
\end{aligned} \tag{4.12}$$

with $s_{ij}'' = (\partial u_i''/\partial x_j + \partial u_j''/\partial x_i)$ and $Sc = \mu/(\rho D)$. There are two additional terms that have been neglected under a high Reynolds number assumption given by $e_1 = \langle\mu\frac{\partial\xi}{\partial x_j}.\frac{\partial}{\partial x_j}\left(\frac{\partial\langle u_i|\eta\rangle}{\partial\eta}\right)Y''|\eta\rangle$ and $e_2 = \langle\rho D\frac{\partial\xi}{\partial x_j}.\frac{\partial}{\partial x_j}\left(\frac{\partial\langle Y|\eta\rangle}{\partial\eta}\right)u_i''|\eta\rangle$. The physical interpretation of the various terms in Eq. (4.12) is as follows. The first and second terms on the l.h.s. signify unsteady accumulation and advection. The first term in the r.h.s. denotes turbulent transport of $\langle u_i'' Y''|\eta\rangle$ and the following two terms signify production/destruction of conditional flux due to conditional mean velocity and scalar gradients. The remainder of the r.h.s. contains contributions due

to the mean and fluctuating pressures, molecular diffusion, chemical reaction, and the correlations between the velocity and scalar and the scalar dissipation N. It is instructive to compare Eq. (4.12) with the more familiar unconditional scalar flux $\langle \rho u_i' Y' \rangle$ transport equation (e.g. [81; 143]). That equation contains terms of similar nature and structure, but lacks the η-space derivatives that are present in Eq. (4.12). The magnitude of the various terms in the conditional scalar flux equation has been measured from the DNS data and is presented later.

4.3 Results and discussion

4.3.1 Flow patterns

Assuming that the mixture fraction obeys a gradient diffusion process, an effective diffusivity D_t has been calculated from the evolution of the $\langle \rho \xi \rangle$ profile in the x-direction (averaging being performed over $y-z$ planes) by measuring $\langle \rho v' \xi' \rangle$ and dividing by $-\partial \langle \rho \xi \rangle / \partial x$. This always gave a positive number that changed very little in time and space. In a calculation, this eddy diffusivity would be used in Eq. (4.2) and hence we can now test the gradient diffusion model. Some details on the flame patterns examined are given next.

Figure 4.2 shows that the thin spark cylinder creates a broadly cylindrical flame that expands in the x and y directions and gets distorted by the turbulence. High temperature zones at fuel rich ($\xi > \xi_{st}$) and lean ($\xi < \xi_{st}$) locations in Fig. 4.2b correspond to rich and lean premixed flames respectively whereas the high temperature zone on the ξ_{st} iso-surface originates due to a diffusion flame. More details on flame structure can be found elsewhere [24]. The flame expands in the y-direction along the ξ_{st} iso-surface, while it expands in the x-direction across mixture fraction contours.

Figure 4.3a and 4.3b show the measured unconditional turbulent flux and the

one estimated from the gradient diffusion hypothesis. The data are for $u'/S_L = 4$. It is clear that some evidence of counter-gradient diffusion is visible at a few locations. This is not the case for $u'/S_L = 12$, where $\langle \rho v' T' \rangle$ and $-D_t \partial \langle \rho T \rangle / \partial y$ always have the same sign (not shown). The fact that counter-gradient diffusion is evident at weak turbulence but not at high u'/S_L has been thoroughly analysed in the context of premixed flames (e.g. [40]) and the present data suggest that the same mechanisms may also apply in the context of partially-premixed and edge flames.

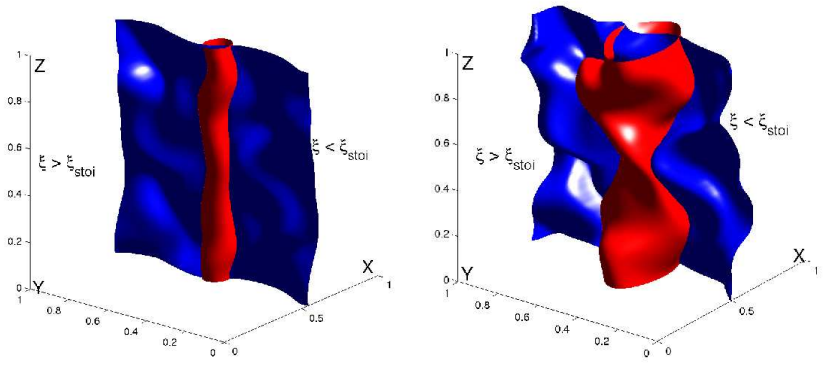

(a) $t = 0.0525 t_{sp}$ (b) $t = 2.1 t_{sp}$

Figure 4.2: The stoichiometric iso-surface (blue) and the iso-surface of $T = 0.5$ (red) for $u'/S_L = 4$.

4.3.2 CMC equation analysis

The pressure increases at the centre of the spark as a result of the sudden increase in temperature, Fig. 4.4. The pressure decreases from the hot region in the centre of the domain, with the pressure gradient becoming smaller with time (Fig. 4.4b). The pressure gradient in η space in the present case is found to be negligible compared to the pressure gradient in physical space.

The situation studied here is statistically unsteady and hence the sums of the

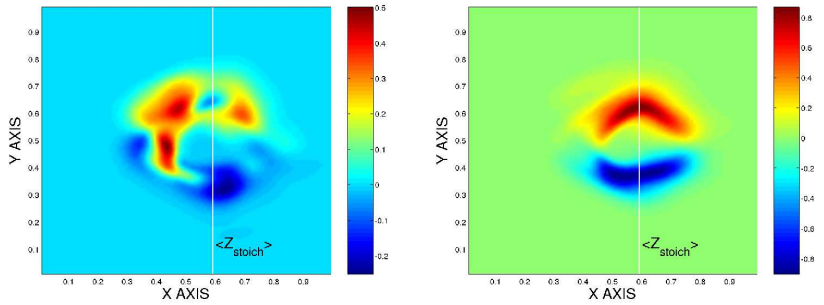

(a) $\langle \rho v' T' \rangle$ (b) $-D_t \partial \langle \rho T \rangle / \partial y$

Figure 4.3: Contours of unconditional flux in the y-direction and of the usual gradient model at $t = 2.1 t_{sp}$ and for $u'/S_L = 4$.

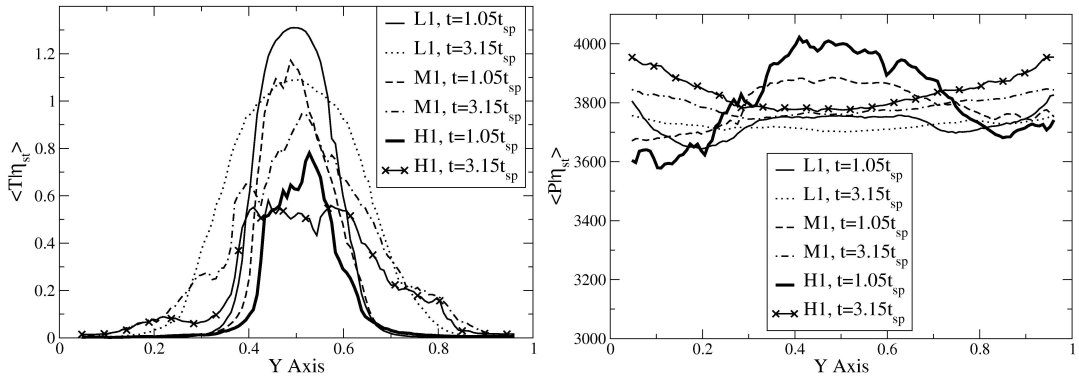

(a) $\langle T | \eta = \xi_{st} \rangle$ (b) $\langle P | \eta = \xi_{st} \rangle$

Figure 4.4: Distributions in the y-direction of the cross stream averaged conditional pressure and temperature at $\eta = \xi_{st}$ and the indicated times.

terms in the r.h.s. of Eqs. (4.4) and (4.6) are not zero. The cross stream averaged terms in the CMC temperature (T) equation are shown in the y-direction for $\eta = \xi_{st}$ in Fig. 4.5, and across mixture fraction space at positions in the flame front defined by $\langle T|\eta_{st}\rangle$ and $y > 0.5$ in Fig. 4.6. The lack of complete symmetry around $y = 0.5$ is due to the limited sample size. Three runs are shown, L1, M1 and H1, at two time instants, $t = 1.05t_{sp}$ and $t = 3.15t_{sp}$. Figure 4.7 displays the flame surface averaged CMC terms for the same runs and times.

Spatial transport of conditional temperature is due to convection, T_{cv}, turbulent flux, T_{tf}, and the PDF diffusion term, T_{pdf}. Figures 4.5, 4.6 and 4.7 confirm previous observations [33] that the PDF term T_{pdf} plays a minor role in the balance of terms.

Since there is no mean flow through the domain, the conditional mean velocity responsible for the convection results from the thermal expansion of the kernel. The initial rapid expansion due to the spark energy source and ignition results in a humped pressure profile at $t = 1.05t_{sp}$ and an outflow. However the volumetric release rate due to the ongoing combustion does not accelerate sufficiently fast and the pressure profile inverts by $t = 3.15t_{sp}$, causing flow to accelerate back toward the kernel, Fig. 4.4b. This can be seen in Fig. 4.5 where the convection term at $t = 1.05t_{sp}$ predominantly moves heat into the unreacted gas. However it also acts to cool the hot side of the flame front, particularly at later times, Figs. 4.5b,d,f, and this is seen at all times from the flame surface averaged plots 4.7. This results from mean flow toward the centre of the flame kernel at these locations. Particularly in the low turbulence case, L1, the cooling effect of the convection term increases consistently through the flame (increasing $\langle T\rangle$). This may be explained by considering the acceleration due to the cumulative volume release rate through the flame. It is interesting to note that while the chemical heat release, $\frac{\partial T}{\partial t}$, is expected to peak close to $\langle T\rangle = 0.85$, the volume release rate is dependent on $\frac{1}{T}\frac{\partial T}{\partial t}$ and consequently peaks closer to the cold side of the flame.

The turbulent flux term has a mixed role in the evolution of the flame kernel, in some cases it appears to act 'diffusively', moving heat from the centre of the kernel to the cold side of the flame front, this is most clearly seen for the $u'/S_L = 12$ case in Fig. 4.5e. In other cases, local counter gradient transport occurs with heat being moved against the mean conditional temperature gradient as seen for the $u'/S_L = 4$ case in Fig. 4.7a. It is notable that the flame surface averaged data exhibits a larger degree of counter gradient transport. This may be due to the cross stream averages including fluid of a particular mixture fraction and y-location that is not within the flame front and hence not subject to pressure gradients, which would encourage counter gradient transport. The nature of the conditional turbulent flux is discussed in further detail in section 4.3.4.

The chemical heat release, T_c, is always positive by definition. For the low turbulence case shown in Fig. 4.5a and b, distinct flame fronts may be seen. However the kernel has not reached sufficient size by $t = 3.15t_{sp}$ for the centre of the kernel to be in steady state, which would be indicated by a horizontal, non-zero, heat release profile. The role of the scalar dissipation or micromixing term, T_m, is generally to redistribute heat from the mixture fractions around stoichiometric with high heat release into cooler mixtures, as seen in Fig. 4.6. Consequently in Fig. 4.5 it tends to oppose the stoichiometric heat release.

It is evident that a complex spatial structure emerges in turbulent non-premixed edge flame propagation. In order to successfully capture these phenomena, the conditional velocity and conditional flux terms must be adequately modelled, in addition to the mean reaction rate. Various models for $\langle u_i|\eta\rangle$ have already been tested [129] and hence we focus next on an evaluation of the modelling of the conditional reaction rate and of the turbulent flux model, section 4.3.4.

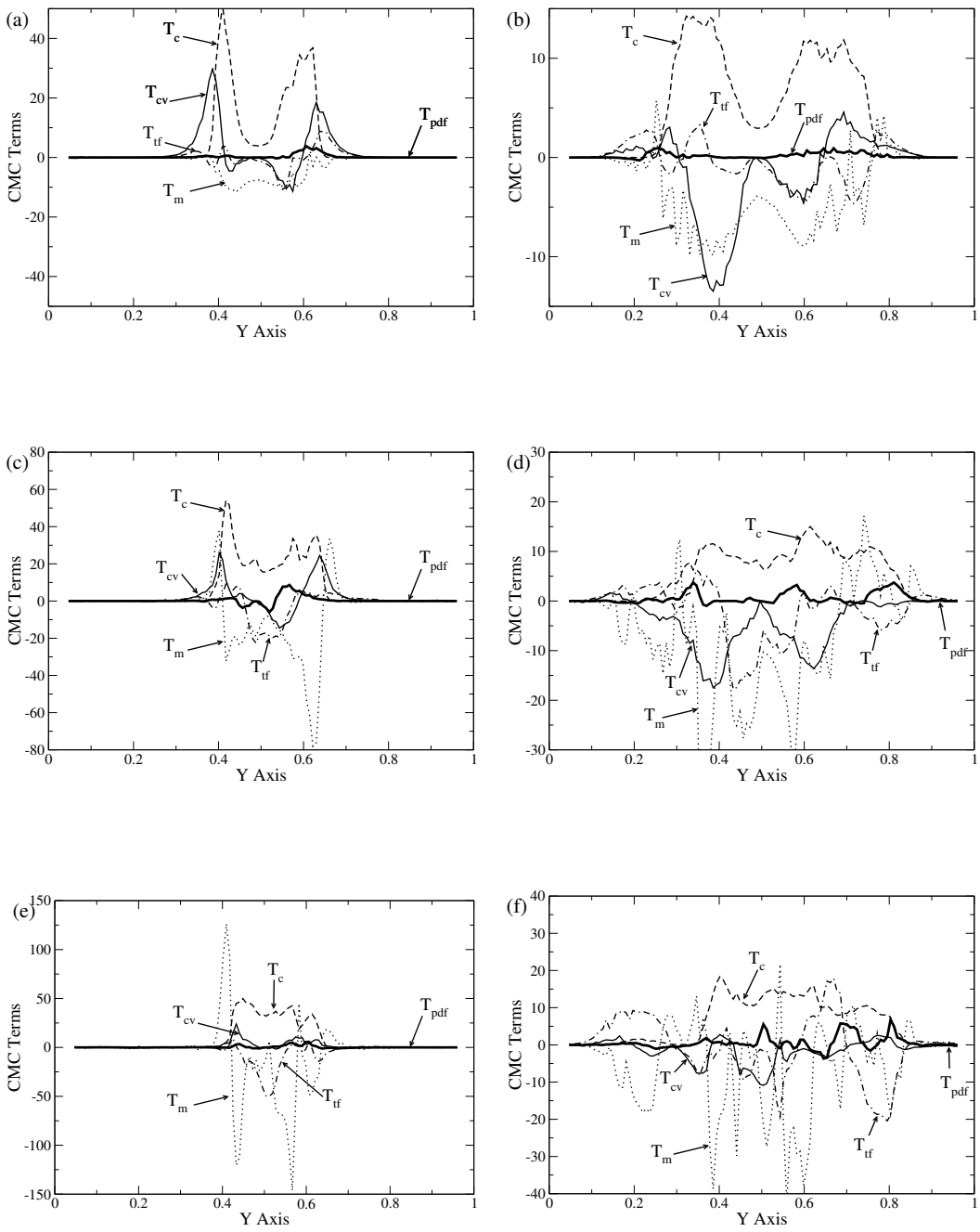

Figure 4.5: The spatial distribution of the various source terms in the CMC equation at $\eta = \xi_{st}$. (a): Run L1, $t = 1.05t_{sp}$; (b): Run L1, $t = 3.15t_{sp}$; (c): Run M1, $t = 1.05t_{sp}$; (d): Run M1, $t = 3.15t_{sp}$; (e): Run H1, $t = 1.05t_{sp}$; (f) Run H1, $t = 3.15t_{sp}$.

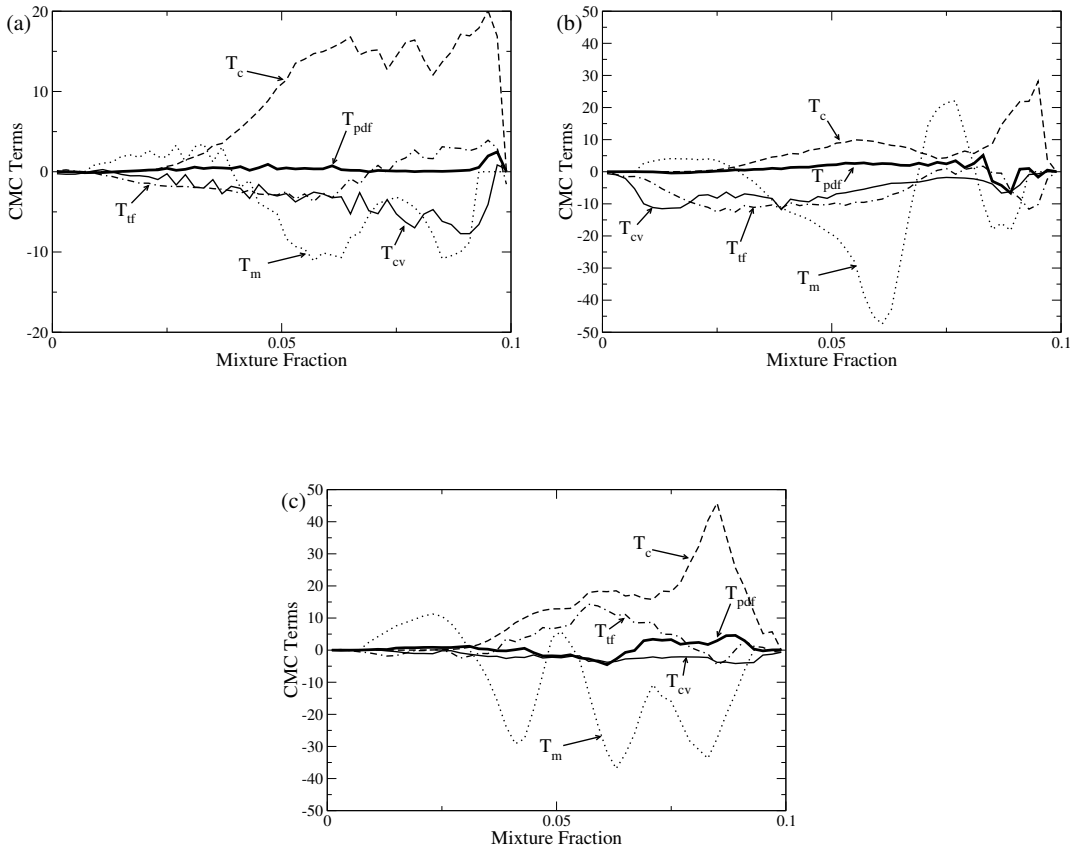

Figure 4.6: The budget for the CMC equation across mixture fraction. (a): Run L1, $t = 3.15t_{sp}$, at $\langle T|\eta_{st}\rangle = 0.85$; (b): Run M1, $t = 3.15t_{sp}$, $\langle T|\eta_{st}\rangle = 0.85$; (c): Run H1, $t = 3.15t_{sp}$, $\langle T|\eta_{st}\rangle = 0.5$.

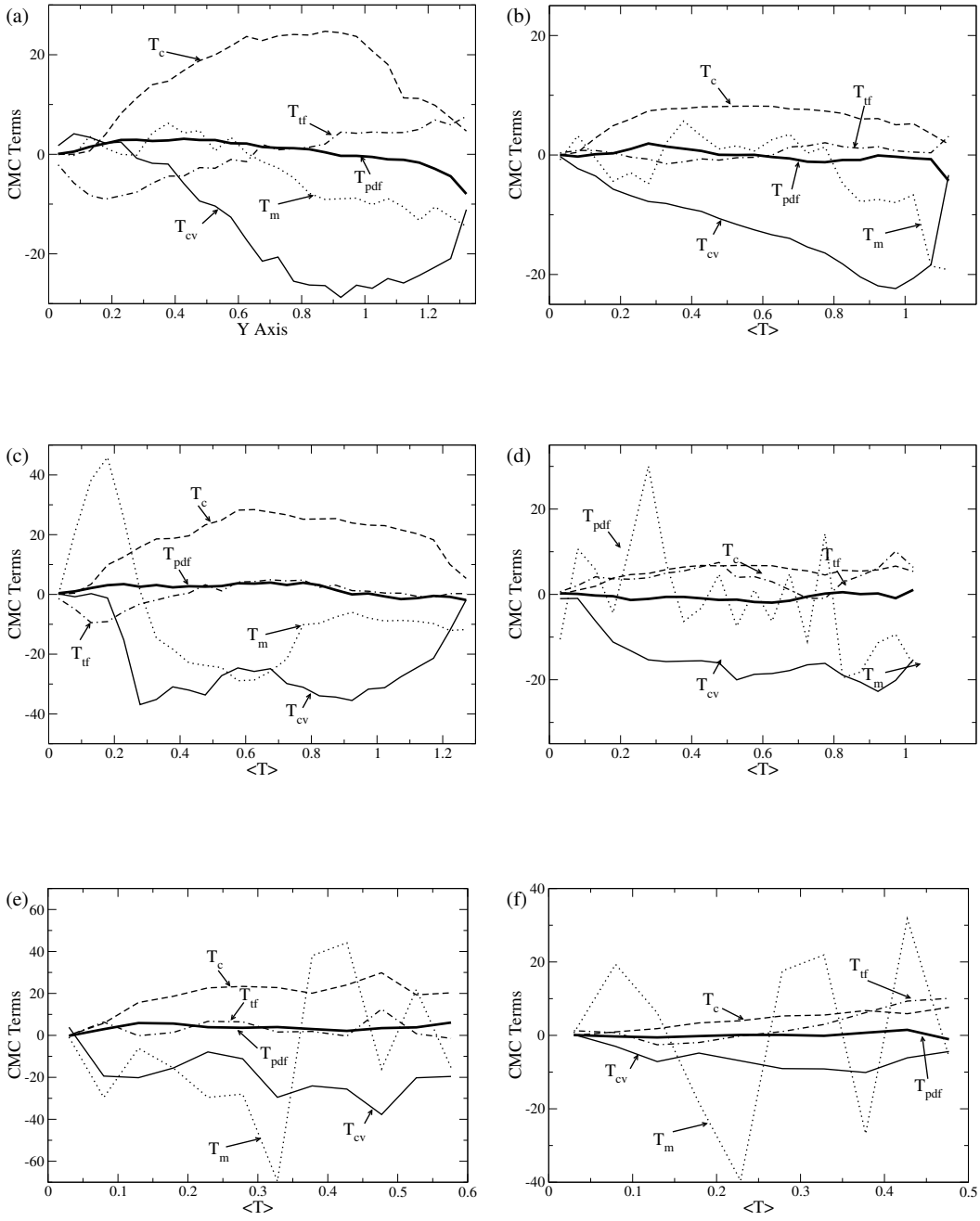

Figure 4.7: The CMC equation terms normal to the flame surface, Eq 4.6 at $\eta = \xi_{st}$. (a): Run L1, $t = 1.05t_{sp}$; (b): Run L1, $t = 3.15t_{sp}$; (c): Run M1, $t = 1.05t_{sp}$; (d): Run M1, $t = 3.15t_{sp}$; (e): Run H1, $t = 1.05t_{sp}$; (f) Run H1, $t = 3.15t_{sp}$.

4.3.3 Reaction rate closure

It is interesting to assess the accuracy of the first-order CMC model for this problem because most elliptic CMC calculations have been performed to this level. Figure 4.8 compares the first and second-order CMC models with the chemical heat release measured from the DNS. It is evident that the first-order closure gives a large error in the reaction rate compared to $\rho_\eta \langle \dot{w} | \eta \rangle$. The error is particularly large in the flame fronts where the conditional temperature fluctuations are high, as indicated by the wide scatter in recorded temperatures across mixture fraction space, Fig. 4.9. The fluctuations around the mean are sufficiently large that correction at only the second order level, [21; 63] appendix A.2, makes matters worse. Given the modelling difficulties in solving high order conditional moment closures this discrepancy suggests that double-conditioning may be necessary for this problem [69; 73].

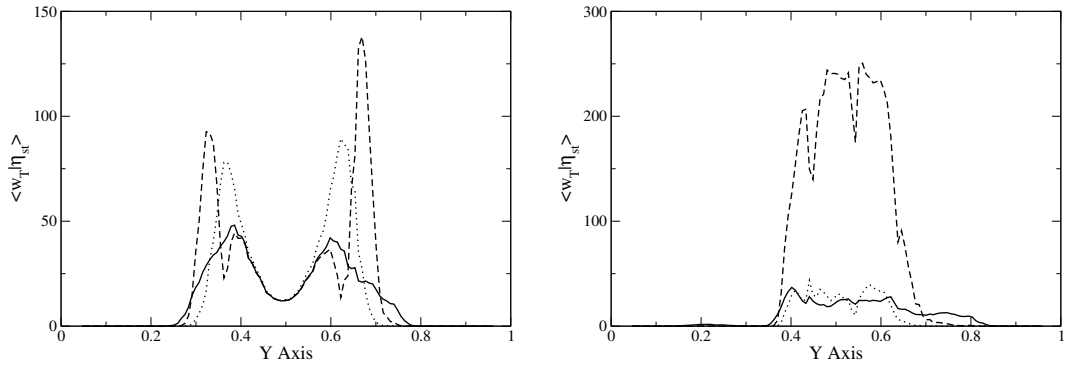

(a) (b)

Figure 4.8: Conditional chemical source term for temperature as measured from the DNS (solid), from the first order closure (dots), and from the second order closure (dashed). (a): Run L1, $t = 3.15 t_{sp}$; (b): Run H1, $t = 3.15 t_{sp}$.

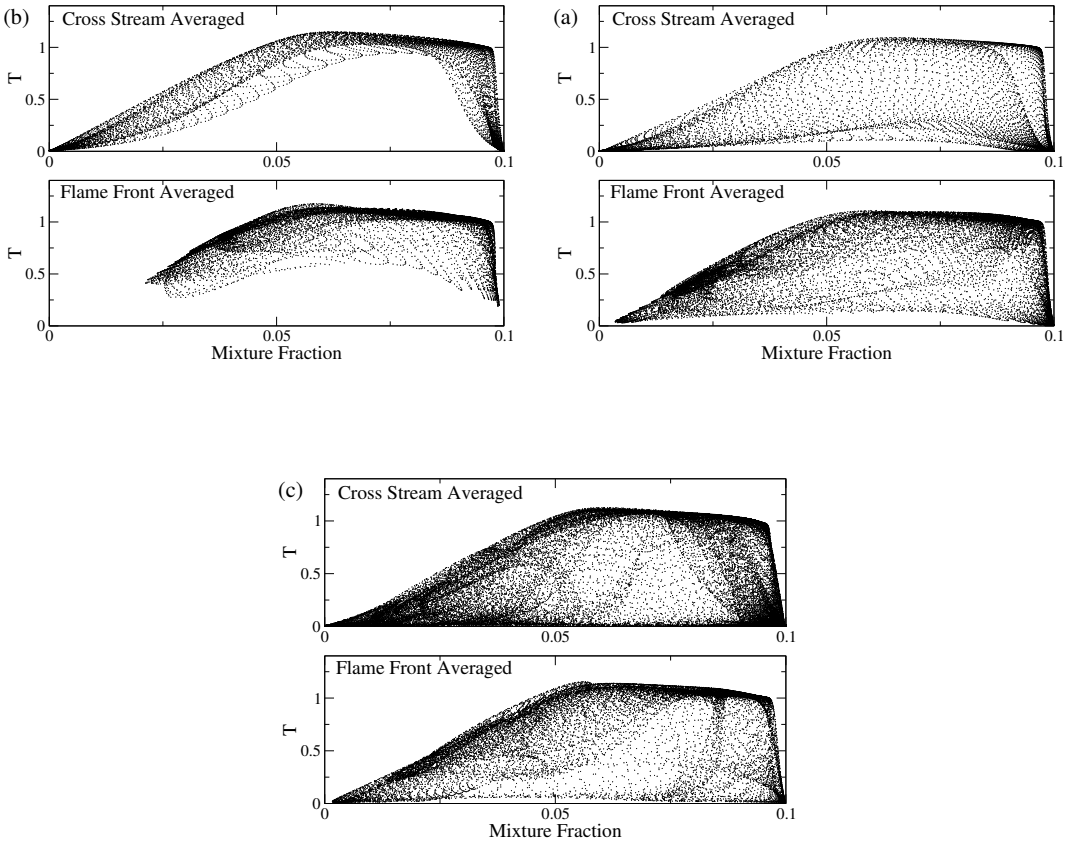

Figure 4.9: Temperature scatter plots for the samples used for cross stream averaging where $\langle T|\eta_{st}\rangle = T_{sample}$ and for flame front averaging where $\langle T\rangle = T_{sample}$. (a): Run L1, $t = 3.15t_{sp}$, $T_{sample} = 0.85$; (b): Run L1, $t = 3.15t_{sp}$, $T_{sample} = 0.5$; (c): Run H1, $t = 3.15t_{sp}$, $T_{sample} = 0.5$.

4.3.4 Conditional fluxes

Figure 4.10 shows a comparison between $\langle v''T''|\eta_{st}\rangle$, the gradient model $-D_t d\langle T|\eta_{st}\rangle/dy$ and the counter gradient flux estimate (section 4.2.2), cross stream averaged as a function of y. The prescribed initial profiles of mixture fraction and the spark energy source definition mean that it takes some time for the scalar mixing profiles to become turbulent and it may take longer than $t = 1.05t_{sp}$ for representative temperature fluxes to develop, particularly in the $u'/S_L = 4$ cases. At later times the cross stream averaged conditional turbulent flux appears predominantly gradient in nature. However the flux tends to be weaker than that predicted by the gradient diffusion model, and in some cases has the opposite sign, indicating a tendency for counter gradient transport to occur.

When the cross stream averaged data is viewed across mixture fraction space, as in Fig. 4.11, the interpretation is made difficult since differing mixture fractions may tend to be further inside or outside of the kernel. The conditional flux quantities are plotted at positions where the stoichiometric temperature equals 0.85, which is indicative of the position of maximum heat release, and the plots are nearly identical if the location of minimum $\frac{\partial\langle T|\eta_{st}\rangle}{\partial y}$ is used. $\langle T|\eta_{st}\rangle = 0.5$ was used for run H1 since $\langle T|\eta_{st}\rangle = 0.85$ was not realised in this case. Since the flame is expected to propagate fastest around the stoichiometric mixture fraction, lean and very rich mixture fractions will tend to be further toward the colder side of the flame for a the given y-location. The measured flux is generally gradient in nature, except in the low turbulence case, L1, where the flux falls close to zero at mixture fractions on the rich side of stoichiometry. This contrasts with the higher turbulence cases where the flux acts in a gradient sense across all mixture fractions. Note that the present observation that $u'/S_L = 4$ shows counter-gradient diffusion, but $u'/S_L = 12$ does not, is quantitatively consistent with the premixed flame data of Ref. [40] that give the same behaviour at $u'/S_L = 3.6$, but a gradient flux at $u'/S_L = 8.8$. We may conjecture that the turbulent edge non-premixed flame propagation involves

qualitatively similar dependencies of the fluxes to the better-known fully premixed flames.

The flame surface averaged data, Fig. 4.12, shows a variation in the type of turbulent flux through the flame brush, with diffusive fluxes occurring at low $\langle T \rangle$ and counter gradient fluxes occurring at higher $\langle T \rangle$ for all turbulence levels.

Conditional turbulent flux equation analysis

The major terms in the conditional flux equation, Eq. (4.12) for the temperature, are shown in Fig. 4.13 for L1, Fig. 4.14 for M1, and in Fig. 4.15 for H1. The way these plots have been made, together with the conditional mean temperature profile in Fig. 4.4, imply that a negative (positive) contribution in the region $\partial\langle T|\eta\rangle/\partial y > 0$ and a positive (negative) contribution in $\partial\langle T|\eta\rangle/\partial y < 0$ suggest gradient (counter-gradient) transport.

Sub-figures 'a' and 'b' contain the main source/sink terms which are the mean and fluctuating pressure terms ($T_\Pi = -\langle T''|\eta\rangle\partial\langle p|\eta\rangle/\partial y$ and $T_\pi = -\langle(T''\partial p''/\partial y)|\eta\rangle$ respectively), the conditional temperature and velocity gradient terms ($T_\theta = -\langle v''v''|\eta\rangle\partial\langle T|\eta\rangle/\partial y$) and $T_U = -\langle v''T''|\eta\rangle\partial\langle v|\eta\rangle/\partial y$ respectively), and the chemistry-velocity correlation ($\langle \dot{w}''u_i''|\eta\rangle$). Of these terms the fluctuating pressure, the conditional temperature gradient and the chemistry - velocity correlation are consistently the largest. By definition, the conditional temperature gradient term always promotes gradient diffusion. The pressure fluctuation term appears to be most responsible for the production of counter gradient fluxes, with the reaction-velocity correlation term having a mixed role promoting gradient diffusion at the cold edge of the flame front and counter gradient transport toward the inside of the kernel.

Sub-figures 'c' and 'd' contain the rate of change of conditional temperature flux due to advection ($T_A = \frac{\partial}{\partial y}\left[\rho_\eta\langle v|\eta\rangle\langle v''T''|\eta\rangle\right]$) and due to turbulent transport ($T_T = \frac{\partial}{\partial y}\left[\rho_\eta\langle v''v''T''|\eta\rangle\right]$). The advection term is relatively small. The triple correla-

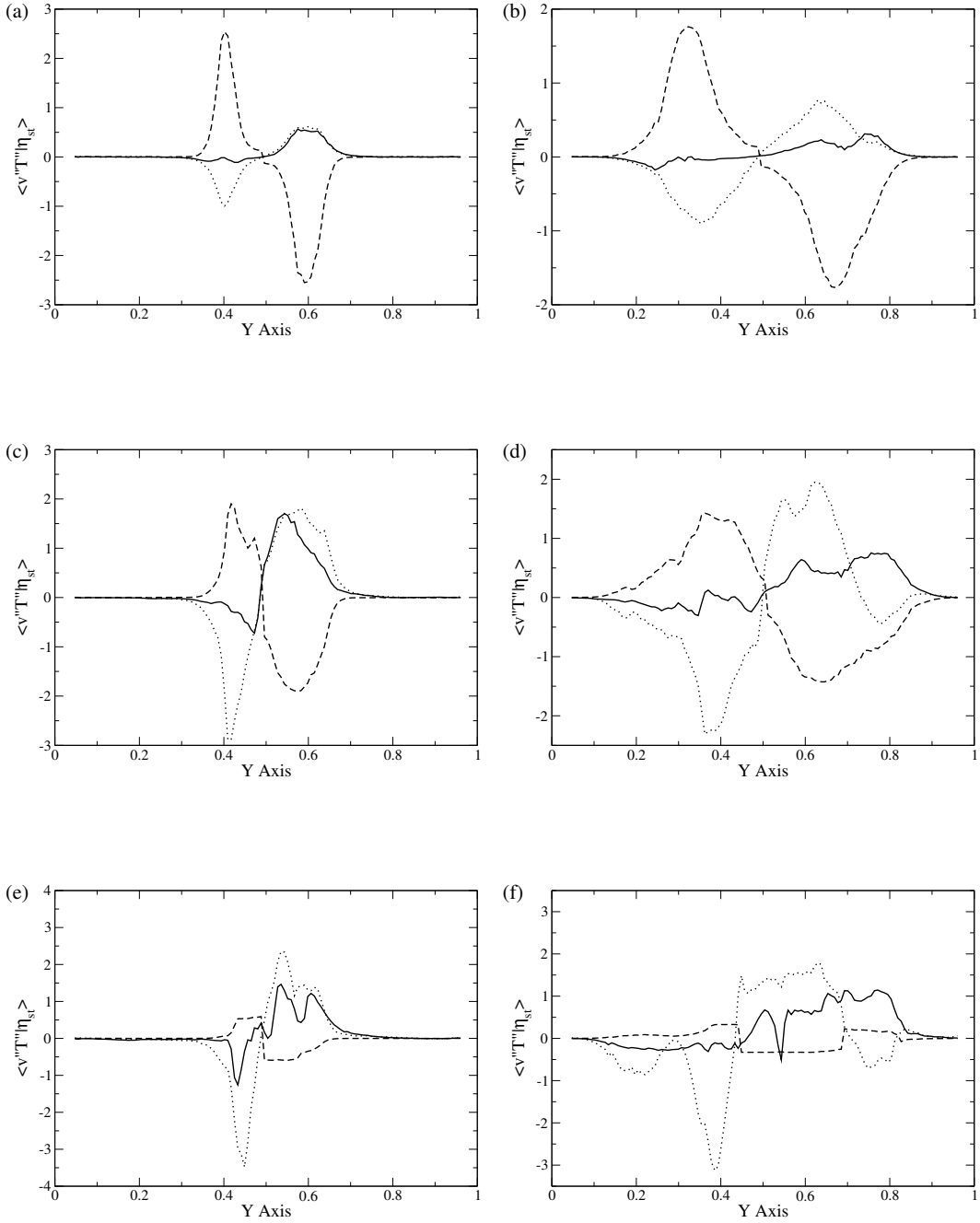

Figure 4.10: The spatial dependence of the stoichiometric conditional turbulent temperature flux (solid), the gradient diffusion model (dotted) and the counter gradient flux estimate from section 4.2.2 (dashed), using cross stream averages. (a): Run L1, $t = 1.05t_{sp}$; (b): Run L1, $t = 3.15t_{sp}$; (c): Run M1, $t = 1.05t_{sp}$; (d): Run M1, $t = 315t_{sp}$; (e): Run H1, $t = 1.05t_{sp}$; (f) Run H1, $t = 3.15t_{sp}$.

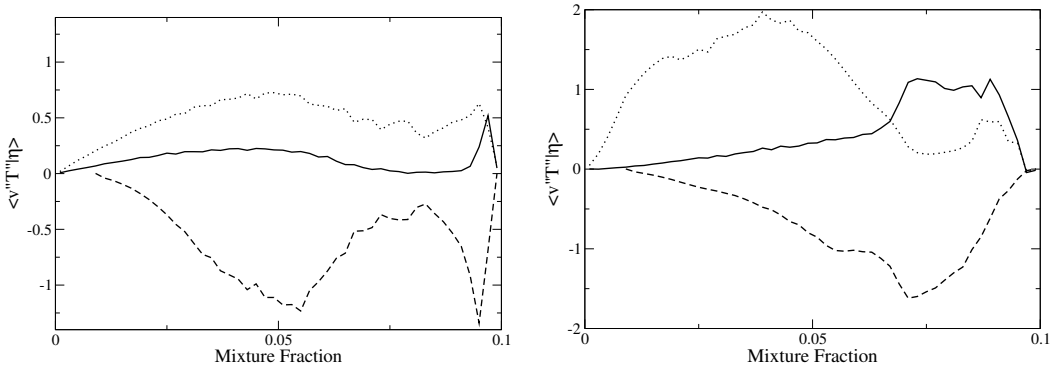

(a) (b)

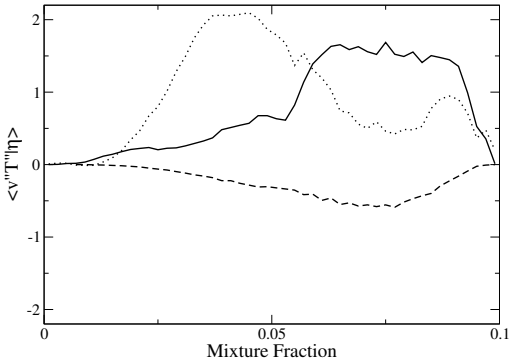

(c)

Figure 4.11: The cross stream averaged conditional turbulent temperature flux plotted versus mixture fraction at $\langle T|\eta_{st}\rangle = T_{sample}$. (a): Run L1, $t = 3.15t_{sp}$, $T_{sample} = 0.85$; (b): Run M1, $t = 3.15t_{sp}$, $T_{sample} = 0.85$; (c): Run H1, $t = 3.15t_{sp}$, $T_{sample} = 0.5$. Key as in Fig. 4.10.

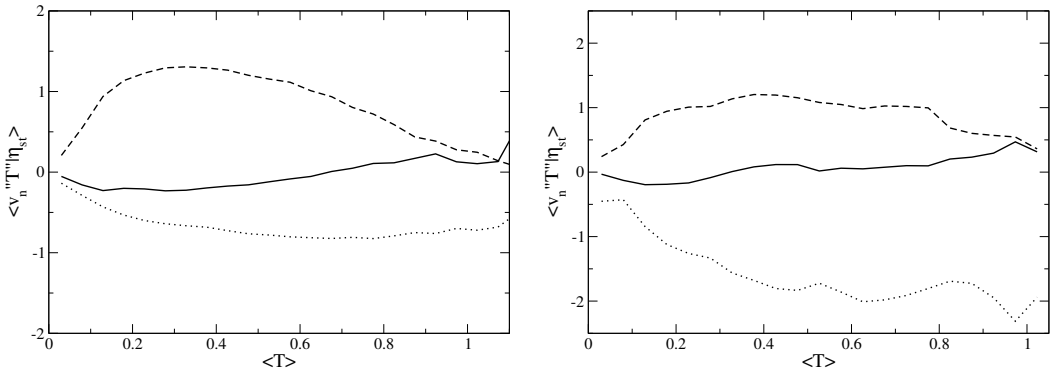

(a) (b)

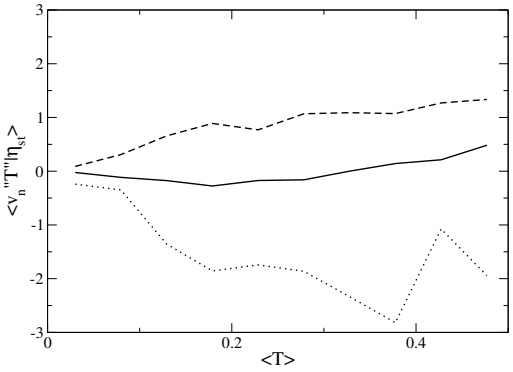

(c)

Figure 4.12: The turbulent temperature flux normal to the mean flame surface conditioned on stoichiometry and averaged over iso-surfaces of $\langle T \rangle$. (a): Run L1, $t = 3.15 t_{sp}$; (b): Run M1, $t = 3.15 t_{sp}$; (c): Run H1, $t = 3.15 t_{sp}$. Key as in Fig. 4.10.

tion turbulent transport term has a larger magnitude although its evaluation appears to be subject to considerable statistical noise. These terms act to redistribute the conditional turbulent flux; however, since they do not generate turbulent flux they are not expected to change the nature of the turbulent flux, say between gradient or counter-gradient.

Sub-figures 'e' and 'f' contain the additional terms due to the mixture fraction space pressure gradient (T_P), due to molecular viscosity and diffusion (T_7 and T_8 respectively), and molecular transport due to mean velocity and temperature profiles across mixture fraction space (T_{10}, T_{11}, and T_{12}). Among these terms, T_7, T_8 and T_{10} typically play a very small role in the balance of terms. The remaining terms, T_P, T_{11} and T_{12} are significant and act to redistribute the turbulent flux across mixture fraction space. However there is currently insufficient data with which to enter into a discussion of conditional temperature-mixture fraction gradient, scalar dissipation-temperature and scalar dissipation-velocity correlations which these terms involve.

In general, the reasons for the presence of counter-gradient diffusion in Fig. 4.12 revealed by Figs. 4.13-4.15 appear similar to those in fully premixed flames [142; 143]. In Ref. [143], the parameter $\tau S_L/u'$ was used qualitatively to distinguish between counter-gradient ($\tau S_L/u' \gg 1$) and gradient ($\tau S_L/u' \ll 1$) transport, where τ is equal to $\rho_u/\rho_b - 1$. In the low turbulence flame $\tau S_L/u'$ is nominally 0.75, but in reality it is higher because the spark energy increases the burning velocity and u' decays at the flame front. At stoichiometry, this parameter is much smaller than unity in the high turbulence case. Hence the present non-premixed edge flame data are qualitatively consistent with the expectations from premixed flames.

4.4 Conclusions

Direct Numerical Simulations of an igniting non-premixed flame are analysed to assess the accuracy of the gradient diffusion model for the conditional turbulent

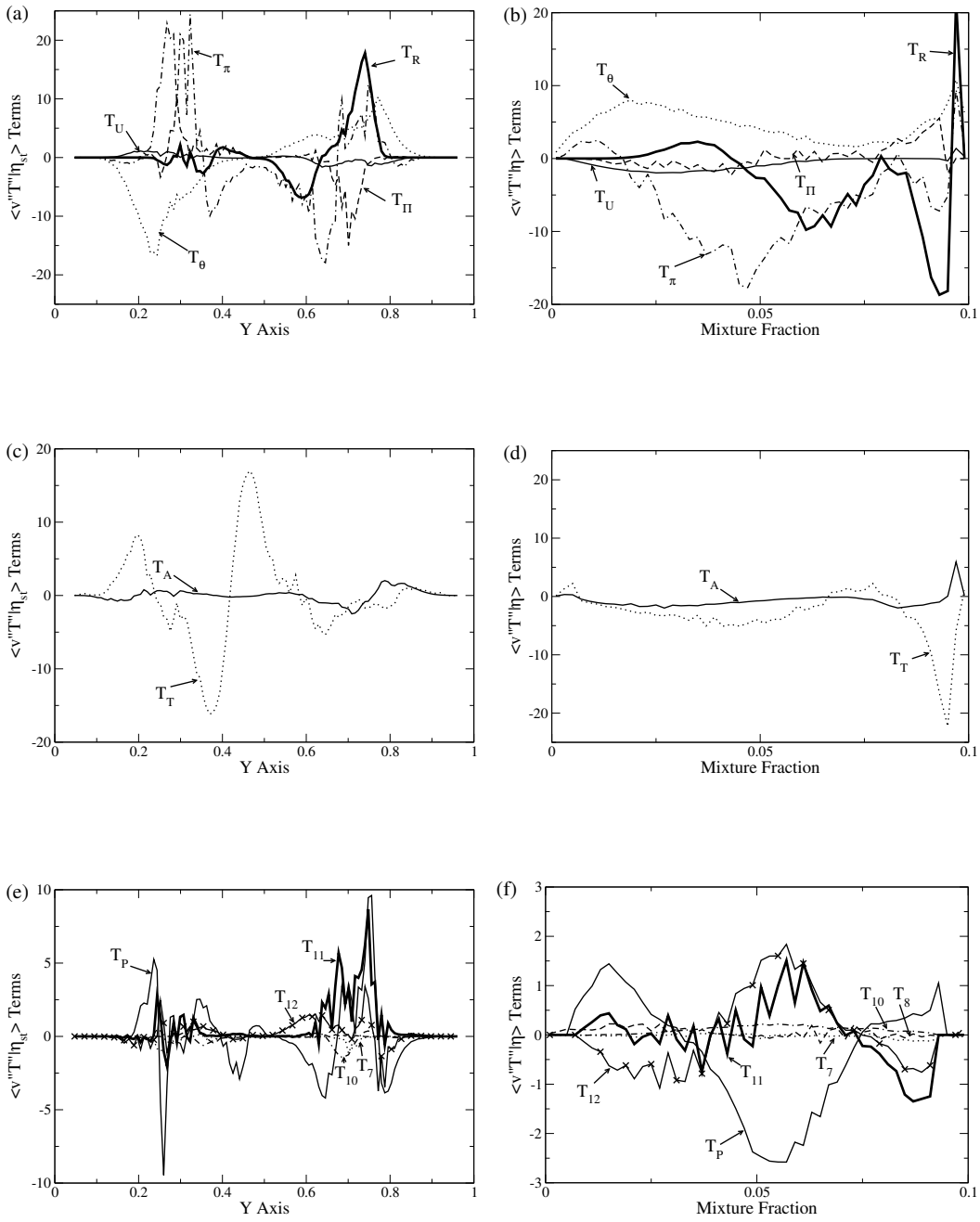

Figure 4.13: The terms of the conditional turbulent flux Eq. 4.12 for Run L1 at $t = 3.15t_{sp}$ using cross stream averages. Spatial plots are conditioned on stoichiometry, mixture fraction plots are stationed at $\langle T|\eta\rangle = 0.85$. (a) and (b): The main source/sink terms; (c) and (d): The main transport terms conditioned on stoichiometry; (e) and (f): The minor terms.

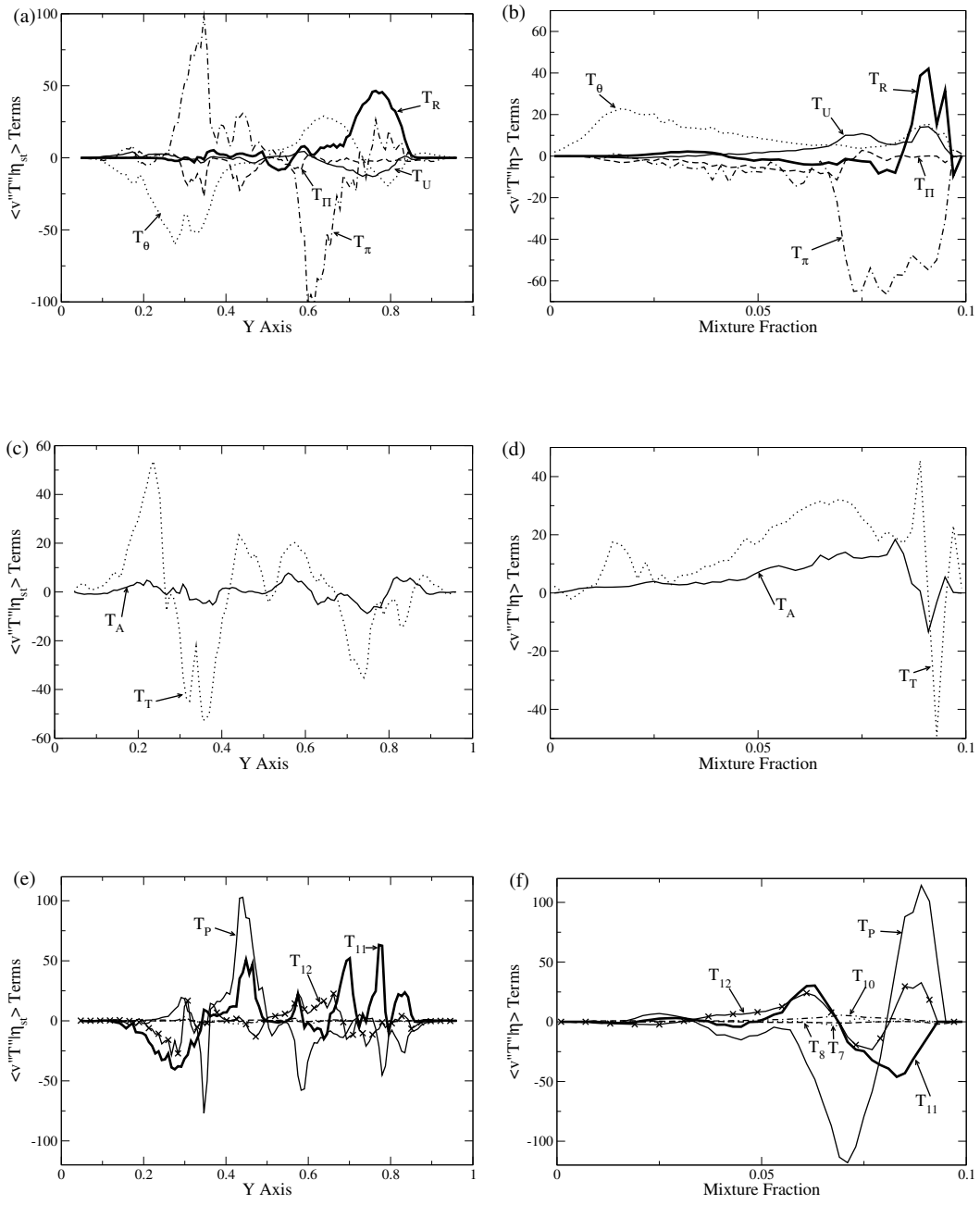

Figure 4.14: The terms of the conditional turbulent flux Eq. 4.12 for Run M1 at $t = 3.15t_{sp}$ using cross stream averages. Spatial plots are conditioned on stoichiometry, mixture fraction plots are stationed at $\langle T|\eta\rangle = 0.85$. (a) and (b): The main source/sink terms; (c) and (d): The main transport terms conditioned on stoichiometry; (e) and (f): The minor terms.

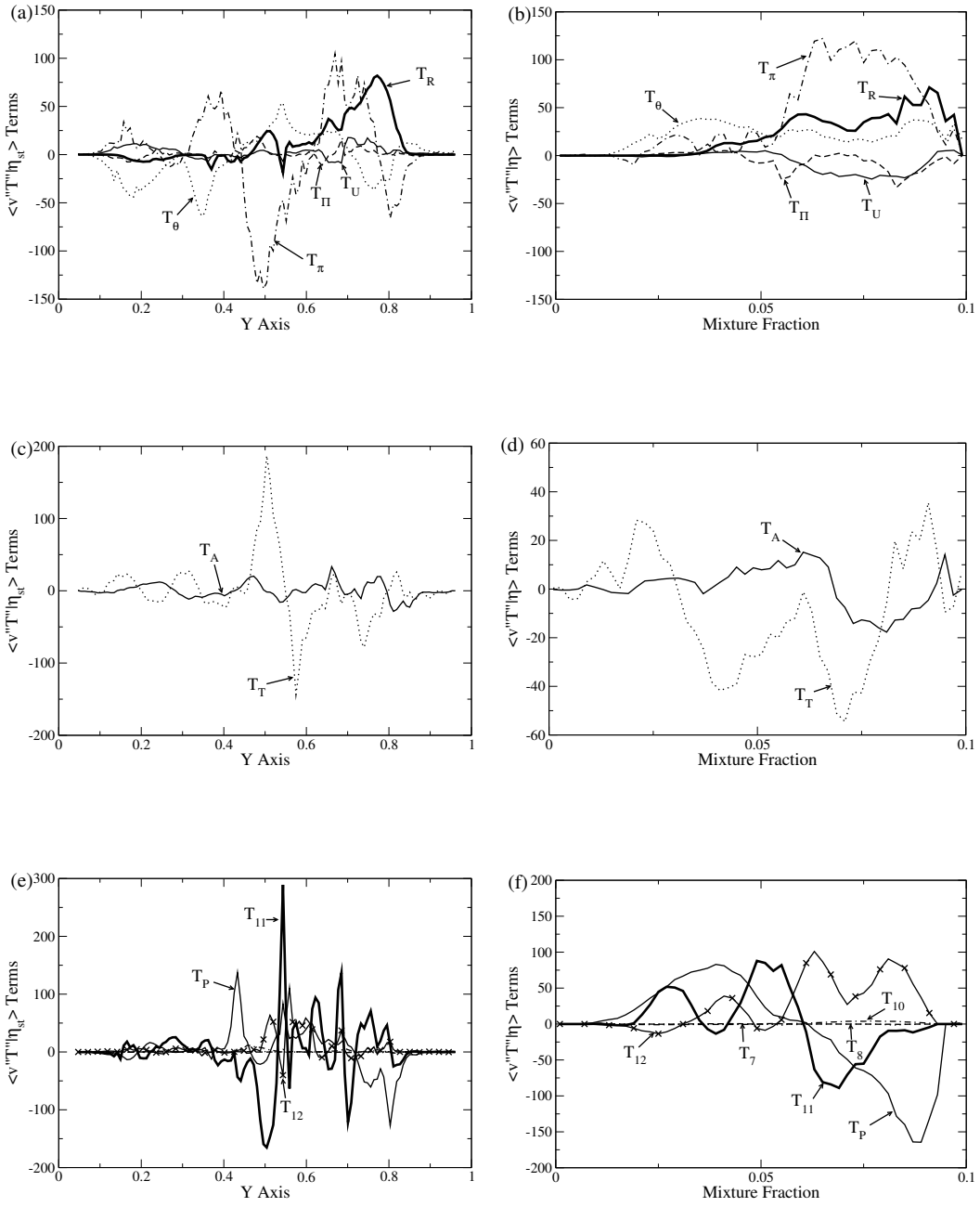

Figure 4.15: The terms of the conditional turbulent flux Eq. 4.12 for Run H1 at $t = 3.15t_{sp}$ using cross stream averages. Spatial plots are conditioned on stoichiometry, mixture fraction plots are stationed at $\langle T|\eta\rangle = 0.50$. (a) and (b): The main source/sink terms; (c) and (d): The main transport terms conditioned on stoichiometry; (e) and (f): The minor terms.

flux term in the CMC equation, and the accuracy of the first and second order reaction rate closures. The results show that due to large conditional fluctuations, neither the first nor second-order models for the conditionally-averaged reaction rate are accurate at the edge flame, indicating that alternative closures may be required. The edge flame structure involves a balance between chemistry, molecular mixing, and spatial transport, which implies that modelling the conditional convection and diffusion are important for capturing flame establishment following ignition, e.g. in diesel engines or gas turbines. The usual gradient diffusion approximation for the conditional turbulent flux seems to be adequate for high turbulence intensity relative to the laminar burning velocity of a stoichiometric mixture, but there is evidence of counter-gradient transport effects, particularly at weak turbulence. An analysis of the major terms in the conditional scalar flux equation shows that the pressure fluctuation is mainly responsible for counter-gradient transport.

Chapter 5

Modelling for ignition of a lifted methane jet flame

This chapter presents the application of the Conditional Moment Closure model to the ignition of a turbulent methane jet and the subsequent stabilisation of a lifted flame. Following an introduction to the relevant theory and literature, the details of the CMC implementation are set out. An analysis of the CMC equation is performed for the spark ignition event, during flame propagation along the jet and also once stabilisation has taken place. Particular emphasis is placed on the role of mean dilatation on the solution since this has not previously been assessed in lifted jet CMC simulations. The ability of the CMC to describe the physics which limit spark ignition and which are involved in partially premixed flame propagation is discussed. The new model to incorporate counter gradient transport effects into the CMC modelling presented in chapter 4 is implemented and its effect on the simulation is demonstrated.

5.1 Background

5.1.1 The turbulent jet

The round turbulent jet is a very well studied free shear flow. Apart from the exact details of the velocity profile at the nozzle, constant density flows are governed by just one dimensionless group $Re_j = W_j D_j/\nu$, with jet velocity W_j, jet diameter D_j and kinematic viscosity ν.

Downstream of an initial development region the radial profiles of mean velocity and Reynolds stresses display self similarity [54]. The Reynolds stresses are anisotropic [101] and develop at different rates. The mean axial velocity and axial velocity fluctuations become self-similar around 30 diameters [148] from the nozzle. However other Reynolds stresses apparently continue to develop out to 60 diameters [101]. The self-similar profile, spreading rate and velocity decay rate are independent of Reynolds number for $Re_j > 10^4$ [101].

The mixing of a turbulent jet with surroundings of a different density introduces a density ratio into the description of the flow, however the developed state of a variable density jet depends only on the rate of momentum addition and is essentially indistinguishable from a constant density jet [108].

5.1.2 Ignition of partially premixed flow

Some theoretical aspects of forced ignition of partially premixed flow were introduced in chapter 3. It is seen that ignitability is a balance between electrical and chemical heat release and dissipation due to conduction and mixing, [2; 24; 114].

In this work work ignition and flame propagation are sometimes analysed separately. Where this distinction is made the ignition phase lasts until the flame either extinguishes or ignites a propagating flame front. The propagation phase involves

flame front propagation once the ignition transient has passed such that the flame propagation at a point in space is independent of the details of the ignition event.

5.1.3 Propagation and stabilisation of jet flames

Following an ignition event the stabilisation of a jet flame involves the propagation of flame fronts. A lifted flame is a particularly well studied case which occurs where the flame front stabilises at a finite distance away from the nozzle. Previous work on these processes are reviewed in this section. Alternative outcomes include an attached flame where the presence of the nozzle plays a role in the stabilisation process and 'blow off' or extinction.

Laminar flames

In most practical situations the flow transitions to turbulence before a lifted flame can be achieved; however, it is possible to observe 'lift off' in the laminar regime [44] and the study of the laminar flame illuminates concepts relevant to turbulent flow.

Far from the nozzle, stabilisation is believed to be accomplished by means of a triple flame [44]. Partial premixing occurs prior to the flame. The triple flame comprises a premixed front spanning rich and lean compositions and which propagates along the stoichiometric mixture fraction line. A trailing diffusion flame consumes excess fuel and oxidiser which survive the premixed flame as shown in Fig. 5.1, [80]. The flame propagates with a characteristic edge flame speed S_E relative to the reactants which depends on various parameters including the Lewis number [26] and the mixture fraction gradient [67]. The flame stabilises where S_E equals the flow speed on the stoichiometric line. The speed of a triple flame is reduced relative to the planar stoichiometric flame due to curvature which is a function of the local mixture fraction gradient but increased due to heat release induced deceleration of

the flow upstream of the flame [119]. Values for S_E up to twice the stoichiometric flame speed [70; 75] have been reported with hydrocarbon fuels. Ruetsch et al. [119] relate the enhancement in propagation speed to the square root of the density ratio across the flame, as used in chapter 4. Analytical studies also highlight the role of Schmidt number (the ratio of viscosity to species diffusivity) on the lift off height, since this parameter determines the relative position of the mixture fraction and velocity contours [26; 44; 75].

Unsteady simulations and experiments of laminar jet ignition fronts [67; 104] and of jet stabilisation [102] also show a triple flame propagation mechanism. The kinetics of methane combustion in the triple flame show dominance of branching and propagation steps at the front with nearly complete fuel decomposition at the premixed fronts. The diffusion flame is being fueled by O and OH from the lean side and CO and H_2 from the rich side [102; 104].

The relative flow and difference in temperature between fuel and oxidiser modifies the shape of the triple flame. A high velocity in the fuel jet tends to move the lean branch upstream relative to the rich branch [104]. Im and Chen [56] applied a pair of vortices to a propagating triple flame solution and observed the negative strain causing the lean branch to collapse onto the diffusion flame and noted that excessive compressive strain and curvature at the flame tip can result in negative displacement speed.

Turbulent flames

Ignition-extinction fronts and lifted flames are also found in turbulent non-premixed jets. The detailed propagation and stabilisation mechanisms remain difficult to access either experimentally or numerically.

Vanquickenborne and Tiggelen [139] argued that the jet is sufficiently well mixed by the lift off height that stabilisation occurs where the local flow velocity

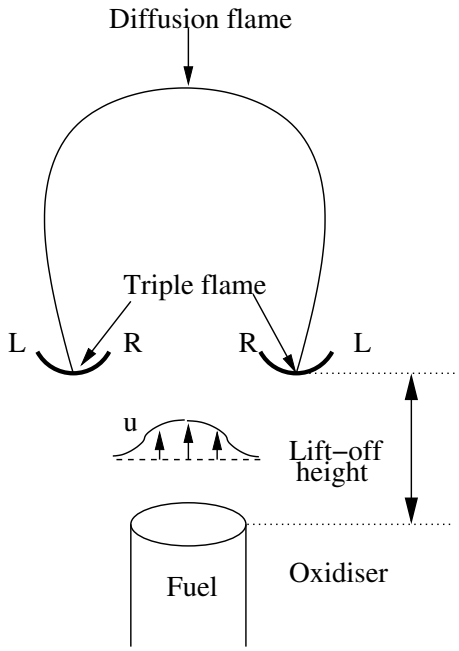

Figure 5.1: Sketch showing the form of the triple flame in a laminar lifted diffusion flame, [44].

along the stoichiometric contour equals the premixed stoichiometric laminar flame speed. Peters and Williams claimed the degree of premixing was insufficient to support that argument and proposed that the flow stabilises at the point where the local strain rate falls below the critical extinction rate for a non-premixed flame [96]. Broadwell attributed the stabilisation process to extinction in large scale turbulent structures [16; 59; 128]. Alternatively stabilisation could be due to the propagation of triple flames in the turbulent flame brush [87; 119; 145].

Experimental results show extensive premixing prior to the flame [120] and that the strain rate at the stabilisation is much lower than the extinction value. Muniz et al. [88] observe stabilisation of the flame at locations where the flow speed is close to the laminar burning velocity, indicating propagation could be due to structures such as the triple flame. Indeed, the occurrence of triple flame is seen in images of lifted flames, for example [120].

The mean stoichiometric iso-surface may reside at a position with mean ve-

locity above the propagation speed for laminar triple flames. However, it has been observed that the mean position of the flame front in a lifted jet flame can be found at radii significantly greater than that of the lean flammability limit. Su et al. [128] provide an explanatory mechanism through which the flame propagates around large, relatively well mixed structures with similar dimensions to the jet width. Thus flammable mixture, bearing flame elements, is transported outward and is slowed by the free stream such that the flame is able to make progress upstream and into another structure which typically has a higher speed and may cause the flame to temporarily recede downstream.

An increasing amount of numerically simulated data is becoming available for various partially premixed propagation configurations [24; 62], and even for and entire lifted turbulent round jets [149]. These provide supporting evidence for the role of the triple flame in partially premixed flame propagation.

5.2 CMC simulation

5.2.1 Flow configuration

The lifted turbulent jet configuration used is that studied by [2], shown in Fig. 5.2. A $5mm$ diameter jet of fuel with volume flow rate Q_j issues into co-flowing air with axial velocity $W_c = 0.1ms^{-1}$. The fuel pipe is 130 diameters long such that the flow may be considered to have fully developed turbulence. The fuel volume flow rates used were $2.45 \times 10^{-4}m^3s^{-1}$ and $5.01 \times 10^{-4}m^3s^{-1}$ giving averaged velocities in the jet of $W_j = 12.5ms^{-1}$ and $W_j = 25.5ms^{-1}$ respectively. The fuel composition was 70% methane by volume mixed with 30% air by volume giving a stoichiometric mixture fraction of $\xi_{st} = 0.0976$. The lean and rich flammability limits are $\xi_{lel} = 0.0502$ and $\xi_{rel} = 0.1582$ respectively.

A pair of electrodes were positioned at locations throughout the flow and the

ignition of the flow was explored by applying sparks of various electrical energies and duration [2]. The experimental results discussed in this chapter use a spark with a nominal electrical energy of $100mJ$ and duration of $400\mu s$ found from the integral of the voltage multiplied by current at some point in the high voltage loop. It must be stressed that this value is different from the amount of thermal energy imparted to the fluid. The spark duration is the total time for which a voltage is applied however the majority of the electrical energy appears to be expended in approximately 25% of the duration quoted in [2]. The electrode spacing was $1mm$ and the tip diameter is approximately $0.1mm$, giving a very crude estimate for the efficiency of transfer of electrical energy into the fluid of 30% [2].

The key observation is the rate at which the flame propagates up the jet, as visualised with high speed photography, Fig. 5.3, or OH-PLIF.

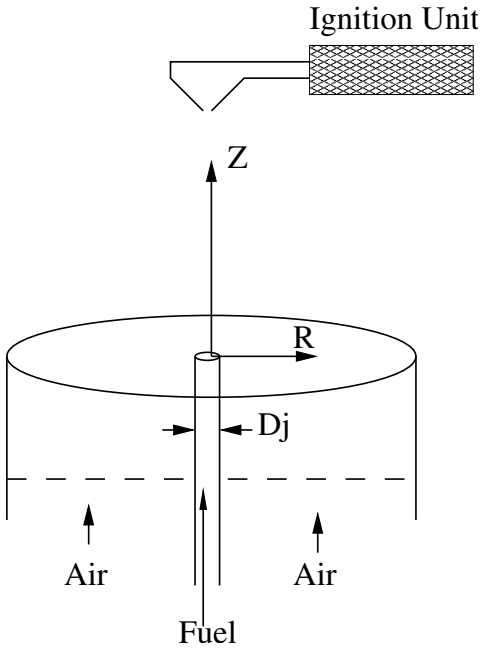

Figure 5.2: Schematic diagram of the turbulent jet burner with the spark electrodes, reproduced from Ahmed and Mastorakos [2].

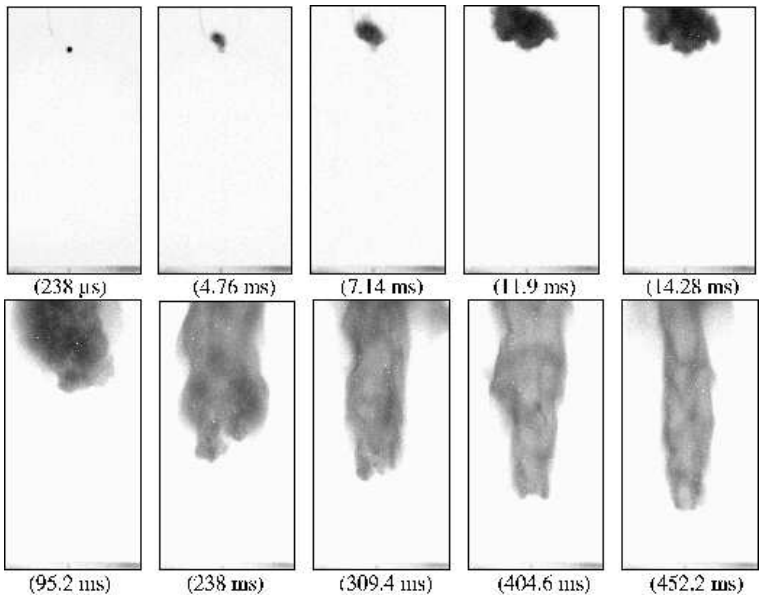

Figure 5.3: High speed camera images of ignition at $r/d_j = 0$, $z/d_j = 40$ followed by flame propagation upstream, $W_j = 25.5ms^{-1}$. The time after the spark is given under each image,[2].

5.2.2 Turbulent flow field

Simulations have been performed using the CFD package STAR CD [20]. The axi-symmetric computational domain extends 60 jet diameters (D_j) radially and $80D_j$ axially which contains the final $10D_j$ of the fuel pipe. An axi-symmetric grid with 85000 cells was used, employing variable refinement such that there are always approximately 70 cells across the jet. The minimum dimension in the grid is $50\mu m$. Solutions on a grid with a minimum dimension of $125\mu m$ confirmed that the steady flow solutions are grid independent. However, the more refined grid was used in order to capture any transient flow phenomena resulting from the spark ignition.

The prescribed velocity profile at inlet to the fuel pipe is parabolic (ie. laminar) but it develops a flatter velocity profile by the time the fuel issues into the free stream due to the application of the $k-\epsilon$ turbulence model. The co-flow turbulence intensity is set to 1%. The radial boundary condition is an inflow of air with $u = -0.005ms^{-1}$ and $w = 0.1ms^{-1}$ to allow for flow entrainment into the jet. The usual outflow

condition is used for the downstream boundary.

The velocity and mixing fields are solved by using the $k-\epsilon$ model in the Reynolds averaged Navier Stokes equations. The value of the model parameters are given in Table 5.1. Note that the value of $C_{\epsilon 3} = 0.079$ has been used in accordance with Pope's correction to account for the round jet anomaly [101]. The flow is treated as incompressible, employing the ideal gas equation of state. Transport equations are solved for $\tilde{\xi}$ and $\widetilde{\xi''^2}$. The flow field used for un-coupled calculations is precomputed, with fuel and air as active scalars in order to give the correct density. In coupled calculations species transport is solved by the combustion model which uses the presumed mixture fraction field to return unconditional mean molecular weights and temperatures for use by the CFD program.

In the absence of experimental velocity and composition data for this non-reacting flow (except with air issuing from the fuel pipe [2]) empirically derived expressions [108; 133] are used to assess the validity of the flow field predictions.

C_μ	$C_{\epsilon 1}$	$C_{\epsilon 2}$	$C_{\epsilon 3}$	$C_{\epsilon 4}$	κ
0.09	1.44	1.92	0.79	-0.33	0.419

Table 5.1: $k-\epsilon$ parameters for the round turbulent jet.

Velocity field

Figures 5.4, 5.5, 5.6 show close agreement between Tieszen's empirical expression (Eq. 5.1) for mean axial velocity $\bar{W}$ in a self preserving jet [133] and the CFD predictions for both the $W_j = 12.5ms^{-1}$ and $W_j = 25.5ms^{-1}$ cases. W_c and W_m refer to co-flow and centre line axial velocities respectively. W_0 is the mean velocity through the nozzle.

$$\frac{\overline{W}}{W_0} = 11.8 \left(\frac{\rho_0}{\rho}\right)^{\frac{1}{2}} \left(\frac{r_0}{z}\right) exp\left[-93.7\left(\frac{r}{z}\right)^2\right] \tag{5.1}$$

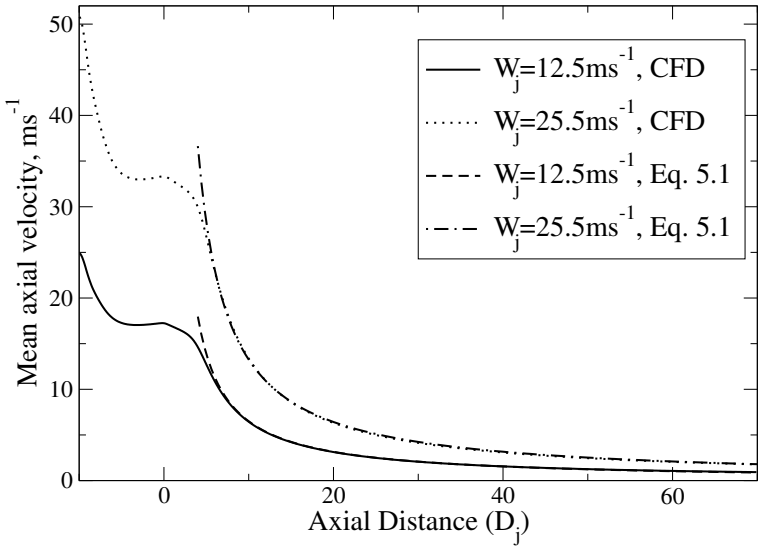

Figure 5.4: Mean axial velocity along the centre line of the jet for $W_j = 12.5ms^{-1}$ and $W_j = 25.5ms^{-1}$ from the CFD solution and from equation 5.1.

The turbulent kinetic energy is shown in 5.7. The axial turbulence intensity is estimated as($\frac{W'}{W-W_C} \approx (\frac{2}{3}k)^{\frac{1}{2}}$) and compared with measurements from a similar $21ms^{-1}$ equal density jet [2] in Fig. 5.8. This shows an over prediction of the velocity fluctuation close to the jet nozzle.

Mixture fraction distribution

The mixture fraction predictions are compared with further empirical expressions for mean (equation 5.2 and the r.m.s fluctuations 5.3 from [108]. Except at $z/D_j < 20$ a close agreement is seen for both $W_j = 12.5ms^{-1}$ and $W_j = 25.5ms^{-1}$,

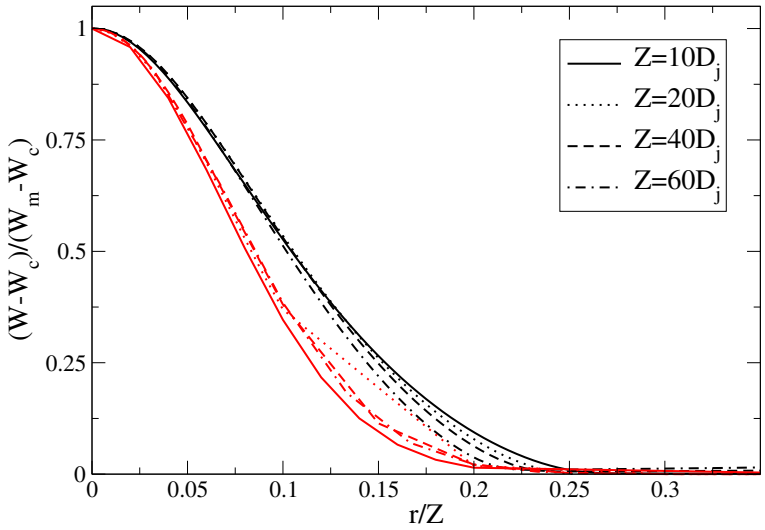

Figure 5.5: Mean axial velocity versus radius at z=10, 20, 40 and $60D_j$ for the $W_j = 12.5ms^{-1}$ case. Black lines are from the CFD solution, red lines from equation 5.1.

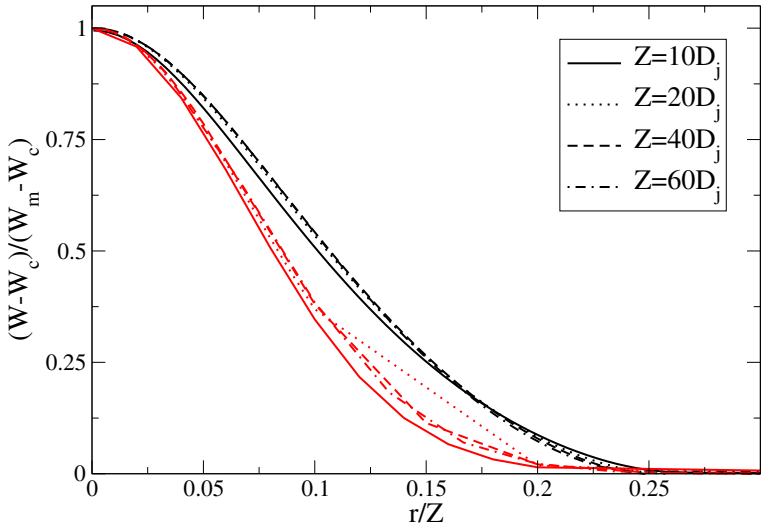

Figure 5.6: Mean axial velocity versus radius at z=10, 20, 40 and $60D_j$ for the $W_j = 25.5ms^{-1}$ case. Black lines are from the CFD solution, red lines from equation 5.1.

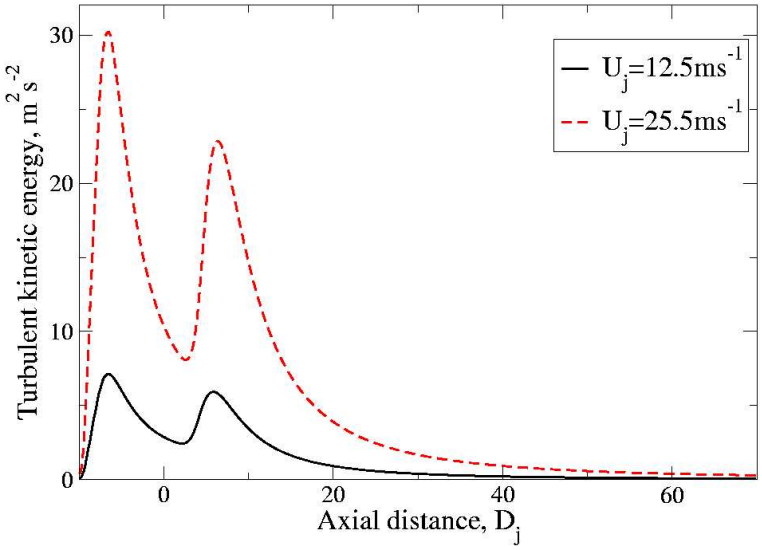

Figure 5.7: Axial turbulent kinetic energy along the centre line of the jet for $W_j = 12.5ms^{-1}$ and $W_j = 25.5ms^{-1}$.

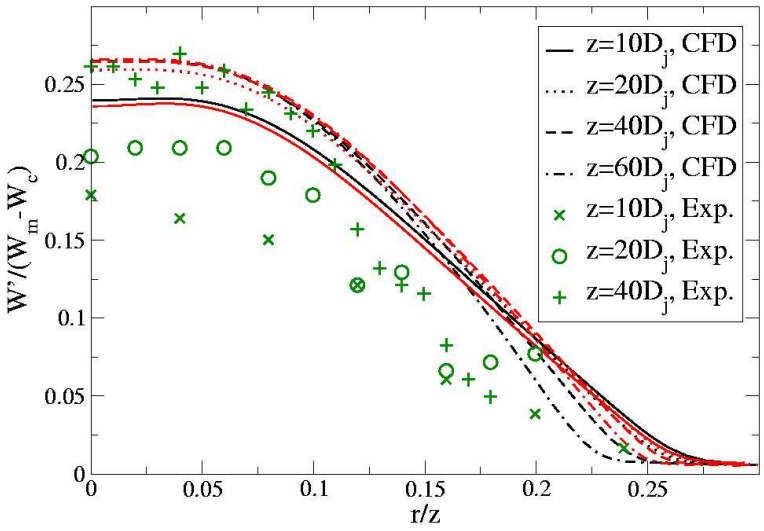

Figure 5.8: Axial turbulence intensity versus radius at z=10, 20, 40 and 60D_j. Black lines are from the $W_j = 12.5ms^{-1}$ CFD solution, red lines for the $W_j = 25.5ms^{-1}$ CFD solution, symbols are measured values for the experiment with an air jet and $W_j = 21ms^{-1}$, [2].

see Figs. 5.9 and 5.10.

$$\bar{\xi}(z,\eta) = \frac{9.52 r_\epsilon}{z - z_{0Y}} exp(-59\eta^2) \tag{5.2}$$

$$\xi'' = \frac{9.52 r_\epsilon}{z - z_{0Y}} [0.23 + 0.35\eta + 9.09\eta^2 - 116.48\eta^3 + 240.81\eta^4] \tag{5.3}$$

The 85000 cell grid and the $k - \epsilon$ RANS model are considered to give sufficiently accurate flow field predictions for this study and are used for the remainder of the chapter.

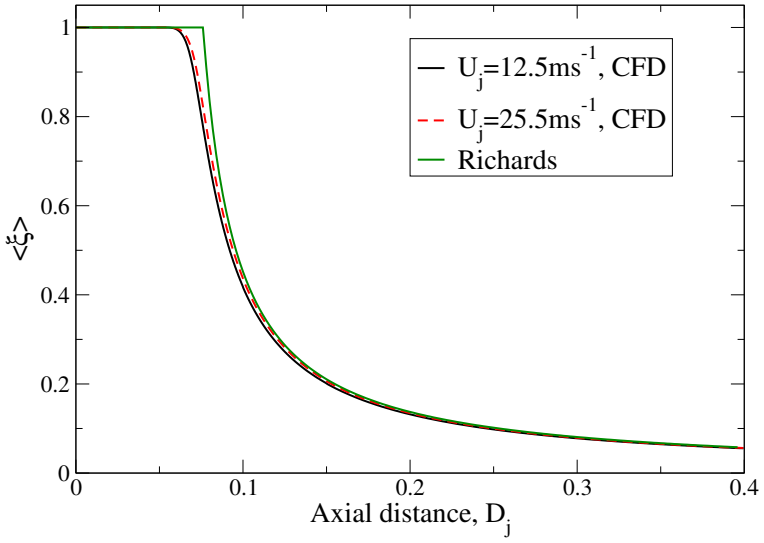

Figure 5.9: Mean mixture fraction along the centre line of the jet for $W_j = 12.5ms^{-1}$ and $W_j = 25.5ms^{-1}$ from the CFD solution. The mixture fraction profile predicted by equation 5.2 is shown in green.

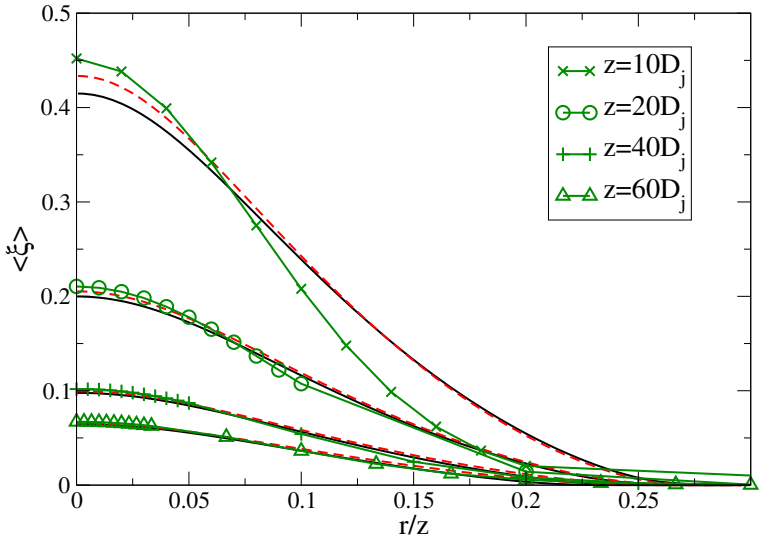

Figure 5.10: Mean mixture fraction versus radius at z=10,20,40 and $60D_j$. Black lines are from the $W_j = 12.5ms^{-1}$ CFD solution, red lines from the $W_j = 25.5ms^{-1}$ CFD solution, and symbols are from equation 5.2.

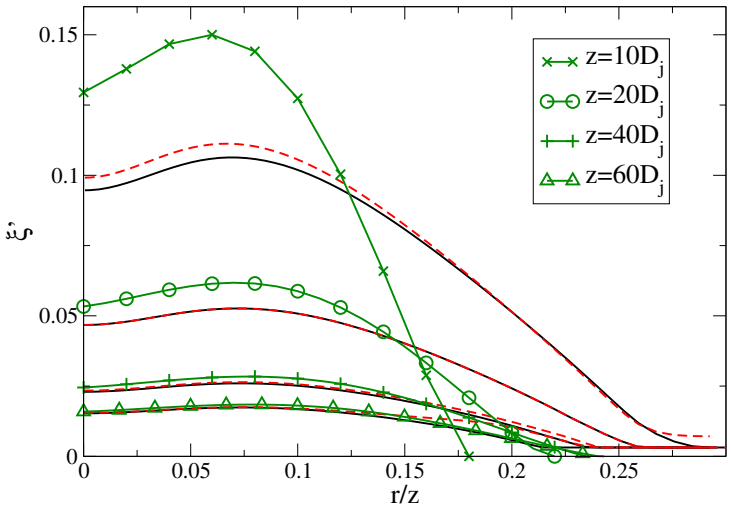

Figure 5.11: Mixture fraction r.m.s versus radius at z=10,20,40 and $60D_j$. Black lines are from the $W_j = 12.5ms^{-1}$ CFD solution, red lines are from the $W_j = 25.5ms^{-1}$ CFD solution, and symbols are from equation 5.3.

5.2.3 Application of the CMC model

Models

The first order CMC model was used as described in chapter 2, both with and without the two-way coupling to the flow field solution. The sub-models used are described in chapter 2. These were: the amplitude mapping closure for the conditional scalar dissipation rate, the linear model for the conditional velocity, and the gradient model for the conditional turbulent flux. Additionally, the new counter gradient modelling approach for the conditional turbulent flux from chapter 4 is developed and assessed in section 5.3.4.

The PDF weighted averaging scheme Eq. 5.4 described in chapter 2 is used to import the necessary quantities from the flow solution in both one and two dimensional grids. It is noted that in the limit of a one dimensional simulation (ie. only one node in the radial direction) our solution procedure is equivalent to the cross stream averaging procedure employed by Devaud and Bray [33] for their 1D simulations of a lifted jet.

$$\begin{aligned} \{M\}_i &\equiv \frac{1}{vol_i}\int_{vol_i} M(\underline{x})dvol \\ \{M\}_{i+} &= \frac{M(\underline{x})\tilde{P}(\eta)\}_i}{\tilde{P}(\eta)\}_i} \end{aligned} \tag{5.4}$$

where subscript i refers to the volume associated with the i^{th} CMC node, and $\{M\}_{i+}$ is the PDF weighted conditional average used for quantity M.

Including the new model counter gradient contributions to the conditional turbulent flux, ($\mathbf{F}_T$ for temperature and $\mathbf{F}_\alpha$ for species), the CMC equations solved

in this chapter are Eqs. 5.5 and 5.6:

$$\frac{\partial Q_\alpha}{\partial t} = - \langle u_i|\eta\rangle \frac{\partial Q_\alpha}{\partial x_i} + \langle N|\eta\rangle \frac{\partial^2 Q_\alpha}{\partial \eta^2} + \langle \dot{w}_\alpha|\eta\rangle - \frac{1}{\bar{\rho}\widetilde{P}(\eta)} \frac{\partial}{\partial x_i}\left(-D_t \frac{\partial Q_\alpha}{\partial x_i}\bar{\rho}\widetilde{P}(\eta)\right) - \frac{1}{\bar{\rho}\widetilde{P}(\eta)} \frac{\partial}{\partial x_i}\left(F_{\alpha i}\bar{\rho}\widetilde{P}(\eta)\right) \quad (5.5)$$

$$\frac{\partial Q_T}{\partial t} = - \underbrace{\langle u_i|\eta\rangle \frac{\partial Q_T}{\partial x_i}}_{T_{cv}} + \underbrace{\langle N|\eta\rangle \left\{ \frac{\partial^2 Q_T}{\partial \eta^2} + \left[\frac{1}{\langle c_p|\eta\rangle} \left(\frac{\partial \langle c_p|\eta\rangle}{\partial \eta} + \sum_{\alpha=1}^{n} c_{p\alpha} \frac{\partial Q_\alpha}{\partial \eta} \right) \right] \frac{\partial Q_T}{\partial \eta} \right\}}_{T_m} - \underbrace{\sum_{\alpha=1}^{n} h_\alpha \langle w_\alpha|\eta\rangle}_{T_c} + \underbrace{\dot{T}_{spark}(\eta)}_{T_{spark}} - \underbrace{\frac{1}{\bar{\rho}\widetilde{P}(\eta)} \frac{\partial}{\partial x_i}\left(-D_t \frac{\partial Q_T}{\partial x_i}\bar{\rho}\widetilde{P}(\eta)\right)}_{T_{tf}} - \underbrace{\frac{1}{\bar{\rho}\widetilde{P}(\eta)} \frac{\partial}{\partial x_i}\left(F_{Ti}\bar{\rho}\widetilde{P}(\eta)\right)}_{T_{CGD}} \quad (5.6)$$

Note that the pressure term has been neglected in the enthalpy equation for this flow configuration.

All conditional scalars are initialised with conditional values representing inert mixing profiles between fuel and air. The inlet boundary conditions are also based on inert mixing, while the outlet boundary condition is the Von Neumann type (zero gradient). At the boundaries in mixture fraction space the conditional scalar dissipation equals zero, however chemical reaction is allowed at $\eta = 1$ due to the presence air in the fuel stream.

The Fernández-Tarrazo et al. kinetic scheme for partially premixed methane oxidation is used throughout, see Ref. [37] and chapter 2. The skeletal mechanism by Smooke [125] is also used to provide a comparison in specific cases.

Numerical implementation

One and two dimensional axisymmetric grids are employed for the spatial discretisation of the CMC equation. Variable grid spacing is employed in both axial and radial directions. In order to resolve the conditional gradients the axial grid refinement is centred on the upstream flame front. If the flame front propagates more than $2mm$ in either direction the solution is interpolated onto a new grid which is refined at the axial location of $(\frac{\partial \langle T|\eta_{st}\rangle}{\partial Z})_{max}$. The downstream flame front is not always well resolved. However the refined zone is sufficiently wide that by the time the downstream flame front is swept out of this zone it no longer significantly influences the development of the upstream front.

Spark model

The spark models described in chapter 2 have been implemented and are investigated in section 5.3.4.

5.2.4 Numerical sensitivity of the CMC solution

Propagation in mixture fraction space

The number of mixture fraction space nodes required and the maximum permissible time step were assessed by simulating the evolution of partially premixed flame fonts in a 0D CMC simulation of non-premixed methane combustion with the Smooke combustion mechanism. The initial condition (as shown in Fig. 5.12) is the Burke-Schumann "infinitely fast chemistry" solution applied over a narrow range of mixture fraction ($0.05 < \xi < 0.06$), and the inert mixing solution applied elsewhere. The peak of the AMC scalar dissipation is set as $N_0 = 5s^{-1}$ which is just below the limit above which this initial condition proceeds to extinction. Note that the ignitable limit is far below the critical strain rate for extinction ($N_0/N_{0crit} \approx 3\%$)

due to the narrow width of the initial flame in mixture fraction space. Due to the absence of initiation reactions in the Smooke mechanism the level of the hydroxyl radical is set to $Y_{OH} = 0.01$ in the Burke-Schumann region to allow the chemistry to evolve.

The η-grid is highly refined around the stoichiometric mixture fraction. Grids of 101 and 81 points with time steps anywhere below $10^{-5}s$ give very similar temporal evolution (shown in Fig. 5.12) and nearly indistinguishable steady burning solutions. In subsequent work η-grids with 81 points will be used and time steps will not exceed $10^{-5}s$.

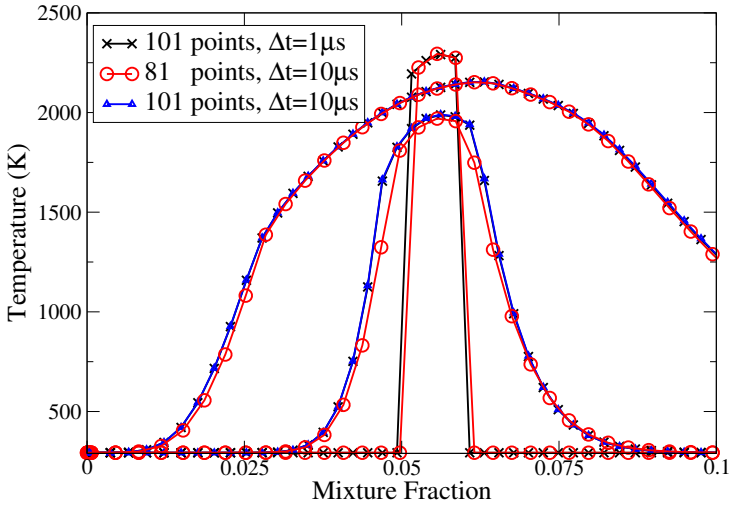

Figure 5.12: Propagation of a partially premixed flame front in mixture fraction space for $n_\eta = 81$ and 101, and $\Delta T = 10^{-5}s$ and $\Delta T = 10^{-6}s$, $N_0 = 5s^{-1}$

.

Stream-wise flame propagation

Sensitivity to the axial grid spacing, the flame tracking regridding procedure, and the time step were investigated using a test problem. The test involved applying a burning flamelet solution given by running the 0D CMC code with $N_0 = 10s^{-1}$

to all points downstream of z_{spark} at $t = 0$, and examining the 1D, uncoupled CMC solution $40ms$ later. This test was performed for $W_j = 12.5$, $25.5ms^{-1}$ at $z_{spark} = 20$ and $40D_j$. The flame position at $t = 40ms$, and the grid details are given in Table 5.2.

A time step of $\Delta t = 10^{-5}s$ with 150 points in the axial direction (giving $\Delta z_{min} = 0.098mm$) appears to be satisfactory for all the 1D cases considered. Devaud and Bray [33] found similar resolution requirements $\Delta z_{min} = 0.04mm$ using 140 nodes in their 1D simulation of a lifted hydrogen flame, while Kim's work on the same problem using 17 nodes and an average spacing of $2.3mm$ may have been under resolved [60].

$W_j(ms^{-1})$	z_{spark}	N_z	Δz_{min}	$\Delta t(\mu s)$	$z_{flame}(mm)$	CPU time
12.5	$20D_j$	150	$0.098mm$	10	0.08325	80mins
12.5	$20D_j$	300	$0.049mm$	10	0.08433	149mins
12.5	$20D_j$	150	$0.098mm$	1	0.08313	348mins
12.5	$40D_j$	150	$0.098mm$	10	0.16039	82mins
12.5	$40D_j$	300	$0.049mm$	10	0.16152	150mins
12.5	$40D_j$	150	$0.098mm$	1	0.16023	351mins
25.5	$20D_j$	150	$0.098mm$	10	0.09678	87mins
25.5	$20D_j$	300	$0.049mm$	10	0.09797	171mins
25.5	$20D_j$	150	$0.098mm$	1	0.09665	365mins
25.5	$40D_j$	150	$0.098mm$	10	0.18000	86mins

Table 5.2: 1D uncoupled grid sensitivity run details, simulation duration $t = 40ms$.

Radial flame propagation

The radial grid sensitivity was assessed in a similar manner. The number of axial grid points and the time step were fixed at 150 and $10^{-5}s$. The test case employed is the evolution of a $3cm$ diameter cylinder of 'burning solution' which extends downstream from $z_{spark} = 20D_j$. The resulting stoichiometric conditional and unconditional temperature contours were compared for 20 and 40 points in the radial direction. 20 points were deemed sufficient to give grid independent results

in the type of problems investigated in this chapter.

The coupling time step

The CMC-CFD splitting time step requirement was assessed in a cross stream-averaged test case. The $W_j = 25.5ms^{-1}$ case was considered the more arduous test due to the shorter flow timescales expected. A burning disk with $\Delta z = 0.2mm$ was inserted at $z = 20D_j$ at time $t = 0$. The CMC grid used had 150 points in the axial direction, and a variety of time-steps were compared indicating that a maximum time step of 2×10^{-6} is suitable for coupled calculations.

5.2.5 Target problems

In section 5.3 the numerical model is used to explore the applicability of the first order CMC to the various phases of combustion during the ignition of the jet flame.

1. Spark ignition: The various ignition models proposed in chapter 2 are evaluated. Particular attention is given to the ability of the CMC to capture the various processes which limit ignition.

2. Turbulent edge flame propagation: Flame propagation is analysed far away from the spark to examine the propagation mechanism in the CMC context.

3. Lifted jet flame: the well known case of the steady lifted flame is studied in detail for comparison with other works.

5.3 Results and discussion

5.3.1 Spark ignition

The predicted minimum energy required to ignite a flame kernel was found at two locations in the $W_j = 12.5ms^{-1}$ jet. The simulations were performed using a refined CMC mesh covering the whole kernel without adaptation of the mesh during the calculation. Both spark locations were on the jet centre line at $z_{spark} = 25D_j$ and $z_{spark} = 40D_j$. The energy input needed in order to avoid the flame extinguishing within the first $10ms$ was $3.5mJ \pm 0.5mJ$ for both locations. This may be compared with the absolute minimum ignition energy for methane $0.29mJ$, [8]. Thus the predicted minimum ignition energy is one order of magnitude higher than the quiescent, premixed ignition limit. The difference can be attributed to heat loss from the kernel, non-optimal composition, and any limitations of the present modelling. The modelled scalar dissipation rate, conditioned on stoichiometry, is less than $0.1\%N_{0ext}$ at both locations. The conditions at the spark location are expected to be far from the critical strain rate at which a flame can not be ignited discussed in chapter 3.

The experimental investigation of this jet used a nominal electrical spark energy of $100mJ$ obtaining ignition probabilities of approximately 80% and 55% for the respective spark locations [2]. It is not known what proportion of the indicated $100mJ$ is lost to the electrical circuitry, to heating the electrodes, or to the far field by the action of radiation or pressure waves, however the experimenters estimate that the spark efficiency will not exceed 30% [3]. Thus it may be assumed that the spark used in the experiment would safely ignite any flammable mixture caught inside the kernel.

The role of the spatial transport terms may be illuminated by a comparison with zero-dimensional CMC ignition calculations based on equivalent spark param-

eters and a range of scalar dissipation rates. The temperature profiles which occur at the end of the spark event ($500ms$), for a range of equivalent ignition energies are shown in Fig. 5.13. These indicate that a minimum energy density, $5.7 \times 10^5 Jm^{-3}$ equating to $3.6mJ$ in the jet, was needed to induce auto-ignition by the time the spark finishes. The proximity of the minimum ignition energies in the two dimensional and zero-dimensional simulations indicates that spatial transport does little to limit the successful formation of a burning kernel in the current flow. This conclusion is expected to be dependent on the local turbulent mixing time scale, and also the size and timescale selected for the spark kernel. Therefore it appears that the predicted turbulence level does not significantly deter the formation of a burning kernel either through conserved scalar dissipation, or turbulent transport processes. Instead, it appears that the observation of a burning flame kernel (as opposed to establishment of a lifted flame) is primarily related to the instantaneous composition at the spark in agreement with the statistical arguments of Smith et al. [123].

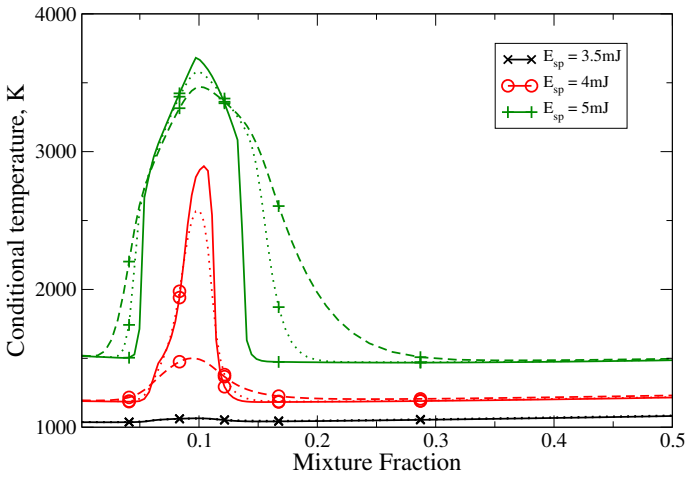

Figure 5.13: Conditional temperature profiles after the $500ms$ spark time, resulting from zero-dimensional CMC calculations corresponding to spark energies of $3.5mJ$, $4mJ$ and $5mJ$. Three levels of scalar dissipation are shown, $\chi/\chi_{ext} = 0.01$ (solid), $\chi/\chi_{ext} = 0.01$ (dotted) and $\chi/\chi_{ext} = 0.19$ (dashed).

In chapter 4 a large variance of reaction progress was observed in the flame kernel, which gave rise to an over prediction of the mean reaction rate due to the first order CMC closure. Therefore second conditioning on a reaction progress variable would be expected to improve the current predictions.

Examination of simulations for a successful ($E_{sp} = 5.0mJ$) spark located at $z_{spark} = 25D_j$ reveals the evolution of the CMC simulated ignition kernel in the first few ms after the spark. The unconditional temperature contours for the full simulation from spark to stabilisation, which uses an adaptive mesh refinement, are shown in Fig. 5.14. This spark is positioned close to the mean stoichiometric iso-surface. The kernel expands rapidly through propagation and thermal expansion. The effects of thermal expansion may be seen in the distortion of the mean mixture fraction contours. By $3ms$ the tip of the stoichiometric contour has been pushed back upstream, and the lean flammability contour is being driven radially outward.

The balance of the terms in the conditional temperature equation is shown for stoichiometry in Fig. 5.15. The plots show the ignition kernels after two spark times, $1ms$, and after 6 spark times, $3ms$, so that the plots may be compared with the ignition kernels studied in chapter 4. At $1ms$ after the spark the axial convection term, $T_{cv,Ax}$, cools the upstream flame front and heats the downstream flame front, however by $3ms$, it appears that the jet stagnates within the upstream flame brush, as indicated by the change of sign in the convection term. Consequently the cold side of the upstream flame front receives heating from the flow arriving from further inside the kernel. The radial convection term (not shown) is zero at the centre of the axi-symmetric domain. The turbulent flux term, using the eddy diffusivity model diffuses heat along the axis, $T_{tf,Ax}$, into the reactants. In the radial direction the turbulent flux term, $T_{tf,Ra}$, is always negative since the conditional temperature takes its peak value in the centre of the kernel.

The one-step chemical reaction is always exothermic and distinctly reveals a reaction front surrounding the kernel, however at $1ms$, the kernel is sufficiently

small, relative to the turbulent flame brush thickness for there to be appreciable heat release at the centre of the kernel. At stoichiometry, the micro-mixing term T_m generally opposes the chemical heat release.

Thus, the ignition kernel development involves a sensitive interaction between the rate of flame propagation and the development of the velocity field resulting from heat release. Its solution is dependent on close numerical coupling and accurate modelling of the turbulent flame propagation processes.

5.3.2 Edge flame propagation

Simulations of flame propagation and stabilisation in the turbulent jets, $W_j = 12.5ms^{-1}$ and $W_j = 25.5ms^{-1}$ were performed using the following model configurations:

1. 1-dimensional, cross stream averaged CMC uncoupled from the flow field;
2. 1-dimensional, cross stream averaged CMC coupled with the flow field solution;
3. 2-dimensional axi-symmetric CMC coupled with the flow field referred to as simulation 1 ($W_j = 12.5ms^{-1}$) and simulation 2 ($W_j = 25.5ms^{-1}$).

The complete ignition process is illustrated by the evolution of the Favre averaged (unconditional) temperature and mean mixture fraction field shown in Fig. 5.14 for simulation 1. The simulated flame front positions vary significantly depending on the model configuration, and always reached the final lift-off height at an earlier time than in the experiment. In particular, introducing the effect of heat release to the flow field calculation has a very large effect on the predictions, accelerating the propagation process and reducing the expected lift off height. The difference between the 1D and 2D coupled calculations is also significant resulting in differing final lift off heights.

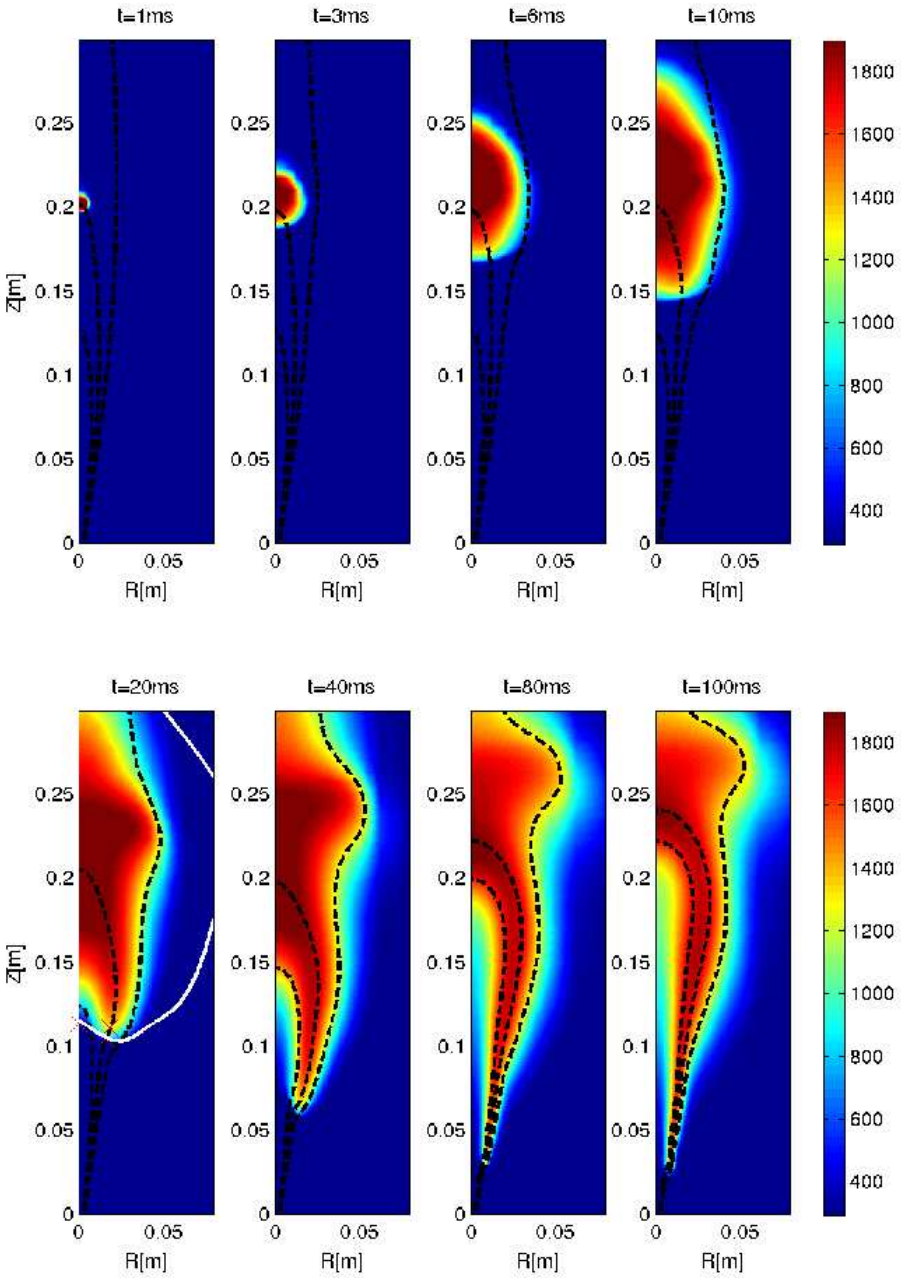

Figure 5.14: Simulated unconditional temperature evolution, in Kelvin, for Simulation 1: $W_j = 12.5ms^{-1}$ with a $5mJ$, $0.5ms$ spark at $z = 40D_j$, with CFD-CMC coupling. Time after spark initiation is given at the top of each image. Iso-lines of mean mixture fraction are shown in black for the lean flammability limit $\tilde{\xi} = 0.0502$ (inner), stoichiometry, $\tilde{\xi} = 0.0976$ (middle) and the rich flammability limit, $\tilde{\xi} = 0.158$ (outer). The plot for $20ms$ contains a white contour of $\langle T|\eta_{st}\rangle = 0.8(T_{ad} - T_0) + T_0$.

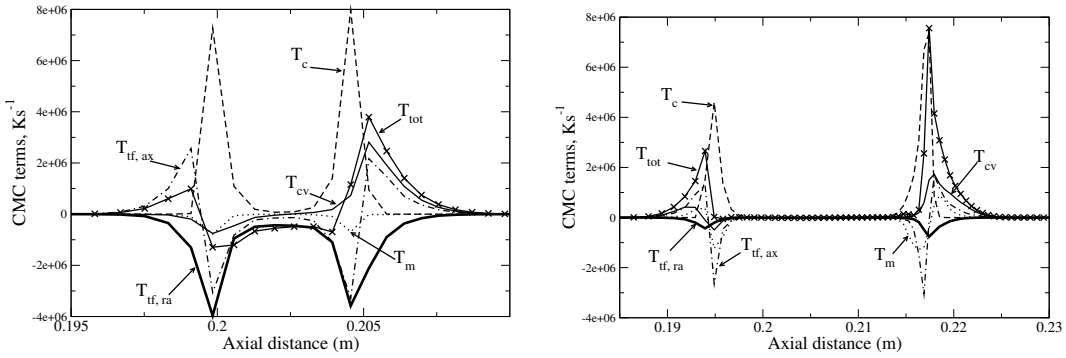

Figure 5.15: CMC temperature equation source terms, Eq: 5.5 and the total rate of change for conditional temperature, at (a): $t = 1ms$; (b): $t = 3ms$. The simulations conditions are the same as in Fig. 5.14.

The position of the upstream flame front (given by $\langle T|\eta_{st}\rangle = 1200K$) is plotted for the various configurations, and from experimental measurements [2] in Fig. 5.16.

Arguably, the uncoupled simulations give the predictions closest to the measurements, however their initial propagation speeds are above that observed experimentally. In chapter 4 the first order reaction rate closure was seen to over-predict the actual heat release from turbulent propagating flames, which may play a part in the over prediction of the propagation speed at early times.

It was noted in section 5.3.1 that the mean dilatation at the upstream flame front acts to reduce the z-direction velocity, allowing a higher propagation speed. Additionally the expansion intensifies the turbulence at the flame front, for example increasing the stoichiometric PDF-weighted average of the turbulent diffusivity from $1.1 \times 10^{-}3m^2s^{-1}$ to $3.8 \times 10^{-}3m^2s^{-1}$ as the flame front passes through $20D_j$ in Simulation 1. The relative turbulent intensification falls as the flame approaches the higher velocity flow close to the nozzle. Provided the flame is far from extinction,

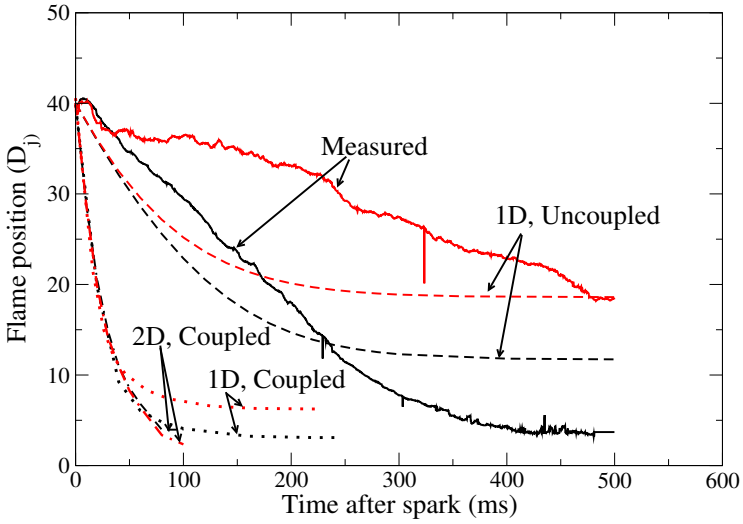

Figure 5.16: Positions of the upstream flame front versus time, for $W_j = 12.5ms^{-1}$ (black) and $W_j = 25.5ms^{-1}$ (red); averaged from 10 fast camera images, [2] (solid), simulated with 1D uncoupled CMC (dashed), simulated with 1D coupled CMC (dotted), and simulated with 2D axi-symmetric coupled CMC (dash-dotted).

both processes may be expected to increase the modelled turbulent burning rate, potentially feeding back into a further increase in the propagation speed. Thus the propagation and stabilisation model may be particularly sensitive to the accuracy of the fluid dynamic and turbulent combustion models. Given the role that specific large scale structures are thought to play in the stabilisation of a lifted, round turbulent jet, Ref. [128], it may be questioned whether a $k-\epsilon$ RANS solution encapsulates enough of the flow physics to form the basis for a simulation of propagation and stabilisation.

While the present modelling appears unsatisfactory for the ignition of the lifted jet flame, it is still instructive to analyse the first order CMC solution since more advanced applications of the CMC model may be attempted for this problem in the future, for example a double conditioning closure in an LES context. Ignition of the $W_j = 12.5ms^{-1}$ flow, Simulation 1, is examined in further detail.

The conditional temperature and the conditional heat release rate are plotted versus η for all points along the mean stoichiometric contour (uniquely defined by their z-coordinate) in Fig. 5.17. These show that due to the low levels of scalar dissipation observed, the flame spreads very little outside of the flammable mixture fraction range by the point the mean stoichiometric contour closes off at around $z = 40D_j$. The mixture fraction space profile of the conditional heat release shows that CMC modelling involves both lean and rich premixed elements and a significantly weaker diffusion flame element. In reality these may occur as tribrachial flames however no particular flame structure is assumed or implied by these CMC calculations, and the mixture fraction space profile must be understood as a local, single point representation of the flame in terms of the local mixture fraction statistics.

The current one step chemistry model greatly simplifies the description of the combustion processes. The effect of this simplification on the results is discussed with reference to a calculation for a stabilised lifted flame using a 16 species skeletal mechanism in section 5.3.3. It is seen that the one step mechanism does capture the same shape and magnitudes for the conditional heat release, however it obviously can not provide the information on the chemical composition which is available from a more detailed study. The computational time consumed in the evaluation of the chemical reaction rate is vastly reduced, in addition to the savings from the reduced number of CMC species equations being solved.

The simulated velocity and mixing fields adapt considerably during the course of the flame stabilisation and continue to develop downstream even after the upstream flame front appears to have stabilised and the downstream flame front has passed away. The height at which the centre line mean mixture fraction becomes stoichiometric increases significantly due to the mean heat release. A similar progression of the mixture faction field may be inferred from the experimental observations, Fig. 5.3 where the flame propagates as a wide turbulent brush, but becomes more

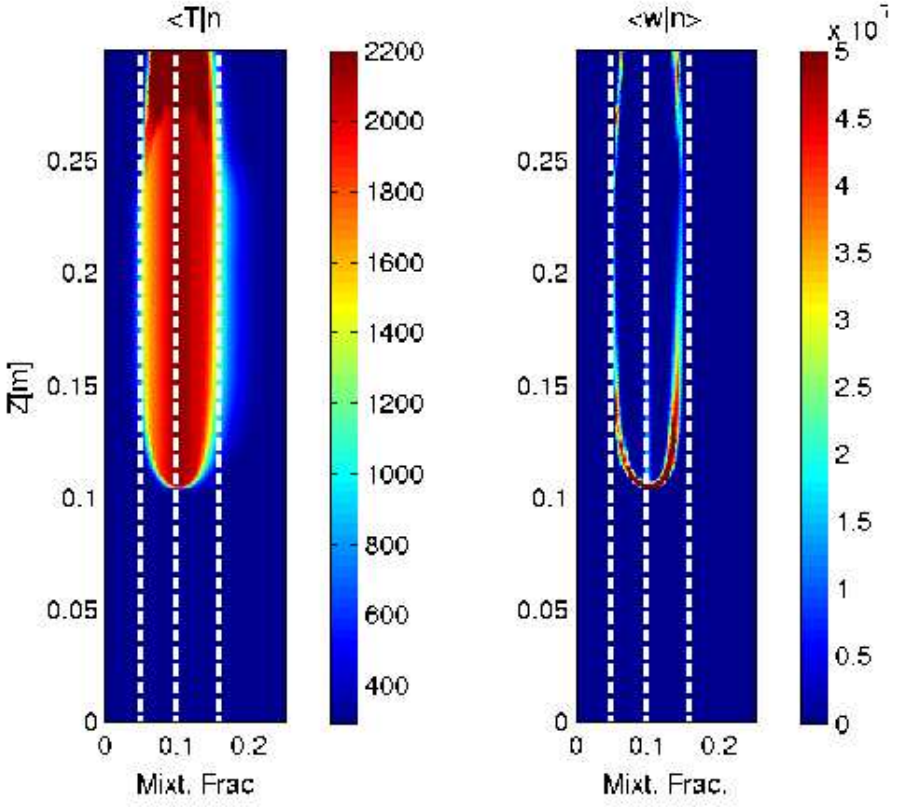

Figure 5.17: Mixture fraction space contours along the mean stoichiometric contour for conditional temperature, K, and conditional heat release, Ks^{-1}. The lean flammability limit ($\xi = 0.0503$), stoichiometry ($\xi = 0.0976$) and the rich flammability limit ($\xi = 0.1582$) are drawn with dotted white lines. Simulation 1.

like a thin tube at later times.

The CMC representation of the propagating front is explored in Fig. 5.18 at $20ms$ after the spark. Figure 5.18a shows the balance of terms through the flame front. The conditional temperature gradients are far greater than the unconditional temperature gradient observed in Fig. 5.14, with the conditional flame front being approximately $2mm$ thick at stoichiometry. The CMC terms contribute as may be expected. Chemical heat release, T_c, is exothermic, peaking at the hot side of the flame, where it is also most strongly opposed by molecular 'micro-mixing', T_m. The conditional convection, T_{cv} term plays a weak cooling effect on the hot side of the flame, however the flow stagnates somewhere near the cold edge of the flame and a very weak heating effect is seen at the cold edge. The turbulent flux, T_{tf} is treated using the turbulent diffusivity, therefore it is seen to move heat down the mean temperature gradient from the products to the reactants.

Figures 5.18b, c and d, show the mixture fraction space profiles of the conditional source terms at selected points in the flame upstream flame front. Figure 5.18b's position is at the intersection of the mean stoichiometric streamline and the white line in Fig. 5.14 representing the conditional, stoichiometric flame front. The furthest upstream position of the conditional flame front is found at a slightly greater radius, where the mean flow is leaner and slower moving. In Fig. 5.18b the narrowness of the flame does not allow a clear distinction between rich and lean premixed fronts or of a diffusion flame as would be the case at the triple point of a tri-brachial flame. After the chemistry the next largest term is the axial turbulent flux, which acts to cool the hotter stoichiometric region and heat the cooler rich and lean areas. This may be explained by the differing positions of the conditional flame front at different mixture fraction, since the rich and lean conditional flames do not propagate as fast. Figure 5.18c is also positioned on the mean stoichiometric iso-surface, at $z = 0.108m$. At this position the stoichiometric temperature is close to its adiabatic value, however the flame is still developing at richer and leaner mixture

fractions. The presence of distinct reaction fronts is seen in mixture fraction space with the scalar dissipation term T_m playing an important role in the transport of heat to the unburned reactants. Figure 5.18d is positioned where the white line in Fig. 5.14 meets the centre line of the jet. As expected, at the centre of the jet the axial convection is stronger than at the previous locations, and the flame propagation is assisted by turbulent transport of burning material from greater radii where the flame is propagating against a slower flow.

5.3.3 The steady lifted flame

Solutions for the stabilised lifted flame are now examined in closer detail. A one dimensional, coupled solution for the $W_j = 12.5ms^{-1}$ case has been evaluated with the one step model and also with the skeletal mechanism. Profiles of selected conditional quantities are shown in Figs. 5.19-5.22. The predicted lift off heights, $3.1D_j$ and $4.2D_j$ respectively are within the variation of the measured mean stabilised flame position shown by Fig. 5.16.

Comparison of the 1-step temperature and heat release profiles for the stabilised flame in Fig. 5.19, with their profiles in the propagating flame in Fig. 5.17 shows that once stabilised the flame has a significantly wider profile in mixture fraction space, which is attributed to the higher scalar dissipation rates encountered nearer to the nozzle. The greater spreading of the flame on the rich side is expected because of the proximity of stoichiometry to the pure air boundary and the greater scalar dissipation rate around $\eta = 0.5$ resulting from the AMC model. Once the flame has stabilised this wider profile is communicated to downstream locations by convection so that the conditional profile continues to develop at downstream locations for some time after stabilisation of the upstream flame front.

The conditional temperature, heat release and reactant mass fractions from the skeletal mechanism simulation are shown in Fig. 5.20, and the conditional carbon

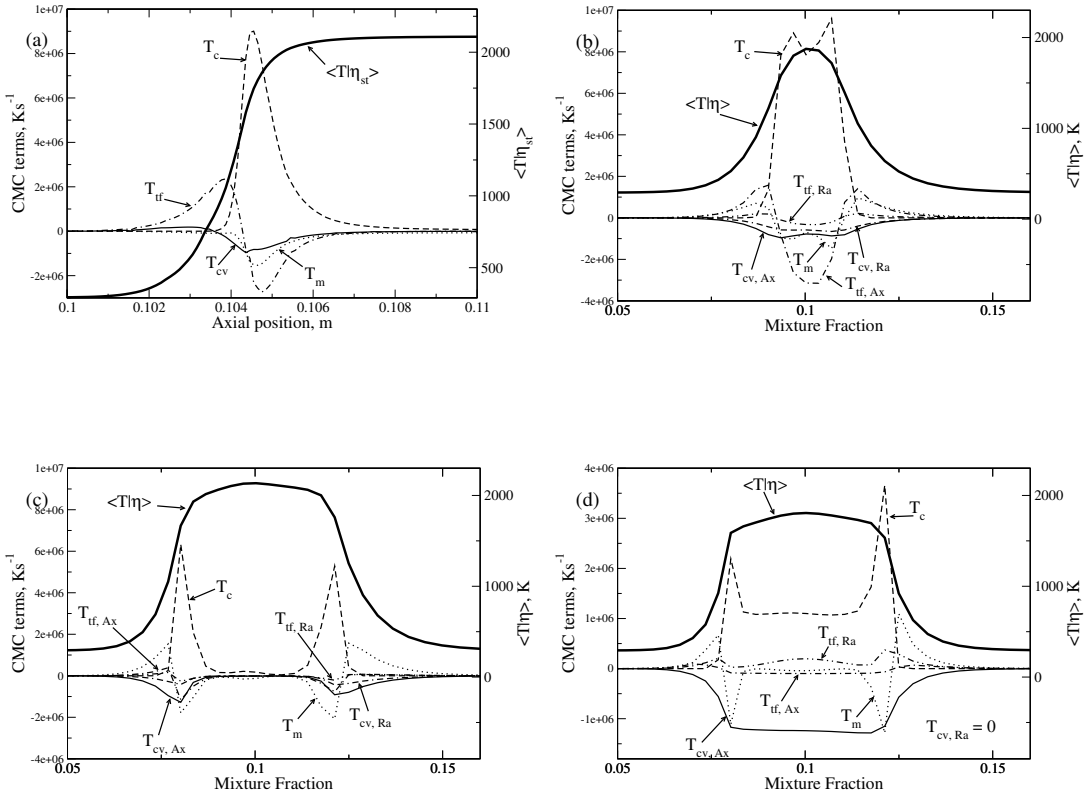

Figure 5.18: Conditional temperature and the balance of terms in the CMC temperature equation for $W_j = 12ms^{-1}$ simulation at $20ms$. (a): Spatial profiles along the mean stoichiometric contour, conditioned on stoichiometry; (b) Mixture fraction profiles at $\langle T|\eta\rangle = 0.8(T_{ad} - T_0) + T_0$ on the mean stoichiometric contour; (c) Mixture fraction profiles at $z = 0.108m$ on the mean stoichiometric contour; (d) Mixture fraction profiles at $\langle T|\eta\rangle = 0.8(T_{ad} - T_0) + T_0$ on the centre line. Simulation 1.

monoxide, molecular hydrogen, hydroxyl radical and atomic oxygen mass fractions are shown in Fig. 5.21. The statistical composition predicted by the CMC model bears a great similarity to the composition observed in detailed calculations of the laminar methane-air triple flame propagation [104]. The most notable feature is the consumption of methane at rich mixture fractions to generate carbon monoxide and hydrogen. It is then the carbon monoxide and hydrogen which are oxidised close to the stoichiometric mixture fraction. It is interesting that the CMC modelling qualitatively reproduces the peak in the oxygen radical concentration at the upstream tip of the flame which is also observed in equivalent laminar flows [104]. Laminar and turbulent DNS studies indicate that differential diffusion effects can be particularly strong at this flame tip, and more precise CMC predictions may require treatment of this process.

The peak value of conditional heat release was $10^7 K s^{-1}$ with the one step and $6 \times 10^6 K s^{-1}$ with the skeletal mechanism, however the scale has been reduced by more than an order of magnitude to bring out less intense regions of heat release. The one step model indicates the lifted flame exhibits three distinct modes of combustion, rich and lean flame fronts and also diffusion controlled reaction close to stoichiometry. The rich propagation is subject to higher oncoming velocity than the lean and it tends to trail the stoichiometric flame more than the lean flames. The skeletal mechanism does not show a rich regime as distinct from the diffusion branch. However a large amount of the heat is released from rich mixtures close to the stabilisation point. The profiles of heat release and major species are remarkably close to those obtained with the one-step mechanism. The stabilisation position has been largely unaffected by using just one reaction step to model the chemistry. In addition to the encouraging agreement in the lift off height prediction, the profiles of heat release and major species are remarkably close to those obtained with a skeletal mechanism. Thus the use of simplified combustion schemes appears appropriate for ignition calculations since the main quantity needed from the combustion model is

the heat release.

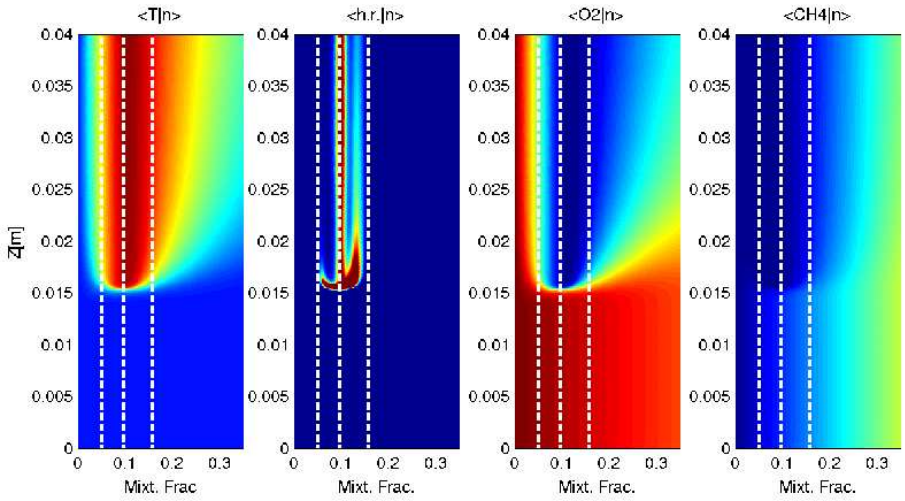

Figure 5.19: Contours of conditional temperature, heat release rate, Y_{O_2} and Y_{CH_4} for the stabilised lifted flame. $W_j = 12.5ms^{-1}$, solved with 1D CMC and the 1-step chemistry model. The lower (blue) and upper (red) bounds of the colour scale for each quantity were; $293 - 2200K$, $0 - 10^6 Ks^{-1}$, $0 - 0.233$ and $0 - 0.35$ respectively. Dashed lines are shown at selected mixture fractions as in Fig. 5.17.

The conditional mean axial velocity is shown in Fig. 5.22. The conditional mean velocity shows a sharp reduction of approximately $0.55ms^{-1}$ on the upstream side of the flame front. It is not clear that the current $k - \epsilon$ modelling is capable of providing an accurate prediction of the mean turbulent flow field through this dilatation, however this reduction in the flame speed is very significant in the stabilisation process. Given the difficulties observed in predicting the flame propagation phase of the ignition process, the accurate prediction of the lift off height by some configurations of the CMC model here, and in previous works [33; 34; 61] may have been fortuitous.

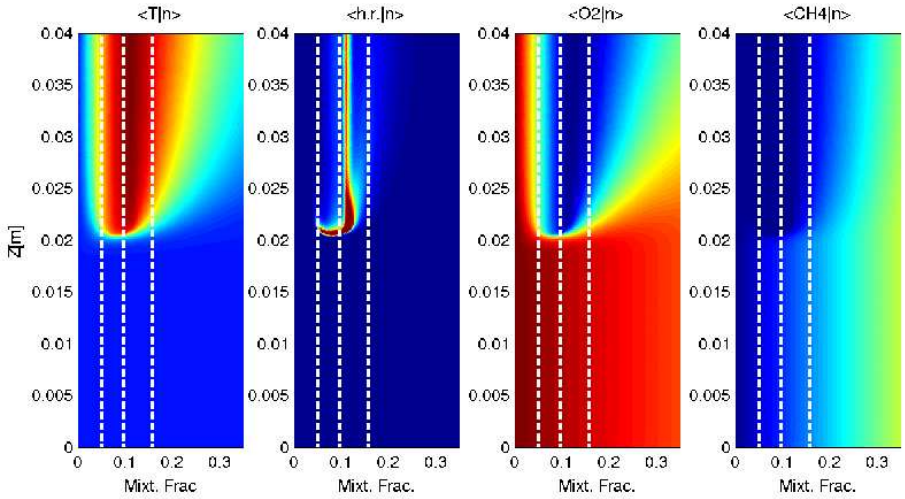

Figure 5.20: Contours of conditional temperature, heat release rate, Y_{O_2} and Y_{CH_4} for the stabilised lifted flame. $W_j = 12.5ms^{-1}$, solved with 1D CMC and the Smooke reaction mechanism. The colour scales and mixture fraction lines are the same as Fig. 5.19.

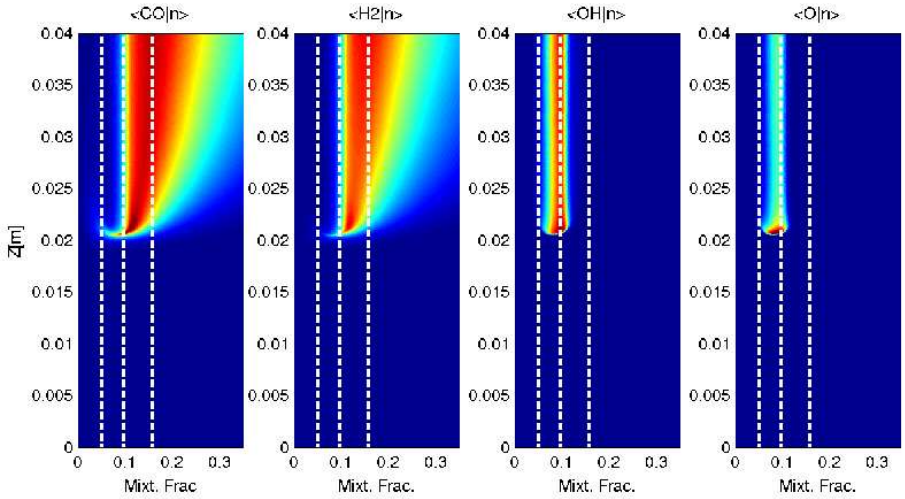

Figure 5.21: Contours of the conditional mass fractions, Y_{CO}, Y_{H2}, Y_{OH} and Y_O for the stabilised lifted flame. $W_j = 12.5ms^{-1}$, solved with 1D CMC and the Smooke reaction mechanism. The the lower (blue) and upper (red) bounds of the colour scale for each quantity were; $0 - 0.045$, $0 - 0.002$, $0 - 0.0045$ and $0 - 0.002$ respectively. Dashed lines are shown at selected mixture fractions as in Fig. 5.17.

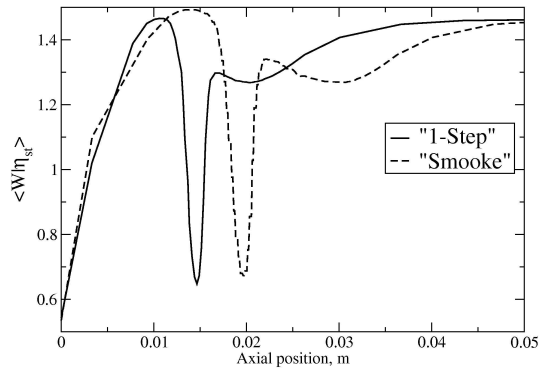

Figure 5.22: The stoichiometric conditional axial velocity for the skeletal and 1-step reaction schemes plotted along the axial direction, for the stabilised lifted flame with $W_j = 12.5ms^{-1}$.

5.3.4 Conditional turbulent flux modelling

An algebraic model for the conditional turbulent flux

An algebraic estimate for the conditional turbulent flux was introduced in chapter 4 based on the debatable assumption of a bi-modal conditional progress variable PDF. The joint progress variable mixture fraction PDF is presented by Veynante and Vervisch in Ref. [144]. The term is similar in form to that arrived at by Bray in the study of premixed flames [14]. It was seen in chapter 4 that this estimate might provide a useful correction to the gradient diffusion model in order to account for counter gradient transport influences present in propagating non-premixed flames. A modelling approach which combines this estimate with the gradient diffusion approximation is now expressed and implemented. In the RANS context the conditional turbulent flux is predicted using Eqs. 5.7-5.9.

$$\langle u_i'' c'' \mid \eta \rangle = -D_t \frac{\partial \langle c \mid \eta \rangle}{\partial x_i} + (\langle u_i \mid \eta \rangle^b - \langle u_i \mid \eta \rangle^u)\langle c \mid \eta \rangle \left(1 - \langle c \mid \eta \rangle\right) \quad (5.7)$$

$$\langle u_i \mid \eta \rangle^b - \langle u_i \mid \eta \rangle^u \approx \tau(\eta) S_E \quad (5.8)$$

$$\tau(\eta) = \left[\frac{\langle \rho \mid \eta \rangle^u}{\langle \rho \mid \eta \rangle^b} - 1\right] \quad (5.9)$$

The most appropriate value used for the laminar edge flame speed S_E is open to debate however it may be useful to express S_E as a function of the scalar dissipation rate based on DNS data [24]. Triple flames reportedly have speeds up to around 1.8 times their planar stoichiometric equivalent. However as a guide S_E should be chosen with the objective of contributing the correct velocity differential $\bar{U}^b - \bar{U}^u \approx \tau S_E$. In this preliminary work the value has been set equal to the laminar stoichiometric flame speed.

Implementation with the conditional moment closure

The gradient and counter gradient components, given by the first and second terms of the right hand side of Eq. 5.7, are used to evaluate T_{tf} and T_{CGD} respectively in Eq. 5.6.

In isolation the counter gradient component or the turbulent flux model leads to numerical instability. The gradient diffusion component combined with the scalar dissipation term in the CMC equation act in a stabilising way and can make the model workable in partially premixed problems like the present lifted flame. It should be noted that if use of Eq. 5.7 results in the unconditional turbulent flux (given by the PDF weighted integral of Eq. 5.7) becoming counter gradient, then the numerical solution of the CMC equation is expected to be unstable irrespective of $\eta-$space dissipation processes. Conversely where the conditional turbulent flux model is counter gradient over a particular range of mixture fraction (perhaps

around stoichiometry where the conditional heat release is highest) but overall the unconditional flux is diffusive, then the numerical stability may be a function of the conditional scalar dissipation rate. Where fractional step methods are employed, a close coupling among these processes is desirable for numerical stability.

The conditional turbulent flux for quantities other than the conditional progress variable may be found by scaling the flux of the conditional progress variable. It is necessary to ensure that this scaling satisfies conservation of mass. To this end, two compositions are selected to represent burned and unburned flow for each mixture fraction, each having its own value of conditional progress variable. Since the progress variable varies from zero to one, the model for the flux of any scalar in the flow becomes Eq. 5.10.

$$\begin{aligned} \langle u_i'' Y_\alpha'' \mid \eta \rangle = & - D_t \frac{\partial \langle Y_\alpha \mid \eta \rangle}{\partial x_i} \\ & + (\langle u_i \mid \eta \rangle^b - \langle u_i \mid \eta \rangle^u) \langle c \mid \eta \rangle \left(1 - \langle c \mid \eta \rangle\right) \frac{\langle Y_\alpha \mid \eta \rangle^b - \langle Y_\alpha \mid \eta \rangle^u}{\langle c \mid \eta \rangle^b - \langle c \mid \eta \rangle^u} \end{aligned} \tag{5.10}$$

In the 1D modelling of the steady lifted jet presented below, the burned and unburned conditional compositions have been selected as those at inlet (inert mixing) and at the exit. The model is not guaranteed to be stable and some initial conditions resulted in numerical problems.

Analysis of the counter-gradient flux modelling

The steady lifted jet flame, $W_j = 12.5 ms^{-1}$ was simulated with and without the new modelling for the turbulent flux term. The resulting profiles of the stoichiometric CMC terms along the axial direction are shown in Fig. 5.23. The roles of the CMC terms in Fig. 5.23a are the same as those observed in the upstream flame front throughout the propagation phase, for example in Fig. 5.18a. The inclusion of counter gradient effects into the model resulted in a slight increase in lift off height

and a notable reduction in the flame thickness. The counter gradient term acts to take heat and products away from the upstream side of the lifted flame front and move it back toward the burned, product rich side of the flame. The resulting reduction in flame thickness leads to an increase of the gradient diffusion component in the turbulent flux model. This model requires extensive development and validation. This might be achieved through comparison with detailed experimental measurements, or further turbulent DNS data. In the first instance though, the model may be improved through experience of its application to a broader range of flows and conditions.

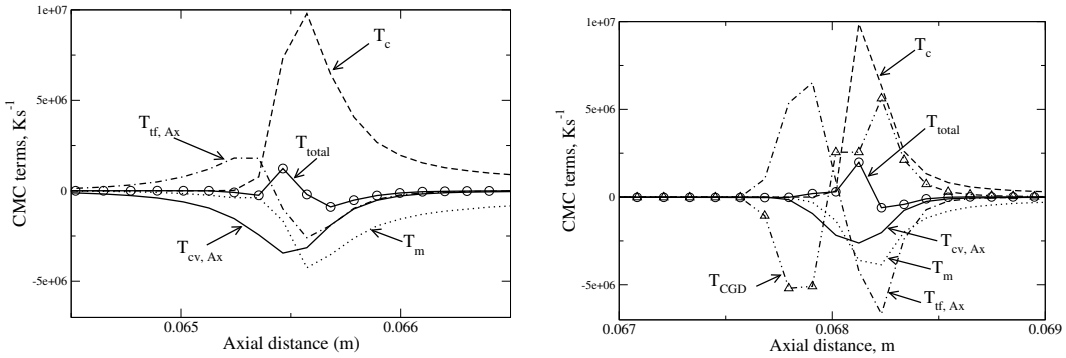

(a) (b)

Figure 5.23: The balance of the CMC temperature equation terms, for 1D coupled simulations of the stabilised $W_j = 12.5ms^{-1}$ lifted flame; (a): with the standard eddy diffusivity model; (b): with the conditional counter gradient diffusion term.

5.4 Conclusions

The CMC modelling described in chapter 2 has been implemented for the solution of flame ignition, propagation and stabilisation in a methane jet. An axi-symmetric formulation of the first order CMC model has been fully coupled with

a RANS flow field solution. This represents a new and challenging test of the CMC model, allowing comparison with the experimental observations of Ahmed and Mastorakos [2; 3], and provides a first step toward the application of the CMC to industrial ignition simulations.

A model for the spark ignition process has been used to explore the processes limiting spark ignition in this flow. The model captured successful and unsuccessful ignition depending on the ignition energy. The model analysis was able to indicate that due to low turbulent mixing rates at the ignition locations ignition was limited by whether the spark's energy density was sufficient to induce auto-ignition in the spark region. Qualitative agreement with chapter 4's CMC analysis of DNS for non-premixed spark kernels is apparent.

Study of the transient flame propagation phase shows that the expansion across the flame has a strong effect on the propagation speed. Therefore a full coupling of the flow field and the combustion processes needs to be included in predictive calculations. The over prediction of flame propagation rates is attributed to possible over statement of the conditional reaction rate due to its first order closure, and the use of the RANS turbulence closure. Alternative CMC closures which account for fluctuations around the conditional averages, and turbulence models where the large scale motions (for example LES) are resolved may be needed.

The propagating turbulent edge flame has a relatively narrow profile across the mixture fraction sample space, with strong heat release associated with rich and lean premixed fronts. The scalar dissipation rate experienced by the flame front increases close to the nozzle, hence the flame spreads further across mixture fraction space as it propagates closer to the nozzle and stabilises. The contribution of diffusion flame elements increases.

The performance of a one-step reaction model with variable model parameters produces excellent results for this problem compared to a skeletal mechanism for

methane combustion. The use of similar reaction models is recommended for intensive industrial simulations of partially premixed propagation where the heat release rate is of primary interest.

A new modelling approach which incorporates counter gradient transport effects into the conditional turbulent flux model has been demonstrated. The model results in a modification to the structure of the conditional flame profiles, however it does not change the prediction of the lift off height greatly. The model needs further development and validation before it may be used reliably, this may require detailed experimental or numerical studies.

Chapter 6

Modelling for ignition of bluff body stabilised flames

This chapter presents the application of the CMC model to the ignition of a bluff body stabilised, non-premixed methane flame, and a swirl/bluff body stabilised $n-$heptane spray fueled flame. The predictions for the global spreading rate of the flame are compared to those from experimental studies of the flows [3; 83].

6.1 Background

The turbulent wake behind bluff bodies is widely used for stabilisation of flames in engineering applications. In addition, bluff body stabilised flames are expected to exhibit similar flow and combustion phenomena to those occurring in more complicated industrial burners. The geometrical simplicity of some bluff body designs makes them useful candidates for experimental and computational study of industrially important combustion processes. Axi-symmetric flows with axial swirl can provide a useful proxy for study of aviation gas turbine combustion. For example, motivated by their study of aero-engine combustion instabilities, Balachandran et al. [6] and Armitage et al. [5] used a cone stabilised flame in a premixed flow for their study of the acoustic response of the flame. A broad range of flow patterns

may be achieved depending the burner geometry and flow conditions. This chapter involves the study of spark ignition in an enclosed, axi-symmetric bluff body flow with non-premixed fuel/air injection, therefore the current discussion is restricted to flows of this type.

The main features of an axi-symmetric bluff body flow are illustrated in Fig. 6.1, which are a conical bluff body of diameter $D1$ and half angle *theta*. Axial swirl may be introduced upstream of the bluff body. The blockage ratio is defined as $D1^2/D3^2$, and the diameter of the enclosure equals $D2$.

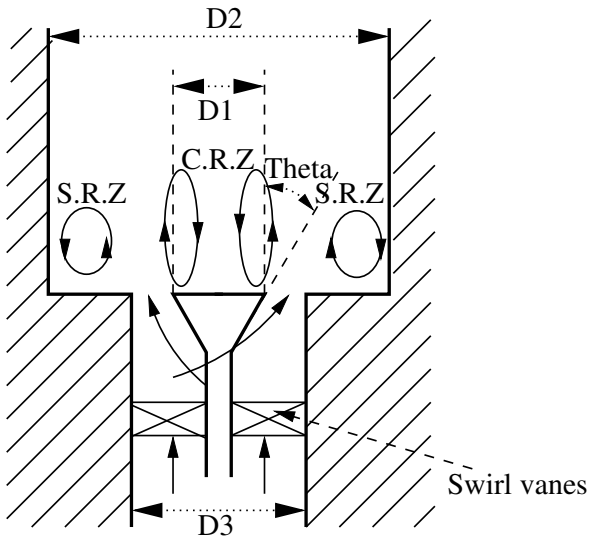

Figure 6.1: A schematic diagram of the bluff body configuration. The expected flow pattern is indicated with solid arrows. The central recirculation zone (CRZ) and side recirculation zones (SRZ) are labeled.

The mean flow field is expected to include a central, toroidal recirculating structure and an outer counter rotating, toroidal recirculation. Swirling flows may exhibit a precessing vortex core [130]. The relative sizes, velocities and turbulence levels associated with these structures are governed by an individual burner's geometry, flow conditions and also the presence of a fuel source and combustion. Some general trends for bluff body aerodynamics are noted below.

Where the Reynolds number based on $D1$ exceeds 10^4, the central recirculation

zone in a non-swirling, non-combusting flow around a bluff body is typically $1.5 \times D1$ long and $1 \times D1$ wide. In general, an increase in the bluff body cone angle increases the peak turbulent kinetic energy of the flow, particularly when approaching the limit of a disk shaped body. This results in greater entrainment of fluid into the recirculation [131]. For a constant volume flow rate, an increase in the blockage ratio also increases the turbulence level [94]. As the confinement ratio, $D1/D2$, is increased the mean velocities associated with the re-circulations rise and their size increases [121]. In non-reacting, non-swirling flows the confinement is not expected to effect the flow field at confinement ratios below 0.5 [121].

Highly swirling flows are relatively insensitive to the details of the bluff body [49]. The increased azimuthal momentum component results in a far larger central recirculation zone, and the swirling flow provides new mechanisms for turbulence generation away from the bluff body [101]. The increased radius of the central recirculation zone means the confinement may be significant at values of $D1/D2 < 0.5$.

The expansion due to combustion will also tend to increase the volume of the central recirculation zone, and to modify the turbulent mixing processes. Therefore the overall flow structure may evolve significantly during ignition and flame stabilisation.

The mixing of fuel streams with the flow behind the bluff body is relevant for non-premixed and spray fueled burners. Three modes of fuel input are considered. These are axial and radial flows of gaseous fuel, and axial liquid fuel sprays. The axial fuel streams in particular influence the flow field [93] since they oppose the back-flow in the central recirculation zone. The mixing of an axial fuel jet with the large scale motions inside the recirculation zone introduce large scale intermittency into the fuel distribution [90]. The fuel concentration distribution resulting from a spray may be less intermittent due to the ability of an inertial spray to penetrate the gaseous structures.

Radial injection from the side of the bluff body is expected to modify the turbulence and velocity profiles past the bluff body. A similar type of changes to the bluff body boundary layer may be expected from altering the cone angle [82]. This analogy suggests that the recirculation zone sizes and turbulence may be modified slightly by radial fuel injection, however the essential flow structure remains unchanged.

6.2 CMC simulation

6.2.1 Flow configuration

The first order CMC model is used to simulate spark ignition of a non-premixed methane-air burner and a swirl stabilised $n-$heptane spray burner. The bluff body geometries used are the premixed, non-premixed and spray fueled configurations of the burner studied in Cambridge by Balachandran [6], Ahmed [1] and Marchione [83], shown in Fig. 6.2.

In all cases the enclosure ($70mm$ diameter, $80mm$ length), bluff body diameter ($25mm$), and cone angle (45^o) are identical. As shown in Fig. 6.2, differences arise in the geometry of the bluff bodies due to the differing modes of fuel input. The non-premixed burner uses annular fuel injection through an opening around the entire circumference, $0.7mm$ high, $2.0mm$ from the bluff body face. The non-premixed bluff body protrudes $1mm$ into the enclosure, while the bluff body face is flush in the other cases. The liquid fueled burner has a 60^0 hollow cone fuel nozzle positioned centrally in the bluff body [83]. The premixed configuration is used for assessment of the velocity calculations since it is the only configuration for which Laser Doppler Anemometry (LDA) data are available.

Ignition is achieved by means of tungsten spark electrodes with $1mm$ electrode thickness and an adjustable spark gap. The nominal spark parameters used

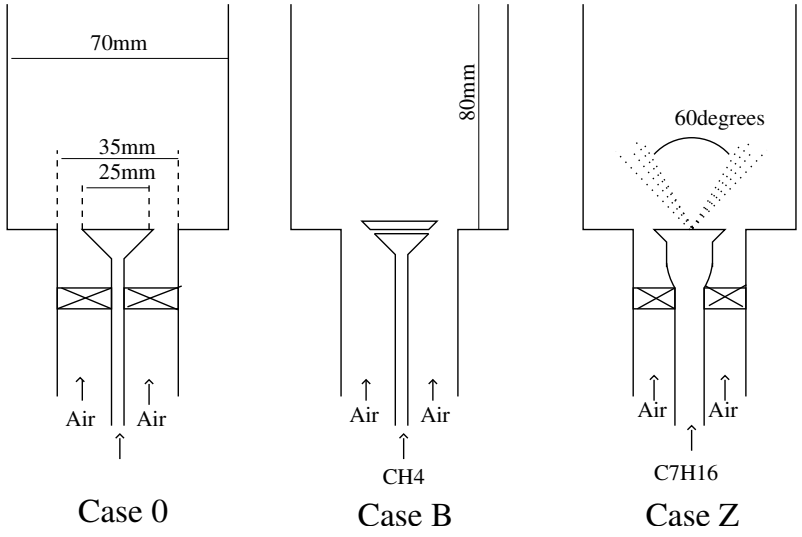

Figure 6.2: Burner geometries: premixed, non-premixed and spray fueled from left to right.

for ignition of the non-premixed burner were a $2mm$ spark gap, $200mJ$ electrical energy, and $500\mu s$ duration. The spray fueled burner used a $3mm$ spark gap $200mJ$ electrical energy, and $400\mu s$ duration.

The bluff body flows considered in chapters 6 and 7 are classified according to Table 6.1.

Run	Fuel flow	$\dot{Q}_1(l.min^{-1})$	$\dot{Q}_2(l.min^{-1})$)	Configuration
0	N/A	N/A	282.28	Premixed
B	CH_4	13.4	282.28	Non-premixed
BP	Air & Acetone	6.6	282.28	Non-premixed
Y	$n-C_7H_16$	0.0366	479.89	$150\mu m$ spray nozzle
Z	$n-C_7H_16$	0.0145	282.28	$100\mu m$ spray nozzle

Table 6.1: Classification of bluff body flows, giving the volume flow rates of the fuel and air streams, $\dot{Q}_1$ and $\dot{Q}_2$ respectively.

6.2.2 Turbulent flow field

CFD meshes have been generated for the three flow geometries and simulated using the CFD package STAR-CD [20]. Previous Reynolds stress RANS CFD of

case 0 solved the flow only within the enclosure and used a uniform $0.5mm$ axi-symmetric mesh [5]. To allow fuel mixing and flow development prior to the flow entering the enclosure the axi-symmetric domain used in this work extends up to the swirler exit plane. Due to apparent sensitivity to the exit boundary location, the solution domain extends $0.08m$ further downstream than the enclosure and has a radius of $0.07m$ radially. The CFD mesh used in this work contains around 26400 cells (depending on the geometry modelled) with refinement down to $63\mu m$ in the region of the non-premixed fuel inlet and the annulus exit shear layers. A 10^5 cell grid was also produced to demonstrate that the flow solutions are grid independent. Reynolds stress (Gibson-Launder) and alternatively the RNG $k-\epsilon$ model solutions were employed without modification, see Ref. [20] and references there-in.

Velocity field

LDA data for the mean velocity and the velocity variance in case 0 have been provided by Balachandran et al. [31]. This technique can provide accurate instantaneous velocity measurements of virtually inertia-less droplets seeded in the flow. The greatest limitation of the technique in this application is likely to be the accuracy with which the measurement location is known in the experiment's coordinate system. The CFD flow field predictions are compared with the averaged velocity and Reynolds stress component profiles in Fig. 6.3. Additional hot wire measurements of the mean and R.M.S. axial velocity across the annular inlet are shown in Fig. 6.4.

The flow through the annular inlet is captured reasonably well. The speed of the recirculation's back flow is over predicted, and the predicted length of the central recirculation zone is larger than the measured length. The prediction of the Reynolds stresses is generally poor, particularly at the $z = 25.5mm$ transect which is close to the end of the measured recirculation zone but relatively near the middle of the recirculation zone in the CFD prediction. The free stream flow field

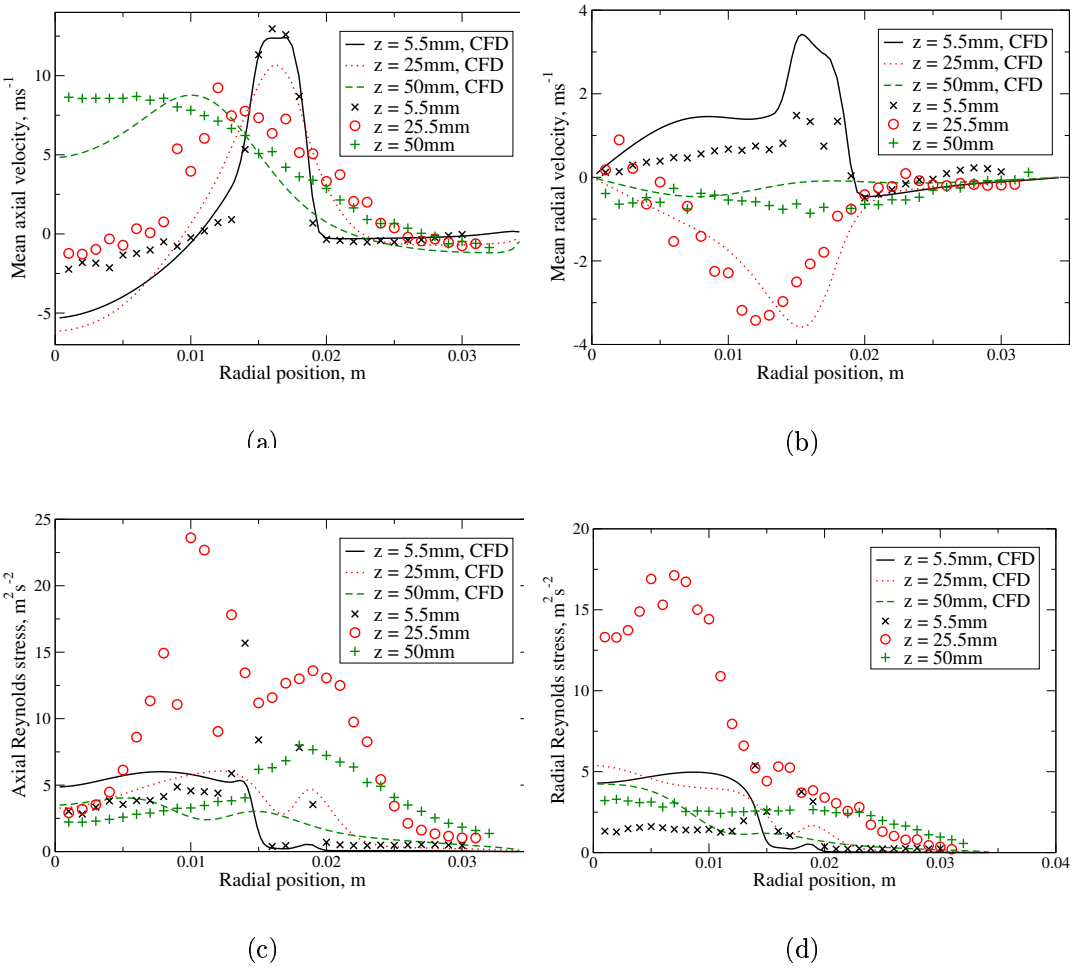

Figure 6.3: A comparison of the Reynolds-stress CFD solution with PDA measured velocity moments for case 0, [31]. (a): mean axial velocity; (b): mean radial velocity; (c): axial Reynolds stress, $\widetilde{ww}$; (d): radial Reynolds stress, $\widetilde{uu}$.

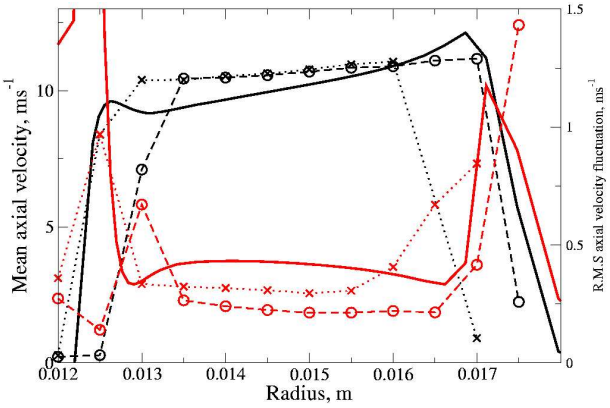

Figure 6.4: Mean (black) and root mean square (red) axial velocity profiles across the inlet annulus. Measurements from positions 180^o apart are shown by crosses and circles, the Reynolds stress prediction is the solid line. Hot wire velocity measurements by S.F. Ahmed.

changes very little with increased numerical resolution, increased inlet turbulence levels, or the use of the Speziale et al. Reynolds stress model [126] (not shown). The predicted recirculation zone size is very close to that predicted entirely independently by Armitage et al. [5] using a Reynolds stress model. It may be expected that the current CFD predictions would be improved by going to the considerable computational expense of a LES solution.

Mixture fraction distribution

The mean and variance of mixture fraction has been measured using acetone-PLIF by Ahmed and Mastorakos [3], and is shown in Fig 6.5. This shows the recirculation bubble is relatively well mixed (low mixture fraction variance compared to $\widetilde{\xi}(1-\widetilde{\xi})$) and that it is surrounded by a turbulent mixing layer where the fuel concentration drops to near zero. Subsequent measurements of mixture fraction using a gas sampling probe and a fast ionisation detector, indicate that the absolute level indicated by the PLIF measurements may be too high, Fig. 6.6.

The mean and R.M.S. mixture fraction contours predicted using the Reynolds

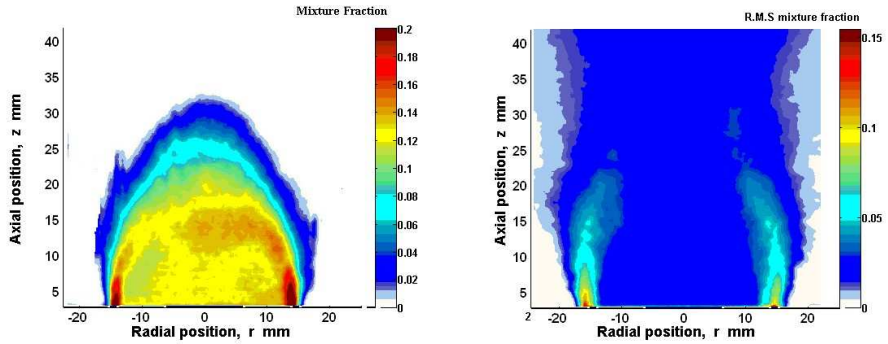

(a) (b)

Figure 6.5: (a) Mean and (b) R.M.S. mixture fraction measurements for case B_{PLIF} [3].

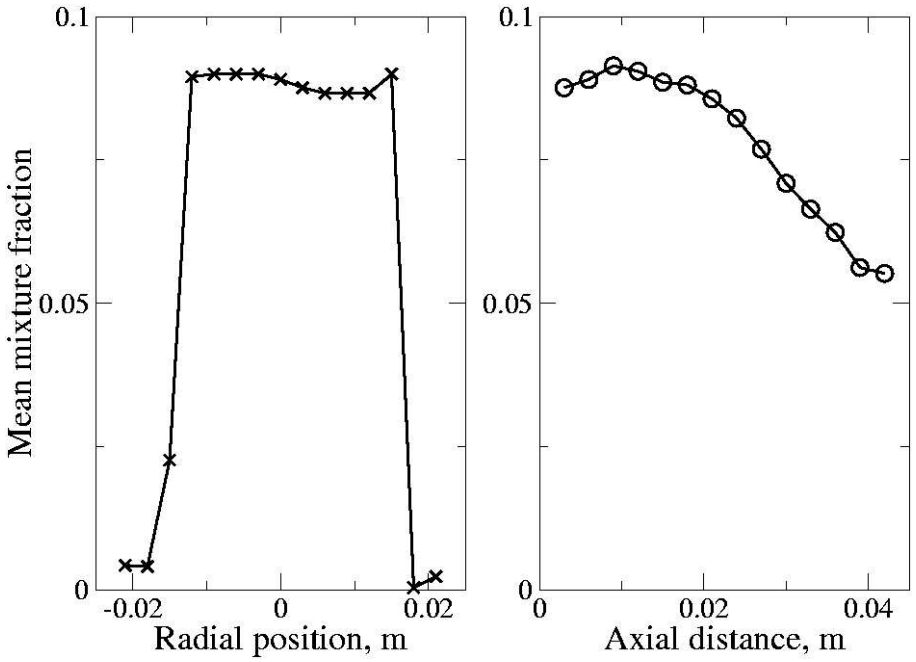

Figure 6.6: Radial ($z = 0.1m$) and axial ($r = 0$) profiles of the mean mixture fraction for un-reacting flow in case B. F.I.D. measurements by S.F. Ahmed.

stress model are plotted for case B in Fig. 6.7. Figure 6.8 shows the solution found using the $k-\epsilon$ model. In general the RANS modelling provides unsatisfactory agreement with the measured mixture fraction distribution for all flow conditions. The $k-\epsilon$ model produces a richer recirculation and hence closer agreement to the measurements for case B.

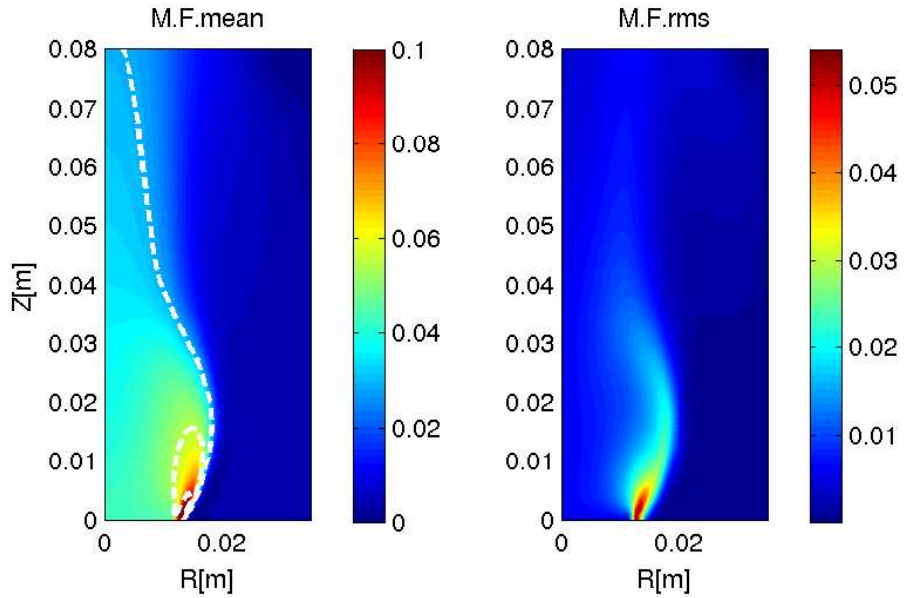

Figure 6.7: Mean and R.M.S mixture fraction contours for case B using the Reynolds stress model.

In view of the uncertainties regarding the experimental data and also the unclear ability of either $k-\epsilon$ or Reynolds stress modelling to capture this flow, this work proceeds to use the Reynolds stress model on the grounds that it is generally perceived to be the better predictive turbulence model, particularly in swirling flows such as case Y.

Spray transport

The $n-$heptane fuel spray of cases Y and Z has been modelled using a Lagrangian parcel based approach with the modelling implemented in STAR-CD [20].

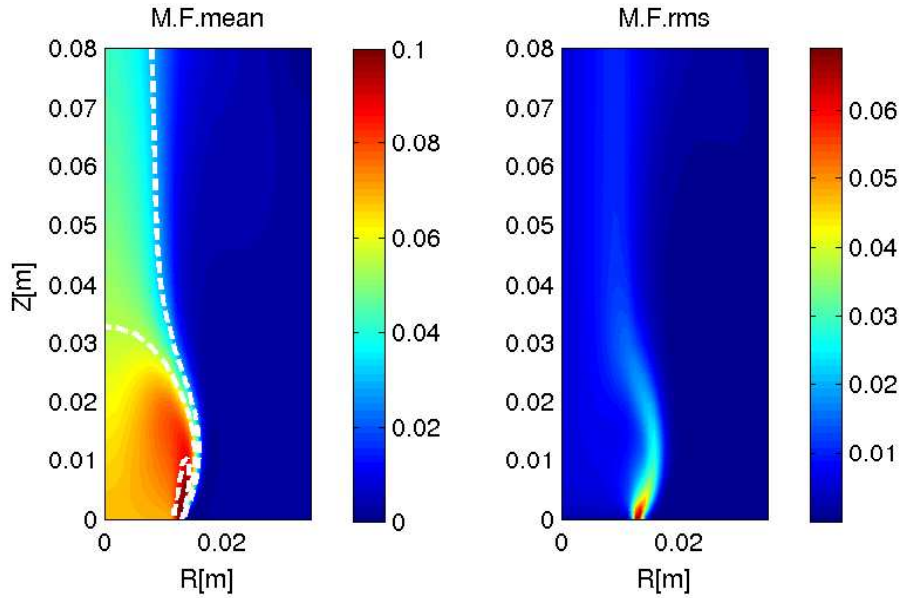

Figure 6.8: Mean and R.M.S mixture fraction contours for case B using the RNG $k-\epsilon$ model.

The conservation equations for the continuous and dispersed phases and the standard modelling used are presented in Ref. [20]. The properties of the liquid $n-$heptane are evaluated as functions of temperature and pressure within the CFD solver. The Reitz and Diwakar [106] model for droplet break up has been selected.

The specification for the pressure swirl fuel injectors indicates that a spray Sauter mean diameter of $30\mu m$ can be expected. The droplet diameter distribution is presumed using the Rosin-Rammler function (with $q = 2$)[117] ensuring that the correct Sauter mean diameter is achieved. The fuel flow rates measured for 5 *bar* injection pressure indicate an extremely high injector discharge coefficients 0.9, as defined by Lefebvre [76]. This indicates the liquid flow through the orifice encounters minimal blockage from any air core, and the droplet injection velocity magnitude has been estimated as the fuel flow rate divided by the orifice area. The resulting velocity is around $34ms^{-1}$ for both injector diameters. The initial droplet trajectories are distributed uniformly within a hollow cone with inner and outer included angles of 55^0 and 65^0, respectively.

The transport equation for the mean and variance of mixture fraction are solved within the CFD code with the additional source terms discussed in chapter 2.

A steady state solution is obtained prior to ignition of the flow. The velocity field for the un-reacting flow is shown in Fig. 6.9. The 60^o swirl imparted to the flow results in a marked change to the flow structure compared to the non swirling flow. The large azimuthal momentum component causes the bulk of the inflow to curve outward and impinge on the enclosure. The axial flow induced by the conical spray is visible in Fig. 6.9b. Significant evaporation takes place in the cold

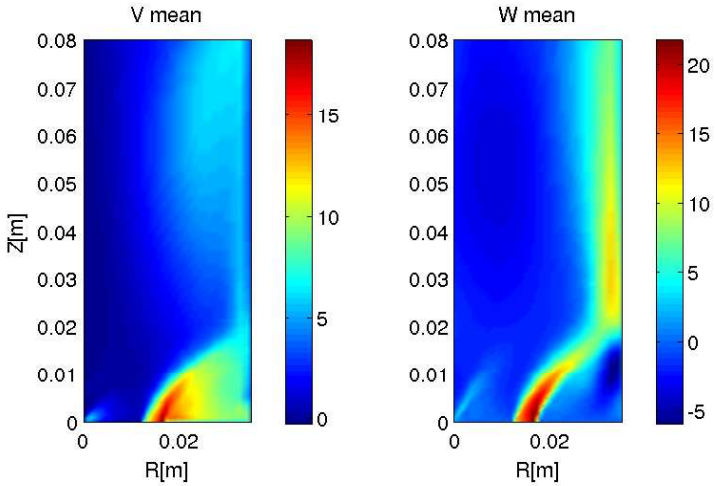

Figure 6.9: (a): Mean azimuthal velocity, V (ms^{-1}); (b): Mean axial velocity, W (ms^{-1}). Case Y prior to ignition.

flow (the saturation mixture fraction at 298K is 0.144). Mixture fraction mean and variance prior to ignition are shown in Fig. 6.10. The instantaneous droplet parcel distribution inside the 20^o axi-symmetric sector for case Y, Fig. 6.11b, shows qualitative agreement when compared with an instantaneous image of the observed droplet field as illuminated by a laser sheet, Fig. 6.11a.

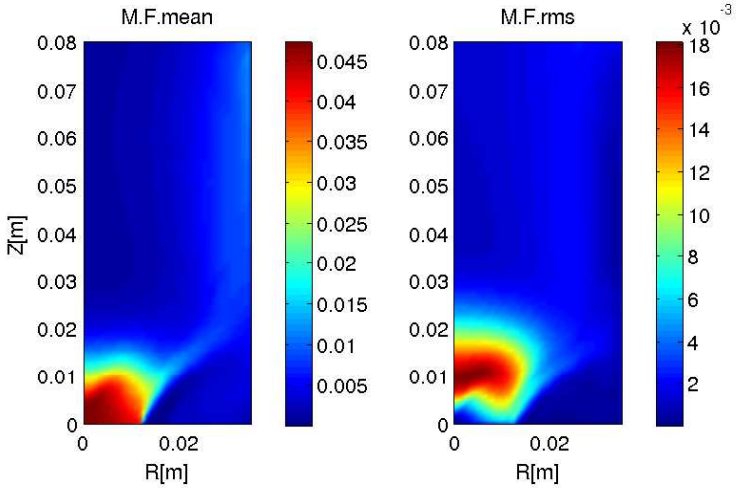

Figure 6.10: (a): Mean and (b): variance contours for mixture fraction, case Y prior to ignition.

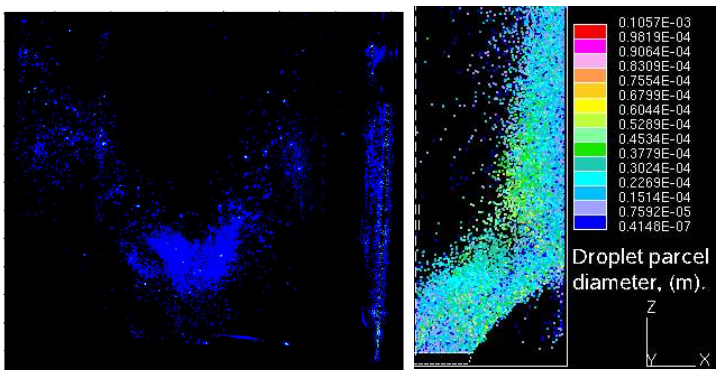

(a) (b)

Figure 6.11: (a): Instantaneous cross sectional Mie scattering image of the non-burning fuel spray, case Z. The bluff body is central, image dimensions: $70mm$ wide and $80mm$ high, a reflection from the glass enclosure shows along the right hand side; (b): A predicted droplet parcel distribution prior to ignition for case Y. The image is the right hand half of a transect across the injector, which is at the bottom left corner, image dimensions: $35mm$ wide and $80mm$ high.

6.2.3 Application of the CMC model

A 2D axi-symmetric solution of the 1st order CMC is coupled with the flow solver as described in chapters 2 and 5. The CMC model is used to compute ignition of both gas and spray fueled flames. The CMC sub-models and their implementation are those described in chapter 2. Both methane and $n-$heptane oxidation are modelled using the Fernández-Tarrazo et al. one step reaction model [37; 112]. The conditional species transport equation including the terms resulting from fuel evaporation is given in equation 6.1:

$$\begin{aligned}\frac{\partial Q_\alpha}{\partial t} + \langle \mathbf{v}|\eta\rangle \cdot \nabla Q_\alpha &= -\frac{div(\rho_\eta \langle \mathbf{v}'' Y_\alpha''|\eta\rangle P(\eta))}{P(\eta)\rho_\eta} + \langle W|\eta\rangle + \langle N|\eta\rangle \frac{\partial^2 Q_\alpha}{\partial \eta^2} \\ &\quad + S(\eta)Y_{S\alpha} - S(\eta)Q_\alpha - (1-\eta)S(\eta)\frac{\partial Q_\alpha}{\partial \eta} \end{aligned} \tag{6.1}$$

The CMC domain is initialised with an inert mixing solution, which is also used for the boundary condition at the domain's inlet and along the surfaces of the bluff body and of the enclosure. The mixture fraction boundaries, $\eta = 1$ and $\eta = 0$ represent pure fuel (either methane or $n-$heptane) and pure air.

Spark model

The flows were ignited by prescribing a burning zero dimensional CMC solution in the ignition region as described in chapter 2.

Numerical implementation

The spatial grid extends 0.16m downstream of the bluff body and is refined in both axial and radial directions throughout the recirculation zone. The grid used ($N_Z = 80$, $N_R = 40$) has minimum cell dimensions of $\Delta Z_{min} = 0.8mm$ and $\Delta R_{min} = 0.75mm$. The discretisation and integration methods are presented in

chapter 2.

6.2.4 Numerical sensitivity of the CMC solution

A detailed sensitivity analysis for the 2D coupled 1st order CMC implementation was conducted in chapter 5 for methane fuel. Based on that experience an 81 node grid is used in mixture fraction space and the maximum Δt_{CMC} considered is $10^{-5}s$. Furthermore, solutions on the $N_Z = 80$, $N_R = 40$ grid with a global time step of $\Delta t_{global} = 10^{-5}s$ are shown to be satisfactory by comparison with ignition simulations on a $N_Z = 120$, $N_R = 60$ grid, and also using $\Delta t_{global} = 10^{-6}s$. This is demonstrated by the close agreement of the mean velocity and temperature contours for a test ignition problem simulated on the 80×40 node grid with $\Delta t_{global} = 10^{-5}$ with those achieved with higher spatial and temporal resolution at $10ms$ after ignition.

The grid resolution necessary to satisfactorily solve the CMC equation in this bluff body burner is around an order of magnitude lower than in the lifted jet of chapter 5. Due to the significant reverse flow in the bluff body stabilised flow, the propagation rate is less sensitive to the number of points resolving the conditional gradients.

The runs that follow use a time-step less than or equal to $10^{-5}s$ and resolution equal to that of the $N_Z = 80$, $N_R = 40$ grid.

6.2.5 Target simulations

The CMC model has been evaluated to predict the transient ignition and stabilisation processes in bluff body flames:

1. Flame propagation in the methane burner (Case B): section 6.3 [3];

2. Flame propagation in the n-heptane burner (Case Y): section 6.4 [83];

6.3 Results and discussion: Methane flame

The ignition of case B by a spark located at $z = 25mm$, $r = 0mm$ has been simulated for comparison with the experimental OH-PLIF provided by Ahmed et al [1], Fig. 6.12. Contours of the simulated mean temperature and mean heat release

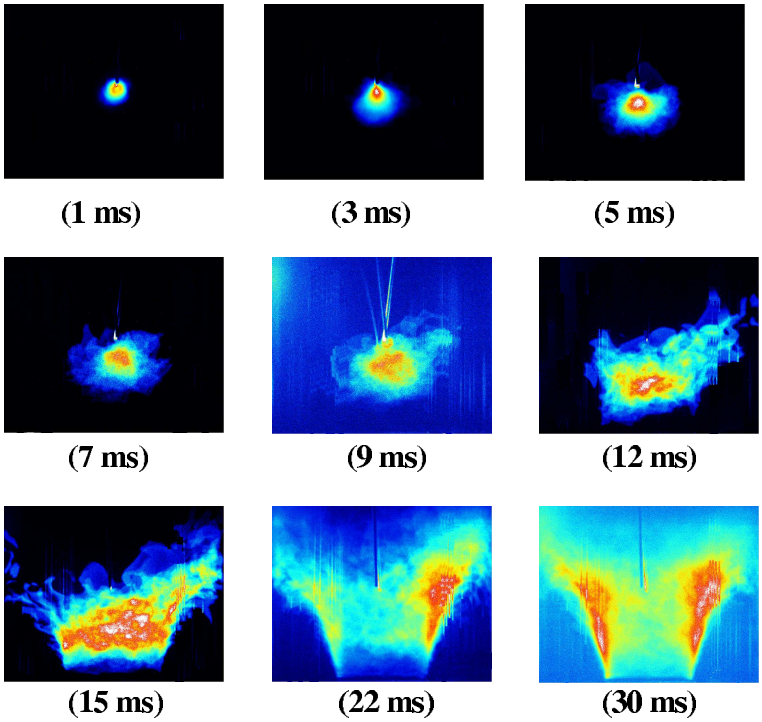

Figure 6.12: Average OH-PLIF images at different times from the spark. Case B. Ignition at $z = 25mm, r = 0mm$. The images cover a region of 70x50mm [1].

rates are shown in Fig. 6.13 and Fig. 6.14. The hydroxyl radical level indicated in Fig. 6.12 is expected to be closely correlated with the reaction rate and hence the heat release rate. The simulation indicates that the flame rapidly propagates and convects across the recirculation zone and then appears to attach to the lip of the bluff body. Subsequently the flame propagates through out the enclosure

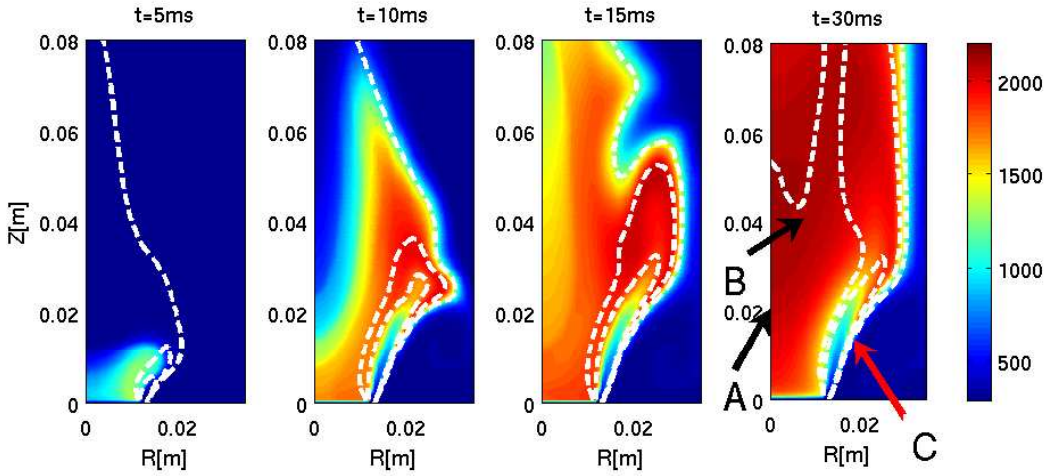

Figure 6.13: Simulated unconditional temperature evolution for case B, (K). The dashed white lines are iso-lines of mean mixture fraction, the inner-most representing the rich flammability limit ($\xi = 0.089$), the next line is stoichiometric ($\xi = 0.055$) and the outer line represents the lean flammability limit, ($\xi = 0.0289$).

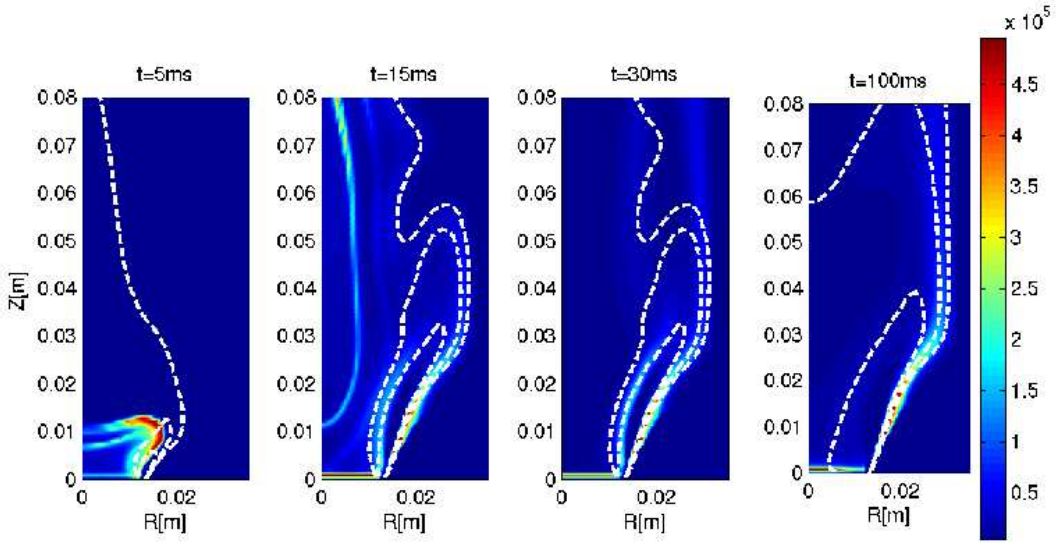

Figure 6.14: Simulated unconditional heat release rate evolution for case B, (Ks^{-1}). Iso-lines of mean mixture fraction are shown as in Fig. 6.13.

accompanied by significant mean thermal expansion. The thermal expansion leads to a permanent change in the nature of the flow, so that when the flow stabilises (after $60ms$) it contains a larger recirculation zone with the inlet air impinging on the enclosure.

The simulation predicts faster growth of the flame kernel than that indicated by the OH-PLIF measurements. The over-prediction of the rate at which the flame moves toward the bluff body is consistent with the over prediction of the reverse flow velocity noted in Fig. 6.3. A further contribution to the over-prediction of the rate of flame propagation may be that the predicted mixture fraction level in the central recirculation zone is close to stoichiometric while the measured value is close to the rich extinction limit.

Mean flow dilatation is seen to have a large effect on the flow by the evolution of the mean mixture fraction and the mean axial velocity as shown in Fig. 6.15. The final position of the flame appears to agree with the available OH-PLIF measurements however the region of peak heat release is thinner.

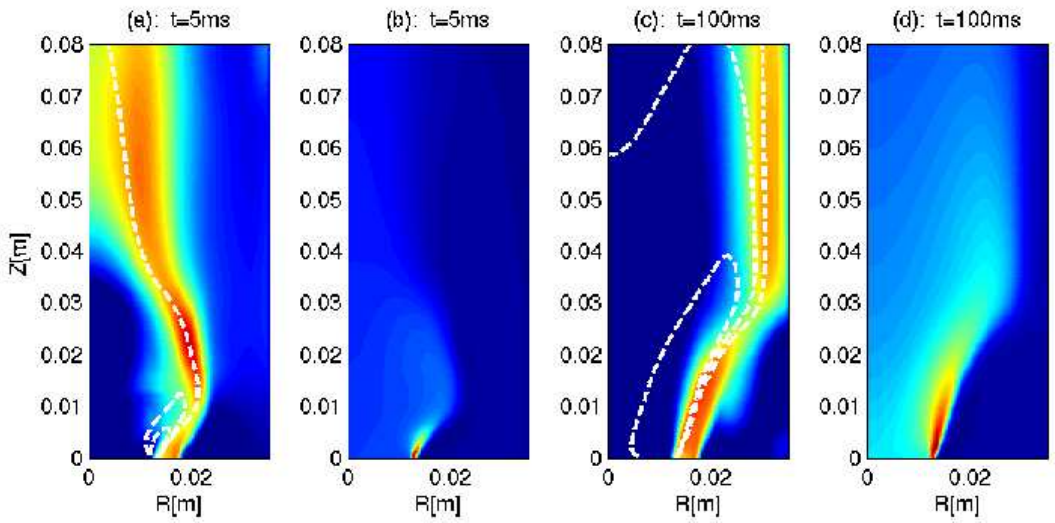

Figure 6.15: Simulated unconditional mean axial velocities for case B at (a): $5ms$ and (c): $100ms$, and the corresponding mean mixture fraction contours (b) and (d). The iso-lines of mean mixture fraction are shown in (a) and (c) as in Fig. 6.13. In the colour scale, red corresponds to $15ms^{-1}$ and $w = \xi = 0.5$, and blue corresponds to $w = 0ms^{-1}$ and $\xi = 0.0$.

The presumed mixture fraction PDF and the conditional temperature profiles at points A ($r = 0m$, $z = 0.02m$), B ($r = 0.01m$, $z = 0.04m$), and C ($r = 0.015m$, $z = 0.021m$), indicated in Fig. 6.13, are shown in Fig. 6.16 for the stabilised flame $t = 100ms$. Points A and B are inside the recirculation and share very similar mixture fraction PDFs and conditional temperature profiles. At rich mixtures the conditional temperature profile is far from the 'triangular' profile which would be expected from a zero dimensional CMC calculation at equivalent conditions. This difference arises due to continual addition of unreacted mixture into the domain. Point C encounters leaner mixtures in the stabilised flame, with the presumed PDF including a delta function corresponding to pure air (not visible). The conditional temperature profile also shows a deviation from that found in the recirculation zone particularly at mixture fractions outside of the flammable range.

The CMC solution around point C is discussed further. Figures 6.17a and 6.17b show the spatial profiles of the CMC temperature equation on axial and radial

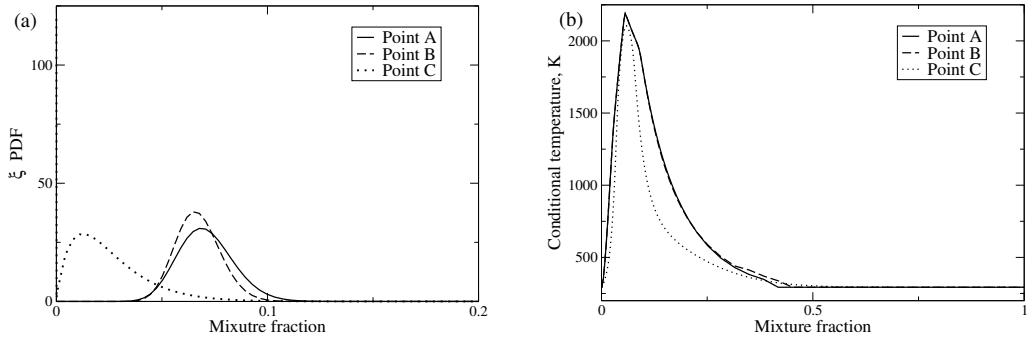

Figure 6.16: Profiles of (a) the mixture fraction PDF, and (b) the conditional temperature at points A, B and C at $t = 100ms$.

transects respectively through point C. These show regions where the CMC terms are negligible corresponding to the un-reacting flow issuing from the inlet. Elsewhere the chemical reaction and molecular mixing are dominant, with convection generally having a greater role than turbulent diffusion in the spatial transport of the flame.

Figure 6.17c shows the mixture fraction space profiles of the terms in the CMC temperature equation at point C. The chemical heat release rate displays three peaks consistent with the presence of tribrachial flame structures.

6.4 Results and discussion: Spray fueled flow

The ignition of case Y by a spark located at $r = 0mm$, $z = 23mm$ has been simulated using the CMC for comparison with the fast camera images of flame propagation shown in Fig. 6.18 by Marchione et al. [83]. These images give an indication of instantaneous flame positions viewed across the flow. Close inspection of the video sequence suggests that the early flame kernel processes around the spark electrodes, however in general, the three dimensional structure of the flame is not easily understood from these images.

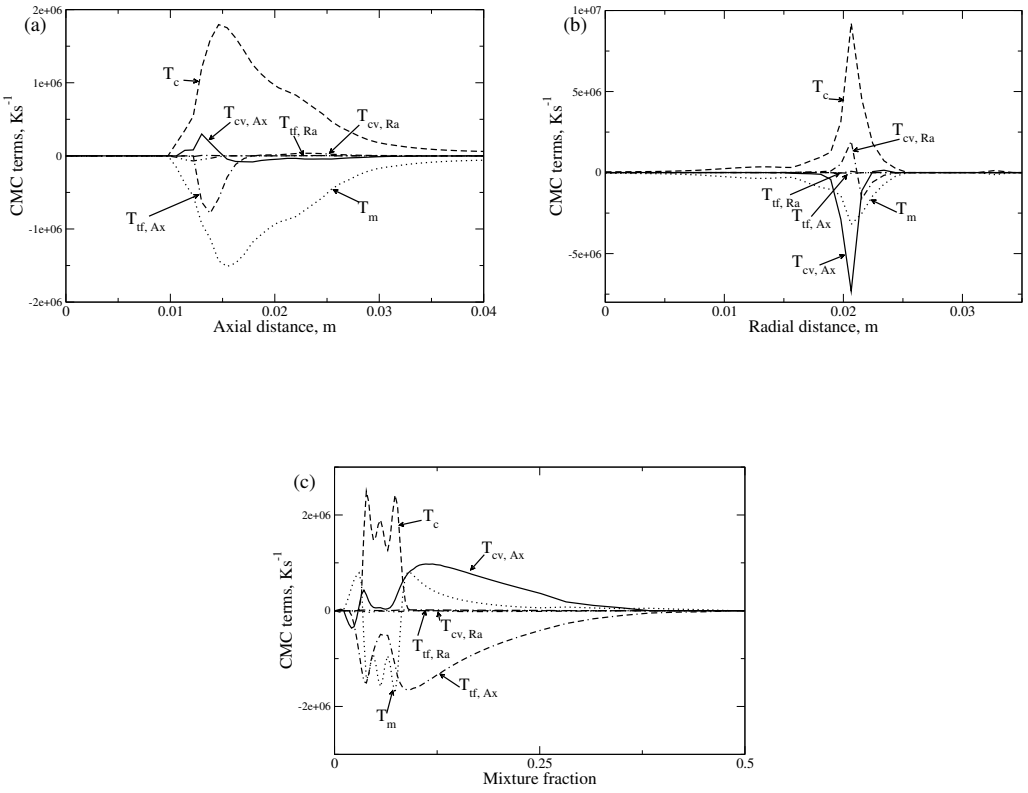

Figure 6.17: Conditional temperature and the balance of terms in the CMC temperature equation for case B, $100ms$ after ignition. (a): Spatial profiles along an axial transect through point C, conditioned on stoichiometry; (b) Spatial profiles along a radial transect through point C, conditioned on stoichiometry; (c) Mixture fraction space profiles at point C.

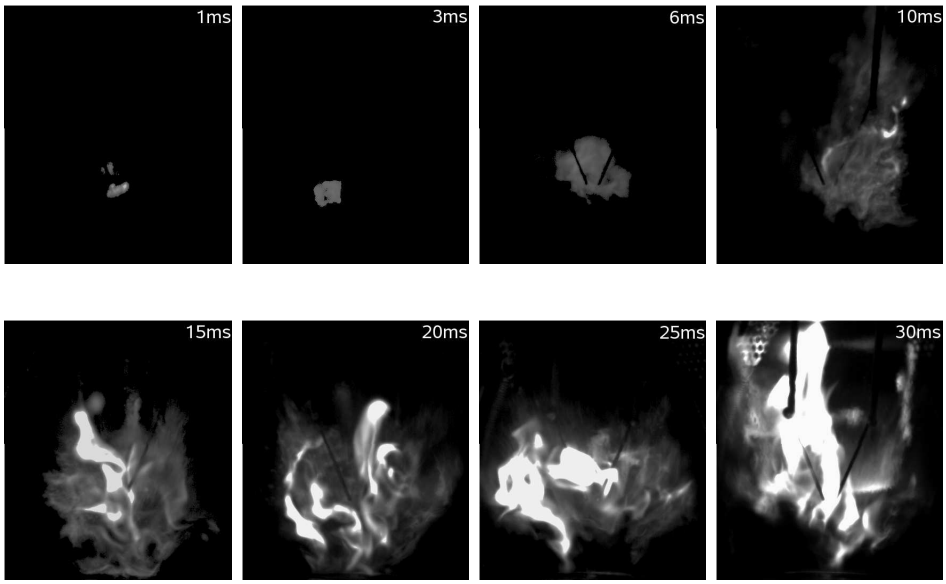

Figure 6.18: 2200Hz fast camera images of the flame evolution at the times indicated for a successful spark at $r = 0$, $z = 23mm$ in case Y. The image contrast has been reduced in order to make the kernel visible, particularly from $t = 3ms$ to $15ms$. The images show the entire cross section of the enclosure ($70mm$ diameter, $80mm$ height). Measurements by Marchione and Mastorakos [83].

The CMC results presented here neglect the contributions of the evaporative source terms in the conditional species and energy equations and the mixture fraction variance equation. Contours of the simulated mean temperature and mean heat release rates are shown in Figs. 6.19 and 6.20. A qualitative comparison with the experimental images suggests that, in common with the RANS-CMC simulations of turbulent jet ignition in chapter 5 and of non-premixed bluff body burner ignition in section 6.3, the current model over-predicts the rate of flame spread. However, the predicted flame propagation sequence and stabilised flame shape broadly agrees with that inferred from the fast camera images, aside from differences in the timings.

The simulated heat release rate indicates that the flame propagates ahead of the mean contour corresponding to the lean flammability limit (which propagates partly due to thermal expansion and evaporation). This situation arises since the mean mixture fraction gradients are relatively low and the mixture fraction variance is relatively high, providing significant amounts of flammable material even where the mixture is inflammable in the mean. The flame front is followed by a large region of diffuse heat release.

As the flame front approaches the enclosure a downstream portion splits off and propagates, downstream and out of the enclosure. The upstream portion propagates against the in-flow and eventually stabilises as an apparently lifted flame. Examination of the conditional temperature close to the burner lip indicates that the flow is in fact predicted to be burning (ie. $\langle T|\eta_{stoich}\rangle \approx T_{ad}$), however the heat release close to the burner lip is not visible in Fig. 6.20 due to the low probability of encountering flammable mixture at that location. The turbulent flame indicated by the region of high heat release at $t = 45ms$ marks the furthest penetration of the un-reacted inflow from the inlet annulus. The flame is curved in the opposite sense to that usually observed in partially premixed laminar triple flames since in this particular case the mean stoichiometric iso-surface resides close to the surface of the maximum speed across the flow, allowing richer and leaner turbulent flames

to extend further upstream.

While there is a significant transient in the mean velocity field caused by the mean thermal expansion during flame propagation, the main features of the velocity field do not change during flame stabilisation, in contrast with the non-premixed bluff body case considered in section 6.3. However the gaseous mixture fraction and the liquid spray field do alter significantly due to the developing evaporation pattern. The predicted spray distribution is indicated in Fig. 6.21 at $t = 3ms$ and $t = 45ms$. The spray evaporation apparently creates a region so rich that the temperatures surrounding the spray are sufficiently low for droplets to penetrate far into the enclosure.

The presumed mixture fraction PDF and the conditional temperature profiles at points A ($r = 0.0m$, $z = 0.01m$), B ($r = 0.01m$, $z = 0.04m$), and C ($r = 0.026m$, $z = 0.0236m$), indicated in Fig. 6.19, are shown in Fig. 6.22 for the stabilised flame, $t = 45ms$. Point C corresponds to the peak unconditional heat release along the mean stoichiometric iso-surface.

Point A is within the spray, and encounters high levels of mean mixture fraction. The conditional temperature profile at point A deviates from the zero-dimensional CMC solution for equivalent conditions due to the continuous mixing in of fresh air. This deviation is more pronounced at points B and C. Figures 6.23a and 6.23b show the spatial profiles of the CMC temperature equation on axial and radial transects respectively through point C. The stoichiometric conditional temperature profiles show the presence of the inflow, which is surrounded by regions of high heat release and mixing of the conditional quantities. Figure 6.23c shows the conditional temperature and the CMC temperature equation terms at point C. The conditional heat release shows two peaks, one close to stoichiometry and one close to the rich flammability limit. The heat release is largely offset by molecular dissipation and the convection term.

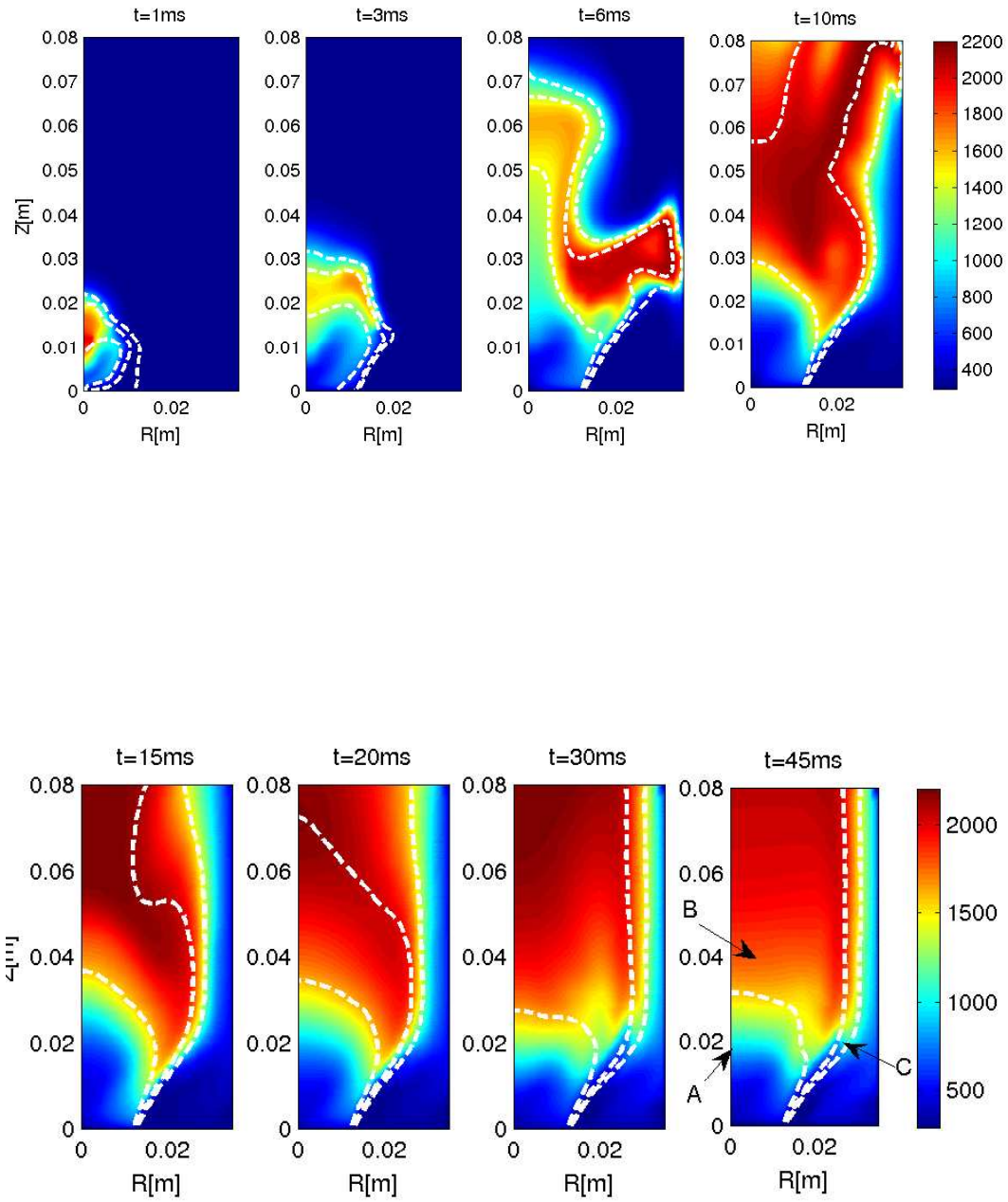

Figure 6.19: Simulated unconditional temperature evolution for case Y, (K). The dashed white lines are iso-lines of mean mixture fraction, the innermost representing the rich flammability limit ($\xi = 0.199$), the next line is stoichiometric ($\xi = 0.062$) and the outer line represents the lean flammability limit, ($\xi = 0.035$).

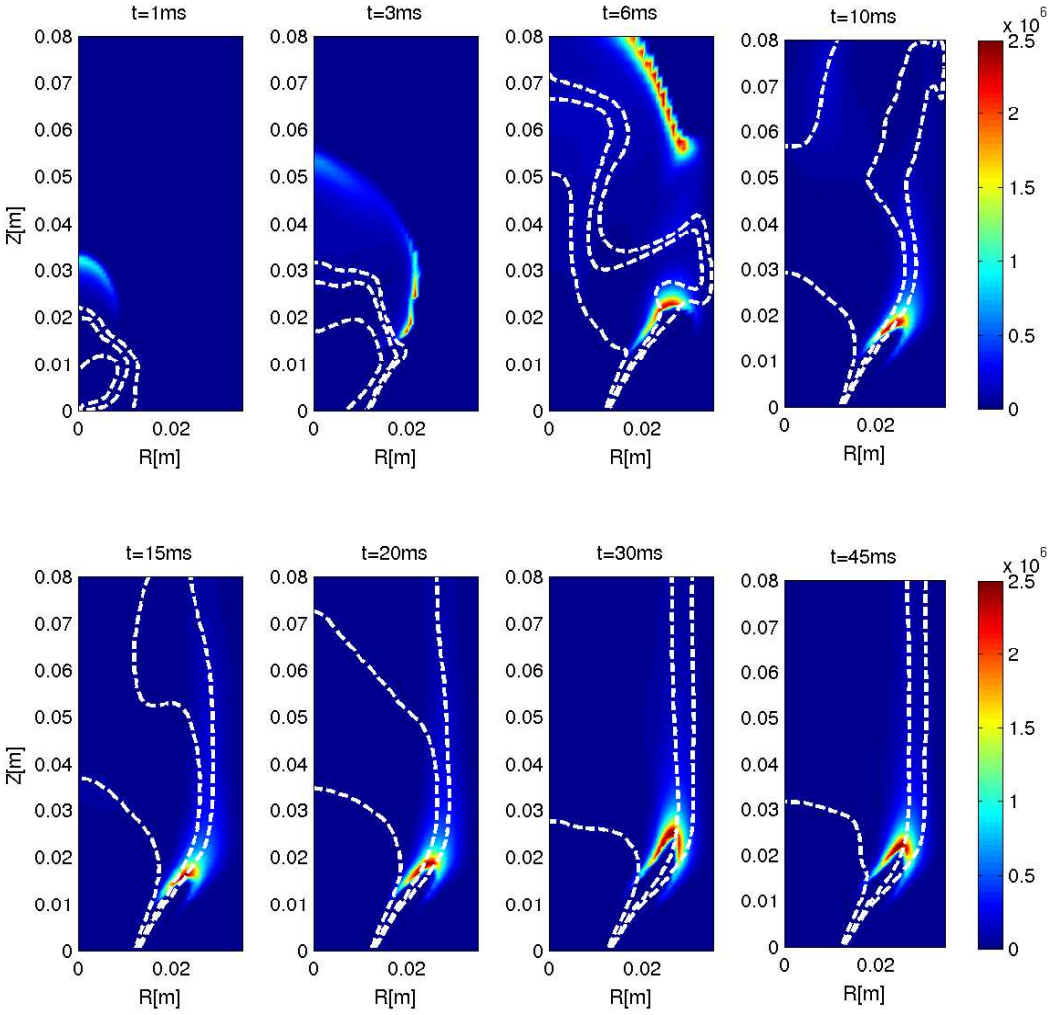

Figure 6.20: Simulated unconditional heat release rate evolution for case Y, (Ks^{-1}). Iso-lines of mean mixture fraction are shown as in Fig. 6.19.

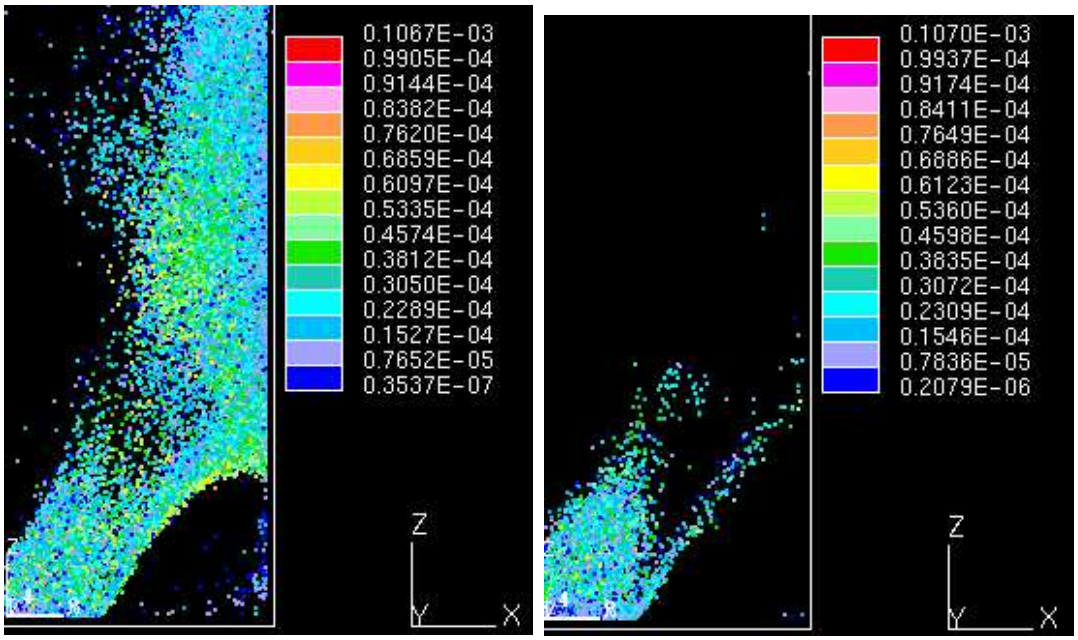

Figure 6.21: Predicted droplet parcel distributions at (a) $3ms$ and (b) $45ms$ after ignition. Image dimensions: $35mm$ wide and $80mm$ high.

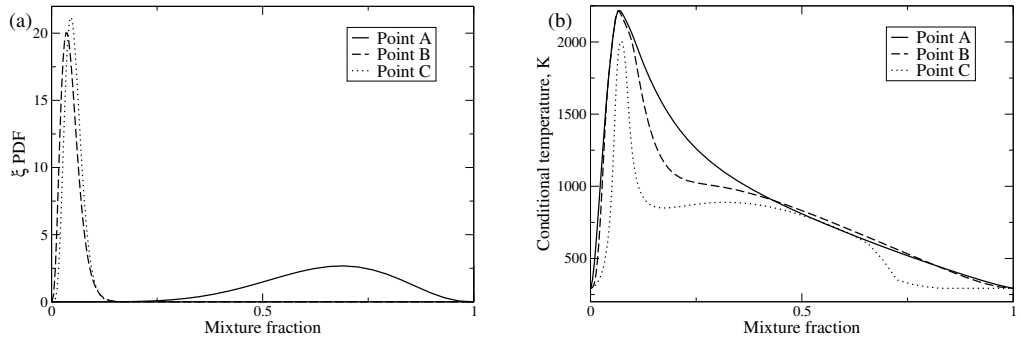

Figure 6.22: Profiles of (a) the mixture fraction PDF, and (b) the conditional temperature at points A, B and C. $t = 45ms$

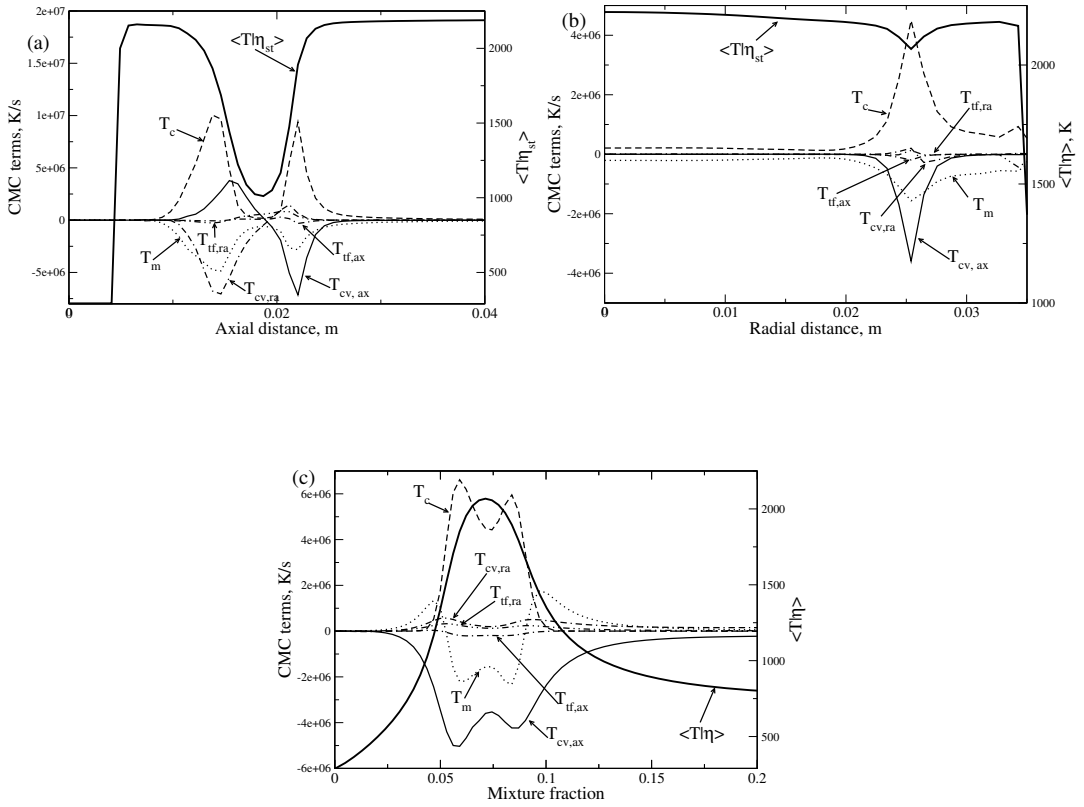

Figure 6.23: The conditional temperature and the balance of terms in the CMC temperature equation for case Y, $45ms$ after ignition. (a): Spatial profiles along an axial transect through point C; (b) Spatial profiles along a radial transect through point C; (c) Mixture fraction space profiles at point C.

6.5 Analysis of the CMC evaporation terms

The evaporation terms of the CMC temperature and species equations have been evaluated (post-processed) based on the solution for the stabilised bluff body spray flame ($t = 45ms$) discussed in the previous section. Attempts to produce a fully coupled solution for comparison have not yet been successful due to implementational difficulties. Therefore the new CMC equation terms have been evaluated, neglecting their influence on the overall CMC solution and on the other terms, to allow an initial discussion of their properties.

Due to the lack of a satisfactorily practical model for the saturation mixture fraction for use with a Lagrangian solution of the fuel spray, the saturation mixture fraction was taken as unity. Since the gaseous temperature in the majority of the stabilised spray flame is well above the boiling point of $n-$heptane this is likely to give little error. The potential modelling for the evaporation term of the mixture fraction variance equation discussed in chapter 2 was not used due to the unreliable implementation of the conditional evaporation rate model. The results presented in this section have been evaluated in a post-processing step using the Vervsish and Domingo [141] model for the conditional evaporation rate, however similar observations may be made based on the model by Sreedhara and Huh [127] (not shown).

The balance of temperature and species terms in the CMC solution of section 6.4 is plotted in Fig. 6.24 at $t = 45ms$, for point A as defined in Fig. 6.19. Additionally the evaporative source terms discussed in chapter 2 are shown. From the temperature equation:

- $S_{cv} = -(1-\eta)S(\eta)\frac{\partial Q_T}{\partial \eta}$
- $S_{evap} = +\frac{\langle \dot{h}_{evap}|\eta\rangle}{\langle c_p|\eta\rangle}$

and from the species mass fraction equation:

- $S_{fuel} = +S(\eta)Y_{S\alpha}$
- $S_{dil} = -S(\eta)Q_{\alpha}$
- $S_{cv} = -(1-\eta)S(\eta)\frac{\partial Q_{\alpha}}{\partial \eta}$.

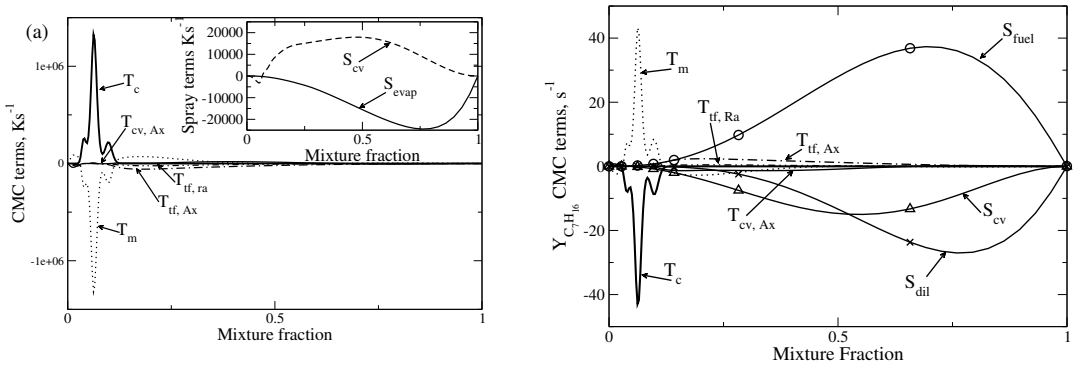

Figure 6.24: The balance of CMC terms at point A (neglecting the spray source terms) in (a) the conditional temperature equation, and (b) the conditional fuel mass fraction equation for case Y at $45ms$ after ignition. The spray source terms of Eq. 6.1 and in the conditional temperature equation (see chapter 2) have been post-processed and are also shown.

The CMC solution at this location is largely a balance between chemical heat release and molecular transport. In comparison, the magnitudes of the spray terms in the temperature equation are relatively small. The term S_{evap} represents cooling due to the conditional heat of evaporation, its shape reveals the profile for the conditional evaporation rate predicted by the Vervisch and Domingo model. The convection term S_{cv} has a similar magnitude and acts in the opposite sense for mixtures rich of stoichiometry. However, the two temperature equation terms do not balance each other exactly, In calculations which directly include the spray terms this imbalance is likely to result in a modification to the scalar dissipation term. While small in magnitude, the evaporative terms may be expected to make a large contribution to the solution at a position such as point A since there is low probability of finding

mixture close to stoichiometry where the chemical reaction dominates, instead the mixture is expected to be extremely rich.

The magnitude of the evaporation terms in the fuel mass fraction equation have a similar order of magnitude to the stoichiometric fuel consumption rate and the micro-mixing term which largely balances it. The fuel evaporation term S_{fuel} has a similar shape to the heat of evaporation term in Fig. 6.24a but with a different sign and magnitude. Since the only spray component is $n-$heptane the S_{dil} term has a very similar form to S_{fuel} at rich mixture fractions where the fuel mass fraction is close to unity. The convection term acts as predicted in chapter 2. It is notable that in contrast with the convection term for temperature in Fig. 6.24a, the convection term is always negative. This is due to the positive gradient of $n-$heptane across all mixture fraction space. The three evaporation terms in the fuel equation are nearly balanced. Note that in the case of evaporation in the absence of spatial conditional gradients and reaction they would balance exactly since $Y_{S\alpha}$, $Q_\alpha = \eta$ and $\partial Q_\alpha / \partial \eta = 1$ when subject only to inert mixing. The imbalance is likely to lead to a significant change in the conditional profiles, particularly away from the flammable range of mixture fraction, resulting in a modification to the molecular mixing term.

6.6 Conclusions

The CMC model has been implemented and used to simulate the complete ignition process up to flow stabilisation, in turbulent bluff body stabilised burners with gaseous and liquid felling. This represents a new and industrially relevant application for the CMC model.

The use of a RANS model to describe the bluff body flow field gives poor predictions of the un-reacting velocity and mixing field compared to the available measurements. The simulated flame evolution broadly agrees with that observed

experimentally, however the propagation rate is over-predicted in all cases.

Ignition of the non-premixed bluff body burner causes both temporary and permanent changes to the flow and mixing field. An attached turbulent flame stabilises in the mixing layer between the incoming mixture and a greatly expanded region of recirculating gas in agreement with experimental observations. The conditional composition predicted for the recirculation zone is significantly different from that which would be predicted by a zero-dimensional CMC solution, or by a steady laminar flamelet model.

The simulation of ignition in the spray fueled flow also highlights the importance of the interaction between thermal expansion and the fluid dynamics. Flame stabilisation leads to an extremely rich region around the spray, and a turbulent flame with peak heat release located on the mean stoichiometric iso-surface where the speed of the in-flow has fallen sufficiently.

The evaporative source terms in the two phase conditional moment closure equations have been evaluated in the turbulent spray burner. The terms are seen to be significant, particularly for very rich mixture fractions. However since flame propagation is generally governed by the reaction and transport processes of flammable mixture, it may not be essential to include all spray effects in simulations where modelling of flame propagation is the primary objective (as opposed to composition predictions, for example).

The present study would benefit from further detailed experimental measurements, particularly of the velocity around the flames. It is expected that many aspects of the current predictions could be improved through use of Large Eddy Simulation.

Chapter 7

Analysis of combustor ignitability

The ability to determine which potential jet engine combustor design satisfies altitude relight criteria early in the design process is a valuable asset to jet engine designers. Historically this judgment has relied upon correlations and intuition developed from gas turbine combustion theory and design experience. Despite the strong drive by the engineering community to develop CFD simulation methods such as the ones presented in the previous chapters, few models are truly predictive and even then computational times tend to present a barrier to their potential.

This chapter presents a new computational, ignitability analysis which avoids the complexity of directly modelling turbulent combustion in order to give instant insight into the likely ignitability of a design. The modelling is informed by the discussion of ignitability running through this thesis and here it is validated against experimental results for the flows analysed in chapters 5 and 6. Finally its application to a production aero-engine combustor is demonstrated.

7.1 Background

Commercial engine designers have a range of methodologies available for assessing relight performance. These include ignitability correlations [76], CFD models

(which are unlikely to have been validated/have the capability for relight predictions), and ignition measurement in sub-atmospheric test rigs (such rigs may only accommodate a small sector from a large commercial jet engine combustor).

Computational research in progress is moving toward LES prediction of relight with simple turbulent combustion modelling [12] and with advanced turbulent combustion modelling [57]. Advanced experimental diagnostics (high speed video, Mie scattering and P-LIF techniques) are also being applied within the confines of sub atmospheric test rigs [39; 105].

The flows considered in this chapter vary widely in character. In the jet, the probability of a spark forming a flame kernel was modelled by Fairweather et al. [123] with the flammability factor Eq. 7.1.

$$F = \int_{\xi_{lel}}^{\xi_{rel}} P(\eta) d\eta \tag{7.1}$$

This represents the presumed probability of finding mixture between the lean and rich flammability limits (ξ_{lel} to ξ_{rel}). However ignition of a stable flame requires that flame fronts propagate against the flow, and eventually stabilise as a lifted flame, see chapter 5. Consequently the criterion for successful flame propagation may be a comparison of the propagation speed and flow velocity. Ignition of the bluff body flows (chapter 6) need not involve flame propagation exceeding the speed at which the flame is advected by the mean flow due to the presence of recirculation. Instead, a more useful criterion for assessing whether a particular flame kernel may go on to ignite a stable flame may be a comparison of the residence time which the kernel spends in the recirculation zone (or in the recirculation zone - fresh reactant mixing layer) versus relevant chemical or mixing timescales [76]. The ignition and stabilisation mechanisms for a gas turbine combustor are expected to be closer to those for the bluff body flame. Hence, modelling of a gas turbine combustor involves many aspects of combustion; creation of a kernel, flame propagation, flame stabilisation

and the subsequent development of the flame after stabilisation (necessary to achieve 'pull-away').

The particle based flame tracking approach adopted in this chapter has similarities to the Arc and Kernel Tracking Ignition Model (AKTIM) for spark-ignition engine calculations [36], [29], however significant differences arise due to the focus on non-premixed ignition in this work.

The development of the ignitability analysis is presented with reference to ignition of a turbulent methane jet (chapter 5, [2; 146]). The analysis is then applied to the methane jet flames from chapter 5 and additional problems including ignition of a methane bluff body flame, an n-heptane spray flame (chapter 6), and also an aero-engine combustor at relight conditions.

7.2 Model development

7.2.1 Modelling

Flame propagation

Figure 7.5(a) shows the probability of flame ignition in a partially premixed methane jet from Ref. [2]. It is evident that the maximum ignition height (40 - 50 D_j) is less than the maximum flammable height given by the mean contour of the lean flammability limit (the outer black contour) or by the flammability factor, Eq. 7.1, as shown in Fig. 7.1(a). Given that the mean velocity falls gradually with axial distance, the propagation speed (defined here as the flame front velocity parallel to the mean flow direction in a fixed frame of reference minus the inert mean flow velocity) appears to be a function of the mixture fraction distribution and not purely a function of flammability. Two modes of flame turbulent flame propagation are now considered - turbulent premixed combustion and turbulent edge flame propagation.

Edge flame propagation involves a specific structure, with the flame residing on the instantaneous stoichiometric iso-surface and possibly one or two premixed flame branches (double/triple flame). The existence of this structure therefore depends on the existence of mixing layers which span from lean to rich mixture fractions. In chapter 5, we presented CMC simulations which reveal the turbulent edge flame structure at the base of the base of a lifted flame. The likelihood of such layers occurring may be indicated by the edge flame index proposed in Eq. 7.2 and shown in Fig. 7.1(b). The edge flame index equals the product of the probability of the mixture fraction taking a lean value and the probability of the mixture fraction being rich at one location, multiplied by 4.0 such that it has a maximum value of 1.

$$EFI = 4.0P(lean)P(rich) \tag{7.2}$$
$$P(lean) = \int_{\xi_{stoi}}^{0} P(\eta)d\eta$$
$$P(rich) = \int_{1}^{\xi_{stoi}} P(\eta)d\eta$$

The maximum value of edge flame index falls off rapidly after 45 jet diameters, Fig. 7.1(b), suggesting that propagation processes which are similar to premixed flame propagation may dominate above this height. A transition between propagation characterised by edge flame processes to propagation similar to that in premixed turbulent flames has been identified in partially premixed flames by Hawkes et al. [50]. Laminar [119] and turbulent [24] edge flame propagation studies suggest the most likely freely propagating edge flame speed to be well approximated by $S_L\sqrt{\rho_u/\rho_b}$ with little dependence on turbulence quantities, given a low scalar dissipation rate.

The turbulent premixed propagation speed may be approximated by equation 7.3 for low $u'/S_L(\tilde{\xi})$ flames [27], which is plotted in Fig. 7.4(c) for the particular jet analysed here. It is seen that the premixed propagation speed only exceeds the laminar edge flame speed (whose contour is shown in white) close to the nozzle

where high mixture fraction gradients are expected to preclude the premixed mode of flame propagation. Hence it is expected that edge flame propagation is dominant in the ignition of the jet flame however, the premixed mode of propagation should also be accounted for since the model will be applied to a variety of other partially premixed flows.

$$S_T = S_L(\xi)\left\{0.5\left[1+\left(1+8Cu'^2/S_L^2\right)^{1/2}\right]\right\}^{1/2} \tag{7.3}$$

Local flow velocity

Figures 7.2(a) and 7.2(b) show mean mixture fraction and velocity contours in the flows corresponding to the inert and lifted flame cases computed in chapter 5

These indicate that if the flame were to propagate along the mean stoichiometric contour it needs to propagate faster than the estimated edge flame speed $\sqrt{\rho_u/\rho_b}S_L$ unless it propagates at positions which are lean in the mean. If the flame is considered as a number of edge flames propagating relative to the instantaneous stoichiometric surface(s) at $\sqrt{\rho_u/\rho_b}S_L$, the flame brush would only move upstream due to turbulent fluctuations presenting the flame with local velocities below the mean. Mixture fraction and axial velocity are expected to be positively correlated in a turbulent jet. Since at a position which is lean on average, a stoichiometric fluctuation tends to bring fast moving fluid with it, small scale turbulent fluxes do not account for the current under-prediction of propagation speed.

Recent simultaneous PLIF-PIV measurements [59; 128] of a stabilised lifted flame support the view that the lifted flame stabilises through interaction with the well organised large scale structures found in a turbulent jet. Su et al. [128] present a model of the stabilisation process where relatively well mixed structures similar in size to the jet radius intermittently provide slow moving flammable mixture in

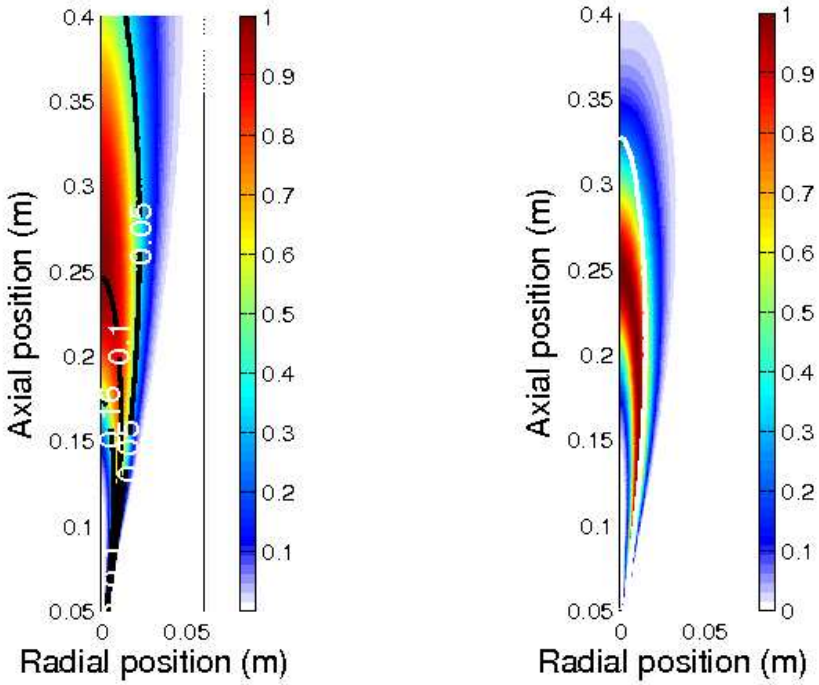

(a) (b)

Figure 7.1: (a): Flammability factor contours (filled coloured contours) using a presumed $\beta-$function pdf and rich flammability limit, stoichiometric and lean flammability limit mean mixture fraction isolines (black) based on the RANS flow field solution from chapter 5; (b): Contours of edge flame index (filled coloured contours) and isoline of mean flow speed equal to $\sqrt{\rho_u/\rho_b}S_L$ (white). Jet with $U_j = 12.5ms^{-1}$ and X_{air}=30%, $D_j = 5mm$.

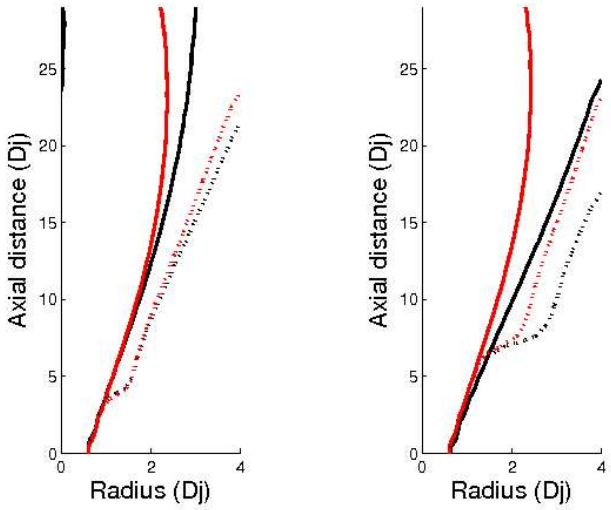

(a) (b)

Figure 7.2: Contours of velocity parallel to the mean mixture fraction iso-surfaces equal to $\sqrt{\rho_u/\rho_b}S_L$ (black) and contours of $\xi = \xi_{st}$ (red), for the inert CFD solution (solid) and the coupled 1D CMC solutions (dots), (chapter 5). (a): $U_j = 12.5ms^{-1}$; (b): $U_j = 25.5ms^{-1}$.

which the flame can progress upstream.

In contrast with the results of Su et al. [128], Upatnieks et al. [137] emphasise the role of mean flow dilatation on stabilisation. Here it is noted that the estimate of laminar edge flame speed proposed by Ruetsch et al. [119] is for a freely propagating, infinitely long edge flame. The following simplified analysis of the flow upstream of an axi-symmetric (ie. circular) edge flame shows how the curvature around the jet's axis can cause a greater velocity differential across the flame front compared to the straight edge flame case. Consider a stabilised, infinitely long edge flame whose position is constant in time. If one subtracts the mean flow and assumes that all the heat release takes place along an infinitely thin line at the leading edge of the flame, the edge flame may be approximated as a line source of volume. Similarly the axi-symmetric flame may also be approximated as a ring shaped volumetric source. The analysis of the incompressible flow field is then particularly simple, since the velocity relative to the mean velocity is given by integrating the influence of the volume flux from the entire line source. Assuming complete combustion the volumetric release rate from a fuel jet is:

$$\dot{Q}_v = u_j \frac{\pi D_j^2}{4} \frac{X_{Fu}}{X_{stoi}} \left(\frac{\rho_u}{\rho_b} - 1 \right). \tag{7.4}$$

In the present case X_{Fu} (the molar fraction of methane in the fuel stream) equals 0.7, $X_{stoi} = 0.095$, $\rho_u/\rho_b - 1 = 6$,$u_j = 12.5ms^{-1}$, $D_j = 5mm$ and r is taken as $10mm$ which is the approximate value at the stabilisation height. The velocity along the centre line of the jet (relative to the mean velocity) is found using Eq. (7.5) and compared to the velocity in the direction of flame propagation $r = 10mm$ to the

side of the linear edge flame in Fig. 7.3.

$$\begin{aligned} w_{ring}(z) &= \frac{zQ_v}{4\pi R^3} \\ w_{line}(z) &= \frac{zQ_v}{2\pi r 2\pi R^2} \\ R^2 &= z^2 + r^2 \end{aligned} \tag{7.5}$$

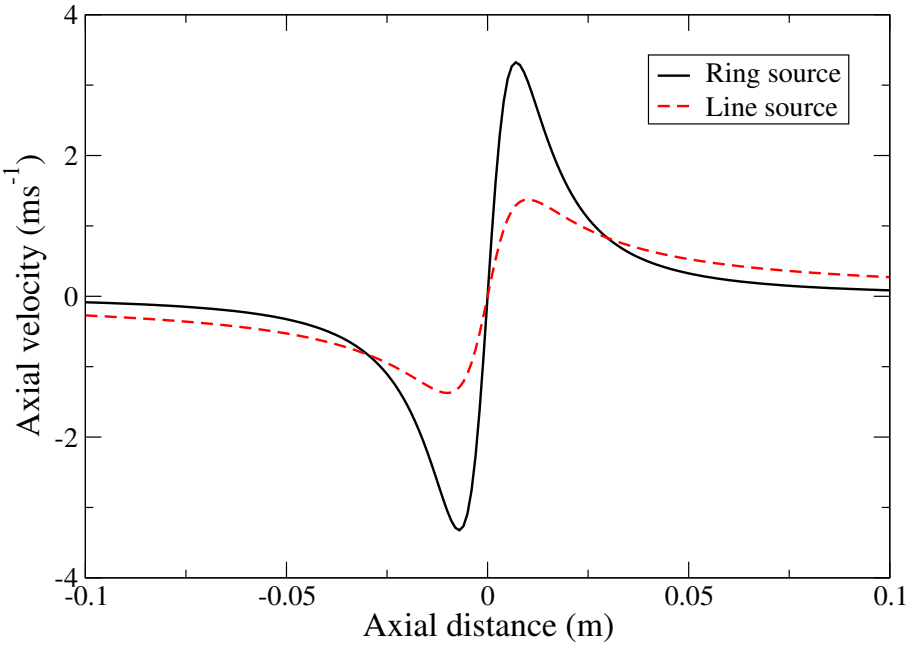

Figure 7.3: Induced velocity from volumetric line sources given by equation 7.5.

This gives a crude indication that the flow velocity seen by the upstream side of the lifted jet flame may be reduced by an amount similar to the freely propagating edge flame speed. The velocity differential across the flame is expected to be greater for a propagating flame than a stationary flame since the integrated rate of heat release is higher in the propagating flame.

Therefore one can expect large modification to the flow field caused by heat release in terms of velocity parallel to the direction of propagation and also significant stretching of velocity and mixture fraction profiles normal to the propagation

direction. These effects can be a strong function of the flow configuration. It would be desirable to incorporate these effects into a partially premixed propagation model however it is not clear how this may be done in a general way without solving unsteady fluid dynamic equations. The results of chapter 5 indicated that standard RANS models may be inadequate in the region of the flame front and that LES may be necessary to accurately capture influence of the heat release on turbulent flame propagation.

The propagation model

The propagation speed at which the flame front propagates normal to the local inert mean flow velocity is now modelled. The inputs to the model are a presumed mixture fraction PDF, turbulence information such as k, ϵ and ξ and an estimated increase in the flame propagation speed due to geometrical factors $\Delta U_{geom}(\mathbf{x})$. The flame is presumed to propagate at the maximum of the turbulent premixed flame speed and the turbulent edge flame speed. The turbulent edge flame speed S_E equals $\sqrt{\rho_u/\rho_b}S_L$ or zero depending on the EFI. The turbulent premixed flame speed is given by an appropriate correlation such as equation 7.3, or zero depending on the Favre averaged scalar dissipation rate. Where the resulting speed is non-zero, a geometrical correction velocity is added $\Delta U_{geom}(\mathbf{x})$ as given in Eq. 7.6.

$$\widetilde{S} = max\left[\left\{\begin{array}{ll} S_T(\tilde{\xi}) & (\tilde{\chi} < \chi_{crit}) \\ 0 & (\tilde{\chi} > \chi_{crit}) \end{array}\right\}, \left\{\begin{array}{ll} S_E & (E.F.I. > E.F.I_{crit}) \\ 0 & (E.F.I. < E.F.I_{crit}) \end{array}\right\}\right] + \Delta U_{geom}(\mathbf{x}) \quad (7.6)$$

This model describes the speed at which the flame spreads along a streamline in the inert flow field. An upstream propagation zone exists where the propagation speed is greater than the local mean flow velocity, a downstream propagation zone exists where the propagation speed is non-zero and less than the local mean flow velocity and a stabilisation surface exists where the local flow velocity equals the

propagation speed.

Thermal memory

It is possible for hot fluid, whether from a flame or from a spark, to move through an inflammable region by turbulent convection and to subsequently ignite a flammable region provided its temperature has remained sufficiently high. It is assumed that if the local propagation speed $S = 0$, the hot fluid interacts with cold reactants and that its temperature decays according to:

$$\frac{\partial T}{\partial t} = -\omega(T - T_{reactants}). \tag{7.7}$$

where the mean mixing frequency $\omega = k/\epsilon$. On reaching a region of finite propagation speed the temperature is restored to the adiabatic flame temperature.

7.2.2 Implementation

The model implementation requirements are:

- Simple meshing and implementation,
- Fast run time to enable parametric investigations,
- Production of a measure of ignition likelihood,
- Insightful graphical presentation of the flame propagation process.

The model has been implemented by defining a coarse, structured grid containing averaged values from the CFD field, and a particle-based representation of the ignition kernel and subsequent propagation of the flame front that uses velocity, turbulence and mixture quantities from the coarse grid. The particles' turbulent

convection is treated according to the simplified Langevin model [51] consisting of a linear drift toward the local Favre mean velocity and an added isotropic diffusion term:

$$dU_i^* = -(\frac{1}{2} + \frac{3}{4}C_0)\omega(U_i^* - \bar{U}_i)dt + (C_0\epsilon)^{1/2}dW_i, \tag{7.8}$$

dU_i^* is a stochastic velocity realisation, C_0 is a constant (assumed to equal 2.0 in this work), and dW_i is a stochastic Wiener increment.

Flame propagation is represented as an additional velocity in the upstream direction,

$$dx_i = U_i^* dt - \tilde{S}\frac{\widetilde{\mathbf{U}}}{|\widetilde{\mathbf{U}}|}dt \tag{7.9}$$

where $\tilde{S}$ is given by equation 7.6. In the limit of $\tilde{S} = 0$ the model represents passive scalar dispersion.

Initial conditions

A statistically spherical ignition kernel is assumed at the start of the computation with a Gaussian particle density profile. The standard deviation of radial position equals the nominal radius of the spark. The initial velocity is randomly distributed with zero mean and $\sigma_{speed} = u'$, where $u' = 2/3k^{1/2}$ using the turbulent kinetic energy k from the inert CFD solution.

Success criterion

A flame particle is deemed successful if it ever enters an upstream propagation zone during its lifetime, ie. before its temperature falls below a critical value T_{crit}. The proportion of particles reaching a propagation zone is referred to as the spark

effectiveness. Contours of spark effectiveness are generated by applying the spark at every node in the flow and tracking a large number of particles from each position.

7.3 Application to a lifted methane jet flame

The spark effectiveness is now evaluated for the lifted jet flames simulated in chapter 5 and compared to ignition probability measurements [2] using a $100mJ, 400\mu s$ spark with $1mm$ electrode thickness and spacing. Based on Fig. 7.3, $\Delta U_{geom} = 0.75ms^{-1}$ is used for the $U_j = 12.5ms^{-1}$ jet case, and since the volumetric release rate from a steady flame is proportional to the fuel flow rate, $\Delta U_{geom} = 1.5ms^{-1}$ is used for the $U_j = 25.5ms^{-1}$ jet case. A comparison of Fig. 7.4(a) to Fig. 7.4(c), and 7.4(b) to Fig. 7.4(d) shows that according to the analysis developed above the edge flame type of propagation is faster than the 'turbulent cascade'/premixed type. Also, without the geometrical factor ΔU_{geom} the predicted propagation speed would never exceed the mean flow speed.

Figures 7.5 and 7.6 show a comparison of the resulting spark effectiveness to the measured ignition probabilities for the $U_j = 12.5ms^{-1}$ and $U_j = 25.5ms^{-1}$ cases. It can be seen that the essential features of the ignition probability map are reproduced by the spark effectiveness model. The rich core of the jet is assigned a spark effectiveness of zero since the flow is too rich to support combustion and the high level of turbulent mixing quenches the flame particles before they are convected into flammable mixture. The size of the core, un-ignitable region increases with jet speed in agreement with the measurements. The other key observation is the rapid fall off in spark effectiveness around 50 diameters from the nozzle in agreement with the measured ignition probability, but in contrast to the indication of the flammability factor. This success results from the the use of 'edge flame index' in the model to determine mixture conditions where edge flames are likely to occur, since the expected premixed propagation speed is also less than the mean flow speed.

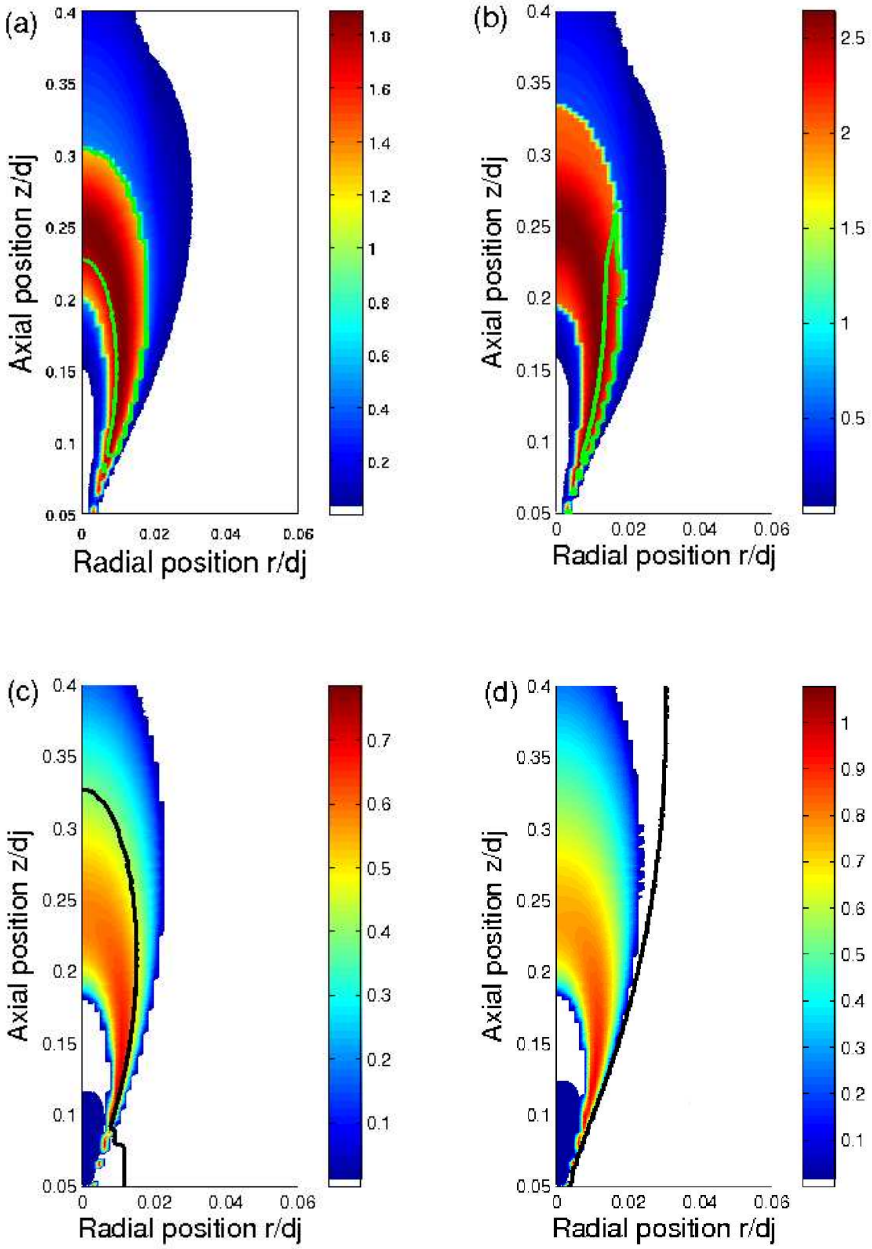

Figure 7.4: (a):Contours of modelled propagation speed (coloured) and stabilisation surface (green), $U_j = 12.5ms^{-1}$; (b): Contours of modelled propagation speed (coloured) and stabilisation surface (green), $U_j = 25.5ms^{-1}$; (c): Contours of premixed turbulent flame speed (coloured) as a function of local mean mixture fraction from Eq:7.3 and isoline of mean flow speed equal to $\sqrt{\rho_u/\rho_b}S_L$ (black); (d): Premixed turbulent flame speed, S_T (coloured) and the iso-line of flow speed equal to $\sqrt{\rho_u/\rho_b}S_L$ (black), $U_j = 25.5ms^{-1}$.

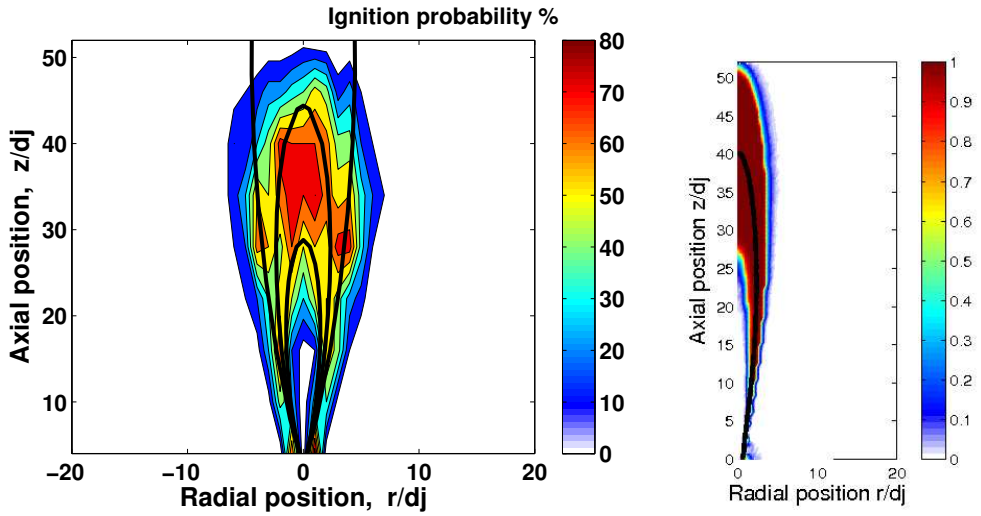

(a) (b)

Figure 7.5: (a): Measured ignition probability (coloured contours) and estimated mean contours of lean flammability limit, stoichiometric and rich flammability limit mixture fraction (black), $U_j = 12.5ms^{-1}$. ; (b): Spark effectiveness (coloured) and mean stoichiometric mixture fraction contour (black) from the CFD, $U_j = 12.5ms^{-1}$.

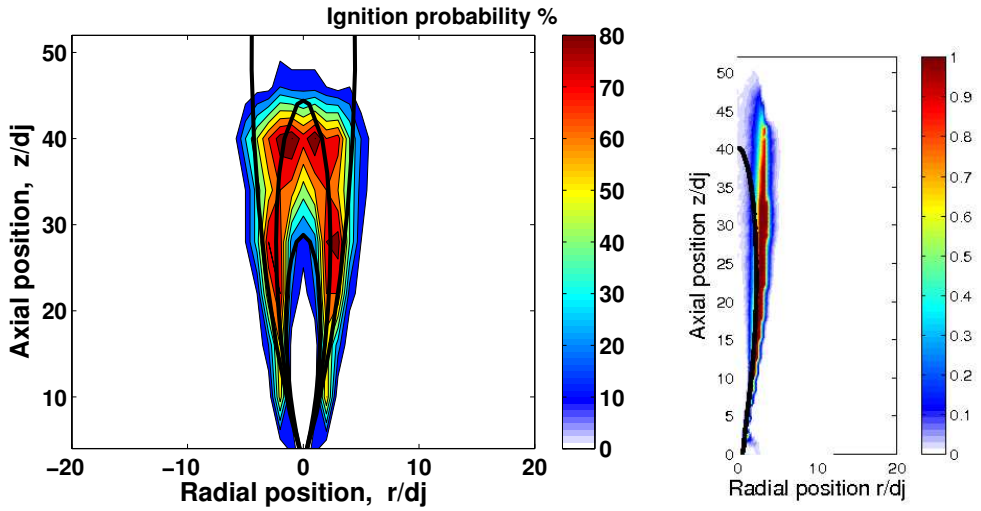

(a) (b)

Figure 7.6: (a): Measured ignition probability (coloured contours) and mean contours of lean extinction limit, stoichiometric and rich extinction limit mixture fraction (black), $U_j = 25.5ms^{-1}$. ; (b): Spark effectiveness (coloured contours) and mean stoichiometric mixture fraction contour (black), $U_j = 25.5ms^{-1}$.

The discrepancy between the width of the spark effectiveness and the measured ignition probability profiles and the failure of the spark effectiveness to meet with the centre line at its downstream tip in Fig. 7.6(b) could be due to the large radial expansions which occur due to the heat release (Fig. 7.2) which are not described in the current modelling approach, and also the initial position and velocity distribution used to describe the spark kernel. The heat release due to the spark and initial kernel growth might justify the use of either a larger initial radius or higher initial particle velocities.

There is a significant region where the predicted spark effectiveness is unity, whereas the measured ignition probability peaks at around 0.8. However the spark effectiveness should not be interpreted in the same way as the ignition probability, since the spark effectiveness is calculated based on just one spark event (represented by large number of particles). The random term used to model the turbulent dispersion of the particles could be replaced by an algebraic diffusion term. Meanwhile the ignition probability is the fraction of sparks which result in a stabilised flame, each spark event experiences a different electrical input and a different realisation of the velocity and mixing fields. Each spark event results in a binary outcome - stabilisation or extinction. A close representation of the ignition probability could be synthesised by choosing a threshold of spark effectiveness that might correspond to a successful stabilisation outcome, and then performing a series of simulations with representatively random perturbations of the spark, velocity and mixture fraction and finally averaging the number of simulations resulting in a successful stabilisation.

7.4 Other applications

7.4.1 Methane bluff body flame

The analysis described above has been applied to the inert RANS solution for 'case B' of the bluff body stabilised non-premixed methane-air flame discussed in chapter 6. The fluid mechanics of this flow were discussed in that chapter, and it is noted that the Reynolds stress model predictions give large differences from the flow measurements. In particular, the mean mixture fraction in the central recirculation, which was close to the rich flammability limit according to the measurements, was under-predicted by around 0.005, which would make the recirculation slightly lean. The analysis based on the predicted flow field is shown here for demonstration purposes rather than quantitative prediction since the underlying CFD data are known to be a poor representation of the flow. The mean mixture fraction, Fig. 7.7(a) and its RMS, give the flammability factor shown in Fig. 7.7(b). Since the measured mean mixture fraction was close to a flammability limit, the flammability factor has probably been over-predicted.

The edge flame index (Eq. 7.2) shown in Fig. 7.8(a) indicates that edge flame elements might be likely in the vicinity of the mean stoichiometric contour, however the magnitude of the propagation speed due to the turbulent premixed type of propagation is predicted to be greatest (Eq. 7.6). The resulting turbulent propagation speed is plotted in Fig. 7.8(b).

Figure 7.9 compares the measured ignition probability [1] with the predicted spark effectiveness. The ignitability model correctly predicts that the edge of the recirculation zone slightly downstream of the bluff body lip results in high ignition probabilities, where the model predicts a region where flame propagation is faster than the mean flow speed. The position of this region is a function of the mixture fraction and velocity predictions. The stabilisation surface occurs radially inward

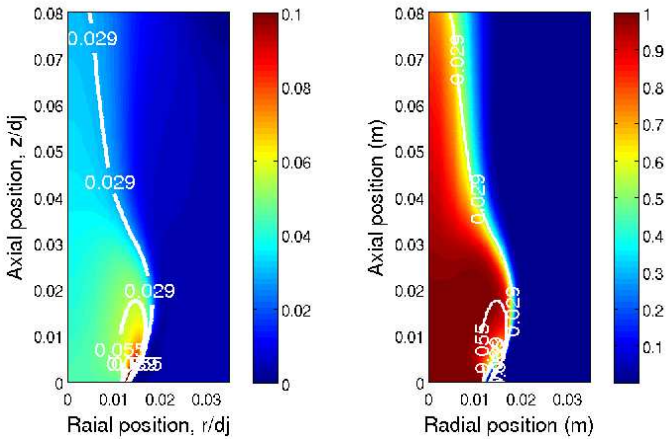

(a) (b)

Figure 7.7: (a): Mean mixture fraction contours (coloured); (b): Flammability factor contours (coloured). Rich ($\xi = 0.089$), stoichiometric and lean ($\xi = 0.029$) mean mixture fraction iso-lines (white), Case B.

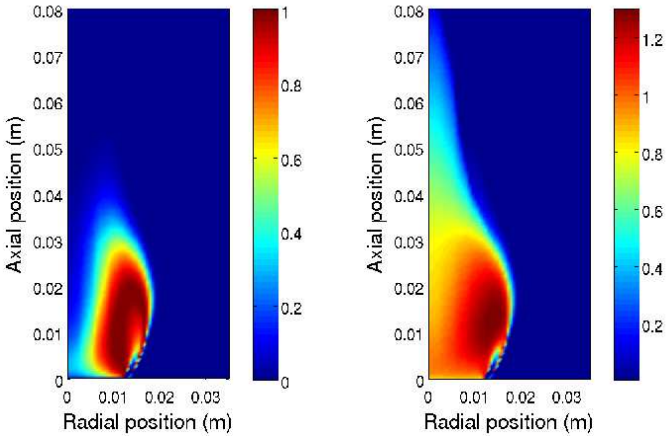

(a) (b)

Figure 7.8: (a): Edge flame index; (b): Predicted propagation speed in ms^{-1}. Case B.

from the observed peak ignitability, and this is consistent with the fact that the CFD prediction under-predicts the mean mixture fraction and hence stoichiometry occurs further toward the burner's centre line. Inside the central recirculation zone the spark effectiveness is zero, consistent with the severe reduction of ignition probability observed in the experiments.

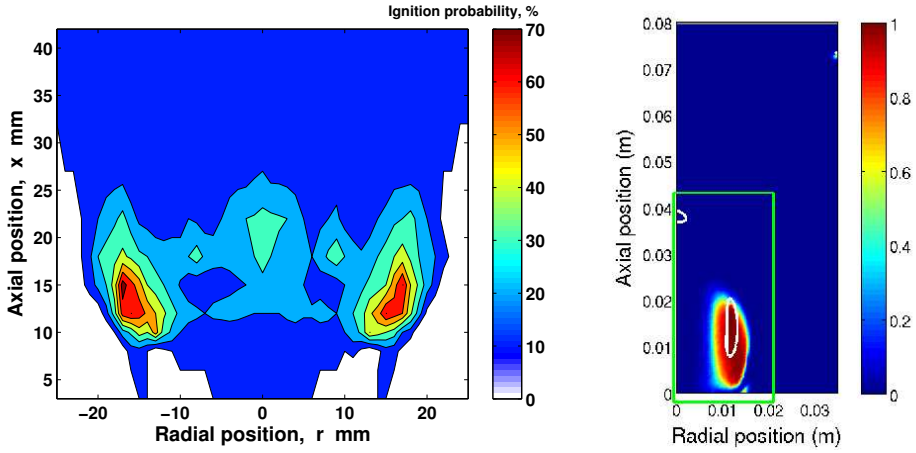

(a) (b)

Figure 7.9: (a): Measured ignition probability for area corresponding to the green rectangle, Ref. [3]; (b): Spark effectiveness contours (coloured), stabilisation surfaces are shown with a white contour. Case B.

7.4.2 Heptane spray flame

The extension of the ignition analysis to spray fueled flows is now discussed with reference to the swirl stabilised n-heptane flame examined in chapter 6. The analysis is based on a Reynolds stress simulation of the flow (Case Z), which includes a Lagrangian treatment of the spray transport. The mean axial velocity is shown in Fig. 7.10. The spray predictions shown in chapter 6 show qualitative agreement with the experimental information currently available [83].

The mean gaseous mixture fraction seen in Fig. 7.11(a) shows significant fuel

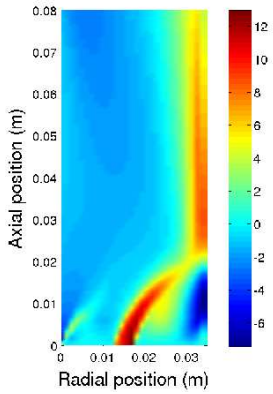

Figure 7.10: Mean axial velocity, case Z.

evaporation and flammable mixture, even at room temperature. The conservative mixture fraction in an un-reacting flow may be defined as the total mass fraction of fuel due to both gaseous and liquid phases present in a control volume. The mean conservative mixture fraction which corresponds to the limit where all fuel evaporates instantaneously with out mixing is available from the current CFD solution, however since the CFD solution corresponds to a narrow sector where individual CFD cells may contain few or even zero spray parcels, the void fraction at a given instant is not smooth in space. In order to find a conservative flammability factor, it is necessary to presume the mixture fraction PDF, and using a $\beta-$function shape requires an estimate of an appropriate the mixture fraction variance. Such an estimate is discussed in appendix A.4. The resulting conservative mixture fraction Fig. 7.11(b) is not smooth in space, however time averaging of the CFD solution should ideally be used to give a smoother result.

In order to estimate the turbulent flame propagation speed some approximations are made which should be viewed as one limiting case of the possible processes, which could occur during flame two phase flame propagation. Firstly, it is assumed that no spatial transport of gaseous or liquid fuel occurs during the ignition process. Secondly, the spray evaporation time does not reduce the propagation velocity. Thirdly, when a flame passes a particular location it will propagate according to the

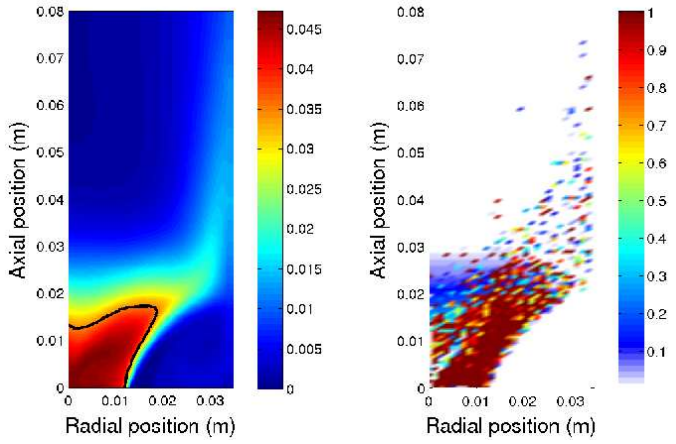

(a) (b)

Figure 7.11: (a): Mean gaseous mixture fraction contours from the steady unreacting flow prediction (coloured), and the mean lean flammability limit contour $\xi = 0.0353$ (black) ; (b): Conservative flammability factor contours, case Z.

fastest gaseous propagation speed, which may be found by considering all equivalence ratios that occur between the gaseous mixture fraction and the conservative mixture fraction (generally this will be the closest to stoichiometry). A suitable definition for a two-phase edge flame index is not apparent and currently only the premixed mode of turbulent flame propagation is considered. In all other respects, the ignitability analysis remains the same as in the gaseous model presented above. These approximations are not generally valid but this limiting case does give reasonable predictions in the heptane spray where there is significant gaseous mixture fraction from evaporation before ignition. They have little influence in the ignition of a gas turbine combustor, considered next, where large flow speeds, low evaporation rate, and low liquid fuel residence time make the ignition prediction insensitive to the details of the propagation model assumptions.

Figure 7.12 compares the measured ignition probability [83] and the predicted spark effectiveness for case Z. The main features of the ignition probability are cap-

tured by the spark effectiveness, specifically the low level of ignitability close to the centre line where sparks gets entrained into the spray. In the CFD the spray is a region of low conservative flammability factor with very intense turbulent dissipation. A vertical band of strong ignitability is correctly predicted between $5mm$ and $15mm$ radius. This region corresponds to a high conservative (and gaseous) flammability factor, low turbulent mixing rates and advection toward the stabilisation surface which is predicted to occur radially inward from the main inlet/recirculation zone shear layer. The axial distance at which the ignitability falls away agrees well with the measurement. This is due to the low levels of flammable material and the increasing distance a kernel has to survive before it reaches flammable mixture. Whether a kernel survives until it reaches flammable mixture is governed by the modelling of the thermal memory effect, section 7.2.1.

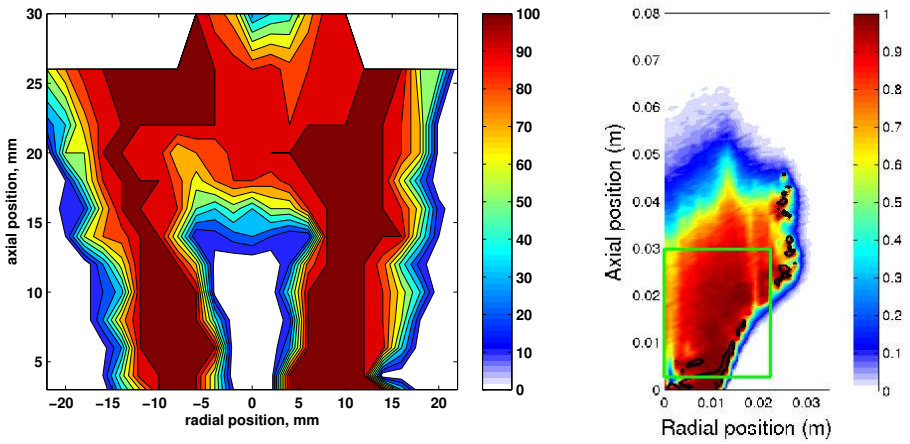

(a) (b)

Figure 7.12: (a): Measured ignition probability for area corresponding to the green rectangle.; (b): Spark effectiveness contours (coloured) and stabilisation surfaces (black), case Z.

7.4.3 Gas turbine ignition

The application of the ignitability analysis is discussed for aviation gas turbine combustors at altitude relight conditions, with $P = 41370Pa$ and $T = 267K$ at combustor inlet, corresponding to an altitude around 20,000ft. Relight conditions are lean of the flash point for civil aviation fuel 'JET A' [48]. At these conditions fuel evaporation in the inert flow is expected to be negligible based on vapour pressures of typical components of JET-A fuel [122].

Following the formation of an ignition kernel (by electric discharge or an alternative technology) the fuel droplets are exposed to elevated temperatures. The droplet evaporation time may be related to its initial diameter D_0 according to equation 7.10, where λ is the steady state evaporation constant. For a spray of kerosene entering a flame λ may be taken as $0.9 \times 10^{-6} m^2 s^{-1}$[25].

$$D_0^2 - D^2 = \lambda t, \tag{7.10}$$

The level of atomisation achieved at altitude relight conditions is highly flow and injector specific, and not easily ascertained experimentally. A production engine's air blast atomiser could give an $80\mu m$ SMD spray at these conditions, resulting in evaporation times of $7ms$. The evaporation time is long compared to the estimated chemical time scale of a laminar hydrocarbon flame close to lean extinction $\alpha/(S_{Llean})^2 \approx 2.15 \times 10^{-5}/(0.1^2) = 2ms$. This is likely to preclude the possibility of a thin deflagration front propagating through the two phase mixture as was implied in the discussion of the n-heptane burner above. Instead, propagation and stabilisation of the combusting kernel ought to be thought of as a process of turbulent mixing and convection, with evaporation and reaction distributed through out the kernel. Note that once stabilisation has occurred and atomisation and evaporation improve, the timescales change significantly.

Additionally the mean flow rates encountered in a gas turbine combustor relative to the expected propagation speeds are far larger in magnitude than in the previous cases considered, such that the previous stabilisation criterion may not suggest any region where stabilisation is possible. It appears that the current modelling approach is inadequate for this problem since it does not incorporate the physics of the propagation and stabilisation mechanisms encountered in the combustor. An approach to extend the ignitability analysis to burners of this kind is discussed in section 7.4.4.

In order to explore the potential of the current ignitability analysis in the gas turbine setting, inert CFD solutions of a combustor for relight conditions are examined, and an estimate is used for the stabilisation region. The estimate is based on an argument that, for a combustor to be ignited, it is necessary, although not sufficient, for the kernel to reach the region immediately downstream of the inlet swirlers and fuel injector. This region may be similar to that containing the lifted base of the flame once the combustor has been ignited. The region is approximated as a disk which is coaxial with the fuel injector and which extends a short distance into the combustor. The stabilisation region should contain flow features with residence times sufficient for the flame to stabilise.

Inert CFD solutions were supplied by C. Goddard [47] for an annular combustor sector at two mass flow rates, one inside the engine's ignition loop (case 1) and one outside it (case 2). The global fuel to air ratio was 0.02 for both cases. A RANS turbulence closure was used and non-evaporative spray was solved (since evaporation is negligible at these conditions). The mean axial velocity plot, Fig. 7.13, shows the main features of the flow which are a highly swirled inlet and significant mass flow through the dilution ports. The conservative mixture fraction and flammability factor are shown in Fig. 7.14, both are confined to the spray cone. The fuel distribution changes dramatically during ignition as gaseous fuel starts to mix and recirculate resulting in an increased fuel residence time.

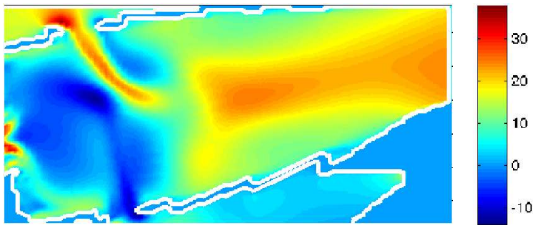

Figure 7.13: Mean axial velocity prediction for combustor inside the ignition loop (case 1). The dimensions and exact combustor shape are not given for reasons of confidentiality.

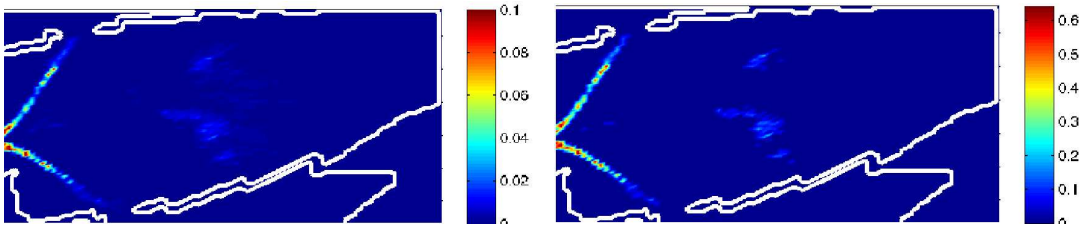

(a) (b)

Figure 7.14: (a): Conservative mixture fraction for combustor, case 1; (b): Conservative mixture fraction based flammability factor, case 1.

The propagation speed is estimated using the variation of laminar flame speed with equivalence ratio for n-heptane. The $n-$heptane laminar, stoichiometric flame speed has been mapped across the entire operating range of contemporary civil gas turbines, Fig. 7.15, using the mechanism by Held et al. [52]. The estimated turbulent propagation speed from Eq. 7.3 using $S_L(\xi)$ from Fig. 7.15 is always less than the flow speed, and the exact details of the flame propagation modelling have negligible influence on the ignitability analysis.

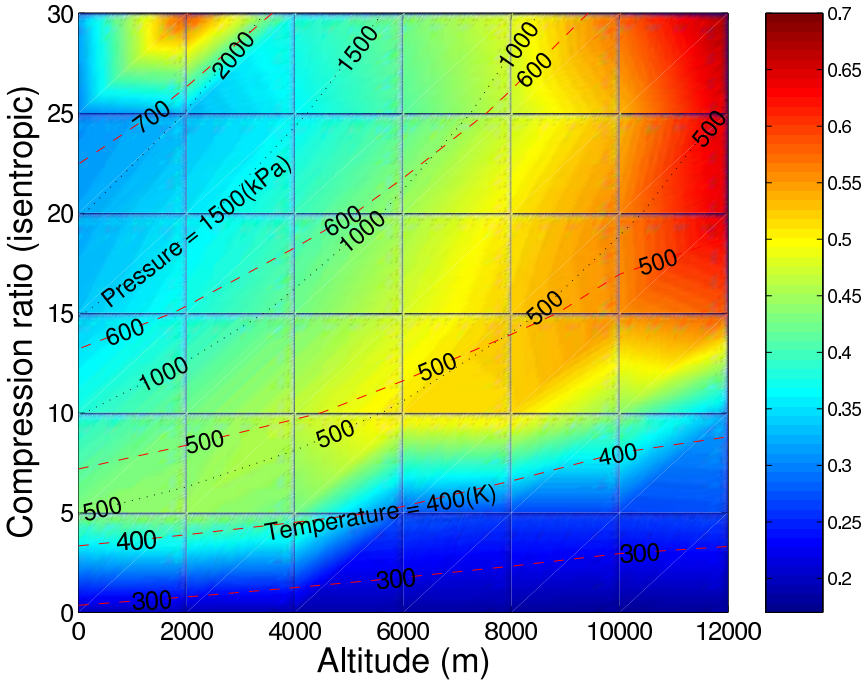

Figure 7.15: Contours of the stoichiometric laminar flame speed for $n-$heptane mixed with air following isentropic compression at a variety of altitudes, based on the standard atmosphere and the Held et al. [52] $n-$heptane mechanism.

The shape of the ignition kernel which is formed by the surface discharge igniter has been estimated based on high speed camera images of the ignition event [105]. The kernel exhibits a high level of variability even when no fuel is present. At the power levels used for relight it typically penetrates across 1/3 to 2/3 of the annulus' height. The ignition kernel is approximated as a cylindrical volume whose axis is normal to the combustor liner at the spark location. The radius, penetration, and

position of the ignition kernel can be varied in order to conduct parametric studies. The kernel initially contains hot fluid particle at a temperature T_{spark} with randomly distributed positions and velocities.

The stabilisation zone thickness is arbitrarily set to equal the inlet swirl radius for case 1, and a spark location is selected on the outer combustor liner in the plane of the injector centre line, midway between the swirler face and the primary injector port. The kernel extends across 2/3 of the annulus height with an RMS radius of $0.75cm$. The spark temperature $T_{spark} = 2000K$ and the critical temperature for ignition $T_{critical} = 1200K$.

Due to the low propagation speeds predicted and the absence of flammable mixture in large portions of the domain, the dominant processes experienced by the flame particles are turbulent convection and mixing of heat with the surrounding cold gas. The ignitability test then becomes a question of how many particles reach the specified stabilisation zone before losing too much heat to ignite a spray. The critical temperature should be chosen such that the auto-ignition delay time is much smaller than the turbulent mixing time k/ϵ. Flame particle trajectories for case 1 are shown in Fig. 7.16(a). The particle tracks are terminated when the temperature falls below the critical level, the particle reaches the stabilisation zone or hits the combustor wall. It is seen that because the kernel penetrates through the spray cone and into the inner recirculation, some of the particles are swept upstream and on to the stabilisation region.

It is conjectured that as the combustor mass flow rate is increased, the velocities throughout the combustor increase meaning that a smaller volume of the combustor will contain structures with sufficiently high residence times to stabilise a flame. For demonstration purposes the stabilisation disk thickness l_2 for case 2 has been scaled by the ratio of mass flow rates between the two cases, $l_1/l_2 = \dot{m}_2/\dot{m}_1 = 0.64$. The effects of this argument are evaluated below. The resulting flame particle trajectories are plotted in Fig. 7.16(b).

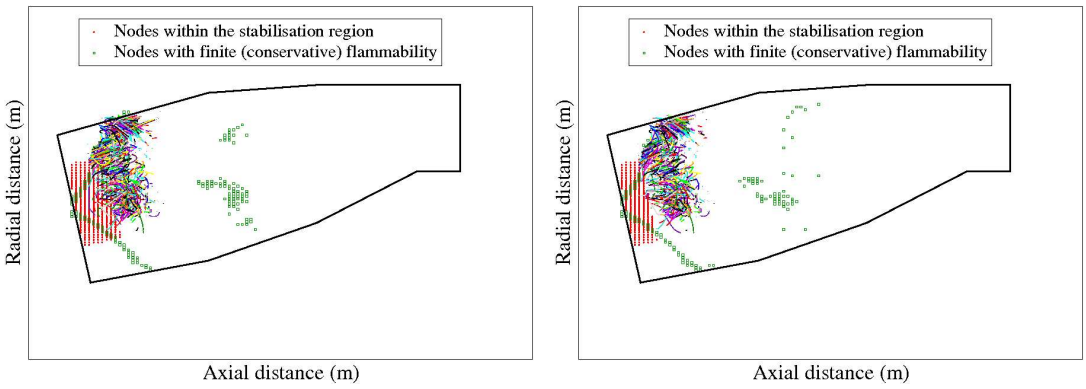

(a) (b)

Figure 7.16: 3D flame particle trajectories viewed in the azimuthal direction with stabilisation and flammable regions indicated, (a): case 1; (b): case 2 with $\dot{m}_2 = 1.57\dot{m}_1$.

The relative ignitability predictions for different igniter penetrations, positions and of the two mass flow rates are shown in Fig. 7.17. The model suggests ignitability increases rapidly with spark penetration (which is likely to be a function of spark energy) since this places more of the kernel in the central reversed flow region. The predicted ignitability is generally lower for the case 2, however this is partly due to its reduced stabilisation zone thickness.

The effect of the stabilisation zone and spark kernel description has been explored and the resulting predictions are plotted in Fig. 7.18 for case 2. The standard case uses a stabilisation zone thickness equal to the swirler outer radius, and a spark penetrating across 2/3 of the annulus height. The other test cases have one parameter varied from the standard case. The model parameters examined are the thickness and radius of the stabilisation zone, the initial temperature of the flame particles and the critical temperature below which a flame particle is assumed to be spent, the turbulent mixing frequency for temperature and the initial radius of the spark kernel. The case with zone thickness $= 0.636R_{swirl}$ corresponds to the $H_{spark} = 0.66$ curve in Fig. 7.17. All the curves give a similar shape, peaking around $4cm$ down-

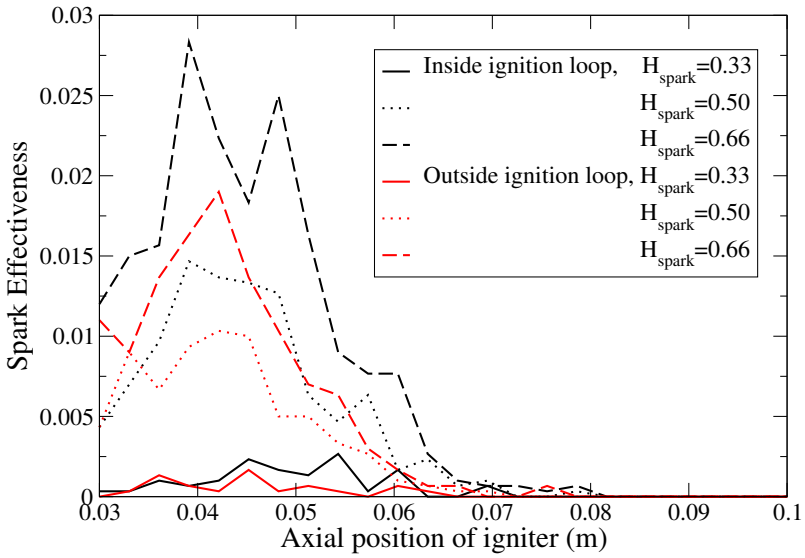

Figure 7.17: Spark effectiveness versus axial spark location and various ignition kernel penetrations for case 1 (black) and case 2 (red).

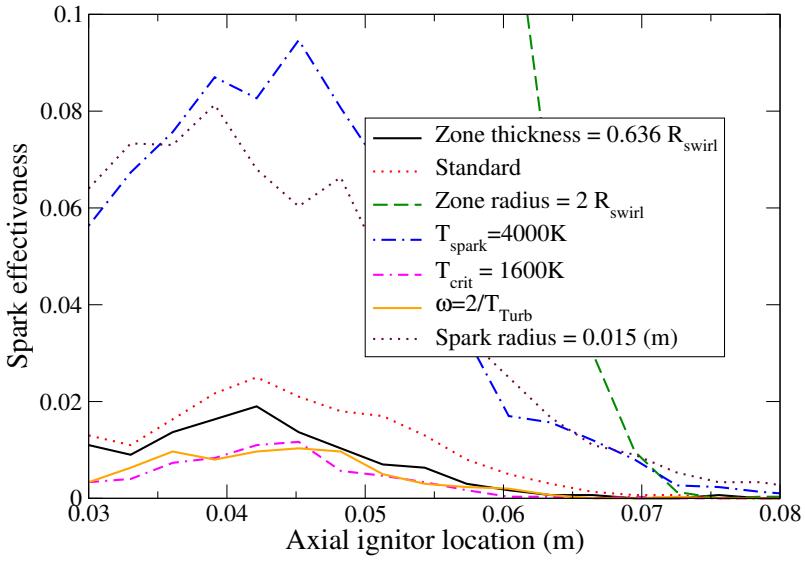

Figure 7.18: Effects of model parameters on spark effectiveness prediction. The curve for stabilisation zone radius $= 2R_{swirl}$ peaks off the graphs at 0.65

stream of the injector and falling to zero close to the primary dilution port. This suggests that the exact choice of modelling parameters does not affect the relative conclusions when comparing design parameters such as spark location.

The current analysis approach is still able to provide helpful technical information and visualisation of a combustor's ignitability despite the simplicity of the modelling. For example, based on the CFD solution for a sector of an annular combustor, 3D flame particle tracks can be plotted for the stabilisation in an individual burner and additionally for the 'light around' process by which flame spreads to adjacent burners. Next, a discussion is presented for how the flame particle tracking procedure can be used to analyse the stability or ignitability of flows with mixing dominated stabilisation mechanisms.

7.4.4 Time scale analysis

The ignitability analysis above has used a flame stabilisation criterion which compares the local mean flow speed to a predicted turbulent flame speed. In the ignition of high speed two phase flows such as a gas turbine combustor at relight conditions, this criterion may not indicate any location where a flame can be stabilised at conditions which in practice are ignitable. Previous discussions of combustor stability [76] have considered stabilisation in flows with recirculation structures in terms of a comparison between flow and combustion time scales. Lefebvre argues that a bluff body stabilised flame can resist blow off if the residence time in its recirculation zone or within the shear layer between the recirculation zone and the incoming unreacted mixture is greater than the relevant combustion times. The combustion time is composed of turbulent mixing times, evaporation time (in liquid fueled flow) and a time for chemical reaction [76]. This concept has been applied to explain the variation in the lean light up limit for specific combustors across a range of combustor inlet conditions by characterising each combustor using its volume and

a characteristic mixing constant.

The inert CFD solutions for flows prior to ignition analysed above may also be analysed to give information on residence times, mixing times and to predict chemical or evaporation time scales. In this way a combustor's geometrical and mixing properties may be directly incorporated in to an analysis of its flame stabilisation. A brief discussion of the time scales present in the bluff body stabilised methane flame from chapter 6 is given here in order to identify metrics which could be used in stability or ignitability predictions.

The mixing layer between the recirculation zone and the fresh reactants can be visualised by plotting contours of $\nabla\xi \times \bar{\mathbf{U}}$, Fig. 7.19(a). This quantity gives a measure of the mixture fraction gradient normal to the mean velocity. In spray fueled flows the velocity curl, $\nabla \times \bar{\mathbf{U}}$, may be a useful marker of the shear layer location. Here, a contour of the mixture fraction curl arbitrarily placed at $|\nabla\xi \times \bar{\mathbf{U}}| = 150$ is used to delineate the stabilisation layer. The average time which burning flame particles spend in the layer has been evaluated by applying the particle transport model described previously. The local turbulent mixing frequency, $\tilde{\epsilon}/\tilde{k}$ plotted in Fig. 7.19(b), can be used to evaluate the average number of turbulent mixing times which flame particles from a particular spark spend in the mixing layer.

There is a large region radially inward from the mixing layer which is swept toward the bluff body and entrained into the mixing layer close to the lip of the bluff body, Fig 7.20(a). The peak average residence time of around 1ms is achieved for sparks close to the lip of the bluff body. Flame particles from such sparks experience an average of one turbulent time scale, Fig7.20(b) and around ten chemical time scales ($\tau = \alpha/{S_l}^2 = 120\mu s$ based on the stoichiometric laminar flame speed of methane). The region expected to give good ignitability is similar that found using the propagation based ignition modelling discussed in section 7.4.1.

This timescale analysis results in another model for ignitability which em-

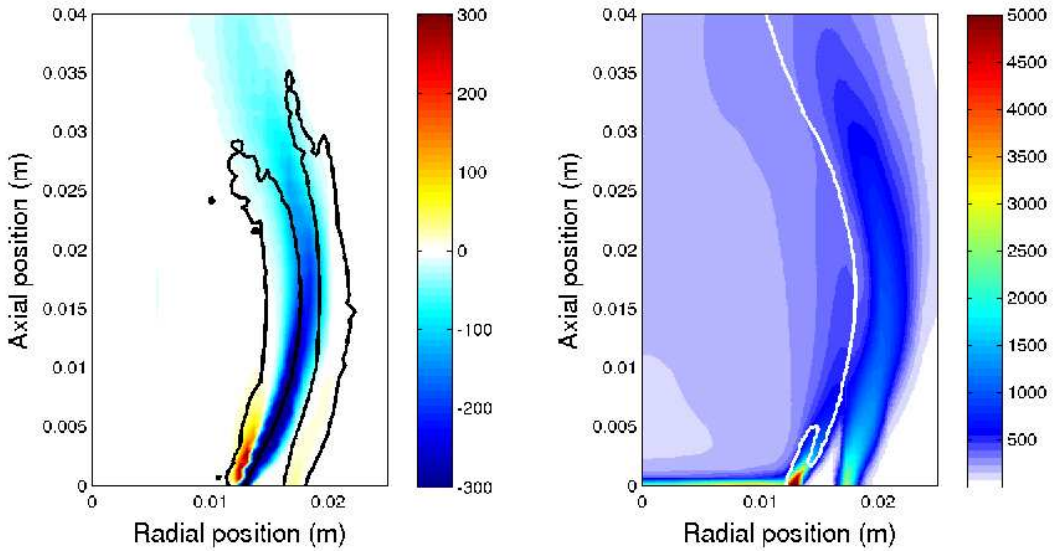

(a) (b)

Figure 7.19: (a): Contours of $\nabla\tilde{\xi} \times \bar{\mathbf{U}}$ (coloured) and $|\nabla \times \bar{\mathbf{U}}| = 2000$ (black); (b): Contours of the turbulent mixing frequency $\tilde{\epsilon}/\tilde{k}$ (s^{-1}) (coloured) and flammability factor = 0.5 (white).

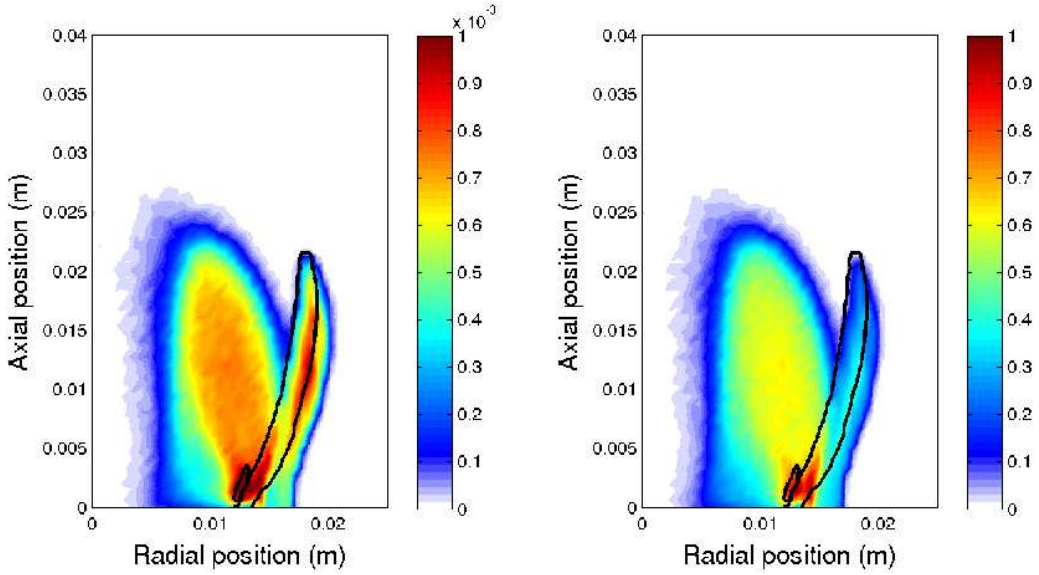

(a) (b)

Figure 7.20: (a): Contours of mean mixing layer residence time; (b):Contours of the mean number of turbulent mixing time scales flame particles are resident in the mixing layer. The mixing layer surface $|\nabla\xi \times \bar{\mathbf{U}}| = 150$ is shown in black.

phasises the role of recirculation of hot products in the successful establishment of a flame. Further development is needed to incorporate the effects of hot product recirculation into the propagation based modelling developed throughout this chapter. This may allow a less arbitrary definition of the stabilisation region for use in predictions such as those in section 7.4.3 .

7.5 Conclusions

This chapter discusses a method for analysing the ignitability of a flow, based only on information available in the un-reacting flow. The model used to describe the ignition process contains sufficient physics to give very good predictions for the ignitability of a jet flame, and also gives good predictions for the bluff body burner subject to the accuracy of the CFD solution.

Predictions for ignition of the spray burner appear very close to measurements. However further consideration needs to be given to the estimation of two phase flame speeds for flows with less volatile or larger droplets. The analysis is also useful for a gas turbine combustor despite the assumptions which have had to be made. Results make sense in terms of location of peak effectiveness and trends.

Chapter 8

Conclusions

This thesis presents development and implementation of the CMC modelling approach for simulation of forced ignition in turbulent flows. Ignition measurements for non-premixed jets [2] and both gas [3] and spray fueled [83] bluff body stabilised burners have been simulated. This represents a new and challenging test of the CMC modelling, and a first step towards the application of the CMC to industrial ignition simulations. Theoretical development has focused on the validation of modelling for turbulent flux processes, the limits of ignitability in non-premixed laminar flows, and CMC for spray fueled combustion. The discussion of the ignition process leads to presentation of an approach for preliminary design analysis and proposals for further developments within the CMC framework intended to advance the accuracy and practicality of predictive design simulations.

8.1 Spark ignition of turbulent non-premixed flow

Ignition of strained laminar mixing layers has been used to illustrate underlying processes and limits which can be encountered during ignition of turbulent flow. The evolution of the flame emanating from the localised ignition source shows intense flame fronts propagating outwards to consume regions of premixed flow, eventually leaving only a diffusion flame positioned at stoichiometry. The results showed that

there is a critical strain rate, which depends on the igniter, above which forced ignition is impossible for all spark positions. This critical value can be less than the extinction strain rate at which a steady flame becomes impossible, even for a spark thickness and energy that would ignite a stoichiometric homogeneous mixture.

A priori analysis of the CMC equation was performed using DNS data for turbulent non-premixed ignition kernels. All of the terms in the elliptic CMC model are significant in this spatially developing problem. The accuracy of the previously unvalidated gradient diffusion model for the conditional turbulent flux was considered. The results also show that due to large conditional fluctuations in the propagating turbulent flame fronts, neither the first nor the second order models for the conditionally-averaged reaction rate are accurate within the edge flame, indicating that alternative closures may be required.

A model for the spark ignition process has been used to explore the processes limiting spark ignition in a turbulent fuel jet. The model captured successful and unsuccessful ignition depending on the ignition energy. The model analysis was able to indicate that due to low turbulent mixing rates at the ignition locations ignition was limited by whether the spark's energy density was sufficient to induce autoignition in the spark region. Qualitative agreement with chapter 4's CMC analysis of DNS for non-premixed spark kernels is apparent.

The ignition models used in this work provide a meaningful initial condition for the study of subsequent flame evolution. The flow resulting from the initial condition is a function of the specified spark position, dimensions, energy, and power profile. However the appropriate values to be used for quantities such as the spark energy should receive further study. This might be achieved with more detailed numerical or experimental information on specific igniter types, and solving for compressible flow.

8.2 Flame propagation in turbulent non-premixed flow

Non-premixed edge flame propagation involves a balance between chemistry, molecular mixing, and spatial turbulent transport, which implies that modelling the conditional turbulent convection and diffusion are important for capturing flame establishment following ignition. Study of the flame propagation from DNS of ignition indicates that the usual gradient diffusion approximation for the conditional turbulent flux seems to be adequate for high turbulence intensities relative to the laminar burning velocity of a stoichiometric mixture, but there is evidence of counter-gradient transport effects, particularly with weak turbulence. An analysis of the major terms in the conditional scalar flux equation shows that pressure fluctuation effects are mainly responsible for the counter-gradient transport.

The first order CMC model was implemented with a two way coupling to the transient CFD solution. Study of the transient flame propagation phase shows the expansion across the flame having a strong effect on the propagation speed. Therefore a full coupling of the flow field and the combustion processes needs to be included in predictive calculations. The over prediction of flame propagation rates is attributed to possible over statement of the conditional reaction rate due to its first order closure, and the use of the RANS turbulence closure. Alternative CMC closures, which account for fluctuations around the conditional averages, and turbulence models where the large scale motions are resolved are appropriate.

The propagating turbulent edge flame has a narrow profile in mixture fraction space compared with that observed in the stabilised flame. This is likely be due to the flame stabilising in regions with high rates of molecular mixing, and is expected to result in modification of the unconditional average composition of burned mixture during flame stabilisation. The propagating flame exhibits strong heat release associated with rich and lean premixed fronts.

The performance of a one-step reaction model with variable model parameters produces excellent results for this problem compared to a skeletal mechanism for methane combustion. The use of similar reaction models is recommended for intensive industrial simulations of partially premixed propagation where the heat release rate is of primary interest.

A new modelling approach which incorporates counter gradient transport effects into the conditional turbulent flux model has been demonstrated. The model results in a modification to the structure of the conditional flame profiles, however it does not change the prediction of the lift off height greatly. The model needs further development and validation before it may be used reliably, this may require detailed experimental or numerical studies.

8.3 Ignition of spray fueled flow

The CMC model has been implemented and used to simulate the complete ignition process up to stabilisation, in a turbulent bluff body stabilised spray burner. This represents a new and industrially relevant application for the CMC model.

The rate of flame propagation is over predicted but qualitative agreement is obtained with experimental observations for the flame stabilisation process. The simulation of ignition in the spray fueled flow highlights the importance of the interaction between heat release and the fluid dynamics, and of the spray modelling.

Newly derived evaporative source terms in the two phase conditional moment closure equations have been evaluated in the turbulent spray burner. The terms are seen to be significant, particularly for very rich mixture fractions. Since flame propagation is generally governed by the reaction and transport processes of flammable mixture, it may not be essential to include all spray effects in simulations where modelling of flame propagation is the primary objective.

8.4 Ignition simulation for design

A design framework is proposed for development of combustors with restrictive ignition requirements, such as aviation gas turbines. The objective is to reduce the risk that a combustor design gets developed that has poor ignitability precluding the certification of an aero-engine. Used intelligently, with the benefit of accumulated design experience and clear objectives, numerical modelling may contribute throughout the evolution of a combustor design. The framework consists of three components presented below.

- Preliminary design survey.

  An initial indication of the main dependencies or uncertainties for ignitability across a range of potential combustor designs and operating regimes may be considered very efficiently using an approach based on chapter 7. The analysis results may be particularly useful for communicating the ignition properties and considerations to engineers focused on other aspects of the design. Where the proposed designs are similar to existing combustors for which ignitability data is available, scaling rules of the type proposed by Lefebvre [76] may also be used.

- Detailed design.

  High quality CFD simulation of the transient ignition process is computationally expensive and should be used sparingly to answer clearly defined design questions. The relative merits of RANS and LES methods will depend on the objectives of a particular study. The questions posed need not be limited to whether a combustor is ignitable at a particular condition since detailed information becomes available on every aspect of the successful or unsuccessful ignition process. Therefore solutions should be thoroughly analysed for opportunities for improving ignitability. It should be noted that while more

costly, LES is necessary to obtain statistics for ignitability, and is highly desirable from the perspective of accuracy. The design engineer may wish to investigate the effects of igniter type, power and placement and the fuel flow rate and placement. Preliminary non-reacting calculations may be useful to observe and optimise the impact of the electric discharge on fuel evaporation and the flow statistics for various designs before recourse to reacting simulation. The CFD tools should be well validated against previous ignitability measurements, however the attraction of advanced CFD modelling is its potential applicability far beyond the existing designs.

- Detailed diagnostics.

  Where an engine entering its ground based or even aircraft borne test phases displays inadequate ignitability, little direct experimental information would currently be available with which to rectify the deficiency. Any supplementary information resulting from detailed CFD simulation becomes very valuable. Numerical simulation may provide direct information on the causes for poor ignition probability observed and hence the aspects of the design requiring further consideration.

8.5 Areas for further research

Theory

- The present work indicates deficiencies in some of the submodels commonly used with the CMC. A first attempt has been made to develop a model for the conditional turbulent flux, however further development and validation is required. In particular, analysis of larger DNS datasets for configurations involving non-premixed flame propagation would be valuable in any further

modelling activity. The modelling of the conditional velocity should also be examined in propagating non-premixed flow since it is not clear that it produces the correct behaviour in non-premixed flame propagation.

- The occurrence of conditional counter-gradient transport in non-premixed flame propagation has implications for a variety of other turbulent reacting flow models, where the gradient diffusion approximation is widely used. The modelling introduced for the conditional turbulent flux combined with the mixture fraction PDF implies a model for the unconditional turbulent flux, and therefore may prove useful outside of CMC modelling.

- More advanced closures for the conditional reaction rate should be employed for flows with non-premixed flame propagation. The double conditioning closure, or the second order closure may both be considered (although chapter 4 indicates the later may still be inadequate). The practicalities of solving these more advanced models in spatially developing flames mean that implementations which afford a reduction in computational expense or modelling complexity should be sought. For example by only solving the second order model for selected species and temperature. For double conditioning, the conditional (cross) dissipation rates require modelling. This might be attempted by analysis of direct numerical simulation, for example by means of an extension of Juneja and Pope's configuration [58] so that the three stream mixing problem comprises fuel, oxidiser and combustion products. However it may be possible to make some progress and identify the underlying form needed for the conditional scalar dissipation rate from basic theory and phenomenological modelling.

- The one step reaction models with variable parameters used in parts of this thesis have been successful and the approach may be extended to represent further fuels such as 'JET-A' used in civil aviation. It is noted that the peak

flame temperature tends to be overestimated with the one step model, this may be remedied by expressing the heat release as more complicated functions of equivalence ratio.

- The currently poor prediction of the jet flame propagation has been partly attributed to the RANS turbulence closure. The supposed dependence of propagation on large scale structures in the jet should be explored by comparison of the RANS solution with LES computations for the flow.

- The range of applicability of the conditional evaporation rate models used in this work is not clear. Models should be validated and if necessary developed for spray combustion at conditions encountered during high altitude relight where droplets are expected to be large relative to those generally considered relevant for combustion systems. The effect of spray evaporation on the conditional scalar dissipation also requires study and if appropriate further modelling.

Implementation

The practical use of advanced turbulent combustion models for industrial predictions of gas turbine relight will require use of parallel computing. The current CMC implementation is able to make use of parallel computing however the current sequential use of CMC and CFD codes might be improved.

As the CMC is applied to more sophisticated geometries the basic structured grid may prove inconvenient. It appears that the approach of Cleary [28] where the CMC is solved in finite volume form having grouped several CFD cells into one CMC cell is attractive. This process may be automated for transient problems which require adaptive griding and resolution of awkward three dimensional flame surfaces (or four dimensions if the grid also adapts in the conditioning variable space). The ability to coarsen the CMC grid in regions of low spatial gradient is a key advantage

of the CMC for LES calculations since the number of CMC solution cells may be decoupled from the number of LES nodes. The CPU time might be compared with the dynamically thickened flamelet approach being pursued for relight computations by Boudier et al. [12] where the chemical reaction must be evaluated at every node throughout the simulation but without having to solve in conditioning space.

Particularly where advanced reaction rate closures need to be attempted, tabulation based solution methods may become attractive. Where a particular conditional flame structure is expected (in this thesis a very similar propagating non-premixed flame structure occurs in a variety of simulations) it may be useful to generate computational tables by sampling detailed one dimensional non-premixed flame propagation solutions for a range of turbulence levels and scalar dissipation rates. The sampled conditional source terms for the representative one dimensional flames would then be combined with presumed PDFs to give source terms for unconditional quantities being used in the 3D CFD (density and temperature).

Bibliography

[1] S.F. Ahmed, R. Balachandran, T. Marchione, and E. Mastorakos.
Spark ignition of turbulent non-premixed bluff-body flames.
Combustion and Flame, submitted, 2007.

[2] S.F Ahmed and E. Mastorakos.
Spark ignition of lifted turbulent jet flames.
Combustion and Flame, 146:215–231, 2006.

[3] S.F.A.F.S. Ahmed.
Spark Ignition of Turbulent Non-premixed Flames.
PhD thesis, University of Cambridge, 2006.

[4] R.E. Alvani and M. Fairweather.
Ignition characteristics of turbulent jet flames.
Transcripts of the Institute of Chemical Engineers, 80:917–923, 2002.

[5] C.A. Armitage, R. Balachandran, E. Mastorakos, and R.S. Cant.
Investigation of the nonlinear response of turbulent premixed flames to imposed inlet velocity.
Combustion and Flame, 146:419–436, 2005.

[6] R. Balachandran, B.O. Ayoola, A.P. Dowling C.F. Kaminski, and E. Mastorakos.
Experimental investigation of the nonlinear response of turbulent premixed flames to imposed inlet velocity oscillations.
Combustion and Flame, 143:37–55, 2005.

[7] D.R. Ballal and A.H. Lefebvre.
Ignition and flame quenching in flowing gaseous mixtures.
Proceedings of the Royal Society London, A., 357(1689):163–181, 1977.

[8] H.C. Barnett and R.R. Hibbard.
Basic considerations in the combustion of hydrocarbon fuel with air.
Technical Report 1300, NACA, 1959.

[9] R.W. Bilger.
Conditional moment closure for turbulent reacting flow.
Physics of Fluids A, 5(2):436–444, 1993.

[10] A.D. Birch, D.R Brown, M.G.Dodson, and J.R. Thomas.
Studies of flammability in turbulent flows using laser raman spectroscopy.
Proceedings of the Combustion Institute, 17:307–314, 1978.

[11] M.V. Blanc, P.G. Guest, G. von Elbe, and B. Lewis.
Ignition of explosive gas mixtures by electrical sparks. (I). Minimum ignition energies and quenching distances of mixtures of methane, oxygen, and inert gases.
Journal of Chemical Physics, 15:798–802, 1947.

[12] G. Boudier, L.Y.M. Gicquel, T. Poinsot, D. Bissieres, and C. Berat.
Comparison of LES, RANS and experiments in an aeronautical gas turbine combustion chamber.
Proceedings of the Combustion Institute, 31:3075–3082, 2007.

[13] D. Bradley, C.G.W. Sheppard, I.M. Shuardjaja, and R. Woolley.
Fundamentals of high-energy spark ignition with lasers.
Combustion and Flame, 138:55–77, 2004.

[14] K.N.C. Bray.
Turbulent Reacting Flows: Turbulent flows with premixed reactants.
(P.A. Libby and F.A. Williams Eds.) Springer Verlag Berlin, Heidelberg, New York, 1980.

[15] K.N.C. Bray, P.A. Libby, G. Masuya, and J.B. Moss.
Turbulence production in premixed turbulent flames.
Combustion Science and Technology, 25:127–140, 1981.

[16] J. Broadwell, W. Dahm, and M. Mungal.
Blowout of turbulent diffusion flames.
Proceedings of the Combustion Institute, 20:303–310, 1985.

[17] P.N. Brown and A.C. Hindmarsh.
Reduced storage matrix methods in stiff ode systems.
Journal of Applied Mathematics and Computation, 31:40–91, 1989.

[18] J. Buckmaster.
Edge-flames.
Progress in Energy and Combustion Science, 28:435–475, 2002.

[19] W.K. Bushe.
Conditional Moment Closure Methods For Autoignition Problems.

PhD thesis, University of Cambridge, 1995.

[20] *STAR-CD Methodology Guide version 3.26, 2005.*
CD Adapco.

[21] C.M. Cha and H. Pitsch.
Higher-order conditional moment closure modelling of local extinction and re-ignition in turbulent combustion.
Combustion Theory and Modelling, 6:425–437, 2002.

[22] N. Chakraborty.
Fundamental Study of Turbulent Premixed Combustion using Direct Numerical Simulation (DNS).
PhD thesis, University of Cambridge, 2004.

[23] N. Chakraborty and R.S. Cant.
Influence of Lewis number on curvature effects in turbulent premixed flame propagation in the thin reaction zones regime.
Physics of Fluids, 17(10)(105105), 2005.

[24] N. Chakraborty, E. Mastorakos, and R.S. Cant.
Effects of turbulence on spark ignition in inhomogeneous mixtures: A direct numerical simulation (DNS) study.
Combustion Science and Technology, 179:1–25, 2007.

[25] J.S. Chin and A.H. Lefebvre.
Steady-state evaporation characteristics of hydrocarbon fuel drops.
AIAA, 21(10):1437–1443, 1983.

[26] S.J. Chung and B.J. Lee.
On the characteristics of laminar lifted flames in a nonpremixed jet.
Combustion and Flame, 86:62–72, 1991.

[27] P. Clavin and F.A. Williams.
Effects of molecular diffusion and of thermal expansion of the structure and dynamics of premixed flames in turbulent flows of large scale and low intensity.
Journal of Fluid Mechanics, 116:251–282, 1982.

[28] M.J. Cleary and J.H. Kent.
Modelling of species in hood fires by conditional moment closure.
Combustion and Flame, 143:357–368, 2005.

[29] O. Colin, A. Benkenida, and C. Angelberger.
3D modeling of mixing, ignition and combustion phenomena in highly stratified gasoline engines.

Oil & Gas Science and Technology - Rev. IFP, 58:47–62, 2003.

[30] S.G. Davis and C.K. Law.
Determination of and fuel structure effects on laminar flame speeds of C-1 to C-8 hydrocarbons.
Combustion Science and Technology, 140:427–449, 1998.

[31] J. Dawson, R. Balachandran, and E. Mastorakos.
Velocity measurements in acoustically forced recirculating flows.
Technical Report 3, Hopkinson Laboratory, Cambridge University Engineering Department, 2007.

[32] F.X. Demoulin and R. Borghi.
Assumed PDF modeling of turbulent spray combustion.
Combustion Science and Technology, 158:249–271, 2000.

[33] C.B. Devaud and K.N.C. Bray.
Assessment of the applicability of conditional moment closure to a lifted turbulent flame: First order model.
Combustion and Flame, 132:102–114, 2003.

[34] C.B. Devaud, J.H. Kent, and R.W. Bilger.
Conditional moment closure applied to a lifted turbulent methane-air flame.
In *3rd Mediterranean Combustion Symposium*, pages 972–981, Marrakech, Morocco, June 2003.

[35] C.B. Devaud, R.W.Bilger, and T. Lui.
A new method of modeling the conditional scalar dissipation rate.
Physics of Fluids, 16(6):2004–2011, 2004.

[36] J-M. Duclos and O. Colin.
Arc and kernel tracking model for 3D spark-ignition engine calculations.
In *The Fifth International Symposium on Diagnostics and Modeling of Combustion in Internal Combustion Engines, Nagoya*, pages 343–350, 2001.

[37] A. Liñán F.A. Williams. E. Fernández-Tarrazo E, A.L. Sánchez.
A simple one-step chemistry model for partially premixed hydrocarbon combustion.
Combustion and Flame, 147:32–38, 2006.

[38] T. Echekki and J.H. Chen.
Structure and propagation of methanol-air triple flames.
Combustion and Flame, 114:231–245, 1998.

[39] N. Farrugia, P. Le Gal, and D.A. Greenhalgh.
Laser sheet dropsizing of dense sprays.

Optics and Laser Technology, 31(1):75–83, 1999.

[40] J.H. Frank, P.A.M. Kalt, and R.W. Bilger.
Measurements of conditional velocities in turbulent premixed flames by simultaneous OH-PLIF and PIV.
Combustion and Flame, 116:220–232, 1999.

[41] B. Gardiner, H. Yang, Z. Qin, G. Smith, D. Crosley, M. Golden, C.T. Bowman, R. Hanson, D. Davidson, M Frenklach, N. Moriarty, and B. Eiteener.
GRI 3.0 natural gas chemical mechanism.
http://me.berkeley.edu/gri_mech, 1999.

[42] A. Garmory, E.S Richardson, and E. Mastorakos.
Micromixing effects in a reacting plume by the stochastic fields method.
Atmospheric Environment, 40:1078–1091, 2006.

[43] H-W. Ge and E. Gutheil.
PDF simulation of turbulent spray flow.
Atomization and Sprays, 16(5):531–542, 2006.

[44] S. Ghosal and L. Vervisch.
Stability diagram for lift-off and blowout of a round jet laminar diffusion flame.
Combustion and Flame, 123:646–655, 2001.

[45] S.S. Girimaji.
On the modelling of scalar diffusion in isotropic turbulence.
Physics of Fluids A, 4(11):2529–2537, 1992.

[46] I. Glassman.
Combustion.
Academic Press Inc., Orlando, Florida, 2^{nd} edition, 1987.

[47] C. Goddard.
Unreacting RANS solutions for spray flows at altitude relight conditions.
Personal Correspondence, 2006.

[48] Fuel Flammability Task Group.
A review of the flammability hazard of jet a fuel vapor in civil transport aircraft fuel tanks.
Technical Report DOT/FAA/AR-98/26, Fire Safety Section, AAR-442, Federal Aviation Administration, 1998.

[49] A.K. Gupta, D.G. Lilley, and N.Syred.
Swirl Flows.
Abacus Press, Tunbridge Wells, 1^{st} edition, 1984.

[50] E.R. Hawkes, R. Sankaran, J C Sutherland, and J.H. Chen.
Scalar mixing in direct numerical simulations of temporally evolving plane jet flames with skeletal CO/H2 kinetics.
Proceedings of the Combustion Institute, 31:1633–1640, 2007.

[51] D.C. Haworth and S.B. Pope.
A generalized Langevin model for turbulent flows.
Physics of Fluids, 29(2):387–405, 1986.

[52] T.J. Held, A.J. Marchese, and F.L. Dryer.
A semi-empirical reaction mechanism for n-heptane oxidation and pyrolysis.
Combustion Science and Technology, 123:107–146, 1997.

[53] Y. Huang, C.J. Sung, and J.A. Eng.
Laminar flame speeds of primary reference fuels and reformer gas mixtures.
Combustion and Flame, 139:239–251, 2004.

[54] H.J. Hussein, S. Capp, and W.K. George.
Velocity measurements in a high-Reynolds-number, momentum-conserving axisymmetric, turbulent jet.
Journal of Fluid Mechanics, 258:31–75, 1994.

[55] H.G. Im and J.H. Chen.
Structure and propagation of triple flames in partially premixed hydrogen-air mixtures.
Combustion and Flame, 119:436–454, 1999.

[56] H.G. Im and J.H. Chen.
Effects of flow strain on triple flame propagation.
Combustion and Flame, 126:1384–1392, 2001.

[57] W.P. Jones, S. Navarro-Martinez, and O. Rohl.
Large eddy simulation of hydrogen auto-ignition with a probability density function method.
Proceedings of the Combustion Institute, 31:1765–1771, 2007.

[58] A. Juneja and S.B. Pope.
A DNS study of turbulent mixing of two passive scalars.
Physics of Fluids, 8(8):2161–2184, 1996.

[59] J.B. Kelman, A.J. Eltobaji, and A.R. Masri.
Laser imaging in the stabilization region of turbulent lifted flames.
Combustion Science and Technology, 135:117–134, 1998.

[60] I.S. Kim.
Conditional Moment Closure for Non-Premixed Turbulent Combustion.

PhD thesis, University of Cambridge, 2004.

[61] I.S. Kim and E. Mastorakos.
Simulations of turbulent lifted jet flames with two-dimensional conditional moment closure.
Proceedings of the Combustion Institute, 30:911–918, 2005.

[62] J. Kim and J.S. Kim.
Modelling of lifted turbulent diffusion flames in a channel mixing layer by flame hole dynamics.
Combustion Theory and Modelling, 10:21–37, 2006.

[63] S.H. Kim, K.Y. Huh, and R.W. Bilger.
Second-order conditional moment closure modelling of local extinction and re-ignition in turbulent non-premixed hydrocarbon flames.
Proceedings of the Combustion Institute, 29:2131–2137, 2002.

[64] S.H. Kim, K.Y. Huh, and R.A. Fraser.
Modelling autoignition of a turbulent methane jet by the conditional moment closure model.
Proceedings of the Combustion Institute, 28:185–191, 2000.

[65] S.H. Kim, K.Y. Huh, and L. Tao.
Application of the elliptic conditional moment closure model to a two-dimensional nonpremixed methanol bluff-body flame.
Combustion and Flame, 120:75–90, 2000.

[66] W.T. Kim and K.Y. Huh.
Numerical simulation of spray autoignition by the first-order conditional moment closure model.
Proceedings of the Combustion Institute, 29:569–576, 2002.

[67] P.N. Kioni, B. Rogg, K.N.C. Bray, and A. Liñán.
Flame spread in laminar mixing layers: The triple flame.
Combustion and Flame, 95:276–290, 1993.

[68] A.Y. Klimenko.
Multicomponent diffusion of various admixtures in turbulent flow.
Fluid Dynamics, 25:327–334, 1990.

[69] A.Y. Klimenko and R.W. Bilger.
Conditional moment closure of turbulent combustion.
Progress in Energy and Combustion Science, 25:595–687, 1999.

[70] Y.S. Ko and S.H. Chung.
Propagation of unsteady tribrachial flames in laminar non-premixed jets.

Combustion and Flame, 118:151–163, 1999.

[71] M. Kono, K. Hatori, and K. Iinuma.
Investigation on ignition ability of composite sparks in flowing mixtures.
Proceedings of the Combustion Institute, 20:133–140, 1984.

[72] A. Kronenburg.
Double conditioning of reactive scalar transport equations in turbulent non-premixed flames.
Physics of Fluids, 16(7):2640–2648, 2004.

[73] A. Kronenburg and M. Kostka.
Modeling extinction and re-ignition in turbulent flames.
Combustion and Flame, 143:342–356, 2005.

[74] V.R. Kuznetsov.
Influence of turbulence on the formation of high non-equilibrium concentrations of atoms and free radicals in diffusion flames.
Fluid Dynamics, 17:815–820, 1982.

[75] B.J. Lee and S.J. Chung.
Stabilization of lifted tribrachial flames in a laminar nonpremixed jet.
Combustion and Flame, 109:163–172, 1997.

[76] A. Lefebvre.
Gas Turbine Combustion.
Taylor and Francis, Philadelphia, 2^{nd} edition, 1999.

[77] J.P. Legier, T. Poinsot, and D. Veynante.
Dynamically thickened flame LES model for premixed and non-premixed turbulent combustion.
In *Proceedings of the Summer Program*, pages 157–168, Center for Turbulence Research, NASA Ames / Stanford University, 2000.

[78] M. Lesieur and O. Metais.
New trends in large-eddy simulations of turbulence.
Annual Review of Fluid Mechanics, 28:45–82, 1996.

[79] P.A. Libby and K.N.C Bray.
Countergradient diffusion in premixed turbulent flames.
AIAA Journal, 19(2):205–213, 1981.

[80] A. Liñán and A. Crespo.
An asymptotic analysis of unsteady diffusion flames for large activation energies.
Combustion Science and Technology, 14:95–117, 1976.

[81] K.H. Luo.
On local countergradient diffusion in turbulent diffusion flames.
Proceedings of Combustion Institute, 28:489–495, 2000.

[82] H.K. Ma and J.S. Harn.
The jet mixing effect on reaction flow in a bluff-body burner.
International Journal of Heat and Mass Transfer, 37:2957–2967, 1994.

[83] T. Marchione, S.F. Ahmed, R. Balachandran, and E. Mastorakos.
Effectiveness of localised spark ignition in recirculating n-heptane spray flames.
Proceedings of 21st ICDERS, submitted, 2007.

[84] E. Mastorakos and R.W. Bilger.
Second-order conditional moment closure for the autoignition of turbulent flows.
Physics of Fluids, 10(6):1246–1248, 1998.

[85] E. Mastorakos, A. M. K. P. Taylor, and J.H. Whitelaw.
Extinction and temperature characteristics of turbulent counterflow diffusion flames with partial premixing.
Combustion and Flame, 90:40–54, 1992.

[86] D.R. Mott and E.S. Oran.
CHEMEQ2: A solver for the stiff ordinary equations of chemical kinetics.
Technical Report 6400-01-8553, Naval Research Laboratory, 2001.

[87] C. Muller, H. Breitbach, and N. Peters.
Partially premixed turbulent flame propagation in jet flames.
Proceedings of the Combustion Institute, 25:1099–1106, 1994.

[88] L. Muniz and M. Mungal.
Instantaneous flame-stabilization velocities in lifted-jet diffusion flames.
Combustion and Flame, 111:16–31, 1997.

[89] R. Mustata, L. Valiño, C. Jimenez, W. P. Jones, and S Bondi.
A probability density function Eulerian Monte Carlo field method for large eddy simulations: Application to a turbulent piloted methane/air diffusion flame (Sandia D).
Combustion and Flame, 145:88–104, 2006.

[90] M. Namazian, J. Kelly, R.W. Schefer, S.C. Johnston, and M.B. Long.
Non-premixed bluff-body burner flow and flame imaging study.
Experiments in Fluids, 8:216–228, 1989.

[91] E.E. O'Brien and T.L. Jiang.

The conditional dissipation rate of an initially binary scalar in homogeneous turbulence.
Physics of Fluids, 3:3121–3123, 1991.

[92] Diophantus of Alexandria.
Arithmetica.
Fermat's 1665 copy, margin therein., c.250AD.

[93] A. Olivani, G. Solero, F. Cozzi, and A. Coghe.
Near field flow structure of isothermal swirling flows and reacting non-premixed swirling flames.
In *4th Mediterranean Combustion Symposium*, number IV 1, Lisbon, Portugal, October 2005.

[94] J.C. Pan, W.J. Schmoll, and D.R. Ballal.
Turbulent combustion properties behind a confined conical stabilizer.
Journal of Engineering for Gas Turbines and Power, 114:33–38, 1992.

[95] G. De Paola.
Conditional Moment Closure methods for autoignition problems.
PhD thesis, University of Cambridge, 2007.

[96] N. Peters.
Laminar diffusion flamelet models in non-premixed turbulent combustion.
Progress in Energy and Combustion Science, 10:319–339, 1984.

[97] N. Peters.
Turbulent Combustion.
Cambridge University Press, Cambridge, 1^{st} edition, 2000.

[98] N. Peters, U.C. Muller, H. Pitsch, and Y.P. Wan.
Modellierung der schadstoffbildung bei der dieselmotorischen verbrennung.
The Working Process of the Internal Combustion Engine, Sept:51–67, 1985.

[99] T.X. Phuoc, C.M. White, and D.J. McNeil.
Laser spark ignition of a jet diffusion flame.
Optics and Lasers in Engineering, 38(5):217–232, 2002.

[100] H. Pitsch and N. Peters.
A consistent flamelet formulation for non-premixed combustion considering differential diffusion effects.
Combustion and Flame, 114:26–40, 1998.

[101] S. Pope.
Turbulent Flows.
Cambridge University Press, Cambridge, 1^{st} edition, 2000.

[102] X. Qin, C.W. Choi, A. Mukhopadhyay, I.K. Puri, S.K Aggarwal, and V.R. Katta.
Triple flame propagation and stabilization in a laminar axisymmetric jet.
Combustion Theory and Modelling, 8:293–314, 2004.

[103] S.A. Rashkovsky.
Spark ignition of ill-mixed gases.
In *1st Mediterranean Combustion Symposium*, pages 1403–1411, Antalya, Turkey, June 1999.

[104] J. Ray, H.N. Najm, and R.B. McCoy.
Ignition front structure in a methane-air jet.
In *2nd Joint Meeting of the U.S. Sections of the Combustion Institute*, number 150, Oakland, CA, March 2001.

[105] R. Read.
Gas turbine relight diagnostics.
PhD thesis, University of Cambridge, 2007 in preparation.

[106] R.D. Reitz and R. Diwakar.
Effect of drop breakup on fuel sprays.
SAE Technical Paper Series 860469, 1986.

[107] J. Reveillon and L. Vervisch.
Spray vaporisation in nonpremixed turbulent combustion modeling: A single droplet model.
Combustion and Flame, 121:75–90, 2000.

[108] C.D. Richards and W.M. Pitts.
Global density effects on the self-preservation behaviour of turbulent free jets.
Journal of Fluid Mechanics, 254:417–435, 1993.

[109] E. Richardson, E.S. Mastorakos.
Numerical investigation of spark ignition in a laminar methane-air counterflow.
In *4th Mediterranean Combustion Symposium*, number I 4, Lisbon, Portugal, October 2005.

[110] E.S. Richardson.
Modelling of homogeneous charge compression ignition engines.
Master's thesis, University of Cambridge, 2003.

[111] E.S. Richardson.
Implementation of CHEMEQ2 for various turbulent combustion simulations.
Technical Report 1, Hopkinson Laboratory, Cambridge University Engineering Department, 2004.

[112] E.S. Richardson.
Application of the Fernández-Tarrazo et al. one-step chemistry model to the partially premixed combustion of n-heptane.
Technical Report 2, Hopkinson Laboratory, Cambridge University Engineering Department, 2006.

[113] E.S Richardson, N. Chakraborty, and E. Mastorakos.
Analysis of direct numerical simulations of ignition fronts in turbulent non-premixed flames in the context of conditional moment closure.
Proceedings of the Combustion Institute, 31:1683–1690, 2007.

[114] E.S Richardson and E. Mastorakos.
Numerical investigation of forced ignition in laminar counterflow non-premixed methane-air flames.
Combustion Science and Technology, 179:293–317, 2006.

[115] J. Rogerson.
Application of conditional moment closure model to a bagasse-fired boiler.
PhD thesis, University of Sydney, 2006.

[116] J. Rogerson, J.H. Kent, and R.W. Bilger.
Conditional moment closure in a bagasse fired boiler.
Proceedings of the Combustion Institute, 31:2805–2811, 2007.

[117] P. Rosin and E. Rammler.
The laws governing the fineness of powdered coal.
The Journal of the Institute of Fuel, 7:29–36, 1933.

[118] *The Combustion Simulation Laboratory, Version 1.3.*
Rotexo GmbH Co. KG, Haan, Germany, 2005.
www.SoftPredict.com.

[119] G. Ruetsch, L. Vervisch, and A. Liñán.
Effects of heat release on triple flames.
Physics of Fluids, 6(7):1447–1454, 1995.

[120] R. Schefer, M. Namazian, and J. Kelly.
Stabilization of lifted turbulent-jet flames.
Combustion and Flame, 99:75–86, 1994.

[121] R.W. Schefer, N. Namazian, J. Kelly, and M. Perrin.
Effect of confinement on bluff-body burner recirculation zone characteristics and flame stability.
Combustion Science and Technology, 120:185–211, 1996.

[122] W.D. Schulz, S.P. Henegan, S.L. Locklear, D.L. Geiger, and S.D. Anderson.
Static tests of jet fuel thermal and oxidative stability.
Journal of Propulsion and Power, 9(1):5–9, 1993.

[123] M.T.E. Smith, A.D. Birch, D.R. Brown, and M. Fairweather.
Studies of ignition and flame propagation in turbulent jets of natural gas, propane and a gas with a high hydrogen content.
Proceedings of the Combustion Institute, 21:1403–1408, 1986.

[124] N.S.A. Smith, C.M. Cha, H. Pitsch, and J.C. Oefelein.
Simulation and modelling of the behaviour of conditional scalar moments in turbulent spray combustion.
In *Proceedings of the Summer Program*, pages 207–218, Center for Turbulence Research, NASA Ames / Stanford University, 2000.

[125] M.D. Smooke and V. Giovangigli.
Reduced Chemical Mechanisms and Asymptotic Approximations for Methane-Air Flames.
(M.D. Smooke Ed.) Lecture Notes in Physics, Number 384,Springer, Berlin, 1991.

[126] C.G. Speziale, S. Sarkar, and T.B. Gatski.
Modelling the pressure-strain correlation of turbulence: an invariant dynamical systems approach.
Journal of Fluid Mechanics, 227:245–272, 1991.

[127] S. Sreedhara and K.Y. Huh.
Conditional statistics of nonreacting and reacting sprays in turbulent flows by direct numerical simulation.
Proceedings of the Combustion Institute, 31:2335–2342, 2006.

[128] L.K. Su, O.S. Sun, and M.G. Mungal.
Experimental investigation of stabilization mechanisms in turbulent, lifted jet diffusion flames.
Combustion and Flame, 144:494–512, 2006.

[129] N. Swaminathan and R.W. Bilger.
Scalar dissipation, diffusion and dilatation in turbulent hydrogen-air premixed flames with complex chemistry.
Combustion Theory and Modelling, 5:241–260, 2001.

[130] N. Syred.
A review of oscillation mechanisms and the role of the precessing vortex core (PVC) in swirl combustion systems.
Progress in Energy and Combustion Science, 32:93–161, 2006.

[131] A.M.K.P. Taylor and J.H. Whitelaw.
Velocity characteristics in the turbulent near wakes of confined axi-symmetric bluff bodies.
Journal of Fluid Mechanics, 139:391–418, 1984.

[132] M. Thiele, J. Warnatz, A. Dreizler, S .Lindenmaier, R. Schiebl, U. Maas, A. Grant, and P. Ewart.
Spark ignited hydrogen/air mixtures: two dimensional detailed modelling and laser based diagnostics.
Combustion and Flame, 128:74–87, 2002.

[133] S.R. Tieszen, D.W. Stamps, and T.J. O'Hern.
A heuristic model of turbulent mixing applied to blowout of turbulent jet diffusion flames.
Combustion and Flame, 106:442–466, 1996.

[134] T.Poinsot and S.Lele.
Boundary conditions for direct simulations of compressible viscous flows.
Journal of Computational Physics, 101:104–129, 1992.

[135] A. Triantafyllidis.
Conditional Moment Closure for Large Eddy Simulation of Turbulent Non-Premixed Ignition.
PhD thesis, University of Cambridge, 2008, in preparation.

[136] S.R. Turns.
An introduction to combustion.
McGraw-Hill, Boston, 2^{nd} edition, 2000.

[137] A. Upatnieks, J.F. Driscoll, C.C. Rasmussen, and S.L. Ceccio.
Liftoff of turbulent jet flames-assessment of edge flame and other concepts using cinema-PIV.
Combustion and Flame, 138:259–272, 2004.

[138] L Valiño.
A field Monte Carlo formulation for calculating the probability density function of a single scalar in a turbulent flow.
Flow Turbulence and Combustion, 60(2):157–172, 1998.

[139] L. Vanquickenborne and A.V. Tiggelen.
The stabilisation mechanism of lifted diffusion flames.
Combustion and Flame, 10:59–68, 1966.

[140] N.B. Vargaftik.
Tables on the Thermo-physical Properties of Liquids and Gases.
John Wiley and Sons, New York, 2^{nd} edition, 1975.

[141] L. Vervisch and P. Domingo.
Modeling source of spray for mixture fraction variance, a two-scale model for turbulent spray mixing.
Personal Correspondence, 2005.

[142] D. Veynante and T. Poinsot.
Effects of pressure gradients on turbulent premixed flames.
Journal of Fluid Mechanics, 353:83–114, 1997.

[143] D. Veynante, A. Trouvé, K.N.C. Bray, and T. Mantel.
Gradient and counter-gradient scalar transport in turbulent premixed flames.
Journal of Fluid Mechanics, 332:263–293, 1997.

[144] D. Veynante and L. Vervisch.
Turbulent combustion modelling.
Progress in Energy and Combustion Science, 28:193–266, 2002.

[145] D. Veynante, L. Vervisch, T. Poinsot, A. Liñán, and G. Ruetsch.
Triple flame structure and diffusion flame stabilization.
In *Proceedings of the Summer Program*, pages 55–73, Center for Turbulence Research, NASA Ames / Stanford University, 1994.

[146] K.A. Watson and K.M. Lyons.
Scalar and velocity field measurements in a lifted CH_4-air diffusion flame.
Combustion and Flame, 117:257–271, 1999.

[147] Y. M. Wright, G. de Paola, K. Boulouchos, and E. Mastorakos.
Simulations of spray autoignition and flame establishment with two-dimensional CMC.
Combustion and Flame, 143:402–419, 2005.

[148] I. Wygnanski and H. Fiedler.
Some measurements in a self-preserving jet.
Journal of Fluid Mechanics, 38:577–612, 1969.

[149] S. Ogawa Y. Mizobuchi, J. Shinjo and T. Takeno.
A numerical study on the formation of diffusion flame islands in a turbulent hydrogen jet lifted flame.
Proceedings of the Combustion Institute, 30:611–619, 2005.

[150] Ya.B. Zel'dovich.
Zh. Eksp. Teor. Fiz., 11, 1941.
See Shchetinkov, Ye.S., "The Physics of the Combustion of Gases", Chapter 5, Edited Translation FTD-HT-23-496-68, Translation Revision, Foreign Technology Division, Wright-Patterson AFB, Ohio, 1966.

Appendix A

Derivations

A.1 Derivation of the CMC energy equations in two phase flow

Bilger's decomposition method [9] is used to derive the conditional moment closure equation for enthalpy in two phase flows. A similar derivation was used by Rogerson [115] in his derivation of the two phase CMC equation for species mass fractions. The enthalpy equation is then transformed into the conditional temperature equation.

A.1.1 The CMC enthalpy equation with fuel evaporation

The conditional fluctuations of density and of the evaporation rate are neglected during the derivation. Equal, non-unity Lewis numbers have been accounted for. The mixture fraction is a conserved scalar and can be defined as the normalised mass fraction of an inert tracer introduced with the fuel, and evaporating or condensing identically to the fuel. The definition of mixture fraction is discussed further by Turns [136].

The conservative instantaneous balance equations are used:

$$\frac{\partial \rho}{\partial t} + \nabla \cdot (\rho \mathbf{v}) = \rho S \tag{A.1}$$

$$\frac{\partial (\rho Y_\alpha)}{\partial t} + \nabla \cdot (\rho \mathbf{v} Y_\alpha) - \nabla \cdot (\rho D \nabla Y_\alpha) = \rho w_\alpha + \rho S Y_{S\alpha} \tag{A.2}$$

$$\frac{\partial (\rho \xi)}{\partial t} + \nabla \cdot (\rho \mathbf{v} \xi) - \nabla \cdot (\rho D \nabla \xi) = \rho S \tag{A.3}$$

$$\frac{\partial (\rho h)}{\partial t} + \nabla \cdot (\rho \mathbf{v} h) - \nabla \cdot (\rho \alpha \nabla \xi) = \rho \dot{h}_{evap} + \sum_{i=\alpha}^{n} S Y_{S\alpha} h_\alpha. \tag{A.4}$$

where $Y_{S\alpha}$ is the mass fraction of species α in the liquid fuel, and $\dot{h}_{evap}$ is the heat transfer to the liquid phase.

Applying the decomposition $h = \langle h|\eta \rangle + h''$, the various enthalpy derivatives used in the derivation become:

$$\rho \frac{\partial h}{\partial t} = \rho \frac{\partial h''}{\partial t} + \rho \frac{\partial \langle h|\eta \rangle}{\partial t} + \rho \frac{\partial \xi}{\partial t} \frac{\partial \langle h|\eta \rangle}{\partial \eta} \tag{A.5}$$

$$\rho \mathbf{v} \cdot \nabla h = \rho \mathbf{v} \cdot \nabla h'' + \rho \mathbf{v} \cdot \nabla \langle h|\eta \rangle + \rho \mathbf{v} \cdot \nabla \xi \frac{\partial}{\partial \eta} \langle h|\eta \rangle \tag{A.6}$$

$$\nabla \cdot (\rho \alpha \nabla h) = \nabla \cdot \left[\begin{array}{ll} \rho \alpha \nabla h'' & + \rho \alpha \nabla \langle h|\eta \rangle + \rho \alpha \nabla \xi \frac{\partial \langle h|\eta \rangle}{\partial \eta} \\ & + \frac{1}{2} \rho \alpha \nabla (\xi - \eta)^2 \frac{\partial^2}{\partial \eta^2} \langle h|\eta \rangle \end{array} \right]. \tag{A.7}$$

Observe that,

$$\nabla \cdot \nabla (\xi - \eta)^2 = 2(\nabla \xi \cdot \nabla \xi + (\xi - \eta) \nabla \cdot \nabla \xi). \tag{A.8}$$

Inserting A.8 into A.7 gives,

$$\nabla \cdot (\rho \alpha \nabla h) = \nabla \cdot \left[\rho \alpha \nabla h'' + \rho \alpha \nabla \langle h|\eta \rangle + \rho \alpha \nabla \xi \frac{\partial}{\partial \eta} \langle h|\eta \rangle \right] + \rho \alpha (\nabla \xi)^2 \frac{\partial^2}{\partial \eta^2} \langle h|\eta \rangle. \tag{A.9}$$

Defining $Le \equiv \alpha/D$, and $N \equiv D(\nabla\xi)^2$, from A.1, A.2, A.3 and A.4 we find,

$$\begin{aligned}\rho\dot{h}_{evap} - h(\rho S) + \rho S\sum_{i=\alpha}^{n} Y_{S\alpha}h_\alpha &= A.5 + A.6 - A.9 \qquad (A.10)\\ &= \rho\frac{\partial h''}{\partial t} + \rho\mathbf{v}\cdot\nabla h'' - \nabla\cdot\rho\alpha\nabla h''\\ &\quad +\rho\frac{\partial Q_h}{\partial t} + \rho\cdot\nabla Q_h - \nabla\cdot(\rho\alpha\nabla Q_h)\\ &\quad +(1-\xi)S\frac{\partial Q_h}{\partial\eta} - \rho\alpha\nabla\xi\cdot\nabla(\frac{\partial Q_h}{\partial\eta})\\ &\quad -\rho LeN\frac{\partial^2 Q_h}{\partial\eta^2} + \nabla(\rho D\nabla\xi) - \nabla(\rho\alpha\nabla\xi)\end{aligned}$$

$\langle\rho|\eta\rangle$ and $\langle S|\eta\rangle$ are denoted by ρ_η and $S(\eta)$ respectively. Neglecting conditional fluctuations of density and evaporation rate, conditional averaging on $\xi = \eta$ gives equation A.13.

$$\begin{aligned}\rho_\eta\langle\dot{h}_{evap}|\eta\rangle - \rho_\eta S(\eta)Q_h + \rho_\eta S(\eta)\sum_{i=\alpha}^{n} Y_{S\alpha}h_\alpha &= \rho_\eta\frac{\partial Q_h}{\partial t} + \rho_\eta\langle\mathbf{v}|\eta\rangle\cdot\nabla Q_h \qquad (A.11)\\ &\quad +(1-\eta)S(\eta)\frac{\partial Q_h}{\partial\eta} - \rho_\eta LeN\frac{\partial^2 Q_h}{\partial\eta^2} - e_1 - e_2\\ e_1 &= \langle\nabla\cdot(\rho\alpha\nabla Q_h) + \rho\alpha\nabla\xi\cdot\nabla\frac{\partial Q_h}{\partial\eta}|\eta\rangle \qquad (A.12)\\ &\quad +(Le-1)\langle\nabla\cdot(\rho D\nabla\xi|\eta\rangle\frac{\partial Q_h}{\partial\eta}\\ e_2 &= -\langle\rho\frac{\partial h''}{\partial t} + \rho\mathbf{v}\cdot\nabla h'' - \nabla\cdot(\rho\alpha\nabla h'')|\eta\rangle \qquad (A.13)\end{aligned}$$

In the above Le is assumed constant even though D and α may be varying. The last term of e_1 in Eq. A.13 is the conditional diffusion term to which Klimenko and Bilger attribute generation of differential diffusion (of heat and mass). This term may be rewritten $(Le-1)/\rho_\eta M_\eta\frac{\partial Q_h}{\partial\eta}$, with $M_\eta \equiv \frac{1}{\rho_\eta}\langle\nabla\cdot(\rho D\nabla\xi)|\eta\rangle = \frac{1}{P(\eta)\rho_\eta}\frac{\partial}{\partial\eta}(\langle N|\eta\rangle P(\eta)\rho_\eta)$. The application of Bilger's closure hypothesis A.15 gives A.16 [9],

$$\begin{aligned}e_1 &= \frac{(Le-1)}{\rho_\eta}M_\eta\frac{\partial Q_h}{\partial\eta} \qquad (A.14)\\ e_2 &= \frac{\nabla\cdot\rho_\eta P(\eta)\langle\mathbf{v}''h''|\eta\rangle}{P(\eta)} \qquad (A.15)\end{aligned}$$

$$\frac{\partial Q_h}{\partial t} + \langle \mathbf{v}|\eta\rangle \cdot \nabla Q_h = -\frac{div(\rho_\eta \langle \mathbf{v}'' h''|\eta\rangle P(\eta))}{P(\eta)\rho_\eta} + \langle N|\eta\rangle \frac{\partial^2 Q_h}{\partial \eta^2} + \frac{(Le-1)}{\rho_\eta} M_\eta \frac{\partial Q_h}{\partial \eta} - (1-\eta)S(\eta)\frac{\partial Q_h}{\partial \eta} + S(\eta)\sum_{i=\alpha}^{n} h_\alpha Y_{S\alpha} + \langle \dot{h}_{evap}|\eta\rangle + S(\eta)Q_h \quad (A.16)$$

A.1.2 The CMC temperature equation with fuel evaporation

The closed CMC equation for temperature is obtained by expressing the specific enthalpy in terms of the composition and species enthalpies, Eq. A.17, resulting in the enthalpy derivatives given in Eq. A.18-A.20.

$$h = \sum_{i=\alpha}^{n} Y_\alpha h_\alpha \quad (A.17)$$

$$\frac{\partial h}{\partial t} = \sum_{i=\alpha}^{n} \frac{\partial Y_\alpha}{\partial t} h_\alpha + c_p \frac{\partial T}{\partial t} \quad (A.18)$$

$$\frac{\partial h}{\partial \eta} = \sum_{i=\alpha}^{n} \frac{\partial Y_\alpha}{\partial \eta} h_\alpha + c_p \frac{\partial T}{\partial \eta} \quad (A.19)$$

$$\frac{\partial^2 h}{\partial \eta^2} = \sum_{i=\alpha}^{n} \frac{\partial^2 Y_\alpha}{\partial \eta^2} h_\alpha + \sum_{i=\alpha}^{n} \frac{\partial Y_\alpha}{\partial \eta} \cdot c_{p\alpha} \frac{\partial T}{\partial \eta} + \frac{\partial c_p}{\partial \eta}\frac{\partial T}{\partial \eta} + c_p \frac{\partial^2 T}{\partial \eta^2} \quad (A.20)$$

Using Eq. A.17-A.18, equation A.16 becomes Eq. A.21.

$$\sum_{i=\alpha}^{n} \frac{\partial Q_\alpha}{\partial t} h_\alpha + \langle c_p|\eta\rangle \frac{\partial Q_T}{\partial t} = Le\langle N|\eta\rangle \left\{ \langle c_p|\eta\rangle \frac{\partial^2 Q_T}{\partial \eta^2} + \left[\frac{\partial \langle c_p|\eta\rangle}{\partial \eta} + \sum_{i=\alpha}^{n} \frac{c_{p\alpha} \partial Q_\alpha}{\partial \eta} \right] \frac{\partial Q_T}{\partial \eta} \right\} + Le\langle N|\eta\rangle \sum_{i=\alpha}^{n} \frac{\partial^2 Q_\alpha}{\partial \eta^2} h_\alpha + \frac{(Le-1)}{\rho_\eta} M_\eta \left[\sum_{i=\alpha}^{n} \frac{\partial Q_\alpha}{\partial \eta} h_\alpha + c_p \frac{\partial Q_T}{\partial \eta} \right] - S(\eta) \sum_{i=\alpha}^{n} Q_\alpha h_\alpha - (1-\eta)S(\eta) \left[\sum_{i=\alpha}^{n} \frac{\partial Q_\alpha}{\partial \eta} h_\alpha + \langle c_p|\eta\rangle \frac{\partial Q_T}{\partial \eta} \right] + \langle \dot{h}_{evap}|\eta\rangle + S(\eta) \sum_{i=\alpha}^{n} h_\alpha Y_{S\alpha} + T_{h_{spatial}} \quad (A.21)$$

where conditional fluctuations of the specific heat capacity have been neglected and the spatial transport terms $T_{h_{spatial}}$ are not shown in full for clarity.

The equivalent equation for the transport of conditionally averaged species has been multiplied by h_α and summed over all species, resulting in Eq. A.22:

$$\begin{aligned}\sum_{i=\alpha}^{n}\frac{\partial Q_\alpha}{\partial t} &= \langle N|\eta\rangle\sum_{i=\alpha}^{n}\frac{\partial^2 Q_\alpha}{\partial\eta^2}h_\alpha+\sum_{i=\alpha}^{n}\langle w_\alpha|\eta\rangle h_\alpha - S(\eta)\sum_{i=\alpha}^{n}Q_\alpha h_\alpha \\ &\quad -(1-\eta)S(\eta)\sum_{i=\alpha}^{n}h_\alpha\frac{\partial Q_\alpha}{\partial\eta}+\sum_{i=\alpha}^{n}S(\eta)Y_{s\alpha}h_\alpha+T_{Y_{spatial}} \qquad \text{(A.22)}\end{aligned}$$

where the spatial transport terms are included in $T_{Y\,spatial}$. Subtracting Eq. A.22 from Eq. A.21 yields the closed form for the CMC temperature equation in the presence of an evaporating fuel spray, Eq. A.24.

$$\begin{aligned}\frac{\partial Q_T}{\partial t}+\langle\mathbf{v}|\eta\rangle\cdot\nabla Q_T &= -\frac{div(\rho_\eta\langle\mathbf{v}''T''|\eta\rangle P(\eta))}{P(\eta)\rho_\eta}+\sum_\alpha\frac{\langle W_\alpha|\eta\rangle h_\alpha}{\langle c_p|\eta\rangle} \qquad \text{(A.23)}\\ &\quad +\langle N|\eta\rangle\left\{\frac{\partial^2 Q_T}{\partial\eta^2}+\frac{1}{\langle c_p|\eta\rangle}\left(\frac{\partial\langle c_p|\eta\rangle}{\partial\eta}+\sum_{\alpha=1}^{N}\frac{\partial Q_\alpha}{\partial\eta}c_{p\alpha}\right)\frac{\partial Q_T}{\partial\eta}\right\}\\ &\quad -(1-\eta)S(\eta)\frac{\partial Q_T}{\partial\eta}+\frac{\langle\dot{h}_{evap}|\eta\rangle}{\langle c_p|\eta\rangle}\\ &\quad +\frac{(Le-1)}{\rho_\eta}M_\eta\left[\sum_{i=\alpha}^{n}\frac{\partial Q_\alpha}{\partial\eta}h_\alpha+c_p\frac{\partial Q_T}{\partial\eta}\right]\end{aligned}$$

A.2 Second order reaction rate closure

In the DNS of chapter 4 the reaction rate of fuel has been defined by the Arrhenius expression:

$$\dot{w}_F=-B^*\rho Y_F Y_O\exp\left[-\beta(1-T)/(1-\alpha(1-T))\right] \qquad \text{(A.24)}$$

with,

$$B^* = B \exp -\frac{\beta}{\alpha} \tag{A.25}$$

$$\alpha = \frac{T_{ad} - T_0}{T_0} \tag{A.26}$$

$$\beta = E_a \frac{T_{ad} - T_0}{R^0 T_{ad}^2} \tag{A.27}$$

$$T = \frac{\hat{T} - T_0}{T_{ad} - T_0} \tag{A.28}$$

The second order closure for the reaction rate is found from a Taylor expansion of Eq. A.24, neglecting terms of third order and above, $O(3)$.

$$\langle w_F|\eta\rangle = \{1 + F\}\, w_F(\langle \mathbf{Y}|\eta\rangle) \tag{A.29}$$

$$F = \frac{1}{2}\frac{\beta^2 - 2\alpha\beta(1 - \alpha(1 - \langle T|\eta\rangle)}{[1 - \alpha(1 - \langle T|\eta\rangle)]^4} . \langle T''^2|\eta\rangle \tag{A.30}$$

$$+ \quad \frac{\langle Y_F'' Y_O''|\eta\rangle}{\langle Y_F|\eta\rangle\langle Y_O|\eta\rangle} + \left[\frac{\langle Y_F'' T''|\eta\rangle}{\langle Y_F|\eta\rangle} + \frac{\langle Y_O'' T''|\eta\rangle}{\langle Y_O|\eta\rangle}\right] \frac{\beta}{[1 - \alpha(1 - \langle T|\eta\rangle)]^2} + O(3) \tag{A.31}$$

A.3 Derivation of the conditional turbulent flux transport equation

A.3.1 Overview

The derivation of the conditional turbulent flux equation presented here uses a decompositional approach with similarities to that used by Bilger for the conditional moment closure [9]. The species Schmidt numbers ($Sc = \mu/\rho D$) have been assumed to be equal but not necessarily unity. The equations are left in unclosed form.

The starting point of the derivation is the instantaneous conservation equations for momentum, species mass fractions $\mathbf{Y}$, mixture fraction and mass. These equations are used to give the transport equations for the conditional expectation of species mass fraction (ie. the unclosed, conservative conditional moment closure equation) $\rho_\eta\langle Y|\eta\rangle$ and of velocity $\rho_\eta\langle u|\eta\rangle$. The conditional velocity fluctuation is then multiplied by the difference between the equations for ρY and $\rho_\eta\langle Y|\eta\rangle$, and

added to the conditional fluctuation of Y multiplied by the difference between the equations for ρu and $\rho_\eta \langle u|\eta\rangle$. A final round of conditional averaging and simplification yields the final conditional turbulent flux equation.

A.3.2 Instantaneous balance equations

The instantaneous balance equations are written in non-conservative form as:

$$\rho\frac{\partial u_i}{\partial t} + \rho u_j \frac{\partial u_i}{\partial x_j} = -\frac{\partial p}{\partial x_i} + \frac{\partial}{\partial x_j}\left[\mu\frac{\partial u_i}{\partial x_j}\right] \tag{A.32}$$

$$\rho\frac{\partial Y}{\partial t} + \rho u_j \frac{\partial Y}{\partial x_j} = \dot{w} + \frac{\partial}{\partial x_j}\left[\rho D\frac{\partial Y}{\partial x_j}\right] \tag{A.33}$$

$$\rho\frac{\partial \xi}{\partial t} + \rho u_j \frac{\partial xi}{\partial x_j} = \frac{\partial}{\partial x_j}\left[\rho D\frac{\partial \xi}{\partial x_j}\right] \tag{A.34}$$

The equation for momentum, Eq. A.32, neglects the viscous term arising in non-solenoidal flows, $\frac{\partial}{\partial x_j}\left[\mu\frac{\partial u_j}{\partial x_i}\right]$.

The mass fractions and velocities are decomposed into density weighted conditional expectations and Favre fluctuations given by:

$$Y = \frac{\langle \rho Y \mid \eta\rangle}{\langle \rho \mid \eta\rangle} + Y'' \tag{A.35}$$

$$u_i = \frac{\langle \rho u_i \mid \eta\rangle}{\langle \rho \mid \eta\rangle} + u_i'' \tag{A.36}$$

however the notation $\langle\cdot|\eta\rangle = \langle\rho\cdot|\eta\rangle/\langle\rho|\eta\rangle$, and $\langle\rho|\eta\rangle = \rho_\eta$ is used throughout this derivation for brevity.

A.3.3 The conditional species mass fraction equation

The following derivatives for the decomposed species mass fraction are used in the derivation of the conditional mass fraction:

$$\frac{\partial Y}{\partial t} = \frac{\partial \langle Y \mid \eta \rangle}{\partial t} + \frac{\partial \langle Y \mid \eta \rangle}{\partial \eta}\frac{\partial \xi}{\partial t} + \frac{\partial Y''}{\partial t} \tag{A.37}$$

$$\frac{\partial Y}{\partial x_j} = \frac{\partial \langle Y \mid \eta \rangle}{\partial x_j} + \frac{\partial \langle Y \mid \eta \rangle}{\partial \eta}\frac{\partial \xi}{\partial x_j} + \frac{\partial Y''}{\partial x_j} \tag{A.38}$$

$$\begin{aligned}\frac{\partial}{\partial x_j}\left[\rho D\frac{\partial Y}{\partial x_j}\right] &= \frac{\partial}{\partial x_j}\left[\rho D\frac{\partial \langle Y \mid \eta \rangle}{\partial x_j}\right] + \rho D\frac{\partial \xi}{\partial x_j}\frac{\partial}{\partial x_j}\frac{\partial \langle Y \mid \eta \rangle}{\partial \eta} \\ &+ \frac{\partial \langle Y \mid \eta \rangle}{\partial \eta}\frac{\partial}{\partial x_j}\left[\rho D\frac{\partial \xi}{\partial x_j}\right] + \rho D\left(\frac{\partial \xi}{\partial x_j}\right)^2\frac{\partial^2 \langle Y \mid \eta \rangle}{\partial \eta^2} + \frac{\partial}{\partial x_j}\left(\rho D\frac{\partial Y''}{\partial x_j}\right)\end{aligned} \tag{A.39}$$

Using Eqs. A.37-A.39, and decomposing the reaction rate term, the equation for species mass fractions is re-written:

$$\begin{aligned}\rho\frac{\partial}{\partial t}\langle Y \mid \eta \rangle &+ \rho\frac{\partial Y''}{\partial t} + \rho\frac{\partial}{\partial \eta}\langle Y \mid \eta \rangle\left[\frac{\partial \xi}{\partial t} + u_j\frac{\partial \xi}{\partial x_j}\right] \\ &+ \rho\left[\langle u_j \mid \eta \rangle + u_j''\right]\left[\frac{\partial}{\partial x_j}[\langle Y \mid \eta \rangle] + \frac{\partial Y''}{\partial x_j}\right] \\ &= \rho\langle \dot{w} \mid \eta \rangle + \rho\dot{w''} + \frac{\partial}{\partial x_j}\left[\mu\frac{\partial \langle Y \mid \eta \rangle}{\partial x_j}\right] + \mu\frac{\partial \xi}{\partial x_j}\frac{\partial}{\partial x_j}\frac{\partial \langle Y \mid \eta \rangle}{\partial \eta} \\ &+ \frac{\partial \langle Y \mid \eta \rangle}{\partial \eta}\frac{\partial}{\partial x_j}\left[\mu\frac{\partial \xi}{\partial x_j}\right] + \mu\left(\frac{\partial \xi}{\partial x_j}\right)^2\frac{\partial^2 \langle Y \mid \eta \rangle}{\partial \eta^2} + \frac{\partial}{\partial x_j}\left(\mu\frac{\partial Y''}{\partial x_j}\right)\end{aligned} \tag{A.40}$$

Subtracting the mixture fraction equation A.34 and rearranging gives

$$\begin{aligned}\frac{\partial}{\partial t}\left[\rho\langle Y \mid \eta \rangle\right] &+ \frac{\partial}{\partial x_j}\left[\rho u_j\langle Y \mid \eta \rangle\right] + \frac{\partial}{\partial t}\left[\rho Y''\right] + \frac{\partial}{\partial x_j}\left[\rho Y {u_i}''\right] = \\ &\rho\langle \dot{w} \mid \eta \rangle + \rho\dot{w''} + \frac{\partial}{\partial x_j}\left[\rho D\frac{\partial \langle Y \mid \eta \rangle}{\partial x_j}\right] + \rho D\frac{\partial \xi}{\partial x_j}\frac{\partial}{\partial x_j}\frac{\partial \langle Y \mid \eta \rangle}{\partial \eta} \\ &+ \rho D\left(\frac{\partial \xi}{\partial x_j}\right)^2\frac{\partial^2 \langle Y \mid \eta \rangle}{\partial \eta^2} + \frac{\partial}{\partial x_j}\left(\rho D\frac{\partial Y''}{\partial x_j}\right)\end{aligned} \tag{A.41}$$

Taking conditional Favre averages,

$$\begin{aligned}\frac{\partial}{\partial t}\left[\rho_\eta\langle Y \mid \eta\rangle\right] \;+\; & \frac{\partial}{\partial x_j}\left[\rho_\eta\langle u_j \mid \eta\rangle\langle Y \mid \eta\rangle\right] + \frac{\partial}{\partial x_j}\left[\rho_\eta\langle Y''u_j'' \mid \eta\rangle\right] = \\ & \rho_\eta\langle \dot{w} \mid \eta\rangle + \langle \rho D\frac{\partial\xi}{\partial x_j}\frac{\partial}{\partial x_j}\frac{\partial\langle Y \mid \eta\rangle}{\partial\eta} \mid \eta\rangle + \rho_\eta\langle N \mid \eta\rangle\frac{\partial^2\langle Y \mid \eta\rangle}{\partial\eta^2} \\ +\; & \langle\frac{\partial}{\partial x_j}\left[\rho D\frac{\partial\langle Y \mid \eta\rangle}{\partial x_j}\right] \mid \eta\rangle + \langle\frac{\partial}{\partial x_j}\left(\rho D\frac{\partial Y''}{\partial x_j}\right) \mid \eta\rangle \qquad \text{(A.42)}\end{aligned}$$

Equation A.42 is then subtracted from the conservative species mass fraction transport equation and multiplied by u_i'':

$$\begin{aligned}\frac{\partial}{\partial t}(\rho Y \;-\; & \rho_\eta\langle Y \mid \eta\rangle).u_i'' + \frac{\partial}{\partial x_j}\left[\rho Y u_j - \rho_\eta\langle Y \mid \eta\rangle\langle u_j \mid \eta\rangle\right].u_i'' - \frac{\partial}{\partial x_j}\left[\rho_\eta\langle Y''u_j'' \mid \eta\rangle\right].u_i'' = \\ & \rho\langle \dot{w} \mid \eta\rangle.u_i'' + \rho\dot{w}''.u_i'' - \rho_\eta\langle \dot{w} \mid \eta\rangle.u_i'' \\ +\; & \rho D\left(\frac{\partial\xi}{\partial x_j}\right)^2\frac{\partial^2\langle Y \mid \eta\rangle}{\partial\eta^2}u_i'' + \frac{\partial}{\partial x_j}\left[\rho D\frac{\partial Y''}{\partial x_j}\right]u_i'' + \rho D\frac{\partial\xi}{\partial x_j}\frac{\partial}{\partial x_j}\left[\frac{\partial\langle Y \mid \eta\rangle}{\partial\eta}\right]u_i'' \\ -\; & \langle\rho D\frac{\partial\xi}{\partial x_j}\frac{\partial}{\partial x_j}\left[\frac{\partial\langle Y \mid \eta\rangle}{\partial\eta}\right] \mid \eta\rangle u_i'' + \left[\frac{\partial}{\partial x_j}\left[\rho D\frac{\partial\langle Y \mid \eta\rangle}{\partial x_j}\right]\right]u_i'' \\ -\; & \langle\frac{\partial}{\partial x_j}\rho D\frac{\partial\langle Y \mid \eta\rangle}{\partial x_j} \mid \eta\rangle u_i'' \\ -\; & \langle\rho D\left(\frac{\partial\xi}{\partial x_j}\right)^2 \mid \eta\rangle\frac{\partial^2\langle Y \mid \eta\rangle}{\partial\eta^2}u_i'' - \langle\frac{\partial}{\partial x_j}\left[\rho D\frac{\partial Y''}{\partial x_j}\right] \mid \eta\rangle u_i'' \qquad \text{(A.43)}\end{aligned}$$

A.3.4 The conditional velocity equation

The following derivatives for the decomposed species mass fraction are used in the derivation of the conditional mass fraction:

$$\frac{\partial u_i}{\partial t} = \frac{\partial \langle u_i \mid \eta \rangle}{\partial t} + \frac{\partial \langle u_i \mid \eta \rangle}{\partial \eta}\frac{\partial \xi}{\partial t} + \frac{\partial u_i''}{\partial t} \tag{A.44}$$

$$\frac{\partial u_i}{\partial x_j} = \frac{\partial \langle u_i \mid \eta \rangle}{\partial x_j} + \frac{\partial \langle u_i \mid \eta \rangle}{\partial \eta}\frac{\partial \xi}{\partial x_j} + \frac{\partial u_i''}{\partial x_j} \tag{A.45}$$

$$\begin{aligned}\frac{\partial}{\partial x_j}\left[\mu\frac{\partial u_i}{\partial x_j}\right] &= \frac{\partial}{\partial x_j}\left[\mu\frac{\partial \langle u_i \mid \eta \rangle}{\partial x_j}\right] + \mu\frac{\partial \xi}{\partial x_j}\frac{\partial}{\partial x_j}\frac{\partial \langle u_i \mid \eta \rangle}{\partial \eta} \\ &\quad + \frac{\partial \langle u_i \mid \eta \rangle}{\partial \eta}\frac{\partial}{\partial x_j}\left[\mu\frac{\partial \xi}{\partial x_j}\right] + \mu\left(\frac{\partial \xi}{\partial x_j}\right)^2\frac{\partial^2 \langle u_i \mid \eta \rangle}{\partial \eta^2} + \frac{\partial}{\partial x_j}\left(\mu\frac{\partial u_i''}{\partial x_j}\right)\end{aligned} \tag{A.46}$$

Substituting Eqs. A.44-A.46 into Eq. A.32, and decomposing the pressure term gives:

$$\begin{aligned}\rho\frac{\partial}{\partial t}\langle u_i \mid \eta \rangle &+ \rho\frac{\partial u_i''}{\partial t} + \rho\frac{\partial}{\partial \eta}\langle u_i \mid \eta \rangle\left[\frac{\partial \xi}{\partial t} + u_j\frac{\partial \xi}{\partial x_j}\right] \\ &+ \rho\left[\langle u_j \mid \eta \rangle + u_j''\right]\left[\frac{\partial}{\partial x_j}[\langle u_i \mid \eta \rangle] + \frac{\partial u_i''}{\partial x_j}\right] \\ &= -\frac{\partial \langle p \mid \eta \rangle}{\partial x_i} - \frac{\partial \langle p \mid \eta \rangle}{\partial \eta}\frac{\partial \xi}{\partial x_i} - \frac{\partial p''}{\partial x_i} \\ &\quad + \frac{\partial}{\partial x_j}\left[\mu\frac{\partial \langle u_i \mid \eta \rangle}{\partial x_j}\right] + \mu\frac{\partial \xi}{\partial x_j}\frac{\partial}{\partial x_j}\frac{\partial \langle u_i \mid \eta \rangle}{\partial \eta} \\ &\quad + \frac{\partial \langle u_i \mid \eta \rangle}{\partial \eta}\frac{\partial}{\partial x_j}\left[\mu\frac{\partial \xi}{\partial x_j}\right] + \mu\left(\frac{\partial \xi}{\partial x_j}\right)^2\frac{\partial^2 \langle u_i \mid \eta \rangle}{\partial \eta^2} + \frac{\partial}{\partial x_j}\left(\mu\frac{\partial u_i''}{\partial x_j}\right)\end{aligned} \tag{A.47}$$

Subtracting the mixture fraction equation A.34 and rearranging gives

$$\begin{aligned}\frac{\partial}{\partial t}\left[\rho\langle u_i \mid \eta\rangle\right] &+ \frac{\partial}{\partial x_j}\left[\rho u_j\langle u_i \mid \eta\rangle\right] + \frac{\partial}{\partial t}\left[\rho {u_i}''\right] + \frac{\partial}{\partial x_j}\left[\rho u_j {u_i}''\right] = \\ &- \frac{\partial\langle p \mid \eta\rangle}{\partial x_i} - \frac{\partial\langle p \mid \eta\rangle}{\partial\eta}\frac{\partial\xi}{\partial x_i} - \frac{\partial p''}{\partial x_i} + \frac{\partial}{\partial x_j}\left[\mu\frac{\partial\langle u_i \mid \eta\rangle}{\partial x_j}\right] \\ &+ \mu\frac{\partial\xi}{\partial x_j}\frac{\partial}{\partial x_j}\frac{\partial\langle u_i \mid \eta\rangle}{\partial\eta} + \frac{\partial\langle u_i \mid \eta\rangle}{\partial\eta}\frac{\partial}{\partial x_j}\left[\left(\mu - \rho D\right)\frac{\partial\xi}{\partial x_j}\right] \\ &+ \mu\left(\frac{\partial\xi}{\partial x_j}\right)^2\frac{\partial^2\langle u_i \mid \eta\rangle}{\partial\eta^2} + \frac{\partial}{\partial x_j}\left(\mu\frac{\partial {u_i}''}{\partial x_j}\right)\end{aligned} \tag{A.48}$$

Taking conditional Favre averages,

$$\begin{aligned}\frac{\partial}{\partial t}\left[\rho_\eta\langle u_i \mid \eta\rangle\right] &+ \frac{\partial}{\partial x_j}\left[\rho_\eta\langle u_j \mid \eta\rangle\langle u_i \mid \eta\rangle\right] + \frac{\partial}{\partial x_j}\left[\rho_\eta\langle {u_i}'' {u_j}'' \mid \eta\rangle\right] = \\ &- \frac{\partial\langle p \mid \eta\rangle}{\partial x_i} - \frac{\partial\langle p \mid \eta\rangle}{\partial\eta}\frac{\partial\xi}{\partial x_i} - \frac{\partial p''}{\partial x_i} + \langle\mu\frac{\partial\xi}{\partial x_j}\frac{\partial}{\partial x_j}\frac{\partial\langle u_i \mid \eta\rangle}{\partial\eta} \mid \eta\rangle \\ &+ \frac{\partial\langle u_i \mid \eta\rangle}{\partial\eta}\langle\frac{\partial}{\partial x_j}\left[\rho D\left(Sc - 1\right)\frac{\partial\xi}{\partial x_j}\right] \mid \eta\rangle + Sc\rho_\eta\langle N \mid \eta\rangle\frac{\partial^2\langle u_i \mid \eta\rangle}{\partial\eta^2} \\ &+ \langle\frac{\partial}{\partial x_j}\left[\mu\frac{\partial\langle u_i \mid \eta\rangle}{\partial x_j}\right] \mid \eta\rangle + \langle\frac{\partial}{\partial x_j}\left(\mu\frac{\partial {u_i}''}{\partial x_j}\right) \mid \eta\rangle\end{aligned} \tag{A.49}$$

Equation A.49 is then subtracted from the conservative form of the momentum equation and multiplied by Y'':

$$\begin{aligned}
\frac{\partial}{\partial t}(\rho u_i \;-\; & \rho_\eta \langle u_i \mid \eta\rangle).Y'' + \frac{\partial}{\partial x_j}\left[\rho u_i u_j - \rho_\eta \langle u_i \mid \eta\rangle\langle u_j \mid \eta\rangle\right].Y'' - \frac{\partial}{\partial x_j}\left[\rho_\eta \langle {u_i}'' {u_j}'' \mid \eta\rangle\right].Y'' = \\
- \; & \frac{\partial p''}{\partial x_i}.Y'' + \frac{\partial}{\partial \eta}\langle p \mid \eta\rangle\langle \frac{\partial \xi}{\partial x_i} \mid \eta\rangle.Y'' + \langle \frac{\partial p''}{\partial x_i} \mid \eta\rangle.Y'' - \frac{\partial \langle p \mid \eta\rangle}{\partial \eta}\frac{\partial \xi}{\partial x_i}Y'' \\
+ \; & \frac{\partial}{\partial \eta}\langle u_i \mid \eta\rangle \left[\frac{\partial}{\partial x_j}\left[(\mu - \rho D)\frac{\partial \xi}{\partial x_j}\right]\right].Y'' + \mu\left(\frac{\partial \xi}{\partial x_j}\right)^2 \frac{\partial^2 \langle u_i \mid \eta\rangle}{\partial \eta^2}Y'' \\
+ \; & \frac{\partial}{\partial x_j}\left[\mu \frac{\partial {u_i}''}{\partial x_j}\right]Y'' + \mu\frac{\partial \xi}{\partial x_j}\frac{\partial}{\partial x_j}\left[\frac{\partial \langle u_i \mid \eta\rangle}{\partial \eta}\right]Y'' - \langle \mu\frac{\partial \xi}{\partial x_j}\frac{\partial}{\partial x_j}\left[\frac{\partial \langle u_i \mid \eta\rangle}{\partial \eta}\right] \mid \eta\rangle Y'' \\
+ \; & \left[\frac{\partial}{\partial x_j}\left[\mu\frac{\partial \langle u_i \mid \eta\rangle}{\partial x_j}\right]\right]Y'' - \langle \frac{\partial}{\partial x_j}\mu\frac{\partial \langle u_i \mid \eta\rangle}{\partial x_j} \mid \eta\rangle Y'' \\
- \; & \frac{\partial}{\partial \eta}\langle u_i \mid \eta\rangle\langle \frac{\partial}{\partial x_j}\left[(\mu - \rho D)\frac{\partial \xi}{\partial x_j}\right] \mid \eta\rangle Y'' \\
- \; & \langle \mu\left(\frac{\partial \xi}{\partial x_j}\right)^2 \mid \eta\rangle \frac{\partial^2 \langle u_i \mid \eta\rangle}{\partial \eta^2}Y'' - \langle \frac{\partial}{\partial x_j}\left[\mu\frac{\partial {u_i}''}{\partial x_j}\right] \mid \eta\rangle Y'' \qquad \text{(A.50)}
\end{aligned}$$

A.3.5 Final steps

Equation A.43 is then added to Eq. A.50. The left hand side is manipulated, firstly giving Eq. A.51,

$$\begin{aligned}
& \rho\left[Y''\frac{\partial u_i''}{\partial t} + u_i''\frac{\partial Y''}{\partial t}\right] \\
& + Y''\rho\frac{\langle u_i|\eta\rangle}{\partial t} - \rho_\eta\frac{\partial\langle u_i|\eta\rangle}{\partial t}Y'' + u_i''\rho\frac{\partial\langle Y|\eta\rangle}{\partial t} - u_i''\rho_\eta\frac{\partial\langle Y|\eta\rangle}{\partial \eta} + \\
& \rho u_j\frac{\partial\langle u_i|\eta\rangle}{\partial x_j}Y'' + \rho u_j\frac{\partial u_i''}{\partial x_j}Y'' - \rho_\eta\langle u_j|\eta\rangle\frac{\langle u_i|\eta\rangle}{\partial x_j}Y'' \\
& \rho u_j\frac{\partial\langle Y|\eta\rangle}{\partial x_j}u_j'' + \rho u_j\frac{\partial Y''}{\partial x_j}u_i'' - \rho_\eta\langle u_j|\eta\rangle\frac{\partial\langle Y|\eta\rangle}{\partial x_j}u_i'' \qquad \text{(A.51)}
\end{aligned}$$

and then Eq. A.52,

$$\begin{aligned}
&\frac{(\rho u_i'' Y'')}{\partial t} + \frac{\partial}{\partial x_j}\left[\rho\langle u_j|\eta\rangle u_i'' Y''\right] \\
&+\frac{\partial}{\partial x_j}\left[\rho u_j'' u_i'' Y''\right] + \left[Y''\rho\frac{\partial\langle u_i|\eta\rangle}{\partial t} - \rho_\eta\frac{\partial\langle u_i|\eta\rangle}{\partial t}Y''\right] + \left[u_i''\rho\frac{\langle Y|\eta\rangle}{\partial t} - u_i''\rho_\eta\frac{\partial\langle Y|\eta\rangle}{\partial t}\right] \\
&+\left[\rho\langle u_j|\eta\rangle\frac{\partial\langle u_i|\eta\rangle}{\partial x_j}Y'' + \rho u_j''\frac{\partial\langle u_i|\eta\rangle}{\partial x_j}Y'' - \rho_\eta\langle u_j|\eta\rangle\frac{\partial\langle u_i|\eta\rangle}{\partial x_j}Y''\right] \\
&+\left[\rho\langle u_j|\eta\rangle\frac{\partial\langle Y|\eta\rangle}{\partial x_j}u_i'' + \rho u_j''\frac{\partial\langle Y|\eta\rangle}{\partial x_j}u_i'' - \rho_\eta\langle u_j|\eta\rangle\frac{\partial\langle Y|\eta\rangle}{\partial x_j}u_i''\right] \qquad \text{(A.52)}
\end{aligned}$$

Conditional averages are then taken giving,

$$\begin{aligned}
&\frac{\partial}{\partial t}\left[\rho_\eta\langle u_i'' Y''|\eta\rangle\right] + \frac{\partial}{\partial x_j}\left[\rho_\eta\langle u_j|\eta\rangle\langle u_i'' Y''|\eta\rangle\right] + \frac{\partial}{\partial x_j}\left[\rho_\eta\langle u_i'' u_j'' Y''|\eta\rangle\right] \\
-\;& \rho_\eta\frac{\partial\langle u_i|\eta\rangle}{\partial t}\langle Y''|\eta\rangle + \rho_\eta\langle u_j'' Y''|\eta\rangle\frac{\partial\langle u_i|\eta\rangle}{\partial x_j} - \rho_\eta\langle u_j|\eta\rangle\frac{\partial\langle u_i|\eta\rangle}{\partial x_j}\langle Y''|\eta\rangle \\
-\;& \rho_\eta\frac{\partial Y|\eta\rangle}{\partial t}\langle u_i''|\eta\rangle + \rho_\eta\langle u_i'' u_j''|\eta\rangle\frac{\partial\langle Y|\eta\rangle}{x_j} - \rho_\eta\langle u_j|\eta\rangle\frac{\partial\langle Y|\eta\rangle}{\partial x_j}\langle u_i''|\eta\rangle \\
-\;& \frac{\partial}{\partial x_j}\left[\rho_\eta\langle u_i'' u_j''|\eta\rangle\right]\langle Y''|\eta\rangle - \frac{\partial}{\partial x_j}\left[\rho_\eta\langle u_j'' Y''|\eta\rangle\right]\langle u_i''|\eta\rangle \\
=\;& -\langle\frac{\partial p''}{\partial x_i}Y''|\eta\rangle + \frac{\partial\langle p|\eta\rangle}{\partial\eta}\langle\frac{\partial\xi}{\partial x_i}|\eta\rangle\langle Y''|\eta\rangle\langle\frac{\partial p''}{\partial x_i}|\eta\rangle\langle c''|\eta\rangle - \frac{\partial\langle p|\eta\rangle}{\partial\eta}\langle\frac{\partial\xi}{\partial x_i}Y''|\eta\rangle \\
&+\rho_\eta\langle\dot{w}'' u_i'' - \rho_\eta\langle\dot{w}|\eta\rangle\langle u_i''|\eta\rangle \\
&+\langle\mu(\nabla\xi)^2 Y''|\eta\rangle\frac{\partial^2\langle u_i|\eta\rangle}{\partial\eta^2} - \langle\mu(\nabla\xi)^2|\eta\rangle\frac{\partial^2\langle u_i|\eta\rangle}{\partial\eta^2}\langle Y''|\eta\rangle \\
&+\langle\rho D(\nabla\xi)^2 u_i''|\eta\rangle\frac{\partial^2\langle Y|\eta\rangle}{\partial\eta^2} - \langle\rho D(\nabla\xi)^2|\eta\rangle\frac{\partial^2\langle Y|\eta\rangle}{\partial\eta^2}\langle u_i''|\eta\rangle \\
&+\frac{\partial\langle u_i|\eta\rangle}{\partial\eta}\langle\nabla\cdot\left[(\mu-\rho D)\nabla\xi\right]Y''|\eta\rangle - \frac{\partial\langle u_i|\eta\rangle}{\partial\eta}\langle\nabla\cdot\left[\mu-\rho D\right]\nabla\xi|\eta\rangle\langle Y''|\eta\rangle \\
&+\langle\mu\nabla\xi\cdot\nabla(\frac{\partial\langle u_i|\eta\rangle}{\partial\eta})Y''|\eta\rangle - \langle\mu\nabla\xi\cdot\nabla\frac{\partial\langle u_i|\eta\rangle}{\partial\eta}|\eta\rangle\langle Y''|\eta\rangle \\
&+\langle\rho D\nabla\xi.\nabla(\frac{\partial\langle Y|\eta\rangle}{\partial\eta})u_i''|\eta\rangle - \langle\rho D\nabla\xi.\nabla\frac{\partial\langle Y|\eta\rangle}{\partial\eta}|\eta\rangle\langle u_i''|\eta\rangle \\
&+\langle\nabla.(\mu\nabla\langle u_i|\eta\rangle)Y''|\eta\rangle - \langle\nabla.(\mu\nabla\langle u_i|\eta\rangle)|\eta\rangle\langle Y''|\eta\rangle \\
&+\langle\nabla.(\rho D\nabla\langle Y|\eta\rangle)u_i''|\eta\rangle - \langle\nabla.(\rho D\nabla\langle Y|\eta\rangle)|\eta\rangle\langle u_i''|\eta\rangle \qquad \text{(A.53)}
\end{aligned}$$

Adding $\langle Y''|\eta\rangle$ times the conditional velocity equation and $\langle u_i''|\eta\rangle$ times the conditional species mass fraction equation gives the conditional turbulent flux equation:

$$\begin{aligned}
&\frac{\partial}{\partial t}\left[\rho_\eta\langle {u_i}''Y''|\eta\rangle\right]+\frac{\partial}{\partial x_j}\left[\rho_\eta\langle u_j|\eta\rangle\langle {u_i}''Y''|\eta\rangle\right]+\frac{\partial}{\partial x_j}\left[\rho_\eta\langle {u_i}''{u_j}''Y''|\eta\rangle\right]\\
&+\rho_\eta\langle {u_j}''Y''|\eta\rangle\frac{\partial\langle u_i|\eta\rangle}{\partial x_j}+\rho_\eta\langle {u_i}''{u_j}''|\eta\rangle\frac{\partial\langle Y|\eta\rangle}{\partial x_j}\\
&=-\langle Y''|\eta\rangle\frac{\partial\langle p|\eta\rangle}{\partial x_i}-\langle\frac{\partial p''}{\partial x_i}Y''|\eta\rangle-\frac{\partial\langle p|\eta\rangle}{\partial\eta}\langle\frac{\partial\xi}{\partial x_i}Y''|\eta\rangle\\
&+\langle Y''|\eta\rangle\langle\nabla.(\mu\nabla u_I'')|\eta\rangle+\langle {u_i}''|\eta\rangle\langle\nabla.(\rho D\nabla Y'')|\eta\rangle+\rho_\eta\langle\dot{w}''{u_i}''|\eta\rangle\\
&+\frac{\partial\langle u_i|\eta\rangle}{\partial\eta}\langle\frac{\partial}{\partial x_j}[(\mu-\rho D)\frac{\partial\xi}{\partial x_j}]Y''|\eta\rangle\\
&+\langle\mu(\nabla\xi)^2Y''|\eta\rangle\frac{\partial^2\langle u_i|\eta\rangle}{\partial\eta^2}+\langle\rho D(\nabla\xi)^2{u_i}''|\eta\rangle\frac{\partial^2\langle Y|\eta\rangle}{\partial\eta^2}\\
&+\langle\mu\frac{\partial\xi}{\partial x_j}.\frac{\partial}{\partial x_j}\left(\frac{\partial\langle u_i|\eta\rangle}{\partial\eta}\right)Y''|\eta\rangle+\langle\rho D\frac{\partial\xi}{\partial x_j}.\frac{\partial}{\partial x_j}\left(\frac{\partial\langle Y|\eta\rangle}{\partial\eta}\right){u_i}''|\eta\rangle
\end{aligned}\tag{A.54}$$

Writing $s_{ij}''=(\partial u_i''/\partial x_j+\partial u_j''/\partial x_i)$, $N=D(\nabla\xi)^2$ and $Sc=\mu/(\rho D)$, and then neglecting $e_1=\langle\mu\frac{\partial\xi}{\partial x_j}.\frac{\partial}{\partial x_j}\left(\frac{\partial\langle u_i|\eta\rangle}{\partial\eta}\right)Y''|\eta\rangle$ and $e_2=\langle\rho D\frac{\partial\xi}{\partial x_j}.\frac{\partial}{\partial x_j}\left(\frac{\partial\langle Y|\eta\rangle}{\partial\eta}\right){u_i}''|\eta\rangle$ due to high Reynolds numbers gives the final form of the conditional turbulent flux used in chapter 4.

$$\begin{aligned}
&\frac{\partial}{\partial t}\left[\rho_\eta\langle {u_i}''Y''|\eta\rangle\right]+\frac{\partial}{\partial x_j}\left[\rho_\eta\langle u_j|\eta\rangle\langle {u_i}''Y''|\eta\rangle\right]=-\frac{\partial}{\partial x_j}\left[\rho_\eta\langle {u_i}''{u_j}''Y''|\eta\rangle\right]\\
&-\rho_\eta\langle {u_j}''Y''|\eta\rangle\frac{\partial\langle u_i|\eta\rangle}{\partial x_j}-\rho_\eta\langle {u_i}''{u_j}''|\eta\rangle\frac{\partial\langle Y|\eta\rangle}{\partial x_j}\\
&-\langle Y''|\eta\rangle\frac{\partial\langle p|\eta\rangle}{\partial x_i}-\langle\frac{\partial p''}{\partial x_i}Y''|\eta\rangle-\frac{\partial\langle p|\eta\rangle}{\partial\eta}\langle\frac{\partial\xi}{\partial x_i}Y''|\eta\rangle\\
&+\langle Y''|\eta\rangle\langle\frac{\partial(\mu s_{ij}'')}{\partial x_j}|\eta\rangle+\langle {u_i}''|\eta\rangle\langle\frac{\partial}{\partial x_j}(\rho D\frac{\partial Y''}{\partial x_j})|\eta\rangle+\rho_\eta\langle\dot{w}''{u_i}''|\eta\rangle\\
&+\frac{\partial\langle u_i|\eta\rangle}{\partial\eta}\langle\frac{\partial}{\partial x_j}[(\mu-\rho D)\frac{\partial\xi}{\partial x_j}]Y''|\eta\rangle+\langle\rho ScNY''|\eta\rangle\frac{\partial^2\langle u_i|\eta\rangle}{\partial\eta^2}+\langle\rho N{u_i}''|\eta\rangle\frac{\partial^2\langle Y|\eta\rangle}{\partial\eta^2}
\end{aligned}\tag{A.55}$$

Chakraborty has arrived at the same result from Klimenko's PDF derivation method, 'and I have assuredly found an admirable proof of this, but the margin is too narrow to contain it.' [92].

A.4 An estimate for the mixture fraction variance during spray evaporation

The mixture fraction variance occurring following evaporation of a fuel spray by a propagating flame is estimated from the available information as $max[(\tilde{\xi}''^2_{gas} + k\tilde{\xi}_{liq}(\xi_{sat} - \tilde{\xi}_{liq})), (\tilde{\xi}_{con}(\xi_{sat} - \tilde{\xi}_{con}))]$. The constant k takes a value between 0 and 1. Its value has been estimated by considering turbulent evaporation of a homogeneous fuel spray and employing some crude approximations for the terms in the equation for the mixture fraction variance balance equation, given as [107]:

$$\frac{\partial \bar{\rho}\widetilde{\xi''^2}}{\partial t} = \rho\bar{S}^+ + \rho\bar{S}^- - \bar{\rho}\chi \tag{A.56}$$

$$\chi = 2D\left(\frac{\partial \widetilde{\xi''^2}}{\partial x_i}\right)^2 \approx 2D\left(\frac{\widetilde{\xi''^2}^{1/2}}{d_{drop}}\right)^2$$

$$\rho\bar{S}^+ = 2\bar{\rho}(1-\tilde{\xi})\int_0^{\tilde{\xi}_s}(\eta-\tilde{\xi})\cdot\langle\dot{W}_v \mid \eta\rangle\bar{P}(\eta)d\eta \approx 2\bar{\rho}(1-\tilde{\xi})\tilde{\xi}\tilde{W}_v \tag{A.57}$$

$$\rho\bar{S}^- = -\bar{\rho}\int_0^{\tilde{\xi}_s}(\eta-\tilde{\xi})^2\cdot\langle\dot{W}_v \mid \eta\rangle\bar{P}(\eta)d\eta \approx 0 \tag{A.58}$$

The droplet diameters are given a Rosin-Rammler distribution [117] and each droplet is assumed to evaporate at the end of its lifetime given by ${D_0}^2/\lambda$ [25]. The steady state evaporation constant λ may be taken as $1.1 \times 10^{-6}(m^2s^{-1})$ for atmospheric combustion of n-heptane, or $0.9 \times 10^{-6}(m^2s^{-1})$ for kerosene combustion at the altitude relight conditions considered in chapter 7 [25]. The scalar dissipation has been estimated by assuming mixture fraction varies on a length scale equal to the inter-droplet spacing of the droplets currently at the end of their life. The positive evaporation source S^+ has been estimated by assuming a bi-modal mixture fraction pdf with the saturation mixture fraction and the mixture fraction of evaporation both equal to one. The negative source S^- has been neglected on the assumption that $S^+ \gg S^-$. The value of k computed in this way is found to remain between 0.1 and 0.2 for the majority of the spray evaporation time and $k = 0.15$ is used throughout chapter 7.